

NASA/CR—2004-212887



# Turbulent Jet Flames Into a Vitiated Coflow

Ricardo Cabra  
University of California, Berkeley, Berkeley, California

---

March 2004

## The NASA STI Program Office . . . in Profile

Since its founding, NASA has been dedicated to the advancement of aeronautics and space science. The NASA Scientific and Technical Information (STI) Program Office plays a key part in helping NASA maintain this important role.

The NASA STI Program Office is operated by Langley Research Center, the Lead Center for NASA's scientific and technical information. The NASA STI Program Office provides access to the NASA STI Database, the largest collection of aeronautical and space science STI in the world. The Program Office is also NASA's institutional mechanism for disseminating the results of its research and development activities. These results are published by NASA in the NASA STI Report Series, which includes the following report types:

- **TECHNICAL PUBLICATION.** Reports of completed research or a major significant phase of research that present the results of NASA programs and include extensive data or theoretical analysis. Includes compilations of significant scientific and technical data and information deemed to be of continuing reference value. NASA's counterpart of peer-reviewed formal professional papers but has less stringent limitations on manuscript length and extent of graphic presentations.
- **TECHNICAL MEMORANDUM.** Scientific and technical findings that are preliminary or of specialized interest, e.g., quick release reports, working papers, and bibliographies that contain minimal annotation. Does not contain extensive analysis.
- **CONTRACTOR REPORT.** Scientific and technical findings by NASA-sponsored contractors and grantees.

- **CONFERENCE PUBLICATION.** Collected papers from scientific and technical conferences, symposia, seminars, or other meetings sponsored or cosponsored by NASA.
- **SPECIAL PUBLICATION.** Scientific, technical, or historical information from NASA programs, projects, and missions, often concerned with subjects having substantial public interest.
- **TECHNICAL TRANSLATION.** English-language translations of foreign scientific and technical material pertinent to NASA's mission.

Specialized services that complement the STI Program Office's diverse offerings include creating custom thesauri, building customized databases, organizing and publishing research results . . . even providing videos.

For more information about the NASA STI Program Office, see the following:

- Access the NASA STI Program Home Page at <http://www.sti.nasa.gov>
- E-mail your question via the Internet to [help@sti.nasa.gov](mailto:help@sti.nasa.gov)
- Fax your question to the NASA Access Help Desk at 301-621-0134
- Telephone the NASA Access Help Desk at 301-621-0390
- Write to:  
NASA Access Help Desk  
NASA Center for Aerospace Information  
7121 Standard Drive  
Hanover, MD 21076

NASA/CR—2004-212887



# Turbulent Jet Flames Into a Vitiated Coflow

Ricardo Cabra  
University of California, Berkeley, Berkeley, California

Prepared under Grant NAG3-2103

National Aeronautics and  
Space Administration

Glenn Research Center

---

March 2004

## Acknowledgments

I first acknowledge and thank my advisor, Professor Robert Dibble for the wealth of guidance, knowledge and personal experience he has shared with me. I thank collaborators and advisors Professor J.-Y. Chen, and Dr.'s Robert Barlow and Adonios Karpets of the Combustion Research Facility at Sandia National Laboratories.

I also appreciate the support given by the hard working staff at Hesse Hall consisting of Scott McCormick, Mike Neuffer, John Austin, and MaryAnne Peters. I acknowledge fellow collaborators who have helped realize the potential of this research: Dr. Don Holve and Frank Acosta of Process Metrix (San Ramon, California), Dr.'s Yugi Ikeda and Jun Kojima of Kobe University (Kobe, Japan), Mr. Yasunori Hamano of IHI (Tokyo, Japan), and Dr. Tore Myhrvold of the Norwegian University of Science and Technology (Trondheim, Norway). I am grateful to those institutions who have financially supported my graduate studies: NASA Glenn Research Center (NAG3-2103) and grant monitor Dr. Jim Holdeman for funding the vitiated coflow burner research project, Chevron Corporation for the Chevron Fellowship, and the Western States Section of the Combustion Institute for travel support to the 29th Symposium on Combustion in Japan. I especially thank fellow cohorts of the Combustion Lab with whom countless collaborations and conversations have made my experience at Berkeley most fulfilling: James Girard, John Torres, Ed Cheng, Nick Frieden, Tom Bronson, Parag Mehresh, Hunter Mack, Fred Ginnebaugh, Michael Au, and Will Gans.

Trade names or manufacturers' names are used in this report for identification only. This usage does not constitute an official endorsement, either expressed or implied, by the National Aeronautics and Space Administration.

This work was sponsored by the Low Emissions Alternative Power Project of the Vehicle Systems Program at the NASA Glenn Research Center.

Available from

NASA Center for Aerospace Information  
7121 Standard Drive  
Hanover, MD 21076

National Technical Information Service  
5285 Port Royal Road  
Springfield, VA 22100

Available electronically at <http://gltrs.grc.nasa.gov>

# Turbulent Jet Flames into a Vitiated Coflow

Ricardo Cabra  
University of California, Berkeley  
Berkeley, California 94720

## Abstract

Examined is the vitiated coflow flame, an experimental condition that decouples the combustion processes of flows found in practical combustors from the associated recirculating fluid mechanics. The configuration consists of a 4.57 mm diameter fuel jet into a coaxial flow of hot combustion products from a lean premixed flame. The 210 mm diameter coflow isolates the jet flame from the cool ambient, providing a hot environment similar to the operating conditions of advanced combustors; this important high temperature element is lacking in the traditional laboratory experiments of jet flames into cool (room) air. A family of flows of increasing complexity is presented: 1) nonreacting flow, 2) all hydrogen flame (fuel jet and premixed coflow), and 3) set of methane flames. This sequence of experiments provides a convenient ordering of validation data for combustion models.

Laser Raman-Rayleigh-LIF diagnostics at the Turbulent Diffusion Flame laboratory of Sandia National Laboratories produced instantaneous multiscalar point measurements. These results attest to the attractive features of the vitiated coflow burner and the well-defined boundary conditions provided by the coflow. The coflow is uniform and steady, isolating the jet flame from the laboratory air for a downstream distance ranging from  $z/d = 50-70$ . The statistical results show that differential diffusion effects in this highly turbulent flow are negligible.

Complementing the comprehensive set of multiscalar measurements is a parametric study of lifted methane flames that was conducted to analyze flame sensitivity to jet and coflow velocity, as well as coflow temperature. The linear relationship found between the lift-off height and the jet velocity is consistent with previous experiments. New linear sensitivities were found correlating the lift-off height to coflow velocity and temperature. A blow-off study revealed that the methane flame blows off at a common coflow temperature (1260 K), regardless of coflow or jet velocity. An explanation for this phenomenon is that entrainment of ambient air at the high lift-off heights prevents autoignition.

Analysis of the results suggests that flame stabilization occurs through a combination of flame propagation, autoignition, and localized extinction processes. Proposed is an expanded view of distributed reaction combustion based on analysis of the distributions of probe volume conditions at the stabilization region of the lifted hydrogen and methane flames. Turbulent eddies the size of the flame thickness mix fuel and hot coflow across the flame front, thereby enhancing the reaction zone with autoignition of reactants at elevated temperatures; this is the reverse effect of turbulent flames in ambient air, where intense turbulence in cool mixtures result in localized extinction. Each of the three processes (i.e., flame propagation, autoignition and localized extinction) contributes to flame stabilization in varying degrees, depending on flow conditions.



# Table of Contents

<b>Abstract</b> .....	iii
<b>Table of Contents</b> .....	v
<b>List of Figure</b> .....	viii
<b>List of Tables</b> .....	xvii
<b>INTRODUCTION</b> .....	1
1.1.Combustion & Society .....	2
1.2.Model Building in Combustion Science .....	3
1.3.Vitiated Air .....	4
1.4.Organization of Chapters .....	6
<b>2. LITERATURE REVIEW</b> .....	11
2.1.Jet Flames in Hot Environments .....	11
2.2.Turbulent Lifted Jet Flames in a Cool Environment .....	14
<b>3. NUMERICAL METHODS</b> .....	20
3.1.StanJAN (Equilibrium Code) .....	20
3.2.Well-Mixed Reactor .....	21
3.3.One Dimension Laminar Premixed Flame Model .....	25
3.4.Laminar Opposed Flow Flame Model (OPPDIF) .....	25
3.5.Eddy Dissipation Concept Combustion Model .....	28
3.6.Probability Density Function Combustion Model .....	29

<b>4. VITIATED COFLOW BURNER</b> .....	31
4.1.Design Requirements .....	31
4.2.Concept Generation and Screening .....	32
4.3.Current Concept Design: Perforated Plate Burner (VC-1) .....	40
4.4.Flow Control System .....	58
4.5.Safety System (Flashback) .....	68
4.6.Chapter Summary .....	73
<b>5. LASER RAYLEIGH-RAMAN-LIF MEASUREMENT SYSTEM</b> .....	75
5.1.Background Physics .....	75
5.2.Experimental Setup .....	78
5.3.Data Reduction .....	85
5.4.System Calibration .....	90
<b>6. SIMULTANEOUS MULTISCALAR POINT MEASUREMENTS</b> .....	99
6.1.Lifted Hydrogen Jet Flame .....	99
6.2.Lifted Methane-Air Jet Flame .....	124
6.3.Chapter Summary .....	147
<b>7. BOUNDARY CONDITIONS (NUMERICAL CONSIDERATIONS)</b> .....	149
7.1.Inlet Flow Field .....	149
7.2.Inlet Temperature Field .....	152
7.3.Mixing (Nonreacting) Jet in Coflow Structure .....	156
7.4.Two-Stream Flow Condition .....	160
7.5.Near-Equilibrium Coflow Conditions .....	166
7.6.Sensitivity of Reactions to Coflow Radical Species and Temperature .....	168

<b>8. PARAMETRIC STUDY</b> .....	172
8.1.Lift-Off Height .....	173
8.2.Lift-Off Height Sensitivity to Jet and Coflow Velocities .....	173
8.3.Lift-Off Height Sensitivity to Coflow Temperature .....	177
8.4.Flame Blow-Off Due to Reduced Coflow Temperature .....	178
<b>9. STABILIZATION OF LIFTED JET FLAMES</b> .....	182
9.1.Hydrogen Flame Observations .....	182
9.2.Methane Flame Observations .....	188
9.3.Autoignition and the Stabilization of Lifted Flames .....	192
<b>10. CONCLUSIONS</b> .....	196
10.1. Vitiated Coflow Flame Data Set .....	196
10.2. Stabilization by Committee (Autoignition-Propagation-Extinction) .....	198
10.3. Future of Vitiated Coflow Flame .....	199
<b>REFERENCES</b> .....	201
<b>APPENDIX</b>	
A. Engineering Drawings & Parts List .....	214
B. Conditional Mean Data Plots .....	222
C. Spray Work .....	224

## List of Figures

1.1	Model building in the combustion science community.	3
1.2	Flow pattern in gas turbine engine combustor.	5
1.3	Current capabilities of computational resources in modeling of vitiated coflow combustion.	6
1.4	Jet flame in a coaxial flow of vitiated gas.	7
2.1	Methane/Air turbulent nonpremixed piloted jet flame.	12
2.2	Turbulent premixed flame in a large, laminar pilot.	13
2.3	CH-PLIF image of a turbulent nonpremixed methane/air flame.	17
2.4	DNS prediction of heat release rate of a lifted hydrogen flame.	18
3.1	Sensitivity of Perfectly Stirred Reactor (PSR) temperature to residence time.	22
3.2	Well-Mixed Balloon (WMB) conceptual simulation of oxidizer entrainment of a fuel jet.	24
3.3	The Tsuji opposed flow geometry and the laminar opposed flow flame model.	26
4.1	Photograph of a jet with a coflow from a catalytic burner.	34
4.2	Photograph of the tube bundle burner.	35
4.3	Photograph of the grid-turbulence screen burner.	37
4.4	Photograph of a 1/8 inch tube at the center of a coarse porous disk.	38
4.5	Photograph of the 4 inch diameter perforated plate burner.	39
4.6	The many combustion modes available with vitiated coflow burner.	41

## List of Figures (cont.)

4.7	Photograph of the current 8 inch diameter vitiated coflow jet flame burner.	42
4.8	The laminar and turbulent flow fields associated with premixed flames stabilized on the perforated plate surface.	43
4.9	Drill pattern for vitiated coflow perforated plate.	46
4.10	Equilibrium oxygen mole fraction in products of premixed hydrogen-air and methane-air flames (StanJAN).	48
4.11	Laminar flame speed of premixed hydrogen-air flame.	49
4.12	Required hydrogen flow rates for the coflow flame.	51
4.13	Heat transfer analysis of the perforated plate.	54
4.14	Steady state radial distribution of temperature for the perforated plate.	56
4.15	Flow system for the vitiated coflow burner.	58
4.16	Air flow rate and pressure drop across the perforated plate as a function of motor drive frequency.	59
4.17	Air mass flow rate as a function of the pressure drop across the perforated plate.	60
4.18	Calibration data for orifice plates.	62
4.19	Agreement of flow and oxygen based stoichiometries for coflow products of methane-air flames show that mixture reaches equilibrium.	65
4.20	Temperature of products from premixed hydrogen-air flames stabilized on the perforated plate.	67
4.21	Schematic of the Vitiated Coflow Burner.	70

## List of Figures (cont.)

4.22	Photos of the vitiated coflow burner setup.	71
5.1	Energy transition processes and spectral emission associated with laser Rayleigh and Raman scattering.	76
5.2	Raman spectra of major species for fuel lean and fuel rich methane-air flames.	77
5.3	Energy transition process and spectral emission associated with laser induced fluorescence	78
5.4	A schematic of the Raman-Rayleigh-LIF experimental facility located at Sandia National Laboratories.	79
5.5	The optical layout for the Raman-Rayleigh system.	81
5.6	Spatial resolution determined by copper pieces that were decomposed by the laser beam used for Raman-Rayleigh diagnostics.	82
5.7	Optical layout of the Laser Induced Fluorescence (LIF) system.	84
5.8	Iterative scheme for inverse Raman-Rayleigh problem.	88
5.9	Rayleigh background is determined by extrapolation of signals from calibration flows of nitrogen and helium.	91
5.10	Processed mean values of temperature and concentrations in the CH <sub>4</sub> -Air Hencken burner calibration flames.	92
5.11	Confirmation of NO calibration from flat premixed methane flames where the N <sub>2</sub> is doped with NO.	93
5.12	NO LIF calibration using Hencken burner calibration flames.	94

## List of Figures (cont.)

5.13	Processed mean and RMS values of temperature and concentrations in the CH <sub>4</sub> -Air Hencken burner calibration flames.	96
6.1	Schematic of the lifted H <sub>2</sub> /N <sub>2</sub> jet flame into a vitiated coflow.	101
6.2	Location of measurement points for lifted H <sub>2</sub> /N <sub>2</sub> jet flame.	103
6.3	Uniform and steady inlet conditions. Radial profiles for temperature and oxygen at $z/d = 1$ for the lifted H <sub>2</sub> /N <sub>2</sub> jet flame into a vitiated coflow.	104
6.4	Evolution of radial distributions of temperature, H <sub>2</sub> , O <sub>2</sub> , H <sub>2</sub> O, OH, and NO for the H <sub>2</sub> /N <sub>2</sub> jet flame into a vitiated coflow.	105
6.5	H <sub>2</sub> /N <sub>2</sub> jet flame structure represented by the OH mass fraction fields. Comparisons between experimental and numerical results.	109
6.6	Centerline profiles of temperature, H <sub>2</sub> , O <sub>2</sub> , H <sub>2</sub> O, OH, and NO for the H <sub>2</sub> /N <sub>2</sub> jet flame into a vitiated coflow.	111
6.7	Centerline profiles of the mixture fraction and oxygen mass fraction. Comparisons between experimental and numerical results.	115
6.8	Evolution of scatter plots of temperature and OH mole fraction for the H <sub>2</sub> /N <sub>2</sub> jet flame into a vitiated coflow.	117
6.9	Comparison of hydrogen and oxygen based mixture fraction formulations at $z/d = 11$ for the H <sub>2</sub> /N <sub>2</sub> jet flame into a vitiated coflow.	123
6.10	Schematic of the lifted CH <sub>4</sub> /Air jet flame into a vitiated coflow.	125
6.11	Location of measurement points for CH <sub>4</sub> /Air lifted jet flame.	127

## List of Figures (cont.)

6.12	Uniform and steady inlet conditions. Radial profiles for temperature and oxygen at $z/d = 1$ for the lifted $\text{CH}_4/\text{Air}$ jet flame into a vitiated coflow.	129
6.13	Evolution of radial profiles for temperature, $\text{CH}_4$ , $\text{O}_2$ , $\text{H}_2\text{O}$ , $\text{CO}_2$ , $\text{OH}$ , $\text{H}_2$ , and $\text{CO}$ for the lifted $\text{CH}_4/\text{Air}$ jet flame into a vitiated coflow.	130
6.14	Intermittency of the $\text{CH}_4/\text{Air}$ jet flame as exhibited by the contour plots of Favre average and RMS of temperature.	135
6.15	Centerline profiles of temperature, $\text{CH}_4$ , $\text{O}_2$ , $\text{H}_2\text{O}$ , $\text{CO}_2$ , $\text{OH}$ , $\text{H}_2$ , and $\text{CO}$ for the lifted $\text{CH}_4/\text{Air}$ jet flame into a vitiated coflow.	136
6.16	Centerline profile of the Favre average and RMS of mixture fraction for the lifted $\text{CH}_4/\text{Air}$ jet flame into a vitiated coflow.	140
6.17	Evolution of scatter plots of temperature and $\text{OH}$ mole fraction for the lifted $\text{CH}_4/\text{Air}$ jet flame into a vitiated coflow	142
6.18	Comparison of hydrogen and carbon based mixture fraction formulations at $z/d = 40$ & $50$ for the lifted $\text{CH}_4/\text{Air}$ jet flame into a vitiated coflow.	146
7.1	Average flow field at the nozzle exit ( $d = 4.57$ mm).	151
7.2	Jet exit temperature dependence on the coflow temperature and the coflow and jet velocities.	155
7.3	The $K_4$ ratio as a function of the jet and coflow velocities.	156
7.4	Schematic of the nonreacting air jet into a vitiated coflow.	157
7.5	Temperature field of a nonreacting air jet in the vitiated coflow	158
7.6	Jet spreading rate and coflow degradation rate for nonreacting conditions.	159

## List of Figures (cont.)

7.7	Structure of the turbulent shear layers between each of the three streams in the vitiated coflow flame.	162
7.8	Nonreacting jet spreading rate for the VCB@Sandia flames and the nonreacting flow.	163
7.9	The coflow potential core height as a function of the coflow temperature.	165
7.10	The two-stream condition height (Figure 7.7) relationship to the coflow temperature.	166
7.11	Ignition delay time versus initial mixture temperature for the VCB@Sandia flames.	169
7.12	Ignition delay time versus departure from equilibrium of OH mole fraction for the VCB@Sandia flames.	171
8.1	Negative image of the lifted jet flame.	174
8.2	Sensitivity of CH <sub>4</sub> /Air flame lift-off height to coflow and jet velocities.	175
8.3	Sensitivity of CH <sub>4</sub> /Air flame lift-off height to coflow and jet velocities.	176
8.4	Sensitivity of CH <sub>4</sub> /Air flame lift-off height to coflow temperature.	178
8.5	Coflow temperature at flame blow-off is independent of jet and coflow velocities.	179
8.6	The extinction time scale increases dramatically with decreased coflow temperature	180
9.1	Effect of stoichiometry on the ignition delay time for the hydrogen jet flame into vitiated coflow.	183

## List of Figures (cont.)

9.2	Parametric relationships for turbulent premixed combustion.	186
9.3	Temperature distribution in the H <sub>2</sub> /N <sub>2</sub> flame stabilization region.	187
9.4	Temperature distribution above the CH <sub>4</sub> /Air flame stabilization region	188
9.5	Effect of stoichiometry on the ignition delay time for the methane conditions.	190
9.6	Illustration of the transient flamelet response to an autoignition event.	192
9.7	Traditional view of distributed reaction mode for premixed turbulent combustion.	194
9.8	Alternative view of distributed reaction mode for premixed turbulent combustion.	194

## List of Tables

4.1	Orifice Meter Calibration Data	63
5.1	LIF system excitation and detection specifications.	85
5.2	Estimated uncertainties of the laser Raman-Rayleigh-LIF systems.	98
6.1	H <sub>2</sub> /N <sub>2</sub> experimental conditions.	100
6.2	CH <sub>4</sub> /Air experimental conditions.	126
7.1	Equilibrium limit of coflow conditions as calculated via StanJAN.	158
7.2	Comparisons between expected and actual inlet boundary conditions.	167
8.1	Base Case Conditions for CH <sub>4</sub> /Air Flame.	172



# Chapter 1

## Introduction

For many, the term “high-tech” is associated with visions of computers, biotechnology and nano-scale devices. These technologies have greatly increased the pace and quality of life; however, the world would be at a complete standstill if it were not for the combustion of fossil fuels. From the energy needed at home, to the various forms of transportation used to traverse cities and oceans, combustion is the primary source enabling all of these activities.

Despite the widespread application of combustion, many questions about the fundamental processes involved remain unanswered. The body of work presented in this manuscript focuses at the fundamental level on combustion processes in a hot environment of vitiated air. Many advanced combustor designs such as gas turbines, furnaces and internal combustion engines utilize hot environments to facilitate and control combustion processes. Therefore, the results presented here are applicable to a wide spectrum of applications.

In combustion science, numerical and experimental researchers work together to build models that can be implemented in the design of advanced combustion systems. This chapter presents this interaction as well as the focus of research on combustion in an environment of vitiated air. An outline of the scope of the research for the remainder of the manuscript is also given.

## 1.1. Combustion and Society

As stated previously, combustion processes enable the vast majority of human activities. However, global warming, rising energy costs and harmful emissions have driven initiatives to develop cleaner and more efficient combustion systems. The greenhouse gas carbon dioxide ( $\text{CO}_2$ ) is an unavoidable product of hydrocarbon combustion; therefore, in order to limit  $\text{CO}_2$  emissions, fuel consumption must be reduced. Fuel consumption must also be reduced through increased combustor efficiency in order to offset the rising costs of energy. The unwanted combustion product nitric oxide (NO) is a health hazard produced by systems with high peak temperatures. Conversely, low peak temperature systems are sensitive and difficult to control. For instance, lean premixed combustors have the tendency to generate severe pressure oscillations. There is also a tendency for these systems not to oxidize the fuel completely, resulting in unburned hydrocarbons, soot and CO emissions. These emissions are health hazards and greenhouse gases.

Advances in combustion sciences have produced alternatives that can provide cleaner and more efficient energy conversion. There are many combustion technologies that are close to being feasible options for providing more efficient and cleaner energy. For example, developing technologies using catalytic combustors, lean premixed gas turbines and Homogeneous Charge Compression Ignited (HCCI) combustion are all possible alternatives. When brought to the limits of operation, flames abruptly extinguish, they do not gradually die down.

Engineers have worked around many of these technological barriers. However, it is now the onus of the combustion science community to provide phenomenological

models of the combustion processes. The successful implementation of these models will guide the effective development of combustion systems. The following section describes the framework through which the combustion science community helps the cause.

## 1.2. Model Building in Combustion Science

Combustion models are built through the interaction of numerical and experimental scientists. Figure 1.1 illustrates how scientists investigate real world problems to produce models that can aid in the design of combustion systems.

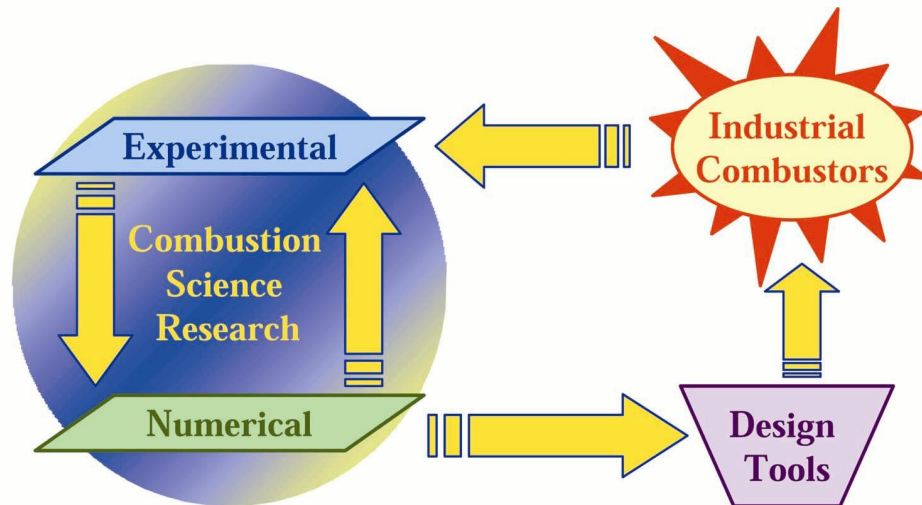


**Figure 1.1.**

Model building in the combustion science community.

The science community analyzes real-world problems (e.g., industrial combustors) and extracts key components. For example, more research needs to be conducted to provide an increased understanding of reacting flows where the turbulence and chemical kinetics are strongly coupled. It is up to the combustion science community to develop a condition that exhibits a less complex, yet still meaningful representation of the real problem. Through successful collaborations, the numerical scientists develop models that accurately represent the combustion processes. These

models can then be incorporated into computer-based design tools. Subsequently, these design tools can then be used to develop cleaner, more efficient combustion systems.

An excellent example of collaborative experimental-numerical research is the International Workshop on Measurement and Computation of Turbulent Nonpremixed Flames (TNF). The TNF workshop is an ongoing series of meetings focused on the investigation of the turbulence-chemistry interaction for turbulent nonpremixed and partially premixed combustion. As stated on the TNF website the collaboration's objectives are (Barlow 2003):

1. To establish a database of experimental results for well-documented flames that are appropriate for model validation.
2. To provide a framework for collaborative comparisons between numerical and experimental results.
3. To identify priorities for future numerical and experimental research efforts.

Through these collaborations, our research group at Berkeley decided to investigate the recirculation zone of advanced combustors where fuel mixes with hot combustion products, not cool air.

### **1.3. Vitiated Air**

The following is Webster's definition of the verb vitiate.

***Vitiate:** To make vicious, faulty, or imperfect; to render defective; to injure the substance or qualities of; to impair; to contaminate; to spoil.*

Advanced combustors utilize high temperature and pressure environments to facilitate reaction, increase efficiency and reduce emissions. Combustion chamber

designs utilize recirculation zones to accomplish this mixing of cool reactants with hot combustion products. The fuel in fact mixes with vitiated air, which is a hot mixture of oxygen, nitrogen and that is diluted (“vitated”) with combustion products like water and carbon dioxide. Figure 1.2 shows a typical combustor design for gas turbine engines. As can be seen from the illustration, the fluid mechanics are detailed, with recirculation zones and air injection ports throughout the chamber.

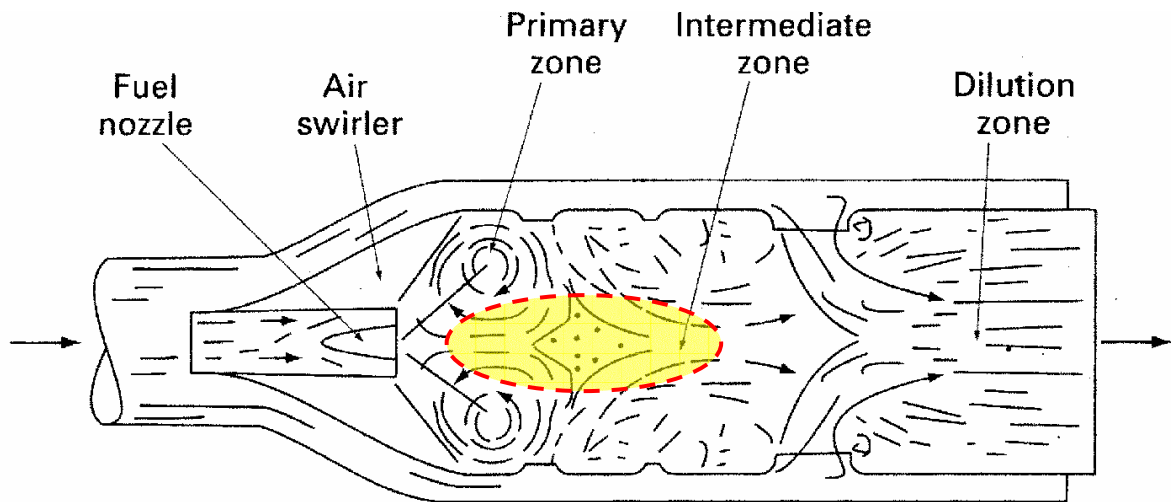


**Figure 1.2.**

Flow pattern in typical gas turbine engine combustor (Borman & Ragland, 1998).

Numerical modeling of these recirculating flows is challenging because of the detailed interaction between turbulence and chemistry. Figure 1.3 illustrates the current capabilities of our computational resources in terms of chemical and turbulent detail. A fully modeled flow, with detailed fluid mechanics and chemical kinetics, is intractable given the current computational resources. Therefore, detailed chemical kinetic modeling comes at the expense of detailed flow modeling, and vice versa. Note that many industrial problems are beyond current capabilities because of 3-D flow and the use of hydrocarbons like diesel and kerosene, which have vast chemical mechanisms.

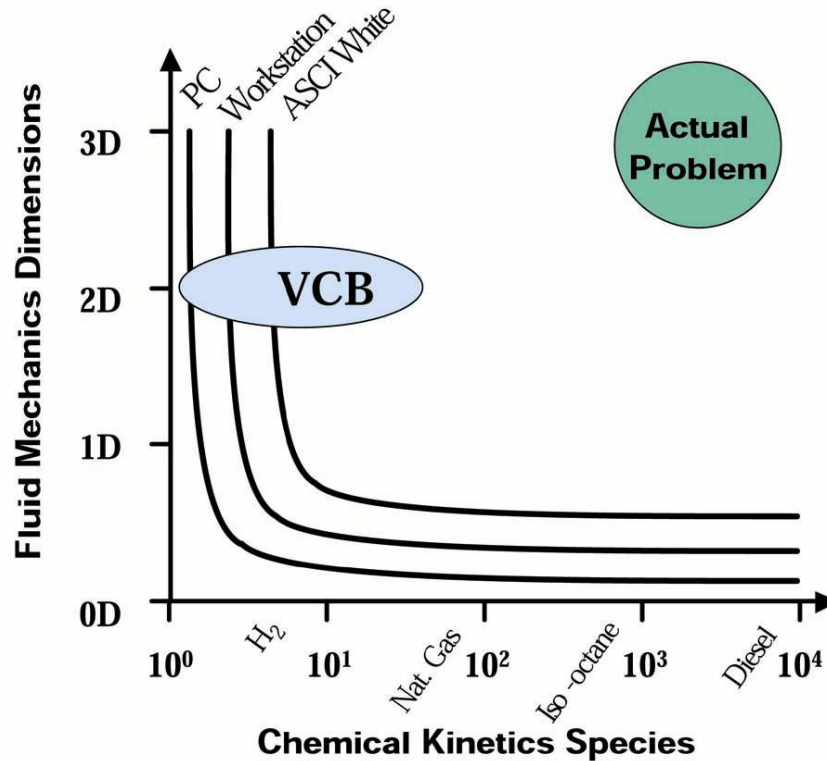


**Figure 1.3.**

Current capabilities of computational resources in modeling of vitiated coflow combustion (VCB). ASCI-White is a supercomputer at Lawrence Livermore National Laboratories (Flowers & Dibble 2001).

#### **1.4. Organization of Chapters**

The objective of this research was to design an experiment that addresses the fundamental combustion processes in vitiated air environments while decoupling the chemical kinetics from the complex recirculating flow. The material presented in the manuscript is comprehensive and meant to help facilitate future experimental and numerical research efforts based from this research. Chapter 2 provides a context for the present work by reviewing the literature on turbulent combustion, with an emphasis on research of jet flames in hot environments and turbulent lifted jet flames. Introductions to the numerical tools used throughout the rest of the presentation are given in Chapter 3.

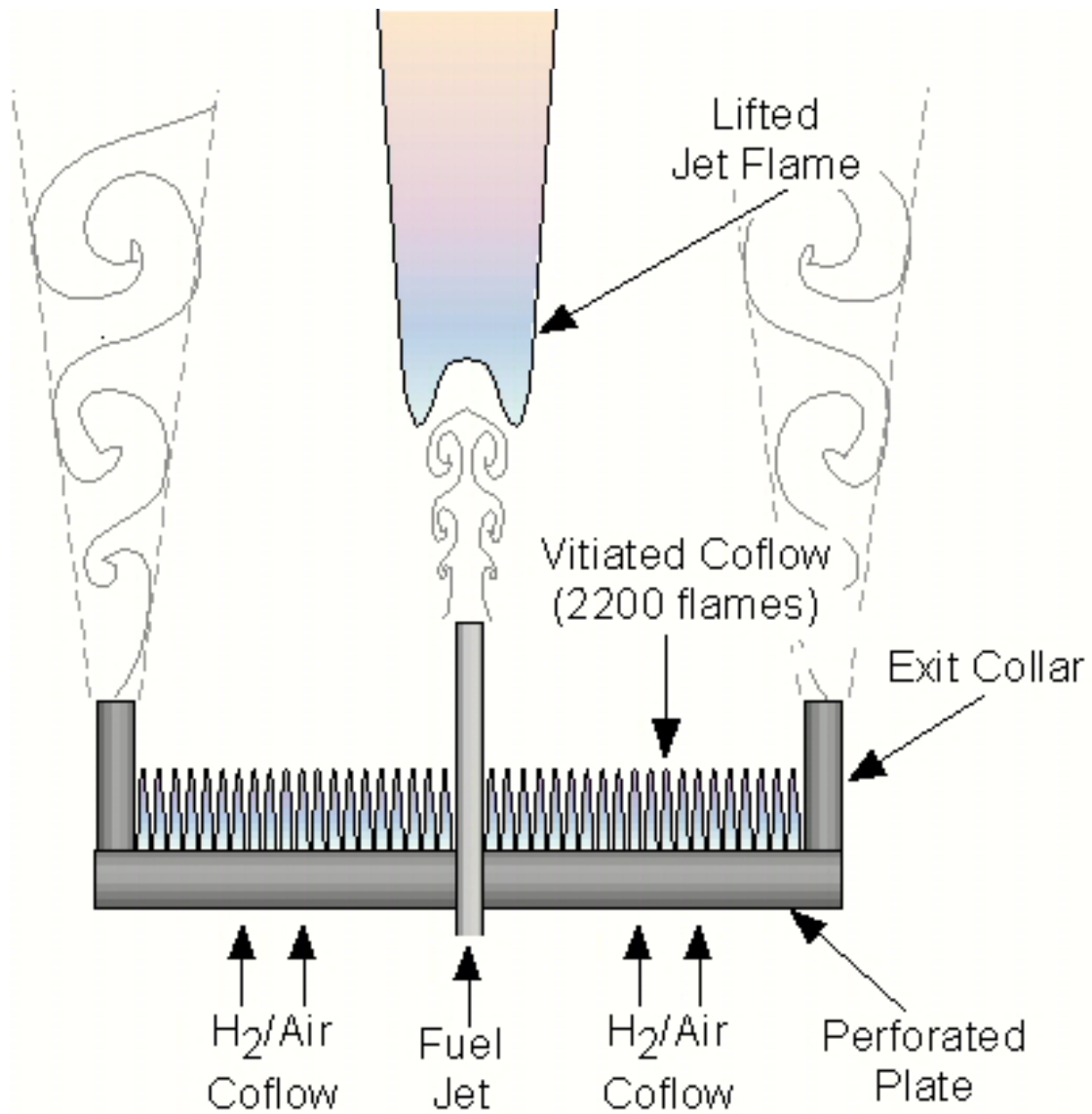


**Figure 1.4.**

Jet flame in a coaxial flow of vitiated gas.

The development process of the vitiated coflow flame is outlined in Chapter 4. Initially, several candidates were considered. Numerical and experimental explorations as well as dialogue with prominent combustion science researchers led to the development of a novel coaxial jet configuration. The design consists of a jet flame in a coaxial flow of hot combustion products from a lean premixed flame (vitiating coflow), as presented in Figure 1.4. The simplified coaxial configuration is a two-dimensional flow, and simple fuels ( $H_2$  and  $CH_4$ ) are suitable for numerical investigation, as shown in Figure 1.3. Chapter 4 also outlines the design and construction of the vitiated coflow flame as well as the safety and control systems. The coflow operating range is also presented.

The next two chapters (5 and 6) present the bulk of the research, simultaneous multiscale point measurements conducted at Sandia National Laboratories. Chapter 5 presents the laser based Raman-Rayleigh-LIF system used at the turbulent diffusion flame laboratory. Descriptions of the applied physics, optical layouts, uncertainties and data reduction procedures are given in Chapter 5. Chapter 6 discusses the experimental results from two conditions; one, a turbulent lifted hydrogen flame, the other, a lifted methane flame. Results attest to the successful design of the flame, with confirmation of well-defined boundary conditions and negligible differential-diffusion effects.

A summary of boundary condition information is presented in Chapter 7. Results from the Sandia TDF measurements are summarized. Information regarding the flow field and thermal interactions are presented; these results are based on analytical, numerical and experimental investigations. The measured temperature field of a nonreacting (pure-mixing) condition is presented for possible use in model validation.

Numerical explorations show that possible undetected radicals in the coflow have a small effect on the combustion processes. More specifically, it is shown that the flame is most sensitive to coflow temperature. Results show that the large vitiated coflow provides a two-stream flow with uniform far-field conditions; therefore, the flame can be modeled as a jet flame in an infinite coflow.

Complementing the comprehensive results from the two flames reported in Chapters 6 and 7, is a parametric study of flame conditions presented in Chapter 8. Trend information is presented regarding the sensitivity of flame structure and blow-off to flow composition, temperature and velocity (of the jet and coflow). Results show that the lifted flame is most sensitive to coflow temperature and rather insensitive to flow conditions. The results presented in Chapter 8 round off the body of validation data for numerical models. The sequence of results is (1) nonreacting conditions, (2) comprehensive hydrogen flame, (3) comprehensive methane flame, and (4) parametric study of methane flames. This sequence of increasing complexity is consistent with the typical approach used to validate analytical and numerical models.

The hot environment of the vitiated coflow provides an opportunity to discuss flame stabilization in Chapter 9. Results suggest that several modes of stabilization are present in flames. This is shown by the scatter plots of data for the hydrogen and methane flames, as well as the methane flame sensitivities obtained from the parametric study. Small scale mixing and autoignition associated with a distributed turbulent premixed flame is present to varying degrees in the hydrogen flame and the methane flame; this autoignition suggests a possible interplay between stabilization mechanisms. In addition, results from numerical models show that either a propagating turbulent

premixed or triple flame is possible. These experimental and numerical results suggest that autoignition of elevated-temperature mixtures (cool reactants with hot coflow) initiate the flame and play a role in the stabilization of these flames by either anchoring the flame, or enhancing the propagating turbulent flame.

Final conclusions are offered in Chapter 10. The interesting features of this research present a multitude of possibilities for future work. Specific recommendations regarding potential experimental and numerical research are given in Chapter 10.

## Chapter 2

### Literature Review

This chapter presents a literature review to provide a context for the research. First, the use of hot combustion products to supply a hot environment for experimental flames is discussed. Then, some of the key turbulent lifted flame research that has been conducted in the past few decades is presented. The chapter concludes with a synopsis of the ongoing debate regarding flame stabilization mechanisms of lifted turbulent jet flames.

#### 2.1. Jet Flames in Hot Environments

The idea of surrounding the jet flame in a hot environment is not new. As stated in the Introduction, many engineering designs exploit recuperated heat. Pilots are typically used to isolate the jet flame base from the cool ambient coflow air. However, other designs with swirling flow fields also provide the high temperature environment needed to stabilize these jet flames.

A classic series of piloted flames are those examined at Sydney University and Sandia National Laboratories. They have been extensively studied both experimentally and numerically through the TNF Workshop series (Section 1.2). Masri, Dibble, and Barlow (1996), and Barlow and Frank (1998) presented simultaneous multiscalar point measurements of temperature and major species for several flow conditions, each with increased jet Reynolds numbers. A photograph of the studied flame is shown in Figure 2.1 (Masri et al. 1996, Barlow and Frank 1998). Measurements of the flow field were

obtained at TU Darmstadt to complement these scalar measurements, the results of which can be found on the TNF website (Barlow 2003). Experimental and numerical investigations showed that the pilot is a key component to flame behavior. Tang and Pope (2001) showed that small temperature variations in the pilot have a major effect on the flame characteristics and the radiative heat losses. While the research conducted on these flames has offered much insight into the turbulence-chemistry interaction, the detailed boundary flow associated with the 3 streams (jet, pilot, entrained air) is rather ambiguous, making the modeling of these flames difficult.



**Figure 2.1.**

Methane/Air turbulent nonpremixed piloted jet flame (Masri et al. 1996, Barlow and Frank 1998).

A series of highly stretched turbulent premixed flames stabilized by a large pilot was the focus of work at RWTH Aachen by Chen et al. (1996). This configuration is presented below in Figure 2.2. A large pilot was used to isolate the jet flame for up to 6 diameters downstream of the nozzle exit. Results show that the pilot stream isolates the flame base from the ambient air (cool) and the turbulence associated with the pilot-ambient air shear layer. Chen (1996) reports that the pilot coflow is merely a hot boundary condition that isolates the jet flame. This hot coflow also permits the stabilization of highly stretched flames. Mansour et al. (1999) report experimental and numerical results showing that turbulent partially premixed flame at the base of the attached flame is in the distributed-reaction regime. As can be seen from Figure 2.2, the low velocity (60 cm/s) pilot is quickly entrained and the flame is a 3-stream flow.

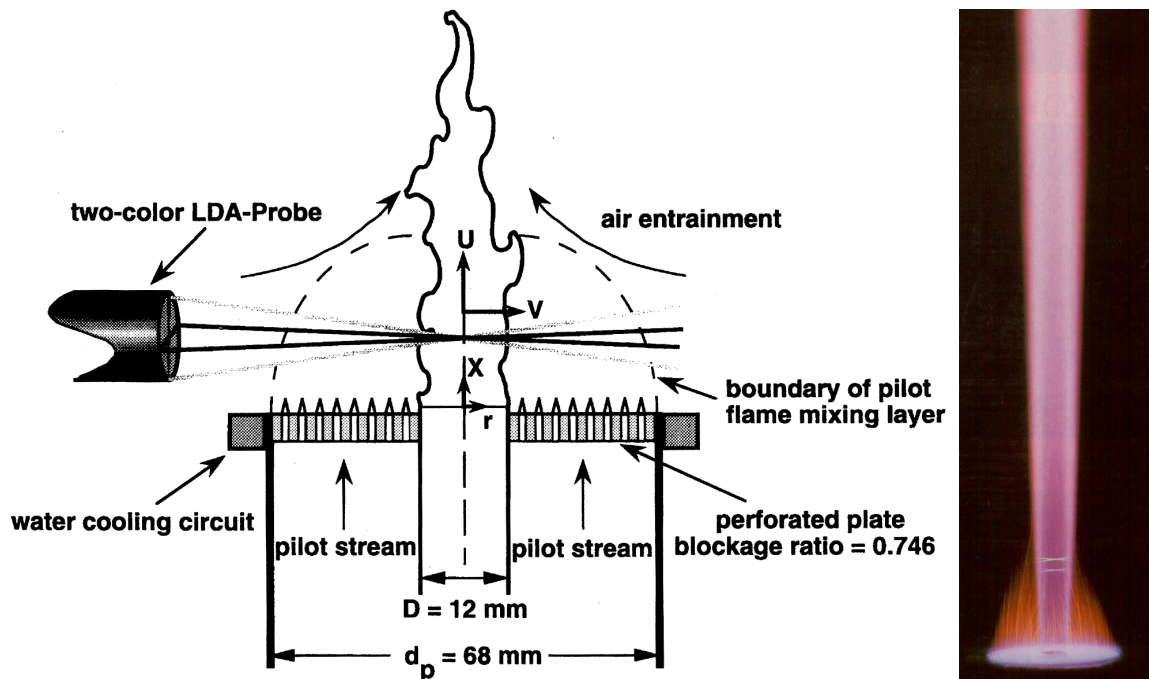


**Figure 2.2.**

Turbulent premixed flame in a large, laminar pilot pioneered by Chen et al. (1996). Streaks in photograph are incandescence from the high temperature PIV particles.

Bluff-bodies are often used to stabilize highly turbulent flames. One example of a highly turbulent jet flame stabilized by a bluff-body is the burner researched at the University of Sydney by Dally et al. (1998). The recirculation zone resulting from the bluff-body provides a hot environment with uniform temperature. This configuration enables the stabilization of highly turbulent jet flames with a wide range of flame conditions. The Sydney University group later added a circumferential swirl to the original bluff-body configuration (Kalt et al. 2002). The addition of swirl provides the possibility of studying even more combustion modes. While there is no doubt that these flames exhibit the turbulence-chemistry interactions inherent to advanced combustion systems, the complexity of the fluid flow due to swirl makes the numerical investigation difficult and often inconclusive. In an effort to research Flameless Oxidation (FLOX), Dally et al. (2002) introduced a jet flame in a hot coflow configuration that provides the same temperature field as the bluff-body flame, but with a coaxial flow configuration. Results show quick entrainment of the hot coflow in this configuration, showing the need for a large turbulent coflow to isolate the flame.

## **2.2. Turbulent Lifted Jet Flames in a Cool Environment**

A number of research efforts have been conducted on lifted turbulent jet flames. To our knowledge, all of this research has focused on flames formed by turbulent fuel jets issuing into an environment of cool air. The cool environment of ambient air has typically been quiescent, or initially stagnant; however, a number of research efforts did have a coaxial flow of air with low velocities ( $u_{\text{coflow}} < 10\text{-}30$  cm/s).

The current review of lifted turbulent flame research is not all-inclusive. The review paper by Pitts (1988) and the recently published text by Peters (2000) together

provide a synopsis of the state of lifted turbulent flames. The conclusion reached by both authors is that the proposed stabilization mechanisms poorly describe the physics of a lifted turbulent jet flame.

Up until rather recently, two stabilization mechanisms were proposed to explain and predict the behavior of lifted flames. At the Third Symposium on Combustion, Wohl and coworkers (1949) proposed that the stabilization point of a lifted flame occurred at the location where the burning velocity and the gas velocity are balanced. At the same meeting, Scholefield and Garsides (1949) showed that lift-off was a result of localized extinction of the flame at the transition of laminar to turbulent flow.

Since then, experimental and numerical research efforts have shown evidence to support each stabilization mechanism. Broadwell et al. (1984) took the extinction proposal one step further, suggesting that vortical structures recirculate and mix hot products from one side of the reaction zone with reactants on the other side. The associated mixing time would then be the critical parameter, by allowing time (or not) for molecular mixing and ignition of the hot, diluted reactants. An analytical model developed by Dahm and Dibble (1988), along with numerical model results by Miake-Lye and Hammer (1988), each incorporating a mixing time criterion, agree well with experimental results. In addition, LIF measurements in the stabilization region made by Schefer et al. (1994) and Watson et al. (2000) support the extinction theory by showing severe manipulation and extinction of flame fronts by vortical structures.

On the other hand, the mixing of hot products and cool reactants by large vortical structures also facilitates reaction. Research has been conducted that supports the existence of these vortical structures and the mixing that occurs, but negates the notion

that these turbulent structures quench the reaction. PLIF images obtained by Schefer and coworkers (1994) show low scalar dissipation rates at the stabilization point, but their results suggest that the vortical structures may enhance flame propagation. Brockhinke et al. (1996, 2000) support through 1-D Raman measurements the notion that the scalar dissipation rate is not dominant in flame stabilization. Hasselbrink et al. (1998) measured through flow field imaging scalar dissipation rates one order of magnitude less than the quenching value. Two-dimensional measurements obtained for a normal fuel jet flame by Tacke et al. (1998) and an acoustically driven fuel jet flame by Chao et al. (2001) show the existence of recirculated products in the unburned region (upstream, and radially outward from the flame base). However, the role of these vortices in flame stabilization are questioned via PIV measurements conducted by Upatneikis et al. (2002); their results show a divergence away from the flame base of the vortices due to thermal expansion of the flow.

While these vortical structures play a role in flame stabilization, there exists a classification problem. What is a large vortical structure? At what point do we have a propagating turbulent flame? Research has been conducted based on the assumptions of Wohl et al. (1949) that the burning velocity and flow velocity are balanced at the stabilization point. Vanquickenborne and van Tiggelen (1966) expanded Wohl's theory suggesting by adding that the propagating turbulent premixed flame stabilizing the flame has a stoichiometric composition. A classic set of experimental results for a number of fuels and flow conditions by Kalghatgi (1984) led to the development of a model for lift-off height; the model is based on scaling arguments stemming from the velocity balance assumption. Kalghatgi's model was developed for jets in still air; Montgomery et al.

(1998) found that the addition of a coflowing stream does affect the lift-off height by creating an offset in the lift-off height vs. jet velocity correlation. Recent research efforts have provided evidence supporting the velocity balance theory; for example, Hasselbrink and Mungal (1998) measured the flow velocity at the flame base to be 0-3 times the laminar flame speed, consistent with turbulent premixed flame speeds.



**Figure 2.3.**

CH-PLIF image of the stabilization region of a turbulent nonpremixed methane/air flame (Watson et al. 1999).

Recent research has suggested a new wrinkle in the velocity balance theory proposed by Wohl et al. (1949). In actuality, the composition at the stabilization region is stratified, or partially premixed, leading to the notion that edge flames in such media may have triple flame structures. Research has shown that this is a possibility. First, Ruetsch et al. (1995) predicted that the triple flame speed is on the order of 3 times that of the laminar flame speed; this means that the triple flame speed and turbulent premixed flame speed are about the same for a given mixture. Therefore, all the previously discussed research supporting the existence of a propagating turbulent premixed flame also supports the notion of a propagating triple flame (e.g, Hasselbrink and Mungal 1998, Han and Mungal 2002). A numerical and experimental investigation by Chen and Bilger (2000) corroborate the triple flame stabilization concept, where the flow field and the

triple flame speeds are balanced for laminar lifted flames. Research conducted by Watson et al. (1999, 2002) and Lyons and Watson (2001) provides evidence that a triple flame structure propagates at the flame base of turbulent nonpremixed methane/air flames, as shown by the CH-PLIF image presented in Figure 2.3. Interestingly, results from a Direct Numerical Simulation (DNS) study conducted by Mizobuchi et al. (2002) are consistent with the image in Figure 2.3; they predict a triple flame structure, in which the flow around the rich premixed branch is vigorously turbulent and in the distributed reaction regime. The structure predicted by this DNS model is indicated by the prediction of the heat release rate as shown in Figure 2.4.

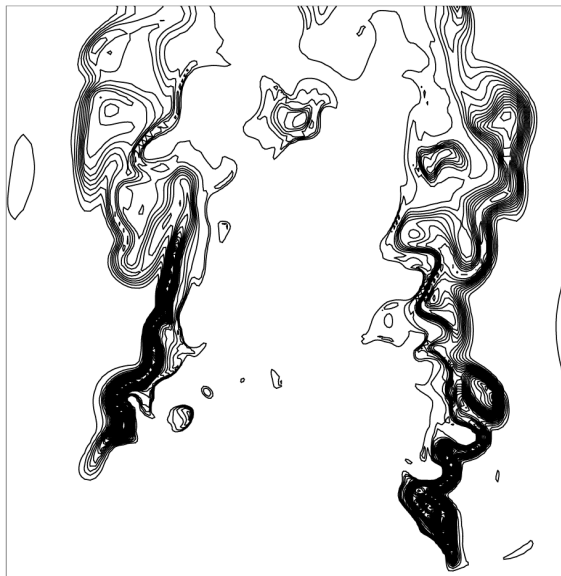


**Figure 2.4.**

DNS prediction of heat release rate of a lifted hydrogen flame (Mizobuchi et al. 2002).

Point Raman measurements obtained at the stabilization region of lifted flames have yielded some results that should also be mentioned. Barlow et al. (1988) conducted the first set of simultaneous laser Raman-Rayleigh-Laser Initiated Fluorescence (LRF) point measurements on a lifted hydrogen flame where they showed suppressed

temperatures and superequilibrium OH concentrations associated with high strain rates. A more comprehensive study of lifted hydrogen flames by Cheng et al. (1992) gave similar results. In validating their new 1-d Raman system, Brockhinke et al. (1995) duplicated the findings of Cheng and coworkers. The Raman point measurements from each of these studies show bimodal distribution of reacting and mixing conditions and peak temperatures at the stoichiometric composition.

## Chapter 3

### Numerical Methods

The challenge of accurately modeling pollutant formation in practical combustors requires major improvements in existing combustion models. Two areas of study important in meeting this goal are: (1) treatment of the turbulence-chemical kinetic interaction, and (2) development of highly accurate reduced chemistry mechanisms. The coaxial jet configuration provides the opportunity to improve and develop models for turbulent mixing and reduced chemistry. These models can be used either in current modeling approaches or in research-orientated approaches, such as Large-Eddy Simulations (LES).

The toolbox of numerical models used to analyze or predict combustion processes in the vitiated coflow jet flame is presented in this chapter. No results are discussed; this chapter is for reference purposes.

#### 3.1. StanJAN (Equilibrium Code)

The StanJAN chemical equilibrium solver, v.3.95 (Reynolds 1987) was used to conduct chemical equilibrium analysis via the method of element potentials. The program, developed at Stanford University, utilizes the database of JANNAF thermochemical tables and henceforth is referred to as “StanJAN.” The program handles gas and condensed phase species, assuming ideal solutions. StanJAN is used to determine the equilibrium limits of chemical reactions for the flame associated with the

fuel jet into the vitiated coflow. These equilibrium limits are particularly useful when analyzing the state of the coflow at the inlet conditions.

### **3.2. Well-Mixed Reactor**

Well-Mixed-Reactor (WMR) is a computer code written for modeling a transient well-stirred reactor (also called a Continuously-Stirred Tank Reactor (CSTR) or called a Perfectly Stirred Reactor (PSR)). The reactor can have multiple injecting streams with time dependent injection rates, and properties (e.g., composition, temperature). The multiple injection stream option enables the WMR code to model different types of reactors. Modifications of the input file make it possible to model a serial system of different reactors in time. The different types of reactors modeled by WMR are presented below.

#### *Plug-Flow Reactor (PFR)*

The Plug-Flow Reactor (PFR) can be modeled by removing both the injection and exit streams. This system takes a reactor at an initial state, and determines the time dependent response as the system evolves toward an equilibrium state. The same PFR model can determine the chemical time scales for (1) a steady state reactor and (2) a batch reactor (closed system). The chemical kinetic response of the sample yields two chemical time scales of interest for combustion; they are the autoignition delay time, and the reaction time scale.

#### *Perfectly Stirred Reactor (PSR)*

The PSR model is the transient version of a Continuously Stirred Tank Reactor (CSTR). The reactor consists of a single inlet and outlet with steady mass flow through the reactor (injection rate = discharge rate). The mixing of incoming reactants with the

fluids inside the reactor is assumed to be infinitely fast, such that the mixture inside the reactor is homogeneous. The residence time is the critical parameter that is determined by the inlet flow rate and the reactor total mass; therefore, the sensitivity of chemical kinetics to the residence time is analyzed with the PSR model as illustrated in Figure 3.1. At large residence times, the reactor properties approach the chemical equilibrium limits. Conversely, flame extinction occurs when the residence time is reduced to a point at which chemical reaction cannot be sustained. Due to its simplicity, numerical calculations of PSR with detailed chemistry up to several thousand steps can be routinely performed.

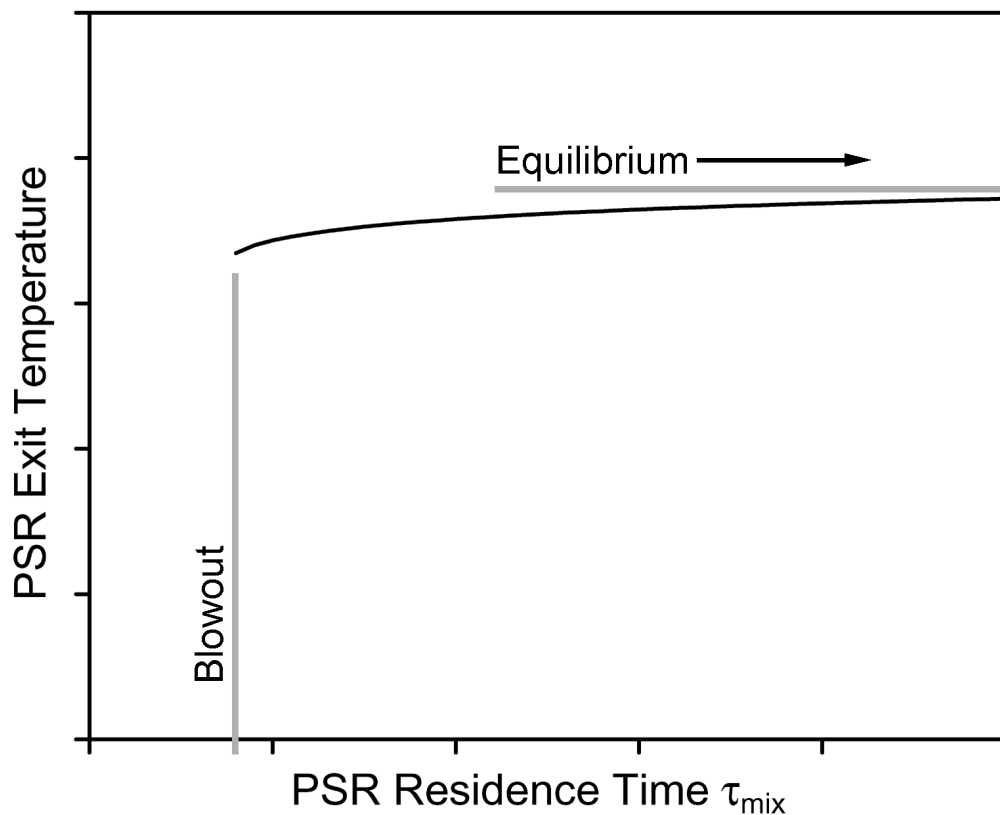


**Figure 3.1.**

Sensitivity of Perfectly Stirred Reactor (PSR) temperature to residence time.

A variation of the PSR model is the Steady State Perfectly Stirred Model (SSPSR). SSPSR is a family of PSR solutions: an iterative solution that provides the sensitivity of the exit stream state to the residence time (Figure 3.1). In other words, SSPSR determines the residence time scale associated with extinction, as well as the response of the reactor's state to decreased residence time.

#### *Well-Mixed Balloon (WMB)*

Well-Mixed Balloon (WMB) is a model with one inlet and no exit stream. Therefore, the reactor grows in size/mass  $M_R(t)$  as shown in Figure 3.2. This model is a simplified treatment of the Lagrangian approach presented by Broadwell and Lutz (1998) and references cited therein, where they found that the inner core of jet flames is homogeneous. Figure 3.2 shows the WMB application to a nonpremixed fuel jet with oxidizer entrainment. The WMB code can therefore be used to analyze the role that vitiated coflow properties play in combustion of the fuel jet. The entrainment rate is adjusted by modifying the injection rate  $m_E$  and the initial reactor mass  $M_R(t=0)$ , such that the characteristic mixing time is  $\tau_E(t)=M_R(t)/m_E$ .

The WMB model is particularly useful when analyzing the dilution and subsequent reaction of a nonpremixed flame of fuel into a reservoir of oxidizer (such as occurs in Diesel engine). For example, the reactor initially begins with fuel. Then oxidizer is injected into the reactor, diluting the fuel. The injection rate of the oxidizer can be adjusted, and the progression in mixing and reaction can be studied.

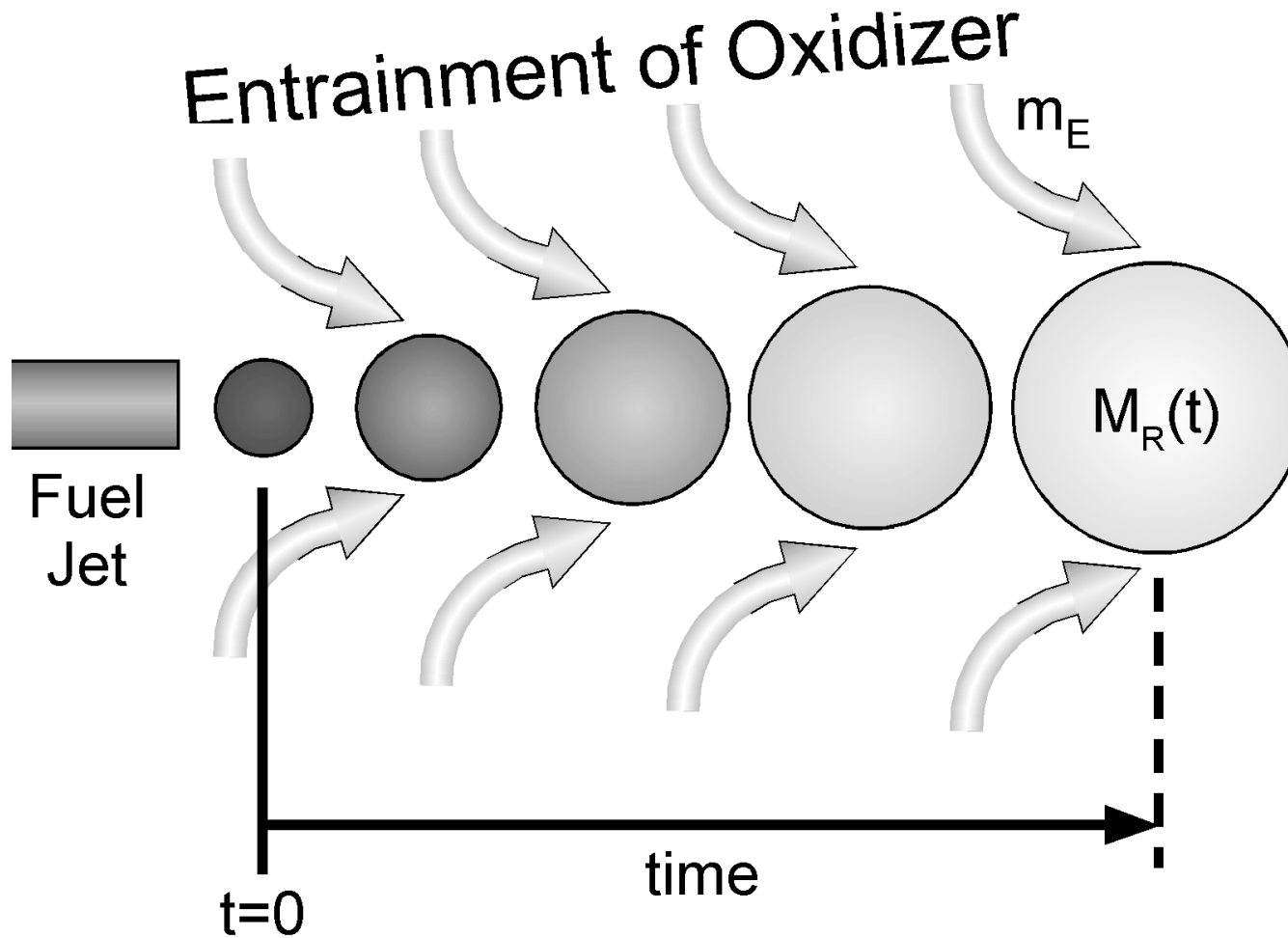


Figure 3.2.

Well-Mixed Balloon (WMB) conceptual simulation of oxidizer entrainment of a fuel jet.

### 3.3. One Dimensional Laminar Premixed Flame Model

The laminar flame speed is one of the parameters essential to the analysis of combustion applications. A FORTRAN code developed at Sandia (Kee et al. 1985) models freely propagating one-dimensional laminar premixed flames. These solutions can be used to study chemical kinetics in flames as well as to evaluate stabilization mechanisms for lifted flames. The laminar flame speed is a determinant factor of the turbulent premixed flame speed and turbulent triple flame speed.

### 3.4. Laminar Opposed Flow Flame Model (OPPDIF)

Opposed flow flames are widely used for studying the effect of stretch rate on nonpremixed and premixed flames. One example is a burner developed by Isizuka and Tsuji (1981) is a cylinder in cross flow geometry, as shown below in Figure 3.3A. This configuration is modeled by an opposed jet configuration, as shown in Figure 3.3B. The Sandia combustion code, named “OPPDIF” (Lutz et al. 1996), is Chemkin based (Kee et al. 1989) and models the steady 1-d flame illustrated in Figure 3.3B.

A critical input parameter of the laminar opposed flow flame model is the velocity gradient, or strain rate. For the opposed jet configuration, the strain rate  $a$  is

$$a = \frac{\partial U}{\partial x} = \frac{2U_0}{R} \quad (3.1)$$

where  $U_0$  is the velocity at the nozzle exit and  $R$  is the distance between nozzles. The strain rate is associated to the scalar dissipation rate for nonpremixed opposed flow flames. The scalar dissipation rate  $\chi$  is defined as

$$\chi = 2\mathcal{D}|\nabla f|^2 \quad (3.2)$$

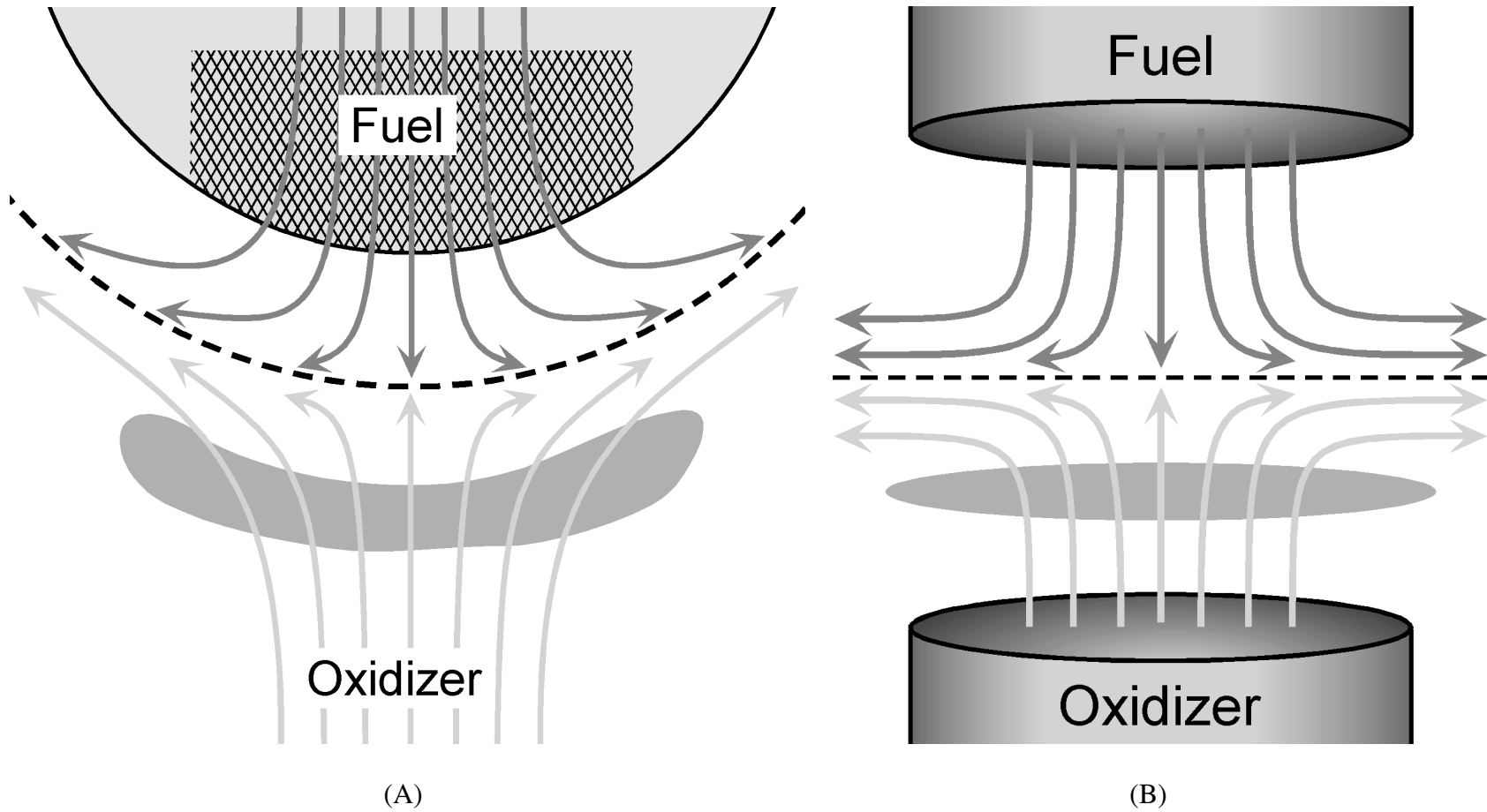


**Figure 3.3.**

The Tsuji opposed flow geometry (A) and the laminar opposed flow flame model (B).

where  $\mathcal{D}$  is the molecular diffusivity and  $f$  is the mixture fraction. The response of the flamelets to strain rates provides a measure from which to analyze ensembles of laser-based measurements of temperature and species. Ensembles of scalar measurements are plotted on a shot-by-shot basis (i.e., one data point per each time and location) in the form of scatter plots. The increased energy dissipation associated with increased strain exceeds the associated increased reaction rates, resulting in suppressed flame temperatures. The extent of this departure from equilibrium can be determined through comparison of the experimental data with the opposed-flow model results.

The extent to which more elaborate combustion models treat molecular mixing may be suggested by laminar opposed-flow flame model results. Differential molecular diffusion between heavier and lighter molecules is always present in nonpremixed flames. The issue becomes, over what length scales does differential diffusion occur? Comparisons of scatter plot data, which is resolved for length scales greater than the probe volume size (Section 5.2.1), and opposed flow flame calculations can provide insight into this question. Smith and coworkers (1995) showed agreement between scatter plot data and opposed-flow flame calculations with differential diffusion for mass disparate  $\text{H}_2/\text{CO}_2$  jet flames with high Reynolds numbers (30,000); therefore, differential diffusion was experimentally resolved and should be incorporated into subsequent combustion models. Conversely, Barlow and coworkers (2000) showed similarities between scatter plot data and opposed flow flame calculations with equal molecular diffusivities for lower Reynolds number (16,000)  $\text{CO}/\text{H}_2/\text{N}_2$  jet flames; thus the Reynolds number alone does not indicate whether turbulent mixing is dominant over

the experimentally resolved length scales and differential diffusion modeling may be confined to the grid cell.

### 3.5. Eddy Dissipation Concept Combustion Model

The general-purpose CFD code called “*Spider*” (Melaen 1990) with EDC was developed at the Norwegian University of Science and Technology division of Thermodynamics in Trondheim. The turbulent reacting flow is modeled by the density-weighted Reynolds-averaged conservation equations for momentum components, energy, and mass fractions of species. Turbulence was modeled either by the standard  $k$ - $\varepsilon$  model or by two versions of Reynolds-stress models by Launder, Reese and Rodi (1975) or by Jones and Musonge (1988, 1994). In the present calculations *Spider* employs a 2-D axisymmetric geometry.

The mean reaction rate  $\bar{R}_j$  of chemical species  $j$  in the cell is modeled by EDC (Ertesvåg 2000, Gran and Magnussen 1996) as:

$$\bar{R}_j = -\frac{\bar{\rho}\gamma^*\dot{m}^*}{(\gamma^*)^{1/3}}(Y_j^0 - Y_j^*) \quad (3.3)$$

where  $\gamma^*$  is the mass fraction of turbulent fine structures and  $\dot{m}^*$  is the reciprocal of the fine-structure residence time ( $\tau^* = 1/\dot{m}^*$ ). These two quantities are expressed as functions of the turbulence energy and the turbulence energy dissipation rate (Ertesvåg 2000, Ertesvåg and Magnussen 2000). Specifically, the fine-structure residence time is assumed proportional to the Kolmogorov time scale. The mass fraction of species  $j$  in the surrounding fluid state is  $Y_j^0$  and the mass fraction of species  $j$  in the fine structure state

is  $Y_j^*$ . The fine structure is regarded as a perfectly stirred reactor and the mass balance for species  $j$  in the reactor is modeled as

$$\frac{dY_j^*}{dt} = \frac{R_j^*}{\rho^*} + \frac{1}{\tau^*} (Y_j^0 - Y_j^*) \quad (3.4)$$

where the reaction rate for species  $j$  in the fine structure is  $R_j^*$  and the fluid density in the fine structure is  $\rho^*$ .

These species mass balances, together with equations for energy and momentum, are integrated in time until steady state is reached. A detailed H<sub>2</sub> mechanism taken from GRI-Mech 2.11 (Bowman et al. 1999) is used.

### 3.6. Probability Density Function Combustion Model

The model utilizes the joint scalar PDF for composition only and the  $k$ - $\epsilon$  turbulence model for a parabolic flow (Smith et al. 1995). The gradient diffusion model and the Curl mixing model (Pope 1990) model the turbulent flux and scalar dissipative terms appearing in the PDF transport equation respectively.

The Monte Carlo simulation technique is used to compute the transport equation for the PDF (Chen and Kollmann 1988). Four hundred stochastic particles per grid are involved in a simulation of convection, turbulent diffusion, molecular diffusion, and chemical reactions. The computation power required by the multi-dimensional joint scalar PDFs limits the detail of the chemical kinetic mechanisms for the combustion process. Thus, a subset of the detailed chemical kinetic mechanism was used; this “reduced mechanism” is integrated directly in time for each particle. The 7-step mechanism listed below is the 6-step H<sub>2</sub> mechanism subset of GRI-Mech 2.11 and the 1-step NO mechanism by Miller (2000).

1.  $2\text{O} \leftrightarrow \text{O}_2$
2.  $\text{H} + \text{O} \leftrightarrow \text{OH}$
3.  $\text{H}_2 + \text{O} \leftrightarrow \text{H} + \text{OH}$
4.  $\text{O} + \text{HO}_2 \leftrightarrow \text{O}_2 + \text{OH}$
5.  $\text{O} + \text{H}_2\text{O}_2 \leftrightarrow \text{OH} + \text{HO}_2$
6.  $\text{H} + \text{OH} \leftrightarrow \text{H}_2\text{O}$
7.  $\text{O}_2 + \text{N}_2 \leftrightarrow 2\text{NO}$

The reduced chemical kinetic model has been thoroughly tested and performs well in calculations of laminar opposed-flow nonpremixed flames, laminar premixed flames, perfectly stirred reactors, and ignition. Therefore, we expect satisfactory performance here.

## **Chapter 4**

### **Vitiated Coflow Burner**

As stated in the Introduction, the turbulence-chemistry interaction is still an area of combustion science where increased understanding is needed. The vitiated coflow jet flame burner was designed in an effort to decouple the detailed fluid mechanics inherent in advanced combustors from the chemical kinetics. The simplified flow provides less complex fluid mechanics, with the coflow environment consisting of hot products from a lean premixed flame. The concept of such a burner was initially presented at the 1<sup>st</sup> International Workshop on Measurement and Computation of Turbulent Nonpremixed Flames in Naples, Italy in 1996 (Barlow 2003). The burner concept was well received and viewed by many as the next logical step beyond piloted jet flames.

This chapter is practical in nature as it presents the design development process of the vitiated coflow burner. The design requirements are first given. Consideration of the design concepts augmented with a series of engineering analysis lead to the selection of the perforated plate burner design. Several key design factors are considered, including operational, control, and safety issues. The experimental control and safety systems are also presented.

#### **4.1. Design Requirements**

The design will allow for investigation of turbulent combustion in a hot coflow environment. The hot coflow environment enables the stabilization of flames with a wide range of combustion modes, making this burner a potential workbench for a wide variety

of flows. Satisfying the following list of design requirements will facilitate new collaborations of numerical and experimental research efforts:

1. The principal objective of the design is to provide a hot environment typical of practical combustors.
2. The jet and coflow configuration will be axisymmetric and therefore may be amenable to 2-dimensional modeling.
3. The coflow diameter and velocity should be large enough to isolate the jet flame from the laboratory air for the maximum downstream distance possible. Isolation of the jet results in a 2-stream flow (i.e., jet and coflow) instead of a 3-stream flow (i.e., jet, coflow, and laboratory air).
4. The coflow stream should be stable and uniform.
5. The control system should provide a range of coflow capabilities (e.g., range of coflow temperature, stoichiometry and velocity).
6. The resulting design should be safe, affordable, and easily reproducible by other researchers.

#### **4.2. Concept Generation and Screening**

The generation and screening of a number of design concepts for the vitiated coflow burner are described in this section. The design requirements listed in the previous section were used to analyze and screen these concepts; the associated advantages and disadvantages of each concept are outlined. Through this process, the perforated plate concept is ultimately selected.

#### **4.2.1. Preheated Air**

Simply preheating air with electrical heaters was quickly dismissed because of the added costs associated with elaborate control and heating systems. A 100 kW heating system is required to provide a 20 cm diameter coflow of air at 4 m/s with a temperature of 1,000 K. Producing a large coflow with uniform temperature with a 100 kW (i.e., 134 horsepower) heating system would require elaborate and expensive experimental facilities similar to those developed by Fujimori and coworkers (2000). Such an expensive design is beyond the project budget; furthermore, it dramatically reduces the probability that other researchers would reproduce the experiment.

#### **4.2.2. Catalytic Burner**

The first candidate considered is the catalytic burner where a catalyst provides the vitiated coflow. A 2 inch diameter enclosed burner was built to test the effectiveness of this type of burner (Kean et al. 1998) to provide a coflow satisfying the given requirements. A catalyst provides a uniform flow field and lower temperatures from leaner mixtures. The catalyst used consisted of platinum supported on a ceramic straight-channel monolith (200 cells per square inch), similar to those used in automotive catalytic converters. Figure 4.1 is a photograph of the catalytic burner. The total length of the catalyst was 10 cm. The fuels used in this burner were  $\text{CH}_4+\text{H}_2$  and  $\text{C}_3\text{H}_8+\text{H}_2$ . The equivalence ratio tested was as low as 0.3 and the flow velocity was on the order of 1 m/s. Hydrogen was added to preheat the premixed hydrocarbon fuel mixture, thereby avoiding the need for an electrical heater (Deutschmann et al. 2000).

A drawback of this catalytic burner was that the system must be enclosed because of heat losses and sub-optimal catalyst efficiencies. The catalyst did not achieve a 100%

conversion of fuel, so some unburned hydrocarbons remain in the products. Increasing the coflow velocity beyond 1 m/s is impractical because it would further reduce catalyst efficiencies.

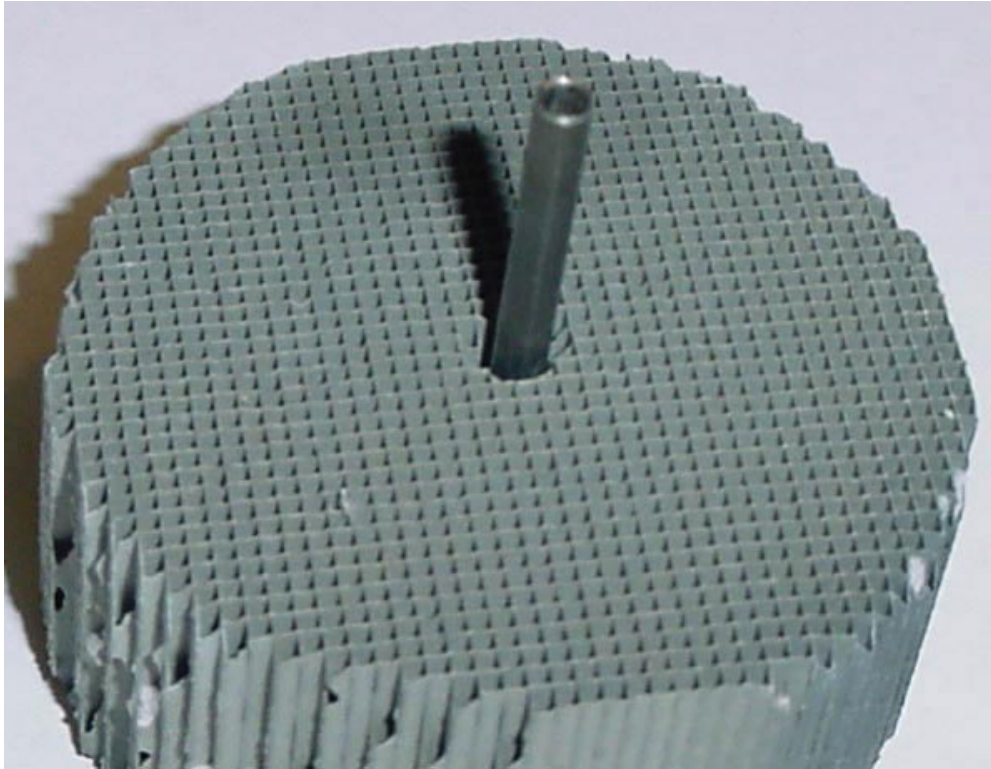


**Figure 4.1.**

Photograph of a jet with a coflow from a catalytic burner. At the center of the 2 inch diameter honeycomb is  $\frac{1}{4}$  inch stainless steel tube for the jet.

A more serious drawback was that the surface of the catalysts glowed strongly, radiating a considerable amount of heat. If a full-scale 12 inch diameter burner were built, radiative heat losses to the environment would be significant. Stabilizing the jet flame in the enclosed environment was also difficult; often the jet flame leaned to one side of the flow against the wall. A stable and symmetric jet flame is a basic design requirement; therefore, the catalyst concept was down selected.



**Figure 4.2.**

Photograph of the tube bundle burner. The design consists of 280  $3/32$  inch diameter tubes in a square pattern over a 3 inch diameter area

#### **4.2.3. Tube Bundle Burner**

The second concept considered provides a vitiated coflow with a tube bundle array. A 3 inch burner was constructed with 280  $3/32$  inch tubes. These  $3/32$  inch tubes were arranged in a square pattern with gaps between adjacent tubes. Figure 4.2 is a photograph of the tube bundle burner without a central jet. Injection of fuel and air into the burner was done by two methods. In the first case, fuel flowed through the tubes, while air flowed through the interstices surrounding the tubes. In a second test, the injection pattern was reversed where air flowed through the tubes, and fuel flowed around the tubes. Lean flames of equivalence ratio as low as 0.3 are achieved with an average

flow velocity at the burner exit of 2 m/s. While this burner provides a stable flame, it does not produce a sufficiently flat flame at these lean conditions.

This burner is a spin-off of the multiple diffusion flame burner described in the text by Fristrom (1995) where he cites the research of Berl and Wilson (1961). Recently, this burner became known as the “Hencken” burner after a commercial supplier by the same name (Dublin, CA). The virtues of this burner are mitigated by the expense of building a large, 20 cm diameter burner; it is difficult to construct such a burner because of the small diameter tubes.

#### **4.2.4. Grid-Turbulence Producing Screen Burner**

The premixed grid-turbulence screen burner is a cylindrical duct topped by a low blockage (less than  $\approx 30\%$ ) stainless steel screen at the exit plane as shown in Figure 4.3. The hope for this burner design was that the screen at the exit would generate grid turbulence, thereby producing a turbulent rather than laminar premixed flame. Furthermore, the screen would serve as a flame holder, producing a flat flame with homogeneous turbulence.

Two prototypes were built to verify the concept. A 2 inch diameter burner achieved a low equivalence ratio of 0.6 and velocity of 2 m/s with a fuel mixture of  $H_2+CH_4$ . Other screen mesh sizes were also tested and found to make little difference in flame structure. An 8 inch diameter burner was built with a  $\frac{1}{4}$  inch diameter stainless steel tube installed at the grid center. The coflow isolated a turbulent hydrogen jet from the ambient air for a downstream distance approximately 80% of the flame height.

Major drawbacks of the screen burner concept are (1) the coflow did not achieve an acceptable flat flame profile and (2) flashback is a routine problem. The low blockage

and mass (i.e., thermal inertia) of the screen resulted in repeated occurrences of flashback. The threat of repeated flashback during experiments is unacceptable and therefore the screen burner concept was also down selected.

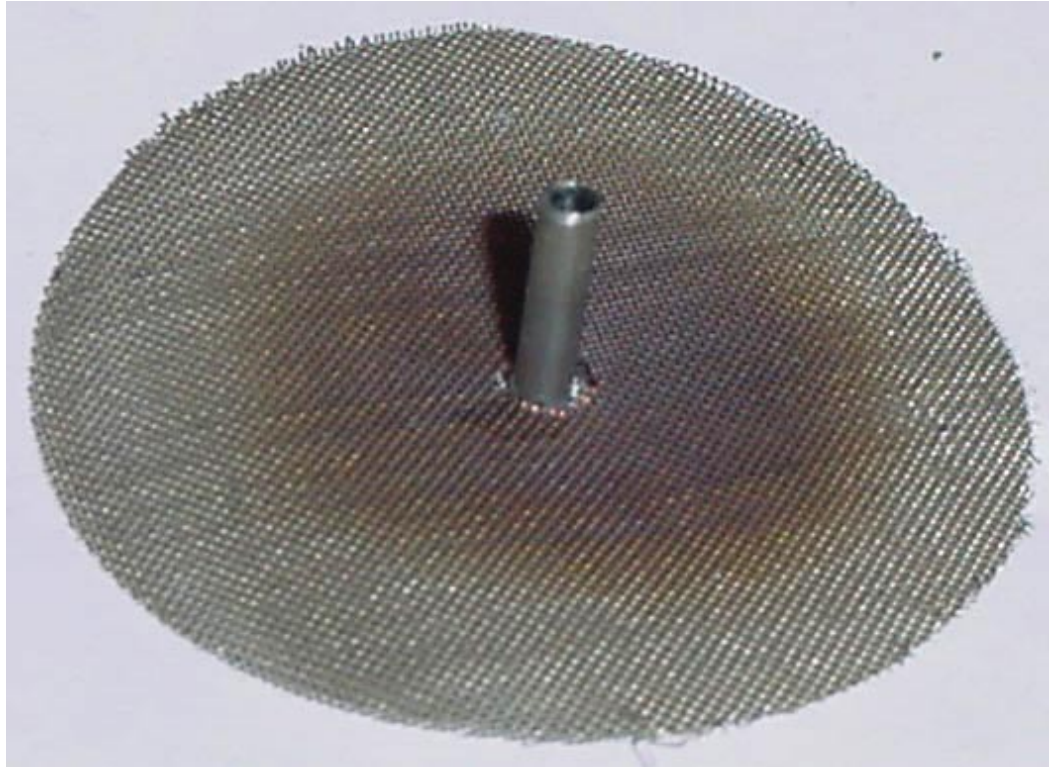


**Figure 4.3.**

Photograph of the grid-turbulence screen burner. The 2 inch diameter screen is constructed of stainless steel blockage.

#### **4.2.5. Coarse Porous Disk Burner**

A coarse porous disk also generates grid-turbulence in the coflow. A 2 inch porous ceramic disk replaced the wire screen of the screen burner. Figure 4.4 shows a picture of the porous disk burner. While the ceramic disk did prevent flashback, it was difficult to obtain a high velocity coflow. Additionally, there is no simple way to add LDV or PIV particles for possible fluid flow measurements. These limitations prevented the coarse porous disk concept from being selected.



**Figure 4.4.**

Photograph of a 1/8 inch tube at the center of a coarse porous disk.

#### **4.2.6. Perforated Plate Burner**

Discussions with Dr. J.A. Lovett (Pratt and Whitney, FL) revealed that the screens being used in the screen burners (Section 4.2.4) would require much greater blockage to effectively prevent flashback. Dr. Lovett presented his research at General Electric (Schenectady, NY) where he used perforated plates with blockage of 85% to generate homogeneous turbulence. These burners showed great promise, as also shown by the research by Chen and coworkers (1996, see Figure 2.2) where highly stretched jet flames could be stabilized in such a coflow. One potential drawback is the possibility of flashback into the mixing chamber. However, this hazard can be accounted for with the proper implementation of safeguards.

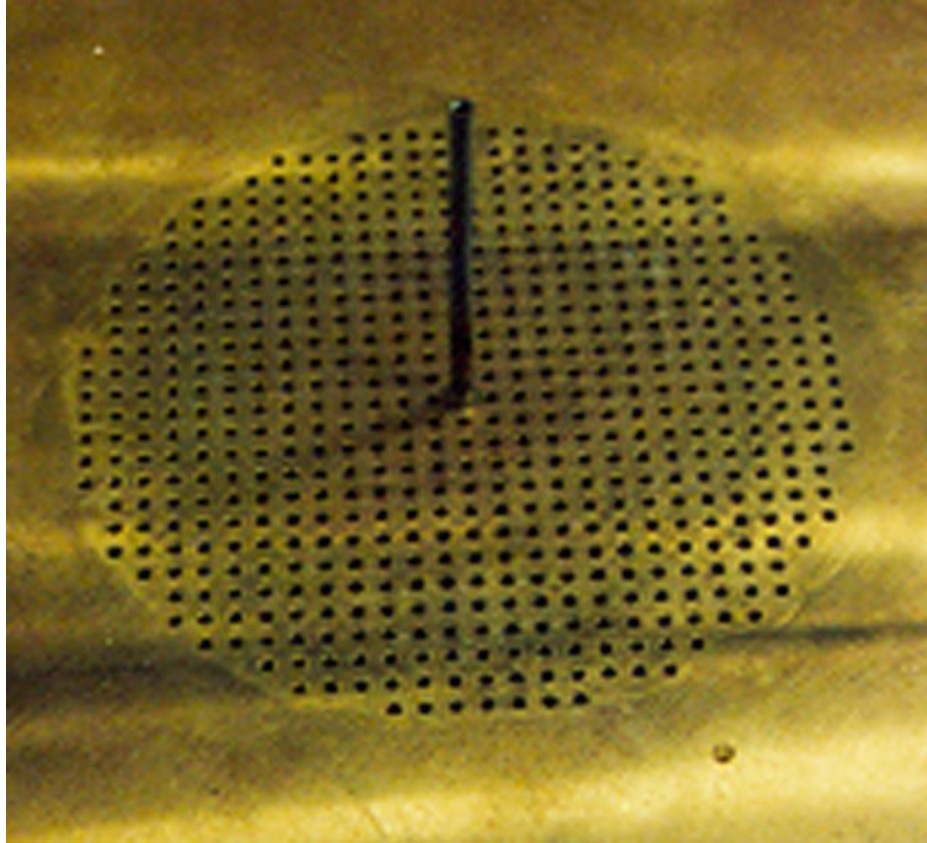


**Figure 4.5.**

Photograph of the perforated plate burner. The 4 inch diameter perforated area of the brass plate has an 85% blockage achieved with 576 1/16 inch holes. The 1/8 inch diameter jet nozzle extends 1.75 inches from the perforated surface.

A 4 inch (10 cm) diameter perforated plate burner was constructed. A blockage of 85% was achieved with 1/16 inch (1.6 mm) diameter holes. A photograph of the perforated plate burner is shown in Figure 4.5. Explorations conducted with this candidate were extremely successful and encouraging. The hot coflow velocity could easily exceed 3 m/s. Additionally, the hot coflow enabled the fuel jet to reach exit velocities on the order of 200 m/s before the jet flame blows out.

A wide range of stoichiometries can be obtained with turbulent premixed CH<sub>4</sub>/Air and H<sub>2</sub>/Air flames stabilized on the perforated plate. Figure 4.6 shows a sampling of

some of the combustion modes that can be studied with this burner. One interesting test that has been observed consisted of a jet of air into a rich methane coflow. The rich coflow has no oxygen. Air is injected into this oxygen deprived flow (Figure 4.6D) and reacts with hot CO, H<sub>2</sub> and unburned hydrocarbons. This flame is an example of an “inside out” or reverse-diffusion flame.

After reviewing all of the design concepts, the perforated plate burner proved to be the most successful coflow flame holder. Premixed methane in air, and hydrogen in air flames are flat, stable, and lean. The system also has a large range of operating conditions.

#### **4.3. Current Concept Design: Perforated Plate Burner (VC-1)**

The VC-1 flame holder design consists of a perforated plate, exit collar and center jet tube (Figure 4.7). The brass perforated plate has a diameter of 8.25 inches (21 cm) and thickness of ½ inch (1.27 cm). To achieve a blockage of 87%, 2200 holes with diameter 1/16 inch (1.58 mm) were drilled through the brass plate. Engineering drawings of the perforated plate and associated components, as well as a parts list are included in Appendix A. A wide variety of hydrocarbon-premixed flames over a range of stoichiometries can be stabilized on the rapid heat dissipating brass. The central ¼ inch OD (6.35 mm) and 0.18 inch ID (4.57 mm) stainless steel tube extends 2.75 inches (70 mm) over the perforated plate surface. An exit collar provides a barrier that creates a complete, uniform, flat flame by preventing the entrainment of ambient air by the many jets emerging from the perforated plate. The exit collar gets extremely hot and glows, this radiation interferes with laser diagnostic methods. Therefore, a water coil is used to cool the exit collar.

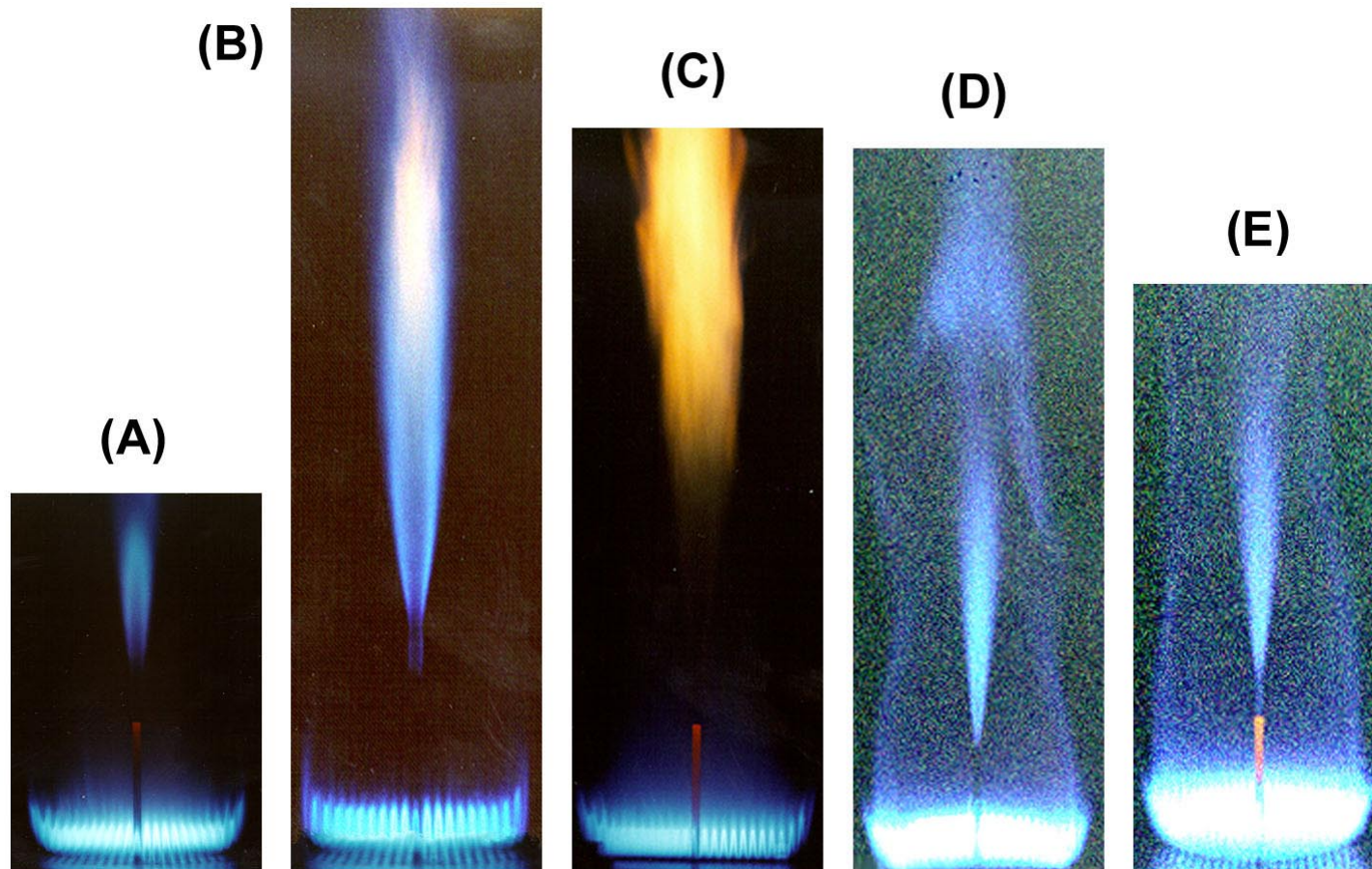


**Figure 4.6.**

Many combustion modes are available with vitiated coflow burner. (A) ultra-lean jet in lean coflow, (B) lean jet in lean coflow, (C) fuel jet in lean coflow, (D) air jet in rich coflow and (E) ultra-lean jet in rich coflow. All jet and coflow flames are  $\text{CH}_4/\text{Air}$ .



**Figure 4.7.**

Photograph of the vitiated coflow jet flame burner. The burner consists of a 8.25 inch diameter brass perforated plate, and a  $\frac{1}{4}$  inch ID, 0.18 inch OD stainless steel tube that extends 2.75 inches above the center of the perforated plate surface.

#### **4.3.1. Perforated Plate Blockage**

Increased blockage has several advantageous qualities for stabilizing the coflow flame. The increased hole spacing results in larger bluff-body recirculation zones. Figures 4.8A and 4.8B illustrate the possible flow fields at the perforated plate surface, depending on whether the flames are laminar (Figure 4.8A) or turbulent (Figure 4.8B). The recirculation zones in Figures 4.8A and 4.8B extend the extinction limits of the coflow flames as a result of the higher temperatures associated with recirculation of hot coflow products.

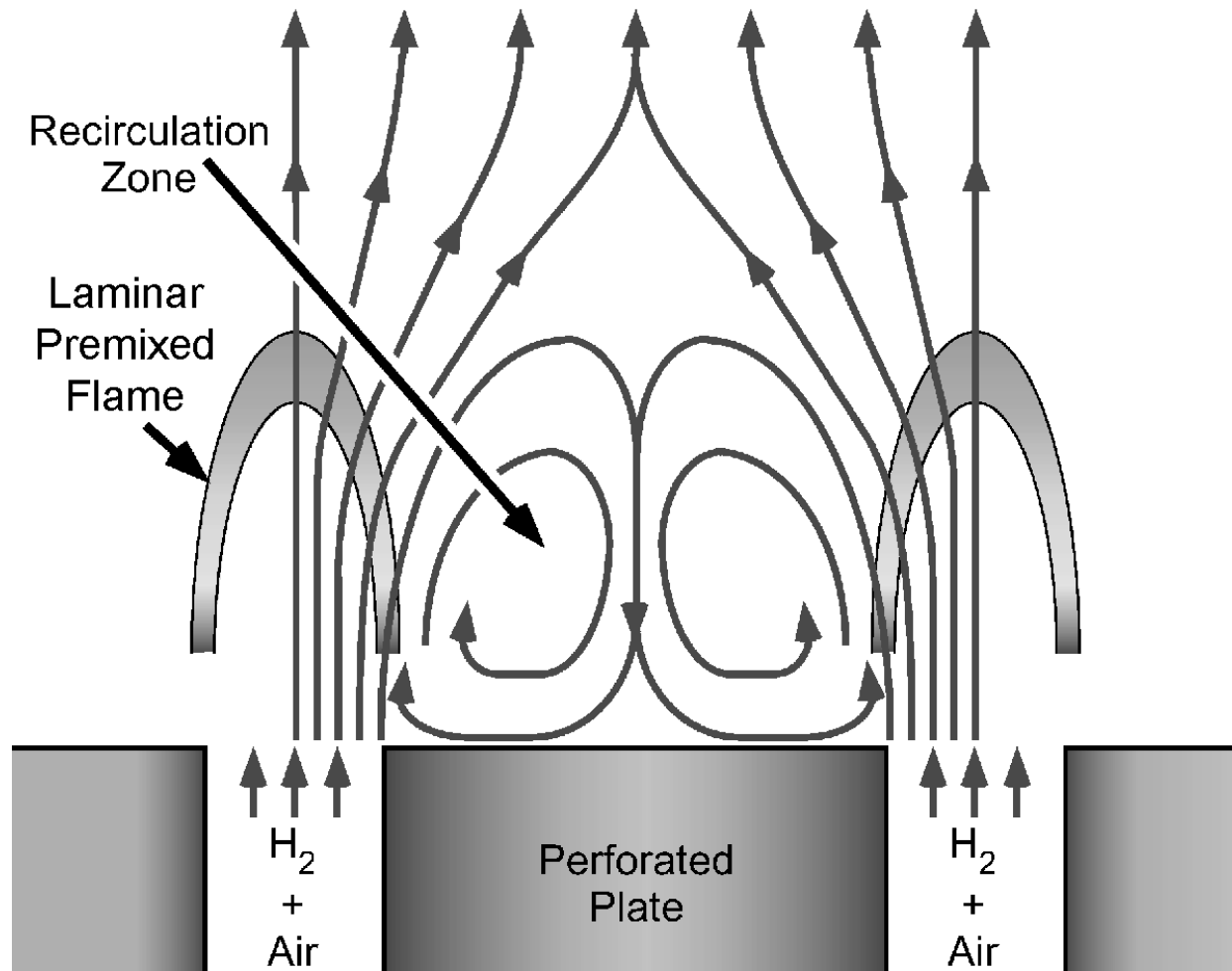


**Figure 4.8A.**

The laminar flow field associated with premixed flames stabilized on the perforated plate surface.

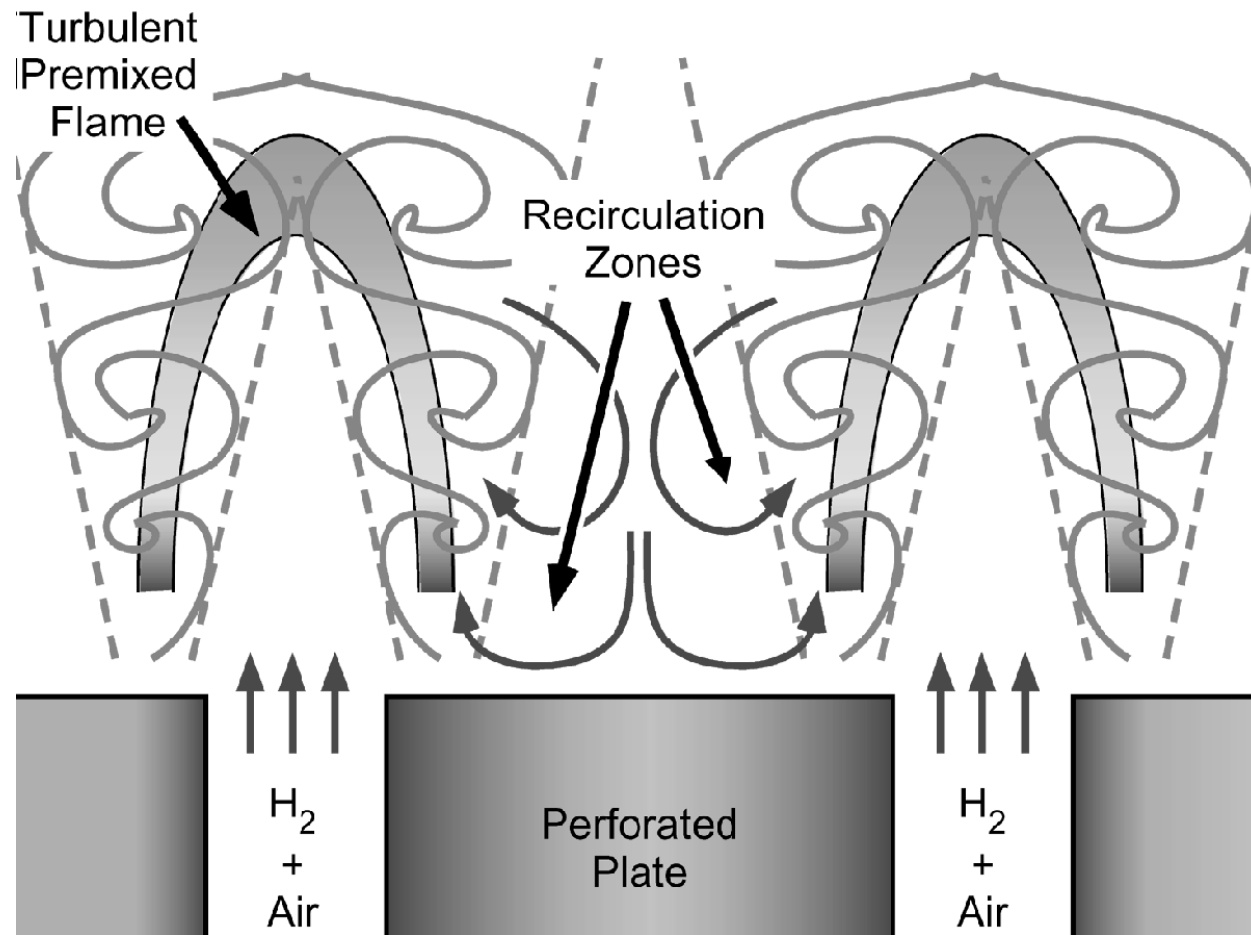


**Figure 4.8B.**

The turbulent flow field associated with premixed flames stabilized on the perforated plate surface.

Increased blockage and smaller holes each contribute to the prevention of flashback into the system. Smaller holes dissipate heat more quickly because of higher surface area, resulting in flame extinction within the hole. Increased blockage results in increased flow velocities within the holes; therefore, most premixed flames cannot propagate upstream. The quenching diameter for premixed flames may be approximated as the flame thickness (Borman and Ragland 1998). The hole diameter was chosen to be 1/16 inch (1.58 mm) for fabrication reasons. This diameter is smaller than the CH<sub>4</sub>/Air quenching diameter (2 mm) but larger than the stoichiometric H<sub>2</sub>/Air quenching diameter (0.6 mm, Borman and Ragland 1998). Flashback is unlikely for CH<sub>4</sub>/Air flames, but for H<sub>2</sub>/Air flames, the stoichiometries and flow velocities must be chosen correctly. For a blockage of 87%, the acceleration ratio of hole velocity to bulk approach velocity would be:

$$\frac{V_{\text{hole}}}{V_{\text{bulk}}} = \frac{1}{1 - B} = \frac{1}{1 - 0.87} = 7.7 \quad (4.1)$$

With a 1 m/s bulk approach velocity, the average velocity through each hole would therefore be 7.7 m/s. This velocity through the hole is 3 times greater than the maximum H<sub>2</sub>/Air laminar flame speed and 22 times greater than the maximum CH<sub>4</sub>/Air laminar flame speed (Borman and Ragland 1998). Chances that flashback would occur under normal operation are small; however, safeguards are still needed and will be discussed in the Section 4.5.

A hexagonal drill pattern was designed so that each hole center was equidistant to all adjacent hole centers as shown in Figure 4.9. This symmetry produces the homogeneous, grid turbulence required.

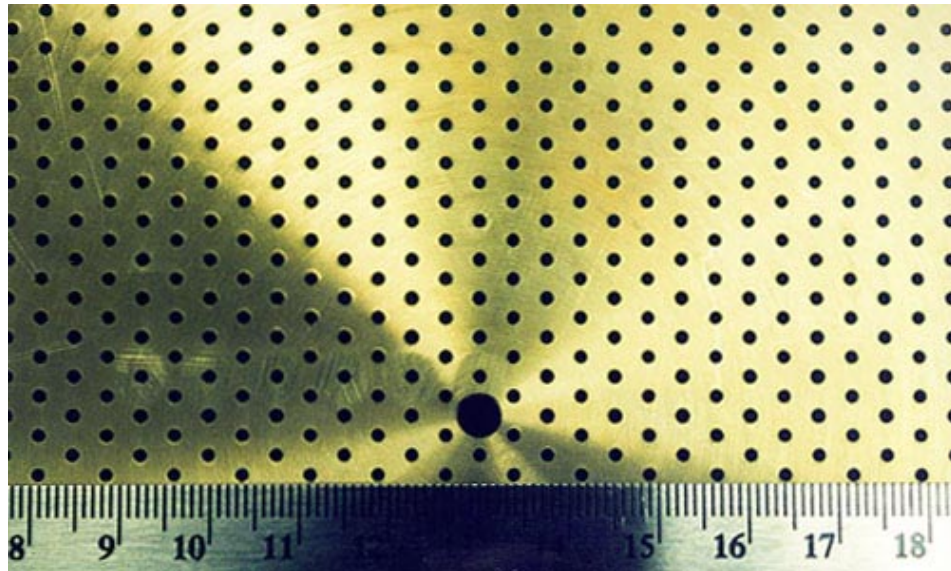


**Figure 4.9.**

Drill pattern for vitiated coflow perforated plate. Perforated plate is made of brass and has 2,184 1/16 inch diameter holes. Units on ruler are centimeters. The center thru hole shown has a 3/16 inch diameter.

#### **4.3.2. Perforated Plate Material**

The material used for the perforated plate could be brass or copper because of their combination of thermal properties (i.e., thermal conductivity and melting temperature) and cost. Increased heat conduction results in a shorter time for the perforated plate to warm up and reach a steady temperature. Other metals with high thermal conductivity are either expensive (e.g., gold) or melt at low temperatures (e.g., aluminum).

The selection between copper and brass was made with respect to practicality in machining these materials. Providing an 87% blockage with 1/16 inch (1.58 mm) diameter holes results in a hole density of 6.6 holes/cm<sup>2</sup>. For a perforated plate diameter of 0.21 m, 87% blockage is attainable with 2,184 holes of 1.58 mm diameter. The large

number of carefully located holes encourages the implementation of a computer numerical control (CNC) machine. It was decided after consultation with CNC operators that drilling so many small holes into brass is more practical than copper. Machining the softer, more ductile copper results in (a) longer chips that do not clear away from the machined face, and (b) higher temperatures and stresses on the cutting tools. Therefore, brass was selected as the perforated plate material.

#### **4.3.3. Hydrogen as the Fuel for the Premixed Coflow Burner**

With respect to safety, designing for a hydrogen coflow flame is over-designing for a methane coflow flame. Therefore, all design issues will be addressed for hydrogen coflow flames. Additionally, a hydrogen flame coflow has several advantages over a methane flame. First, any and all carbon containing specie measurements (i.e., CO, CO<sub>2</sub>) in the flow are known to be products of the fuel jet. Leaner and lower temperature flames can also be obtained with a hydrogen flame; which can result in higher velocities. Lower temperature flames also have low production of NO; therefore the central jet flame would be the source of any NO measured in the flow.

The principal role of the coflow is to deliver a hot oxidizer for the central fuel jet. Adjusting the equivalence ratio  $\phi$  controls the temperature of the premixed coflow flame; however, changes in stoichiometry also result in changes in oxygen content of the coflow flame. The range of equivalence ratios for lean premixed flames as the coflow is therefore limited because of the experiment's oxygen requirements. The equivalence ratio range was determined by calculating the equilibrium oxygen mole fraction for hydrogen and methane flames with StanJAN; these results are shown below in Figure 4.10. In fact, methane and hydrogen flames have essentially the same oxygen content per

given stoichiometry since there is no oxygen at  $\phi = 1$ . As can be seen from the plot below, the stoichiometries between 0.2 and 0.6 yield oxygen mole fractions between 6% and 16%.

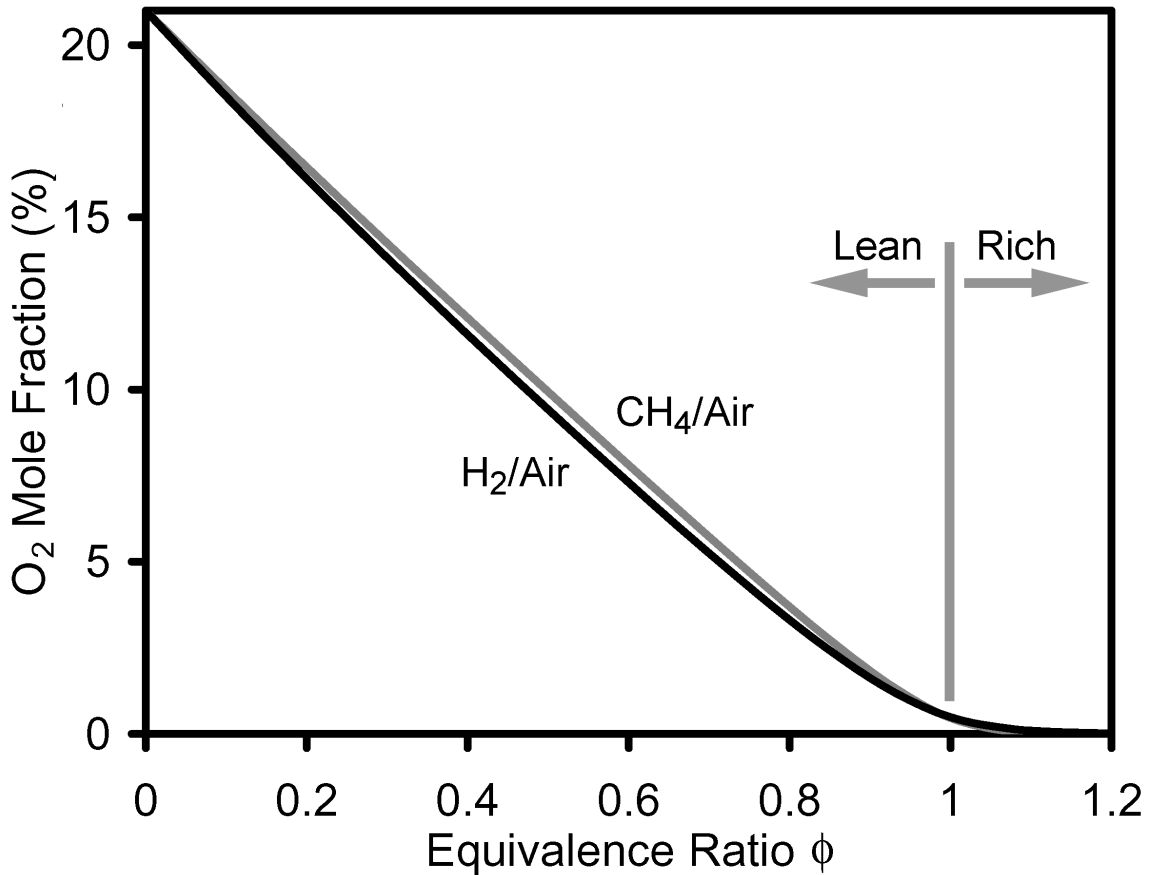


**Figure 4.10.**

Equilibrium oxygen mole fraction in products of premixed hydrogen-air and methane-air flames (StanJAN).

Now that the equivalence ratio range has been determined for lean hydrogen coflow flames, the flashback issue can be revisited. The laminar flame speed for premixed hydrogen flames as reported by Elliott and Denués (1936) is plotted in Figure 4.11 as a function of equivalence ratio. As can be seen from the plot, the laminar flame speed is 1 m/s for a lean ( $\phi = 0.8$ )  $\text{H}_2/\text{Air}$  flame; therefore, these reduced flame speeds (of

$\phi = 0.8$ ) further reduces the possibility of flashback since the flow velocity through the holes is 7.7 times (Equation 4.1) that of the laminar flame speed at  $\phi = 0.8$ .

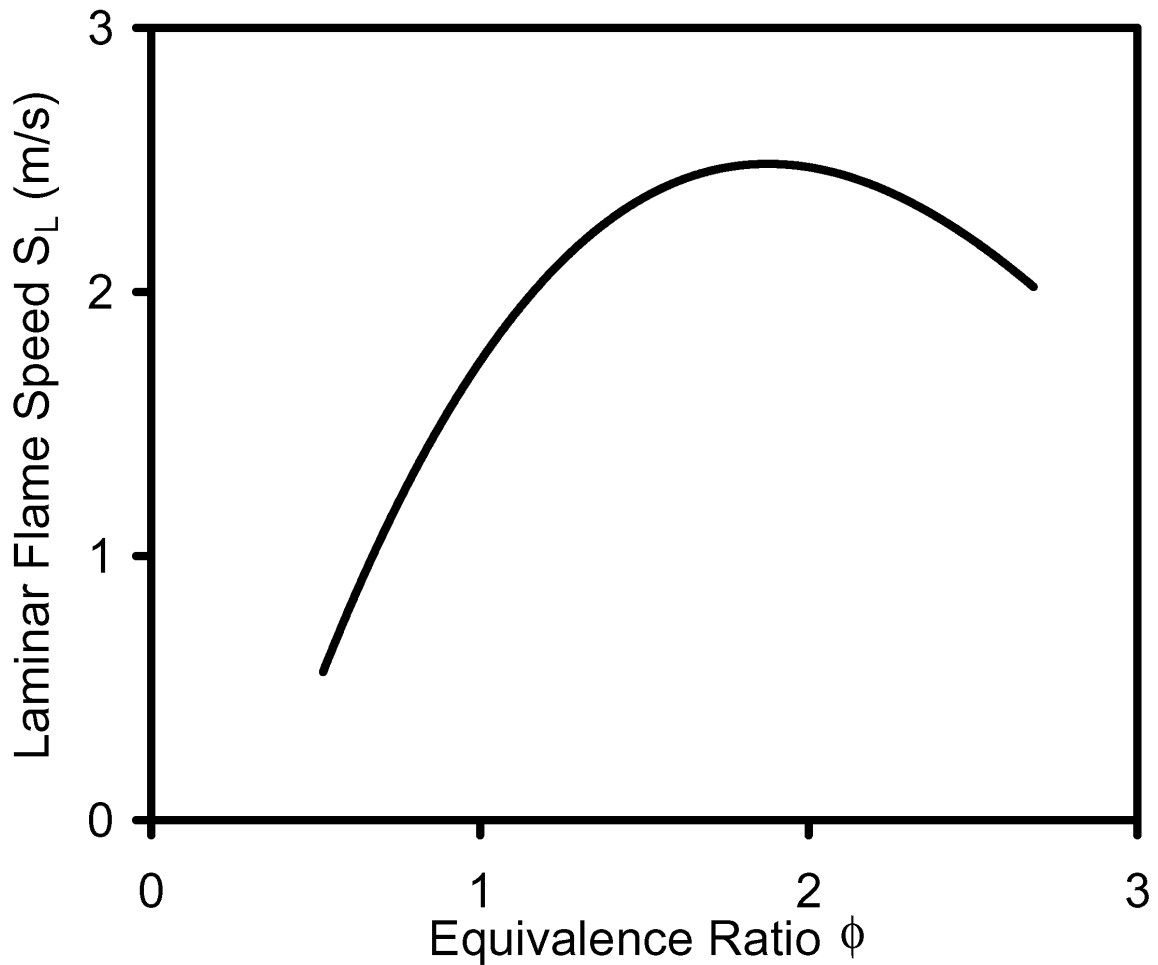


**Figure 4.11.**

Laminar flame speed of premixed hydrogen-air flame. Relationship is an adaptation of the experimental data reported by Elliott and Denues (1936).

#### **4.3.4. Coflow Diameter**

In order to maximize the test volume, or the coflow's potential core, the coflow diameter should be as large as possible. The present coflow diameter of 21 cm was set as a compromise between test volume, brass availability, air flow rate, and fuel flow rate

considerations. To insure that buoyancy effects do not reduce the potential core of the coflow, the Froude number for the coflow is approximated.

#### *Air and Fuel Flow Rates*

The limiting factor to coflow size is the maximum hydrogen flow rate that can be supplied by typical size A bottles. Each bottle contains 195 ft<sup>3</sup> of hydrogen (5,520 liters), and only one bottle can be brought down to the laboratory at a time. Therefore, a minimum bottle lifetime must be imposed in order to conduct the experiments practically and economically. The minimum lifetime for the hydrogen bottles was determined to be between 5 and 10 minutes, resulting in average hydrogen flow rates between 550 to 1,100 standard liters per minute (slm). In order to determine the optimal coflow diameter, the required hydrogen flow rate was determined for a range of coflow diameters, cold bulk velocities, and flame equivalence ratios. The flame equivalence ratios considered were the average ( $\phi = 0.6$ ) or maximum ( $\phi = 0.8$ ) equivalence ratio as determined in the previous section. Figure 4.12 shows the required hydrogen flow rate as a function of the given parameters. As can be seen in the plot, a coflow diameter of 0.3 m would barely satisfy the 5 minute bottle lifetime requirement. A coflow diameter between 0.15 and 0.25 m would be best, creating the possibility of increasing the coflow velocity, a crucial requirement if the flame sensitivity to coflow velocity is to be studied.

The air flow rate to the premixed coflow flame is supplied by a 1.5 hp blower. Measuring the stagnation pressure at the blower exit allows for an approximate measure of the maximum air flow rate. A stagnation pressure of 5.8 inches of water was measured at the 4 inch diameter exit; this corresponds to a maximum velocity of 48 m/s and a maximum flow rate of 18,800 slm (assuming a fully developed turbulent flow). Based on

the hydrogen limitations (Figure 4.12), the optimal coflow diameter is between 0.15 and 0.25 m for cold bulk flow velocities between 1 and 3 m/s. For a coflow with a diameter of 0.25 m and a cold velocity of 3 m/s, the volumetric flow rate is 8,800 slm, about 46% that of the maximum air flow rate. Therefore, the blower should be able to supply the required air flow rate.

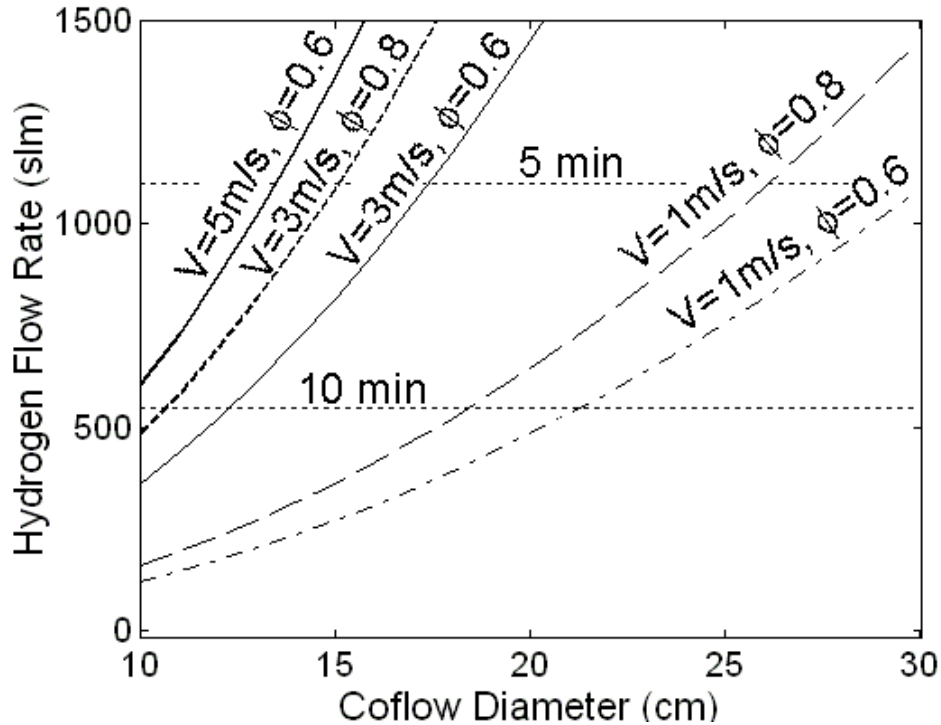


**Figure 4.12.**

Required hydrogen flow rate for the coflow flame. The velocity given is the cold bulk velocity of the air, the time associated with each dotted horizontal line is the lifetime of one hydrogen bottle.

*Momentum Driven Coflow*

As stated previously, a large potential core for the coflow corresponds to a 2-stream flow. A momentum driven coflow has a larger potential core, where the coflow is undisturbed by the growing shear layer between the coflow and the ambient air.

Conversely, a buoyancy-controlled coflow accelerates and quickly contracts, minimizing the test volume and creating nonuniformities in the coflow. The Froude number is defined as the ratio of the momentum flux and the buoyant forces experienced by the coflow stream. To avoid these adverse buoyancy effects, the coflow should be momentum driven, or quantitatively have a Froude number greater than unity.

The coflow Froude number is dependent on coflow diameter  $d_C$ , coflow velocity  $U_C$ , and density ratio of the coflow and the ambient air  $\rho_C/\rho_\infty$  (source Froude number from Delichatsios 1993).

$$Fr = \frac{U_C}{\sqrt{gd_C} \left( \frac{\rho_C}{\rho_\infty} \right)^{1/4}} \approx \frac{U_O}{\sqrt{gd_C}} \left( \frac{T_C}{T_\infty} \right)^{5/4} \quad (4.2)$$

The approximated Froude number (right hand side) assumes a uniform molecular mass in the two streams (coflow and ambient air), making it a simple function of the coflow diameter  $d_C$ , cold flow velocity prior to expansion  $U_O$ , and temperature ratio  $T_C/T_\infty$ . The Froude number is approximately 3 for a minimum coflow temperature of  $T_C = 900$  K, ambient temperature of  $T_\infty = 290$  K, coflow cold velocity of  $U_O = 1$  m/s, and a maximum coflow diameter of  $d_C = 0.2$  m. The Froude number is greater than unity; therefore, buoyancy effects should not reduce the coflow potential core. Furthermore, given this coflow diameter, the Froude number will only increase with an increase in either coflow temperature or cold velocity per Equation 4.2.

#### 4.3.5. Perforated Plate Thickness

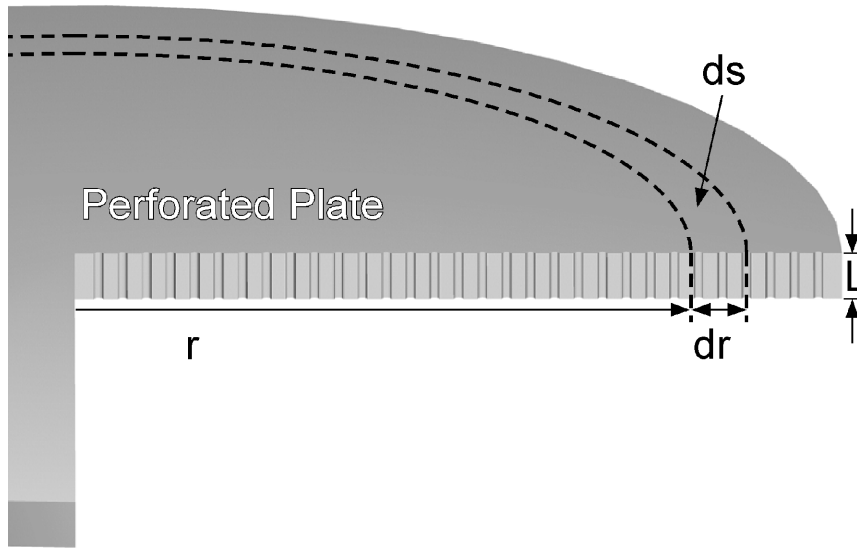
Further consultation with the CNC operators suggested the perforated plate thickness of  $\frac{1}{2}$  inch should be used to reduce the probability of breaking the  $\frac{1}{16}$  inch

drill bits. A perforated plate thickness that is too thin would result in higher plate temperatures during experiments; these higher plate temperatures would compromise the integrity of the perforated plate, and provide an environment more conducive to flashback. The viability of this thickness was determined by approximating the plate temperature via a heat transfer analysis. A finite difference code was developed to model the thermal response of the perforated plate to the given flow and thermal load from the flame.

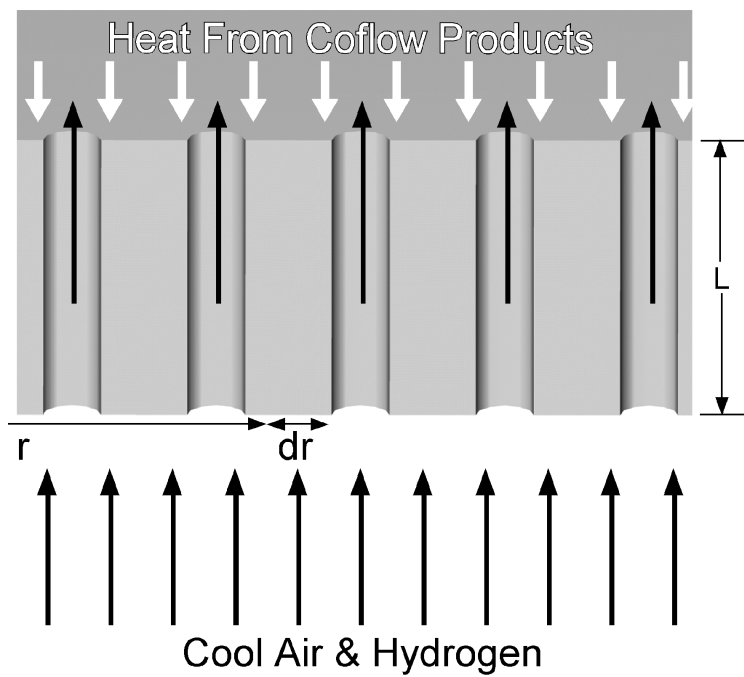
In order to model the thermal response of the plate, several assumptions regarding the flow and thermal load were made. The perforated plate was modeled as a 1-dimensional cylindrical system as shown in Figure 4.13A. The 1-dimensional (radial) approximation was made based on a Biot number analysis. Effects in the axial direction are negligible when the Biot number is less than unity ( $Bi = hL/k \ll 1$ ). For brass ( $k = 110 \text{ W/m-K}$ ) with a thickness of  $L = \frac{1}{2}$  inch, a maximum Biot number of  $Bi = 0.1$  corresponds to a very large convective heat transfer coefficient of  $h = 780 \text{ W/m}^2\text{K}$ . It is safe to assume that convective heat transfer is below this level. The governing heat conduction equation for this radial heat transfer problem may therefore be presented as a simple 1-dimensional equation:

$$\frac{d^2T}{dr^2} + \frac{1}{r} \frac{dT}{dr} + \frac{1}{k} g(r) \quad (4.3)$$

The volumetric heat generation term  $g(r)$  is uniform and is modeled to consist of (1) heat transfer from recirculation, impingement and radiation coflow products  $q_H$  (white arrows in Figure 4.13B) and (2) convective cooling from the internal flow of the cool hydrogen and air mixture  $q_C$  (black arrows in Figure 4.13B).



(A) One-Dimensional System



(B) Close up view

**Figure 4.13.**

Heat transfer analysis of the perforated plate with internal flow of cool air and hydrogen, and a heat load provided by the recirculation (Figure 4.8) and radiation of products from the coflow flame.

$$g(r)dsdx = q_H ds - q_C X ds \quad (4.4)$$

A differential volume analysis with the ring area  $ds$ , plate thickness  $dx$ , and inner surface area of the holes  $Xds$  determines the volumetric heat generation term  $g(r)$ .

$$\begin{aligned} g(r)dsdx &= q_H dsdx - h[T(r) - T_\infty]Xds \\ g(r) &= q_H - \frac{Xh}{dx}[T(r) - T_\infty] \end{aligned} \quad (4.5)$$

Again, the convective heat transfer coefficient  $h$  is for the cooling that occurs within the holes. The flow in the holes is laminar and in the entrance regime; therefore, the correlation proposed by Sieder and Tate (1936) is used:

$$\overline{Nu}_D = 1.86 \left( \frac{Re_D Pr}{L/D} \right)^{1/3} \left( \frac{\mu}{\mu_s} \right)^{0.14} \quad (4.6)$$

The velocity in the holes for a 1 m/s cold bulk flow was determined to be 7.7 m/s in Section 4.3.1. Assuming an elevated flow temperature  $T_\infty$  of 400 K, the Reynolds number is 424, the Nusselt number is 6, and the heat transfer coefficient is  $h = 124 \text{ W/m}^2\text{K}$  (much less than the maximum  $780 \text{ W/m}^2\text{-K}$  allowed for the 1-d assumption). For a plate with 87% blockage from 1/16 inch diameter holes, the multiplier  $X$  is 4.2. The heat release rate for hydrogen emptying out of a size A bottle in 10 minutes is approximately 100 kW. Thermocouple measurements made on the original perforated plate burner (Section 4.2.5) suggest that 5% of the flames heat release ( $Q_H = 5 \text{ kW}$ ) is transferred back to the plate via convection (recirculation zone) and thermal radiation. The volumetric heat load  $q_H$  is therefore  $Q_H/V_{\text{plate}}$ . Since the plate is perforated, the thermal conductivity in the radial direction is reduced and is assumed to be 87% that of solid brass ( $k \approx 96 \text{ W/m-K}$ ).

The finite difference model was executed for a 0.2 m diameter perforated plate and the results are shown in Figure 4.14. The temperature at the outer radial boundary was assumed to be 100 °C. As can be seen, the perforated plate temperature is expected to be elevated to levels above 200 °C. Since the predicted temperatures are not too high, the recommended perforated plate thickness is sufficient. Once the burner was constructed, typical plate temperature measurements were from 150 to 200 °C. The fluid exiting the perforated plate (prior to burning) does not exhibit any discernable increases in temperature (i.e., uniform or flat temperature distribution); this is due to the short residence time within the holes.

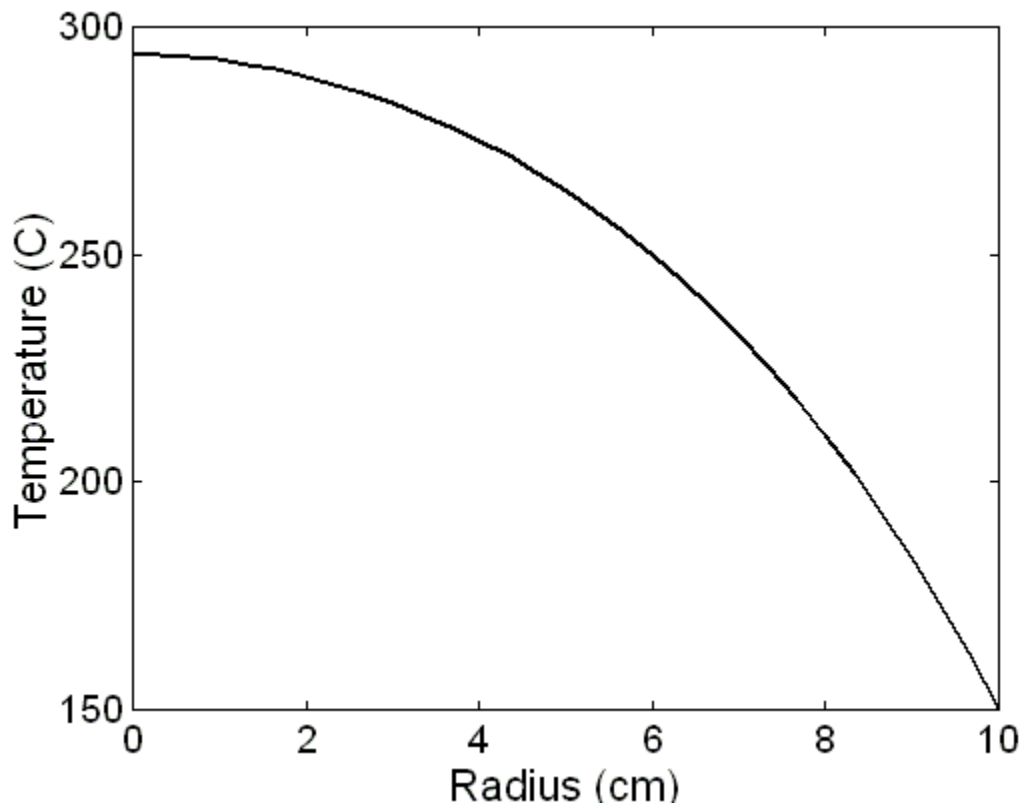


**Figure 4.14.**

Steady state radial distribution of temperature for the perforated plate.

#### **4.3.6. Exit Collar**

Recirculation zones at the perforated plate surface (Figure 4.8) result in ambient air entrainment along the outer edge of the perforated plate. Many of the coflow flames along the perforated plate edge cannot be stabilized because of this cool ambient air entrainment. An exit collar, or a stainless steel wall surrounding the coflow, was built to prevent entrainment of ambient air (Figure 4.7). The tallest coflow flames were established with lean methane-air mixtures; the lean flame tips were 1 inch tall. The exit collar was therefore designed to be 1.25 inch tall and 0.25 inch thick.

The hot coflow heats the exit collar significantly. Under normal operating conditions, the exit collar begins to glow red, and would interfere with laser diagnostics. The exit collar therefore needs to be cooled by water flowing through a surrounding coil of ¼ inch copper tubing, as shown in Figure 4.7.

#### **4.3.7. Central Jet Nozzle**

The central jet nozzle is a ¼ inch OD (6.35 mm) stainless steel tube with a 0.18 inch ID (4.57 mm). The inner seam is welded and smoothed for a circular cross-sectional flow. The nozzle exit height was set at 70 mm above the surface of the perforated plate, almost 3 times the height of the highest coflow flames. The nozzle exit is square and blunt; there is no tapering. Insulating the jet flow with a quartz or ceramic tube was considered; however, the use of such brittle materials would be problematic because of (1) the difficulty of machining and (2) the thermal expansion of the perforated plate would apply mechanical stress to the tube.

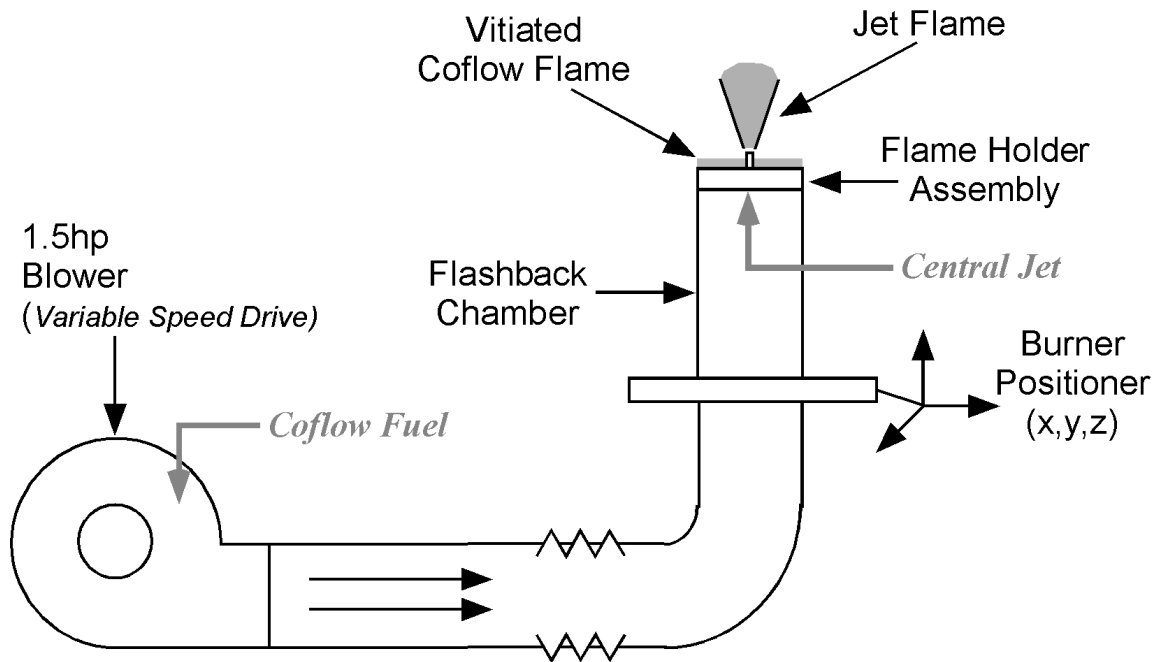


**Figure 4.15.**

Flow system for the vitiated coflow burner.

#### 4.4. Flow Control System

The flow control system consists of the burner, flow supply and the data acquisition and control systems. A schematic of the burner assembly is shown in Figure 4.15. An electric motor driven blower supplies the coflow air. The coflow fuel is injected at the blower inlet to produce a well-mixed mixture. The mixture travels through 12 feet of 4 inch diameter plastic hose before it expands into the flashback chamber and exits out through the perforated plate. The central jet flow also enters through the flashback chamber and exits through the center of the perforated plate.

##### 4.4.1. Coflow Air Flow Control

A 1.5 hp (1.1 kW) blower supplies the coflow air. An variable speed drive enables control of the coflow air (Allen-Bradley 160-SSC, Series B). The correlations

between the pressure drop across the perforated plate and the air flow rate to the motor drive frequency were measured and are shown in Figure 4.16.

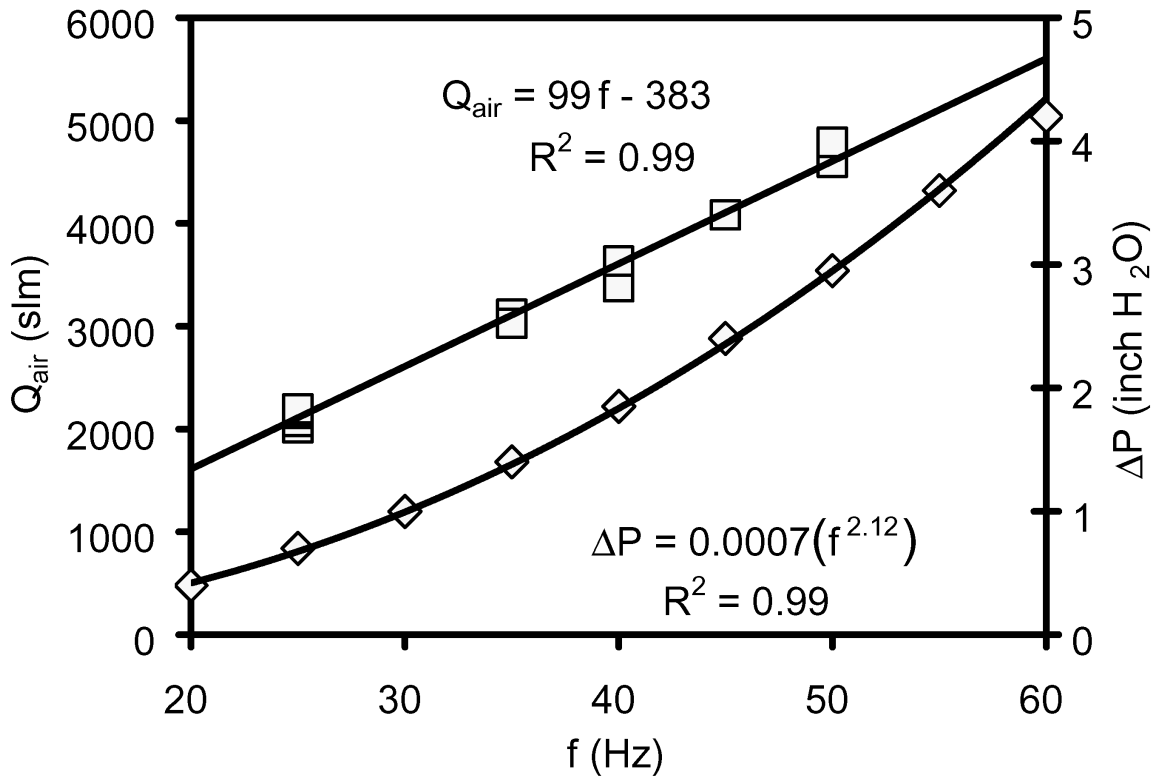


**Figure 4.16.**

Air flow rate and pressure drop across the perforated plate as a function of motor drive frequency.

The specific variable speed drive and blower used are not required to reproduce the experiment. The pressure drop across the perforated plate can be used to determine the mass flow rate of air. Figure 4.17 shows the correlation between the perforated plate pressure drop and the air flow rate. The relationship is consistent with Bernoulli's equation, where the velocity is proportional to the square root of the pressure drop. It is important to emphasize at this point that the data presented in Figure 4.16 and 4.17 are for cold nonreacting air flowing through the perforated plate.

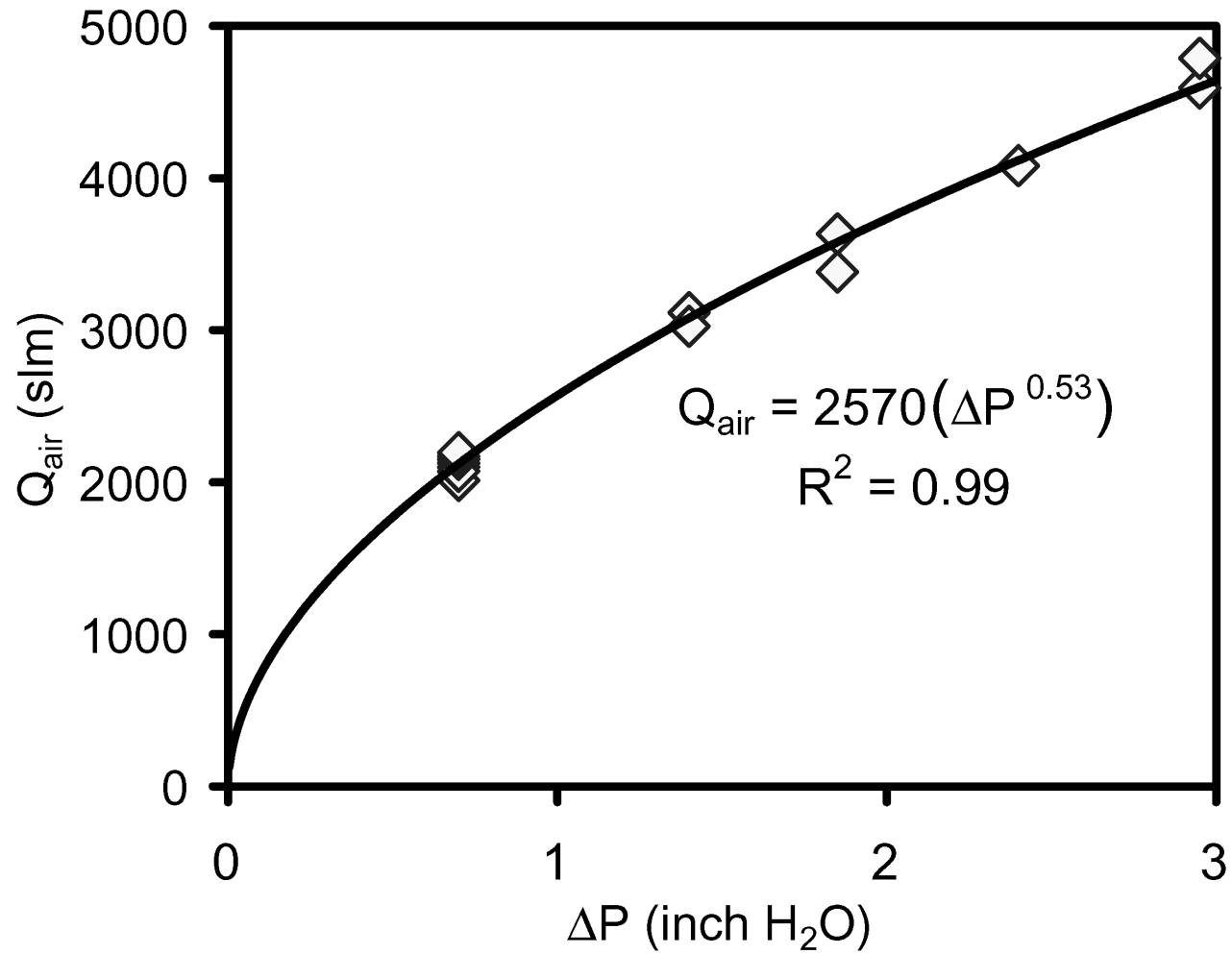


**Figure 4.17.**

Air mass flow rate as a function of the pressure drop across the perforated plate.

#### 4.4.2. Coflow Fuel and Jet Mixture Flow Control

High-pressure systems supply the jet mixture and coflow fuel. Pressurized type A bottles supply hydrogen, methane and nitrogen flows, and the laboratory compressed air system provides the jet air flow. Sharp-edged orifice meters monitor all flow rates. The orifice meters are designed and calibrated to operate under choked conditions. Flow through an orifice is classified as “choked” when the flow velocity is sonic. It is convenient to operate under choked conditions because a simple calibration can be made where the flow rate is dependent on the upstream pressure and temperature.

$$\dot{m} = A \frac{P}{\sqrt{T}} \quad (4.7)$$

Substance and geometric factors determine the calibration constant  $A$ . This relationship is valid when the pressure drop is great enough to drive a sonic flow through the orifice such that  $P_2/P_1 = 0.5$  to  $0.6$ .

Corroborating volume displacement meter measurements determine the calibration constant  $A$ . Methane flow calibration measurements are divided by and plotted against the  $P/\sqrt{T}$  combination as shown below in Figure 4.18. The calibration curves for orifice meters made from #54 and #65 drill bits show the transition to sonic flow beyond  $P/\sqrt{T} \approx 10 \text{ kPa}/\sqrt{\text{K}}$ .

The temperature dependence of the mass flow rate is significant for the coflow fuel flow. The high mass flow rates result in a rapid evacuation of the bottles; the gaseous expansion associated with the rapid evacuation results in decreases in temperature down to about  $0^\circ\text{C}$ . Temperature is practically constant for the jet flows because the mass flow rates are considerably lower. Since the jet air flow is supplied by

a compressed air system, the temperature is constant. For the constant temperature air and nitrogen flows, the calibration constant  $A$  is determined for a flow temperature of 297 K. Table 4.1 lists the calibration data for the orifice meters.

In some instances, the orifice meters could not supply small enough fuel flow rates. In these cases, calibrated mass flow controllers metered the flow rates of hydrogen and methane in the central jet.

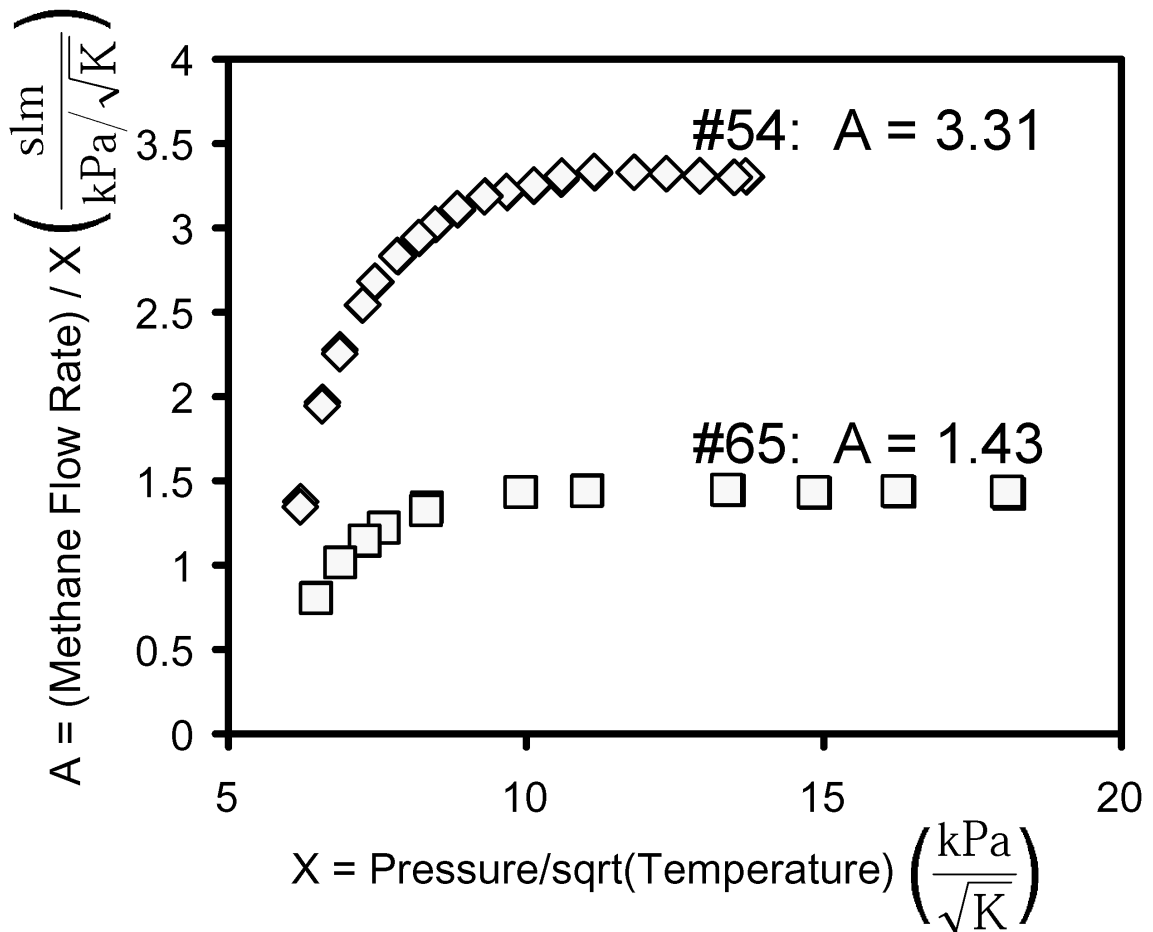


**Figure 4.18.**

Calibration data determines the calibration constant  $A$  for Equation 4.7.

**Table 4.1.**

## Orifice Meter Calibration Data

Gas	Orifice Diameter bit size (inch)	Line Diameter (inch)	$A^*$ (slm $K^{1/2}/kPa$ )	Flow Range (slm)
CH <sub>4</sub>	#65 (0.035)	½	1.43	10-50
CH <sub>4</sub>	#54 (0.055)	½	3.31	30-150
H <sub>2</sub>	#54 (0.055)	½	11.23	150-400
Air	#60 (0.04)	1	1.89	10-50
Air	#52 (0.0635)	1	4.43	50-150
Air	3/32 (0.0938)	1	8.68	120-260
N <sub>2</sub>	#60 (0.04)	1	2.09	10-50
N <sub>2</sub>	#52 (0.0635)	1	4.46	50-150
N <sub>2</sub>	3/32 (0.0938)	1	8.44	100-260

\* Calibration constant for Equation 4.7. Temperature is 297 K for air and N<sub>2</sub>.

**4.4.3. Coflow Flame Stoichiometry Control**

The temperature and oxygen content of the coflow products provide redundancy to the coflow control system. The flow rate meters described in the preceding section are the basis for calibrating these stoichiometric controls. Besides the calibration data, the flow rates were also confirmed by measuring the fuel-air ratio for a set of methane-air flows using the Real-Time Fuel-Air Analyzer (RFA) probe described in Appendix C.

*Oxygen Content of Coflow Products*

The oxygen content of the vitiated coflow is measured with a Percent Oxygen Analyzer by Teledyne Analytical Instruments (S/N 50711). An ice bath condenses and separates the water from the extracted sample, and the oxygen content of the dry mixture

is measured. Laboratory air and a span gas containing 5% oxygen in nitrogen calibrate the oxygen sensor.

Assuming the products reach equilibrium and all the water is removed, the oxygen content of the coflow products determine the coflow flame stoichiometry. The central jet nozzle exit is 70 mm above the perforated plate surface, and each hole of the perforated plate is 1.58 mm. The downstream distance of 45 diameters from the perforated plate surface should be sufficient for the coflow products to reach equilibrium conditions. This assumption is tested through a series of CH<sub>4</sub>/Air premixed flames stabilized on a 4" diameter perforated plate (Figure 4.5).

Figure 4.19 shows a comparison of the stoichiometry calculated by the reactant flow rates and the stoichiometry calculated by the product oxygen content. The ratio of volumetric flow rates determines the stoichiometry based on the global reaction.

$$\phi_{\text{CH}_4} = 9.29 \frac{\dot{V}_{\text{CH}_4}}{\dot{V}_{\text{Air}}} \quad (4.8)$$

$$\phi_{\text{H}_2} = 2.38 \frac{\dot{V}_{\text{H}_2}}{\dot{V}_{\text{Air}}} \quad (4.9)$$

Where  $\dot{V}$  is the volumetric flow rate, typically in slm. The oxygen content of the dry coflow mixture also determines the stoichiometry, assuming the products are at equilibrium.

$$\phi_{\text{CH}_4} = \frac{1}{22.03} (22.03 - \text{O}_2 [\%, \text{dry}]) \quad 0.6 < \phi < 0.9 \quad (4.10)$$

$$\phi_{\text{H}_2} = \frac{1}{21.71} (22.29 - \text{O}_2 [\%, \text{dry}]) \quad 0.2 < \phi < 0.8 \quad (4.11)$$

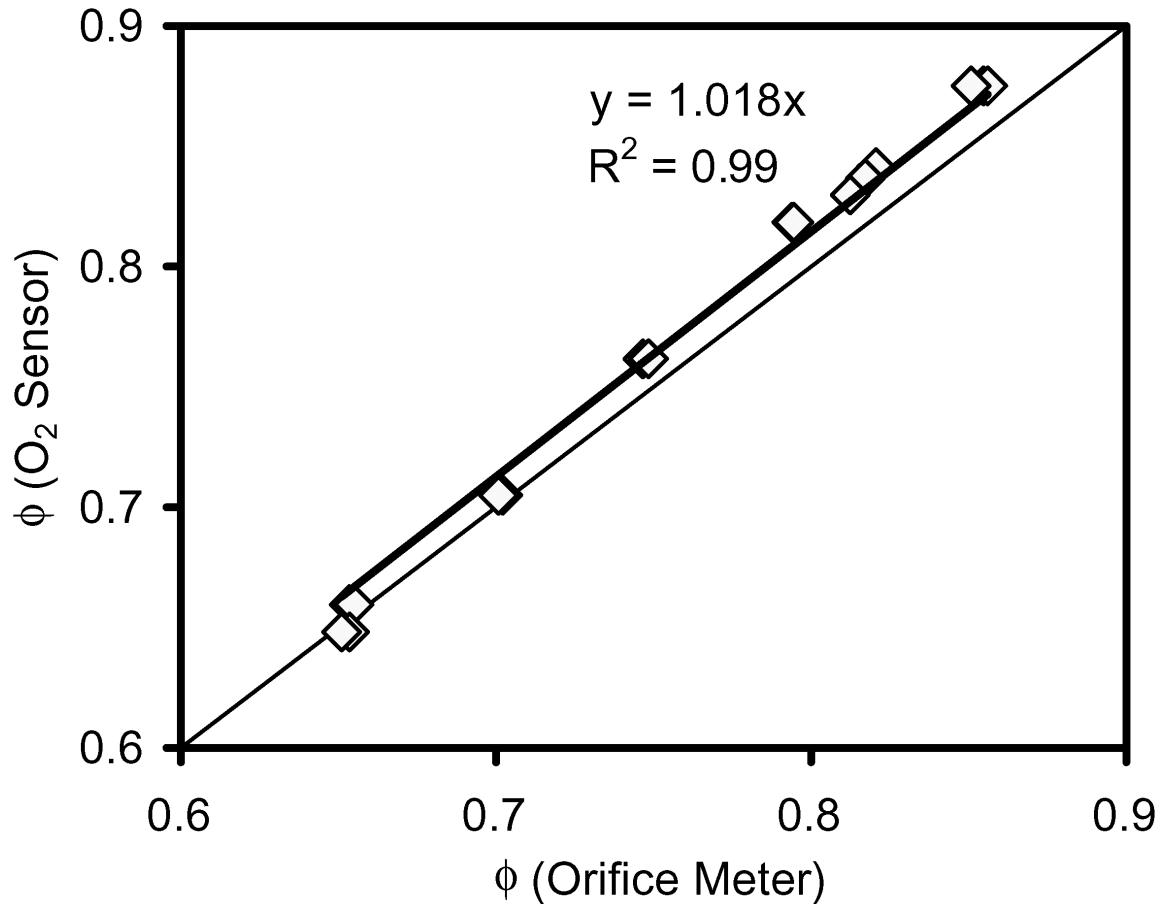


**Figure 4.19.**

Agreement of flow and oxygen based stoichiometries for coflow products of methane-air flames show that the mixture reaches equilibrium.

As seen in Figure 4.19, both methods of determining the coflow stoichiometry are in agreement. The equilibrium composition assumption of the methane coflow flame is valid. Furthermore, the shorter chemical time scales associated with hydrogen flames will also result in equilibrium conditions.

#### *Coflow Temperature*

Subsequently, the temperature of the coflow products is also used as a redundant check of the coflow stoichiometry. The coflow temperature is measured with an exposed type K thermocouple with a 1/8 inch diameter uninsulated sheath. The estimated

uncertainties are  $\pm 5\%$  ( $\approx 60$  K) for the thermocouple as provided by the manufacturer OMEGA.

The radiative heat loss is significant for thermocouple measurements in flames. For simplicity, a radiative correction factor was sought such that the measured temperature  $T_{\text{exp}}$  may be converted to the actual temperature  $T_{\text{gas}}$ .

$$T_{\text{gas}} = C_{\text{rad}} T_{\text{exp}} \quad (4.12)$$

Absolute temperatures are used in this correlation. The radiative correction factor is determined by analyzing the steady problem of a sphere in a hot flow of air with radiative heat losses to the ambient surroundings. The convective and radiative heat transfer fluxes balance each other.

$$h(T_{\text{gas}} - T_{\text{exp}}) = \sigma \epsilon (T_{\text{exp}}^4 - T_{\infty}^4) \Rightarrow T_{\text{gas}} = T_{\text{exp}} + \frac{\sigma \epsilon}{h} (T_{\text{exp}}^4 - T_{\infty}^4) \quad (4.13)$$

The convective heat transfer is determined by Whitaker's (1972) correlation for a sphere in a flow.

$$\overline{\text{Nu}}_D = 2 + \left( 0.4 \text{Re}_D^{1/2} + 0.06 \text{Re}_D^{2/3} \right) \text{Pr}^{0.4} \left( \frac{\mu_{\text{gas}}}{\mu_{\text{exp}}} \right)^{1/4} \quad (4.14)$$

The bead diameter used to determine the Reynolds number is  $D = 1$  mm. The emissivity of the thermocouple bead is taken to be  $\epsilon = 0.5$ . For a range of thermocouple measurements from 600 to 1500 K, the corresponding gas temperatures were determined using Equations 4.13 and 4.14. The average radiative correction term was then determined to be  $C_{\text{rad}} = 1.17$ . In fact, this approximation is in agreement with the measurements made at the TDF laboratory (laser Raman-Rayleigh scattering) for coflows

in this temperature regime. The radiative correction factor determined via the laser diagnostic results is  $C_{\text{rad}} = 1.225$ .

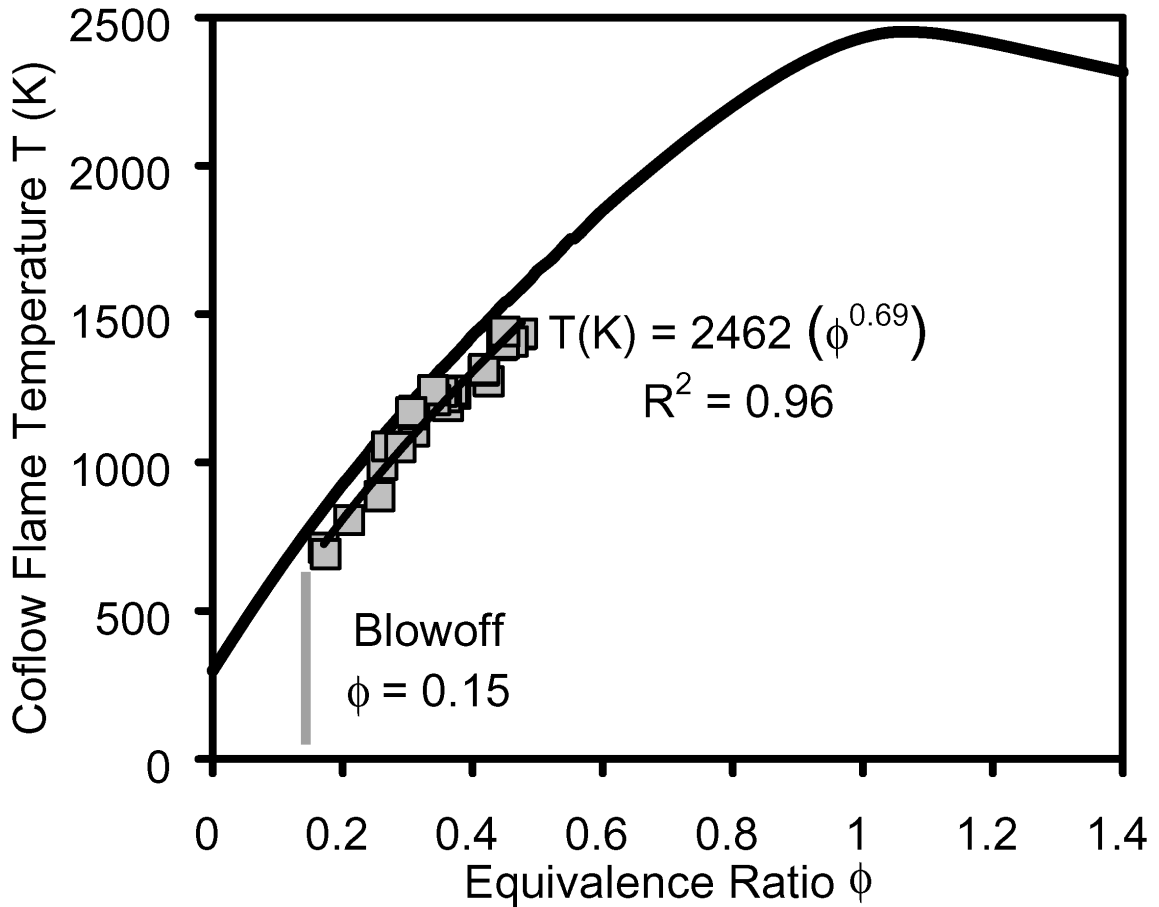


**Figure 4.20.**

Temperature of products from premixed hydrogen-air flames stabilized on the perforated plate

The corrected thermocouple measurements for a series of hydrogen-air flames stabilized on the perforated plate are shown in Figure 4.20. The results are plotted against the stoichiometry determined by the reactant flow rates. A correlation was then derived for a temperature-based stoichiometry from the data.

$$\phi_{\text{H}_2} = 1.43 \times 10^{-5} (T[\text{K}])^{1.43} \quad (4.15)$$

Also plotted is the adiabatic flame temperature as determined by StanJAN. The plot shows that the coflow flame is approximately adiabatic, regardless of thermal dissipation by the perforate plate, whose temperature reaches 200 °C.

The data presented in Figure 4.20 also show the range of this experiment. Similar to the “Hencken” or tube bundle burners, the perforated plate burner enables the stabilization of ultra lean flames. The leanest hydrogen flame stabilized on the perforated plate had a stoichiometry of  $\phi = 0.15$ .

#### **4.5. Safety System (Flashback)**

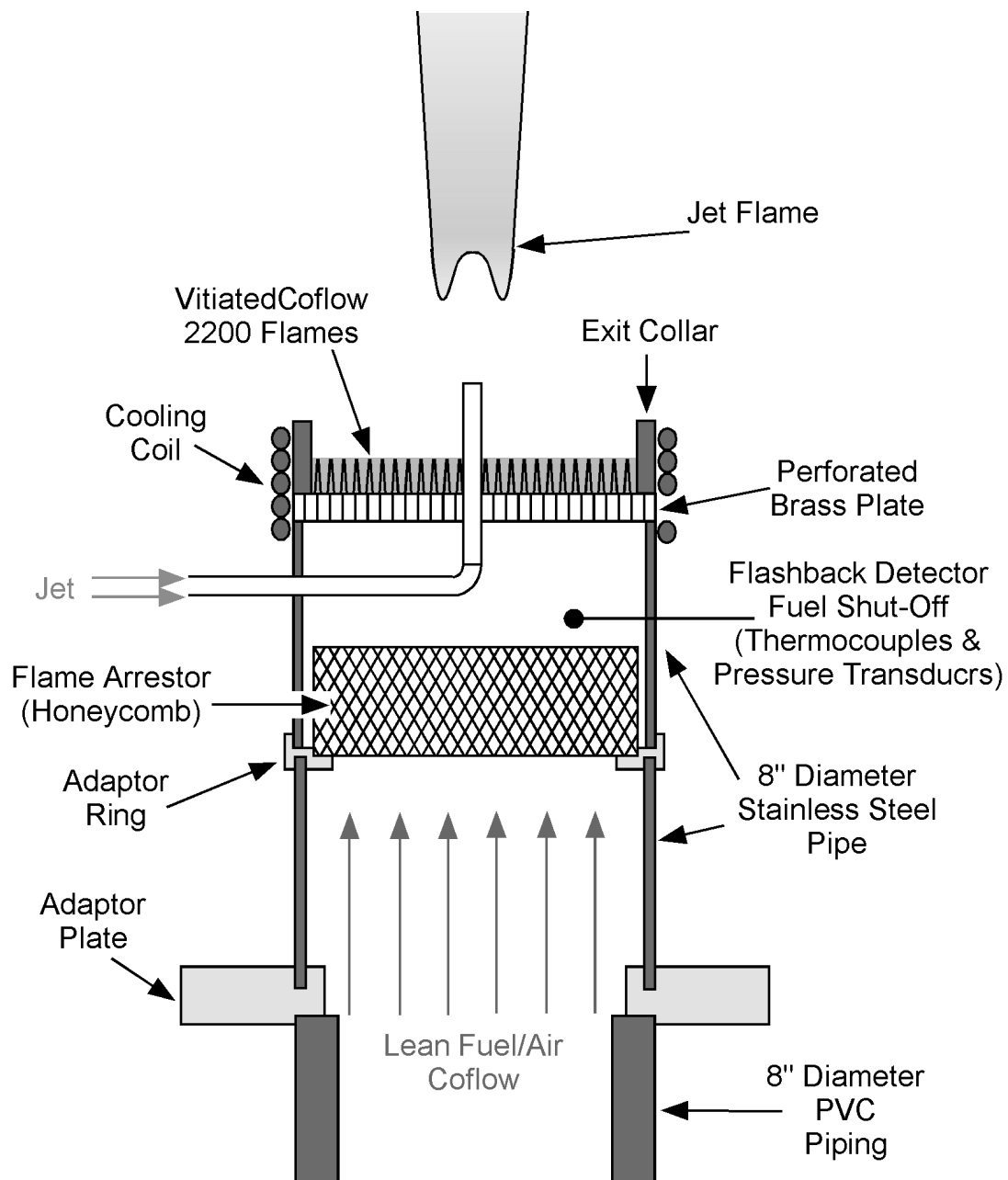
The perforated plate is an excellent flame holder. However, the fuel-air mixture poses a substantial threat of flashback. Flashback is the propagation of the flame upstream through the holes of the perforated plate, possibly generating explosive conditions. Therefore, the burner must be designed to (1) prevent propagation upstream through the perforated plate, (2) withstand the rapid increases in pressure and temperature, and (3) automatically cut off the fuel given any slight increase in pressure or temperature inside of the burner.

The first line of flashback defense is the perforated plate itself. As discussed in Section 4.3.1, the blockage is the critical design factor in safeguarding against flashback. First, the quenching diameter for premixed flames is on the order of the flame thickness; therefore, the perforated plate holes are smaller than the flame thickness. By flow continuity, the smaller holes accelerate the flow by a factor of 7.7. For bulk velocities greater than 1 m/s, the accelerated velocities are much greater than the laminar flame

speeds. The lean premixed coflow flame should therefore be unable to propagate through the perforated plate.

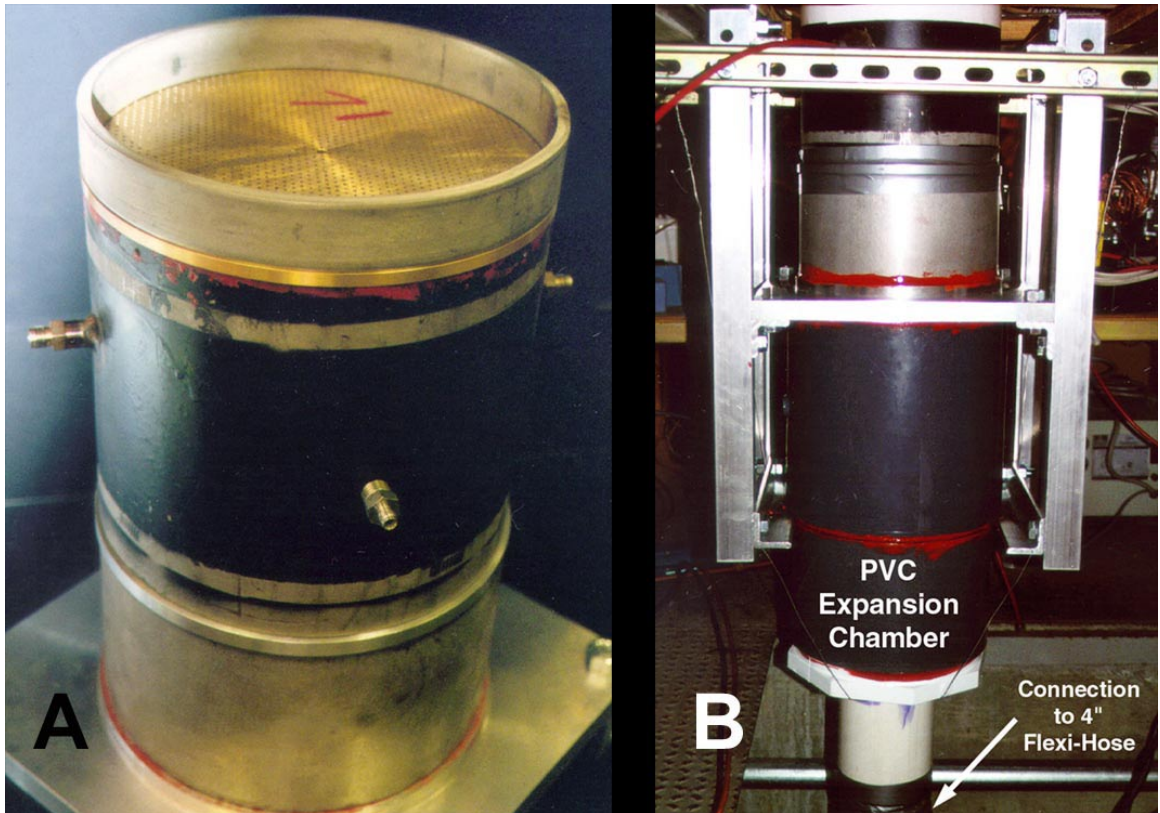
The system upstream of the perforated plate is named the flashback chamber as shown in Figure 4.15. The flashback chamber is a stainless steel 8 inch diameter compartment capable of withstanding the increase of pressure and temperature due to flashback. There are two sections in this compartment. A schematic of the flashback chamber and flame holder assembly is shown in Figure 4.21. Photos of this assembly are shown in Figure 4.22. At the midsection of this chamber, a 7.5 inch diameter by 2.5 inch thick uncoated ceramic monolith with 2 mm square channels provides an excellent flashback arrestor and flow straightener. Catalytic Solutions Incorporated in Oxnard, California manufactures the honeycomb. This straightener is held on a adaptor ring (Appendix B). In the event of flashback, the internal flame is stabilized on the square channel honeycomb, providing time to stop the fuel flow manually in the event that the flashback sensors fail to close the solenoids. All parts are fitted together by machining the ends for lip and sink connections.

Figure 4.22 shows how the components fit together. The PVC expansion chamber connects to the adaptor plate, and machined lip/sink ends connect all parts. Use of this design is purely for cost reduction and sealed fit. All interfaces are sealed with high temperature silicon (RTV) and fire resistant duct tape.



**Figure 4.21.**

Schematic of the Vitiated Coflow Burner.



**Figure 4.22.**

Photos of the vitiated coflow burner. (A) The flame holder and flashback chamber, and (B) the burner attached to the positioning device by the adaptor plate.

A flashback sensor assembly was designed to close automatically the solenoid valves in the fuel lines with any increase of pressure or temperature inside the flashback chamber. Two redundant safety systems were built:

1. The Cabinet Safety System is the permanent system housed in the same cabinet with all control and data acquisition systems.
2. The Portable Safety System is a modular system that is independent of the cabinet control system. This system was built to travel with the burner to other laboratories (e.g., Sandia National Laboratories).

The electrical schematics for each safety system are presented in Appendix A. Each system consists of both a temperature and pressure switch assembly; these assemblies are 2 electronic switches (OMEGA Limit Controller, CN1602), one monitoring thermocouple readings in the flashback chamber, the second monitoring the pressure transducer readings of the pressure drop across the perforated plate. The temperature switches are set to shutoff power to the solenoids when the chamber temperature increases beyond 35 °C. The pressure switches safeguard against both flashback and the unintentional shutoff of coflow air (i.e., loss of power to the blower). Accordingly, the high-low pressure switch was set to allow fuel delivery only when there is a pressure drop across the perforated plate between 0.5 and 5 inches of water; this range of pressure corresponds to the operation range of the blower (Figure 4.17). Each system also has a manual shutoff button and status indicators (i.e., LEDs or an audible alarm). These safety systems proved to be quick and reliable in a series of tests where the premixed gases upstream of the perforated plate were intentionally ignited.

## 4.6. Chapter Summary

In this chapter, the vitiated coflow burner development process and design are presented. The concept requirements centered on the objective of providing a two-stream flow for investigation of combustion in vitiated environments. Several candidates were screened and the perforated plate burner proved to be the strongest candidate (Figure 4.7).

Several factors were considered in developing the present perforated plate design consisting of a coaxial jet flow. The flow consists of a central turbulent fuel jet with a coaxial flow of hot combustion products from a lean premixed H<sub>2</sub>/Air flame. The central nozzle is a tube with a 4.57 mm inner diameter and the coflow flame is stabilized on a 210 mm diameter perforated plate with 87% blockage from 2,184 holes with 1.58 mm diameter. The central nozzle extends 70 mm above the surface of the perforated plate. Photographs of the flame and burner are shown in Figure 4.6 and 4.7.

A control system filled with redundancy ensures the correct flows and mixture compositions are obtained. A variable speed blower supplies the coflow air. High pressure bottles supply the fuel flow rates and the laboratory compressed air system provides the central jet air flow rate; all of these flows are controlled using orifice meters. The reactant flow meters were calibrated extensively; however, redundancies in the system were included to monitor the coflow stoichiometry. The products of the coflow flame are monitored through measurement of the temperature by thermocouples and oxygen content by an oxygen sensor. Results show that the coflow stream is nearly at

equilibrium. A correlation between the pressure drop across the perforated plate and the air flow rate (Figure 4.17) provides another means of monitoring the coflow.

Safeguards against the threat of flashback were designed into the experiment. The perforated plate was designed to prevent the propagation of a flame through its holes. A flashback chamber was designed (Figure 4.21) to contain flashback, and a redundant safety system shuts off the fuel flow rates via a set of temperature and pressure switches. Electrical schematics of the safety systems are included in Appendix A along with engineering drawings and a parts list of all burner components described in this chapter.

## Chapter 5

# Laser Rayleigh-Raman-LIF Measurement System

The Turbulent Diffusion Flame (TDF) laboratory at the Combustion Research Facility (CRF) of Sandia National Laboratories in Livermore, CA was employed to obtain simultaneous multiscalar point measurements of temperature, major species and minor species. A combination of laser Raman scattering, Rayleigh scattering and laser induced fluorescence (LIF) measures temperature, O<sub>2</sub>, N<sub>2</sub>, CH<sub>4</sub>, H<sub>2</sub>O, H<sub>2</sub>, CO<sub>2</sub>, CO, OH and NO. Acquiring a large quantity of simultaneous measurements provides a means to analyze joint statistics for the complex turbulent reacting flow.

This chapter begins with an introduction of the physics applied to combustion diagnostics. The advanced facility at Sandia National Laboratories is then discussed, with the introduction of experimental techniques, calibration procedures and system uncertainties.

### 5.1. Background Physics

In order to present the experimental system in a clear fashion, the physics involved is first discussed. The Rayleigh and Raman effects are discussed and then laser-induced fluorescence is introduced.

#### 5.1.1. Rayleigh and Raman Effects

The Rayleigh and Raman effects are typically used in combustion diagnostics to measure the temperature and specie concentrations. The physics behind these effects are illustrated in Figure 5.1. A collimated laser beam consisting of photons at a given energy

(wavelength) pass a group of molecules. Some molecules absorb a photon and are then excited to a virtual state. These molecules then equilibrate, emitting a photon. If the molecules return to their initial energy state, the emitted photon has the same energy and wavelength as the oncoming photons. This “elastic” absorption and emission of photons is called the Rayleigh effect. Conversely, if the excited molecules return to a new energy level, the emitted photon is of different energy/wavelength. This inelastic process is known as the Raman effect. The effect is further classified as Stokes Raman scattering if the excited molecules return to a higher energy state, and as Anti-Stokes Raman scattering if it returns to a lower energy state. The majority of the absorption-emission processes are elastic, where the weak Rayleigh effect is about 2,000 times stronger than the Rayleigh effect (Eckbreth 1996).

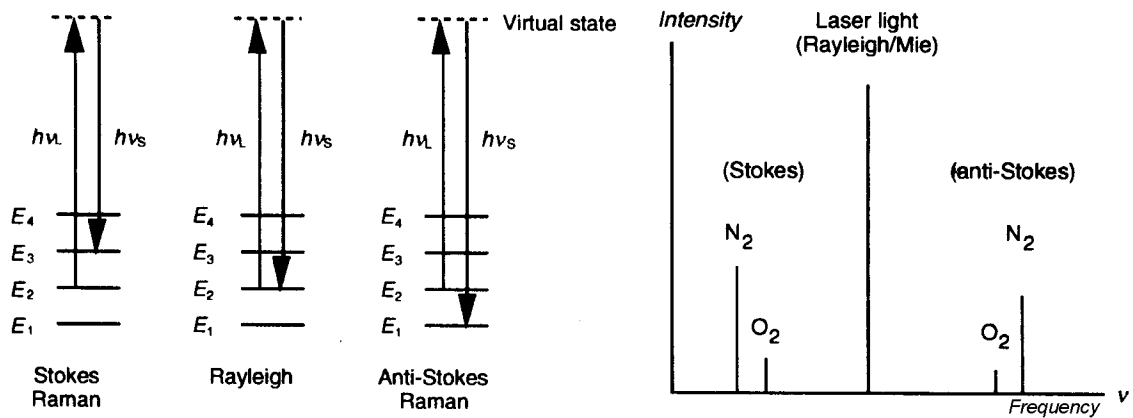


**Figure 5.1.**

Energy transition processes and spectral emission associated with laser Rayleigh and Raman scattering (Warnatz et al. 2000).

The basis for application of the Raman effect to combustion research is that the wavelength of the Raman response is unique to each molecule (Figure 5.1). Recently, Barlow et al. (2000) implemented a cooled CCD array to measure the Raman spectra for

various methane-air flames and some of the results are shown in Figure 5.2. The amplitude of each peak in Figure 5.2 is related to the concentration of the associated specie.

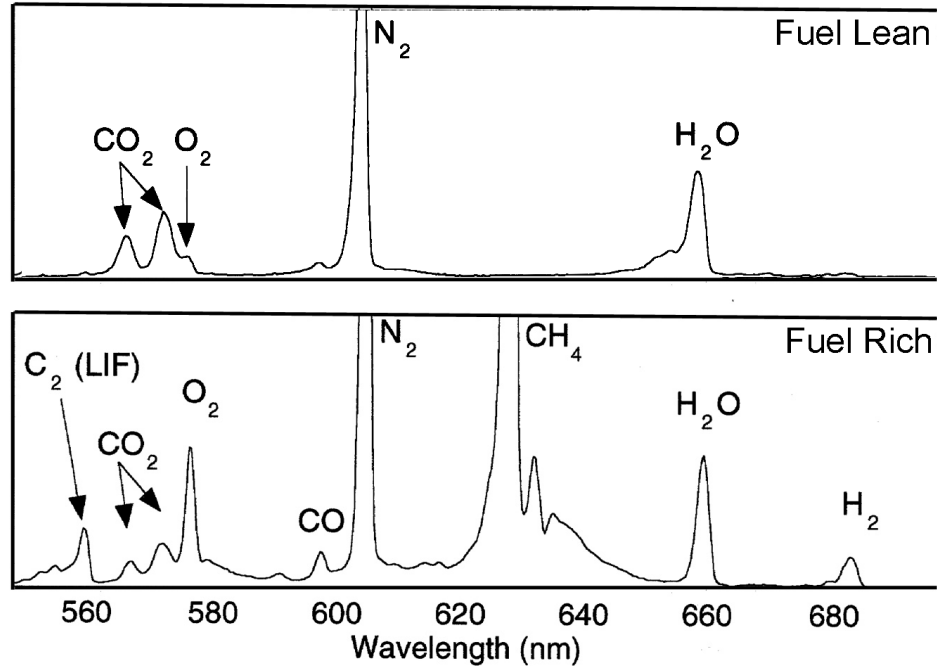


**Figure 5.2.**

Raman spectra of major species for fuel lean and fuel rich methane-air flames. The laser wavelength is  $\lambda_{\text{laser}} = 532 \text{ nm}$ . The ordinate units are a measure of the photon count (Barlow et al. 2000).

### 5.1.2. Laser Induced Fluorescence

The laser initiated fluorescence (LIF) effect is employed to measure the minor species CO, OH and NO. An illustration of the physics behind LIF is shown in Figure 5.3. A laser pulse is used to excite molecules to selective electronic states (Wolfrum 1998). Unlike the Rayleigh and Raman effects, during LIF the molecules are excited to a real state with a different electronic structure. The change in energy during these transitions is often quite large; therefore, photons in the UV (shorter wavelength, higher

energy) are required. As shown in Figure 5.3, there are many transitions that may occur, resulting in absorption and emission over a wider spectrum. It is important to note that while LIF provides good selectivity and sensitivity, it can be difficult to obtain quantitative results since calibration is required.

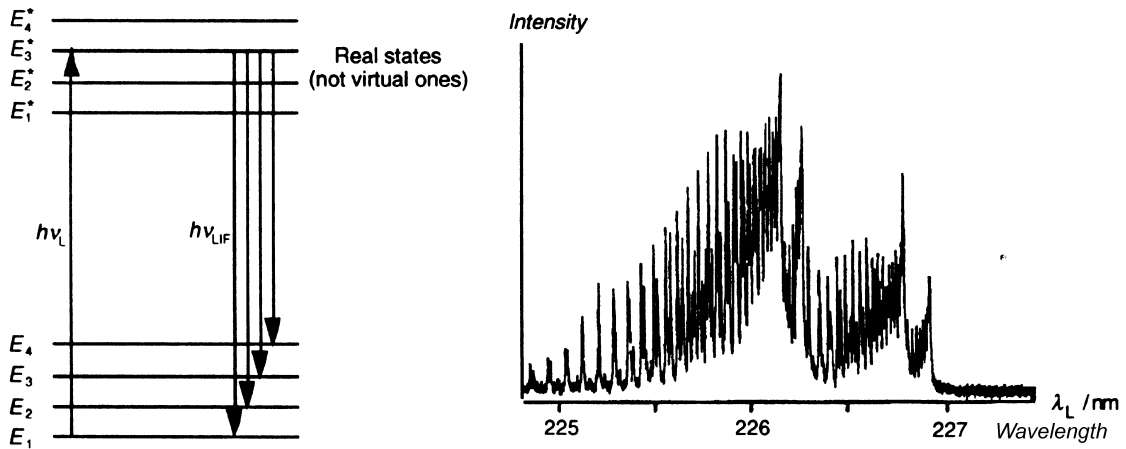


**Figure 5.3.**

Energy transition process and spectral emission associated with laser induced fluorescence (Warnatz et al. 2000).

## 5.2. Experimental Setup

Through collaboration with the Combustion Research Facility at Sandia National Laboratories, the world-class Turbulent Diffusion Flame (TDF) laboratory was used to survey the flow field for three specific conditions. The following is a summary of the experimental setup at this facility. For additional background information the reader is referred to the extensive descriptions in the literature (Nguyen et al. 1996, Dally et al. 1996, Barlow et al. 1990, 2001, and Kohse-Höinghaus and Jeffries 2002).

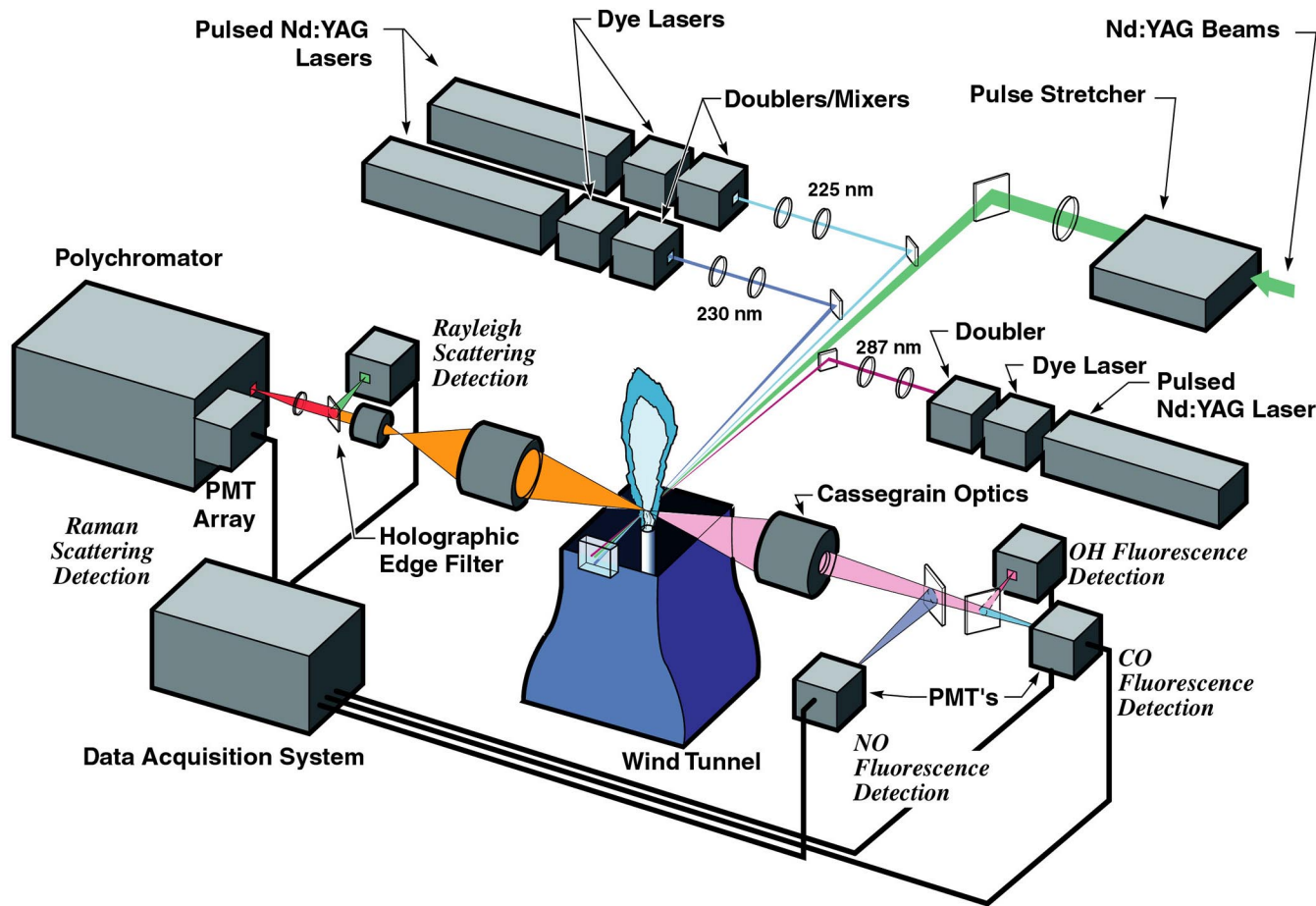


**Figure 5.4.**

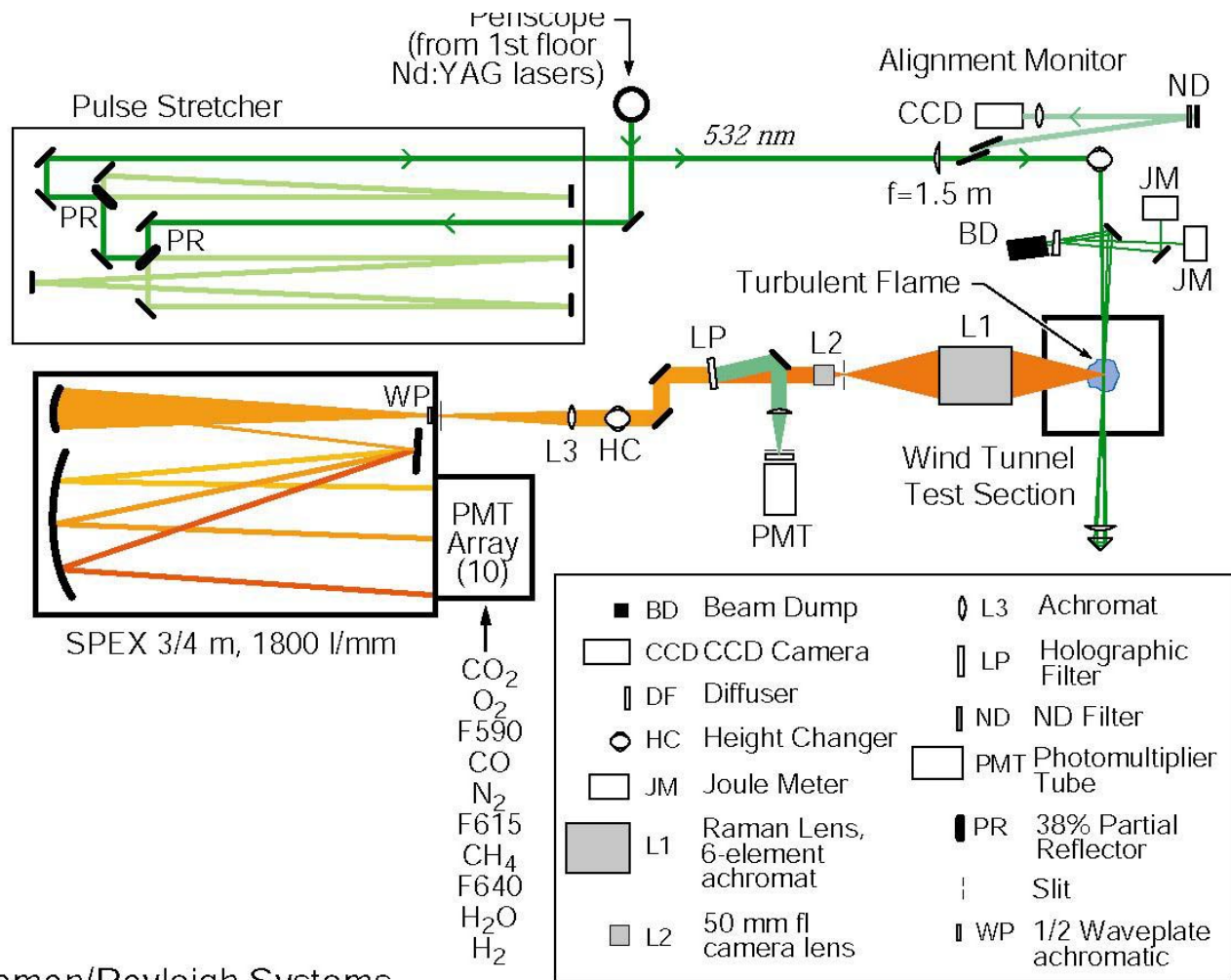
A schematic of the Raman-Rayleigh-LIF experimental facility located at Sandia National Laboratories (Barlow 2002).

The system consists of five pulsed laser systems with time delays of 100 ns between pulses. With this short time delay, the cumulative measurement time is less than 1  $\mu$ s. This short time scale is less than turbulent and chemistry time scales in most flows; therefore, the 5 pulses are effectively simultaneous. The entire system operates at a frequency of 10 Hz.

Figure 5.4 shows the experimental setup at the TDF laboratory. As can be seen, 2 Nd:YAG lasers are used for the Rayleigh and Raman experiments that measure the major specie concentrations. Three Nd:YAG pumped dye lasers emit beams in the UV for the CO, OH, and NO LIF measurements.

### **5.2.1. Raman-Rayleigh System**

Two Nd:YAG frequency doubled lasers with a 532 nm wavelength are used for the Raman-Rayleigh measurements. Figure 5.5 below shows a schematic for the optical layout of the Raman-Rayleigh system. The two 10 ns, 700 mJ pulses are stretched and staggered by a pulse stretcher assembly so that one pulse follows another through the probe volume. The pulse is stretched in order to prevent optical breakdown due to the high incident energy rate, which occurs in the event that all pulses arrive at the probe volume simultaneously. This optical breakdown is a sparking event that occurs in the probe volume with a brightness that far exceeds the products of Rayleigh, Raman and LIF effects. Two pyroelectric Joule meters are used to measure the shot to shot laser energy. To increase effective laser power, the transmitted beam is collimated and reflected back through the probe volume.



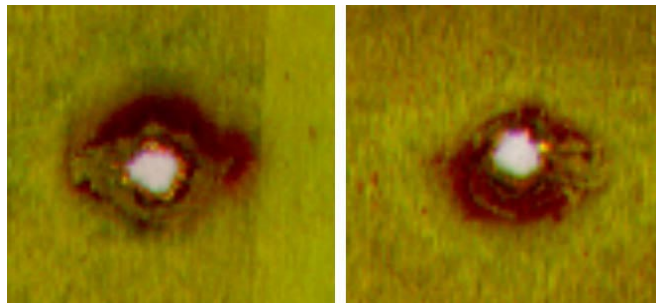
Raman-Rayleigh Systems

Figure 5.5.

The optical layout for the Raman-Rayleigh system (Barlow 2003).

The scattered light from the probe volume used for the Raman and Rayleigh measurements is collected with a low f-number achromatic lens and collimated with a camera lens. A holographic edge filter transmits the Raman scattered light and reflects the Rayleigh scattered light towards the Rayleigh photomultiplier tube. Concurrently, the Raman scattered light is spectrally decomposed in a 0.75 m grating polychromator. The spectrometer consists of a graded mirror, two concave mirrors, and a photomultiplier tube array. These photomultiplier tubes (PMTs) are positioned so that each views a band of the Raman spectra as shown in Figure 5.2. Three additional PMTs are positioned to measure fluorescence interference at 590, 615 and 640 nm.

Beam waist diameter is 750  $\mu\text{m}$  and the length of this probe volume is also roughly 750  $\mu\text{m}$ . The beam waist diameter is calibrated using thin copper pieces that are placed in the beam path. The incident energy from the Raman-Rayleigh pulses induces a breakdown of the copper atoms, removing them from the surface of the metal piece. Eventually, the pulses clear a hole through the copper stock piece, and that hole is measured to determine the beam waist diameter of the pulses. The copper pieces used for this calibration are shown below in Figure 5.6.



**Figure 5.6.**

Spatial resolution determined by copper pieces that were decomposed by the laser beam used for Raman-Rayleigh diagnostics. Holes are approximately 750  $\mu\text{m}$  in diameter.

### 5.2.2. Laser Induced Fluorescence System

Three LIF Nd:YAG pumped dye lasers are used to measure the minor species CO, OH and NO using a laser induced fluorescence (LIF) technique. A schematic of the optical layout is presented below in Figure 5.7. While maintaining the approximate initial wavelength, each UV pulse is split twice; once to measure the beam energy with a PMT, and a second time for simultaneous system calibration. The OH and NO systems are simultaneously calibrated with laminar reference flames of methane and air ( $\phi = 1$ ). The CO system is simultaneously calibrated using a cold cell with a known amount of CO ( $X_{\text{CO}} = 0.05$ ,  $X_{\text{He}} = 0.45$ ,  $X_{\text{N}_2} = 0.5$ ). The laser induced fluorescence is collected by a low f-number Cassegrain system. The focused light is then passed through two dichroic beam splitters that diverge the signal towards three filtered PMT systems.

The OH excitation beam (287.9 nm) excites the  $A^2\Sigma^+ - X^2\Pi(1,0)$  band to the  $O_{12}(8)$  transition. The OH PMT system consists of a band pass filter and colored glass filters to detect fluorescence in the band of  $304 \text{ nm} < \lambda < 318 \text{ nm}$ . The NO excitation beam (226.1 nm) excites the  $A^2\Sigma^+ - X^2\Pi(0,0)$  band to the  $Q_1(12)$  and  $Q_2(20)$  transitions. The NO PMT system consists of colored glass filters and a solarblind photocathode to detect fluorescence in the band of  $230 \text{ nm} < \lambda < 300 \text{ nm}$ . The two photon LIF system (TPLIF) is described in detail by Nguyen and coworkers (1996), where two 230.1 nm photons excite transitions in the  $B^1\Sigma^+ - X^1\Sigma^+$  band of CO. The fluorescence is measured over the range of  $480 \text{ nm} < \lambda < 488 \text{ nm}$ , and the laser energy is 700  $\mu\text{J}$  per pulse. A summary of specifications for the LIF system excitation and detection band pass filters is listed in Table 5.1.

### LIF Systems

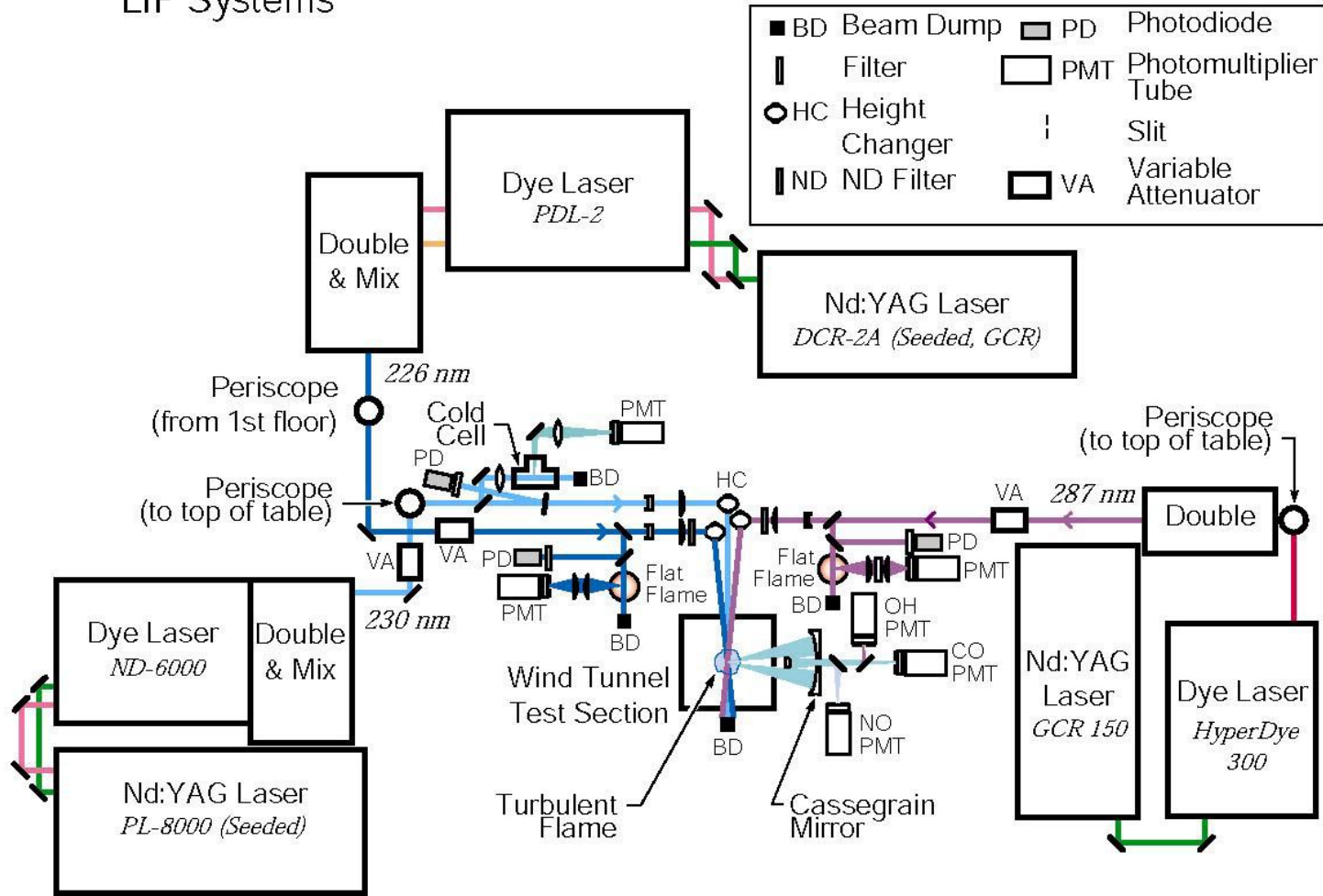


**Figure 5.7.**

The optical layout of the Laser Induced Fluorescence (LIF) system (Barlow 2003).

**Table 5.1.**

LIF system excitation and detection specifications.

Species	Excitation (nm)	Lower Detection Limit (nm)	Higher Detection Limit (nm)
CO	230.1	480	488
OH	287.9	304	318
NO	226.1	230	300

The CO LIF system was not available for these experiments. Large uncertainties, due to a breakdown of the seeding laser for the Nd:YAG laser, made the CO LIF system useless. Fortunately, the Raman CO measurements are sufficiently reliable because of the low levels of interference measured due to the lean nature of these flames.

### 5.3. Data Reduction

Several hundred laser-shots per spatial location in a turbulent reacting flow provide a means to analyze statistically the turbulent reacting flow. For each flame, one axial and several radial profiles of temperature and composition are obtained. The basis of the experiments is the collection of photons by the large number of PMTs of the system. The general procedure of reducing these signals to multiscalar measurements consists of two coupled steps. The first step is determination of temperature and major species concentrations via the Raman-Rayleigh data. The second step is determination of the minor species concentrations with the additional LIF data.

The coupled problem of determining the temperature and composition of major species is known as the iterative, inverse Raman-Rayleigh problem. In order to best describe this scheme, first it is necessary to present the relationships between the diagnostic systems and the measured scalars.

### 5.3.1. Rayleigh Temperature

The Rayleigh temperature ( $T_R$ ) is determined via the Rayleigh signal ( $S_R$ ) and the Rayleigh scattering cross-section ( $\sigma_R$ ). Equation 5.1 shows this relationship (including the calibration factor,  $C_R$ ).

$$T_R = \frac{C_R \sigma_R}{S_R} \quad (5.1)$$

Furthermore, the Rayleigh scattering cross-section is mixture based, depending on the mixture composition and the Rayleigh scattering cross-section for each specie.

$$\sigma_R = \sum X_i \sigma_i \quad (5.2)$$

Where  $X_i$  is the mole fraction of specie  $i$ , and  $\sigma_i$  is the Rayleigh scattering cross-section of specie  $i$ . The Rayleigh temperature is dependent on the mixture composition, which is determined via spontaneous Raman scattering and LIF.

### 5.3.2. Probe Volume Composition by Laser Raman Scattering

Reduction of the Raman signals to mixture composition is a more detailed process. First of all, the Raman effect is approximately three orders of magnitude less than the Rayleigh effect. Secondly, as can be seen in Figure 5.2, there also can be large amounts of cross talk between the adjacent Raman and LIF signals from different species. The spectral broadening of the Raman signals is due to the different rotational and vibrational bands of the species. LIF emissions also interfere with the Raman signals. As a result, several species contribute to a given Raman signal. An example of this interference is the overlapping of the  $O_2$  signal and the  $CO_2$  signal for the fuel rich conditions shown in Figure 5.2. On the other hand, typically there are negligible interferences in hydrogen and lean methane air combustion, as can be seen in Figure 5.2.

The reduction in LIF and Raman response interferences in lean conditions is due to the reduction in the number of species present and the absence of intermediate species (e.g., C<sub>2</sub>) associated with fuel rich combustion.

All the signal contributions, including the interferences, are additive and linearly proportional to the given species number density. This additive relationship between linear contributions and the signal S<sub>i</sub> is shown below.

$$S_i = \sum_j C_{ij}(T)N_j \quad (5.3)$$

Where N<sub>j</sub> is the number density of specie j, and C<sub>ij</sub>(T) is the temperature dependent Raman response (when i = j) and signal overlapping (when i ≠ j) between species i and j. Since the composition is what is required, Equation (5.3) is solved for the number density vector, yielding the inverse Raman problem (Nguyen et al. 1996).

$$\vec{N} = \overline{\overline{C}}(T)^{-1} \vec{S} \quad (5.4)$$

Where  $\vec{S}$  and  $\vec{N}$  are the specie Raman response and number density vectors respectively. The matrix  $\overline{\overline{C}}(T)$  contains the relationships for Raman responses (diagonal elements) and cross talk (off-diagonal). Calibrations by Barlow and Frank (1998) were used to develop the elements for the temperature dependent matrix  $\overline{\overline{C}}(T)$ . The Rayleigh temperature, via a calibrated polynomial relationship, determines each element in the correlation matrix. The LIF interferences are not included in this discussion because the signals were negligible. For more information regarding LIF interferences, the reader is referred to the analysis of fuel rich natural gas combustion done by Nooren et al. (2000).

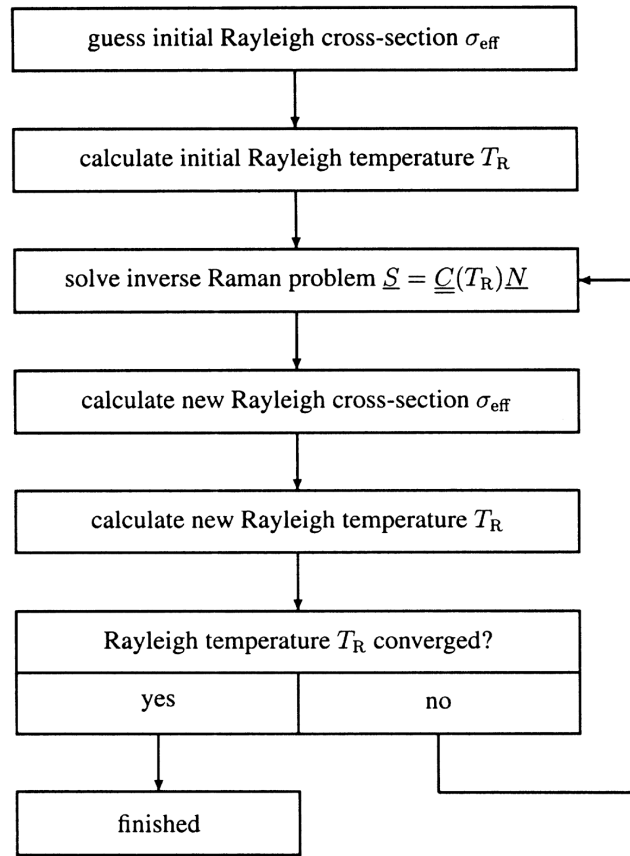


**Figure 5.8.**

Iterative scheme for inverse Raman-Rayleigh problem (Nooren 1996).

### 5.3.3. Inverse Raman Problem

As stated in the previous section, the elements of the correlation matrix are determined via the Rayleigh temperature. However, the Rayleigh scattering cross-section is dependent on the Raman composition, requiring a simultaneous determination of the Rayleigh temperature and the Raman composition. This inverse Raman-Rayleigh problem is solved through the iterative technique outlined in Figure 5.8. Initially, the effective Rayleigh cross-section is guessed to be  $\sigma_{\text{eff}} = 0.95\sigma_{\text{N}_2}$  in order to estimate the Rayleigh temperature. This Rayleigh temperature is then used to determine the elements of the correlation matrix  $\overline{\underline{C}}(T)$ , so that the Raman composition can be evaluated. This

composition is then used to determine the effective Rayleigh cross-section and reevaluate the Rayleigh temperature. The procedure is repeated until the values of successive Rayleigh temperatures differ by less than 1 K (typically 2-3 iterations).

#### 5.3.4. Laser Induced Fluorescence

The number density of OH and NO is obtained by the fluorescence signal  $S_f$  as well as other parameters obtained via the calibration flames (Barlow et al. 1993 and Nguyen et al. 1996).

$$N = \left[ \frac{N}{S_f} \right]_{\text{cal}} \left( \frac{[F_B]_{\text{cal}}}{F_B} \right) \left( \frac{Q}{[Q]_{\text{cal}}} \right) \left( \frac{[g(v_0)]_{\text{cal}}}{g(v_0)} \right) S_f \quad (5.5)$$

All the parameters with subscript “cal” refer to those values obtained from the calibration flame. The calibration procedure will be described in subsequent sections. The laser signal  $S_f$  is normalized by the laser intensity and the other factors are:

1.  $\left[ \frac{N}{S_f} \right]_{\text{cal}}$  = LIF calibration factor, as determined in the calibration procedure.
2.  $\left( \frac{[F_B]_{\text{cal}}}{F_B} \right)$  = Accounts for differences in population levels between test and calibration conditions (temperature), determined by Boltzmann factors.
3.  $\left( \frac{Q}{[Q]_{\text{cal}}} \right)$  = Probe volume to calibration flame ratio of collision electronic quenching rates.
4.  $\left( \frac{[g(v_0)]_{\text{cal}}}{g(v_0)} \right)$  = Accounts for differences due to temperature in the calibration and test flames of the spectral overlaps between laser and selected transitions. This is only applied to NO.

The temperature and composition values needed to determine these factors are supplied by the Raman-Rayleigh data.

#### **5.4. System Calibration**

The Raman-Rayleigh-LIF system acquires signals from several PMTs that integrate photons for specific spectra. This section details the systematic approach of calibrating these interdependent signals.

##### **5.4.1. Background Rayleigh Scattering**

The first step in the calibration process is to determine the amount of background noise in the Rayleigh system. The Hencken burner supplies two conditions to determine the Rayleigh background. These conditions are (1) a pure nitrogen stream and (2) a pure helium stream. The Rayleigh scattering cross-section of helium is 1.33% that of nitrogen. The background (B) is determined by linearly extrapolating the Rayleigh response from these two conditions ( $S_{R,N_2}$  &  $S_{R,He}$ ), as shown below in Figure 5.9. For these ambient temperature conditions, an initial calibration factor ( $C_R$ , Equation 5.1) is determined for the Rayleigh temperature.

##### **5.4.2. Hencken Calibration Flame**

The calibration process utilizes a set of methane-air flat flames to determine the gain for each PMT as well as the required OH LIF calibration factors. The methane-air flames were stabilized on a Hencken burner, and the flame stoichiometry was varied from 0.8 to 1.4.

As stated earlier, there are interdependencies between Raman responses due to signal overlap and cross talk. Therefore, a systematic approach for matching the data to the known values for the calibration flames is required. First, the calibration factors are

adjusted for the  $N_2$ ,  $H_2O$ ,  $H_2$ ,  $CO$ ,  $CO_2$  and  $O_2$  PMTs in that order. Second, the OH calibration factors are adjusted. The calibration factors for these major and minor species, as well as the Rayleigh calibration factor, are adjusted gradually until the best fit occurs. Figure 5.10 shows an example of a calibrated match for the temperature and species. The solid lines are the known values for the flames; the circles denote pre-experiment calibration; and the squares denote the post-experiment calibration.

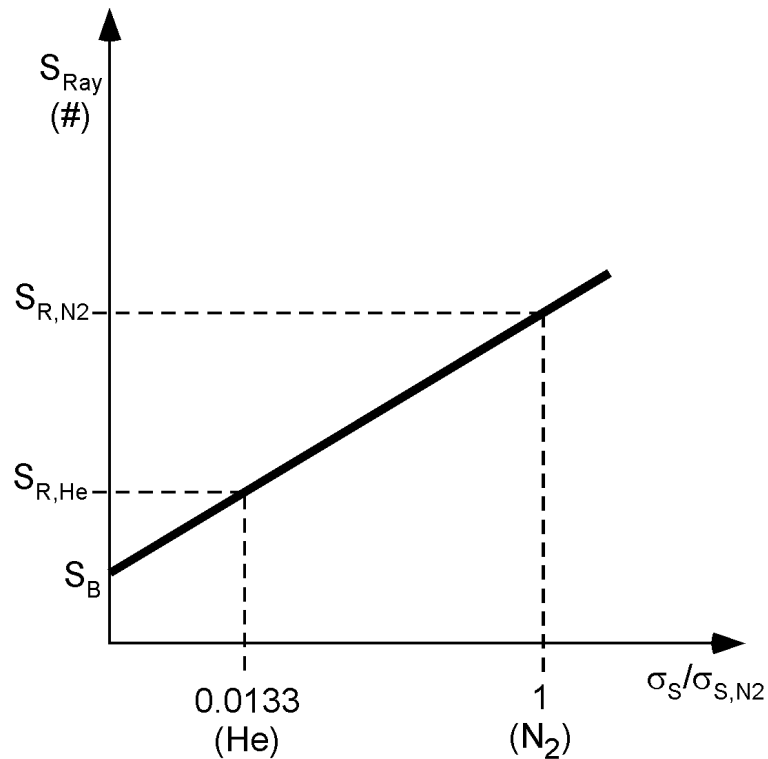


**Figure 5.9.**

Rayleigh background is determined by extrapolation of signals from calibration flows of nitrogen and helium.

Calibration of the Raman response for methane is difficult since methane does not exist in practical experimental conditions at elevated temperatures. More specifically, at higher temperatures, methane usually burns. The methane response must then be calibrated with a flow at ambient temperature. The methane calibration was obtained

using the central jet of the vitiated coflow burner. The nonreacting premixed CH<sub>4</sub>-Air stream was at the same conditions as in the experiments (i.e. 1:3 CH<sub>4</sub> to air, V = 100 m/s). It should be noted that the Raman response is actually an excitation of the of the C-H bond which essentially is common for most hydrocarbons. The Raman signal for C-H is due to all the hydrocarbons in the probe volume. For the conditions studied in the vitiated coflow burner, this effect is negligible in the lean methane flames, and not present in the hydrogen flame.

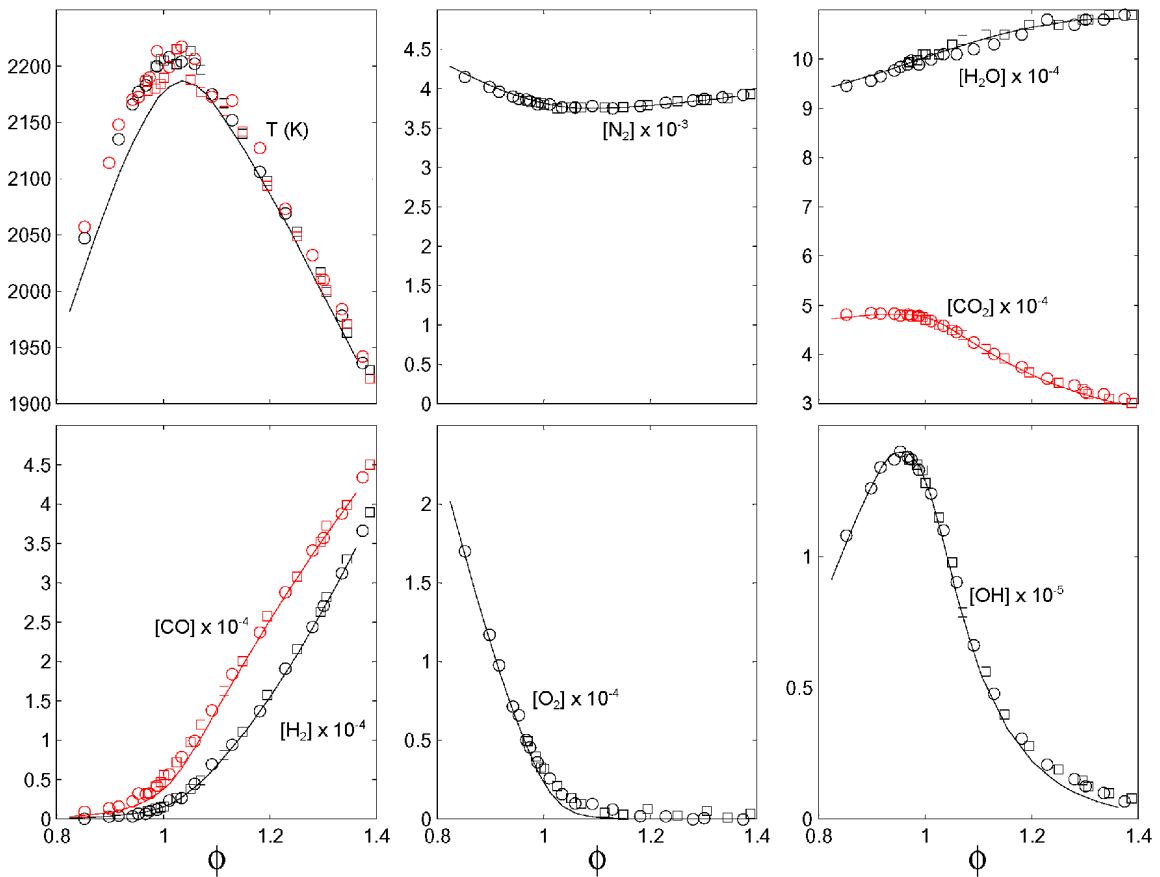


**Figure 5.10.**

Processed mean (normal mean) values of temperature and concentrations in the CH<sub>4</sub>-Air Hencken-burner flames.

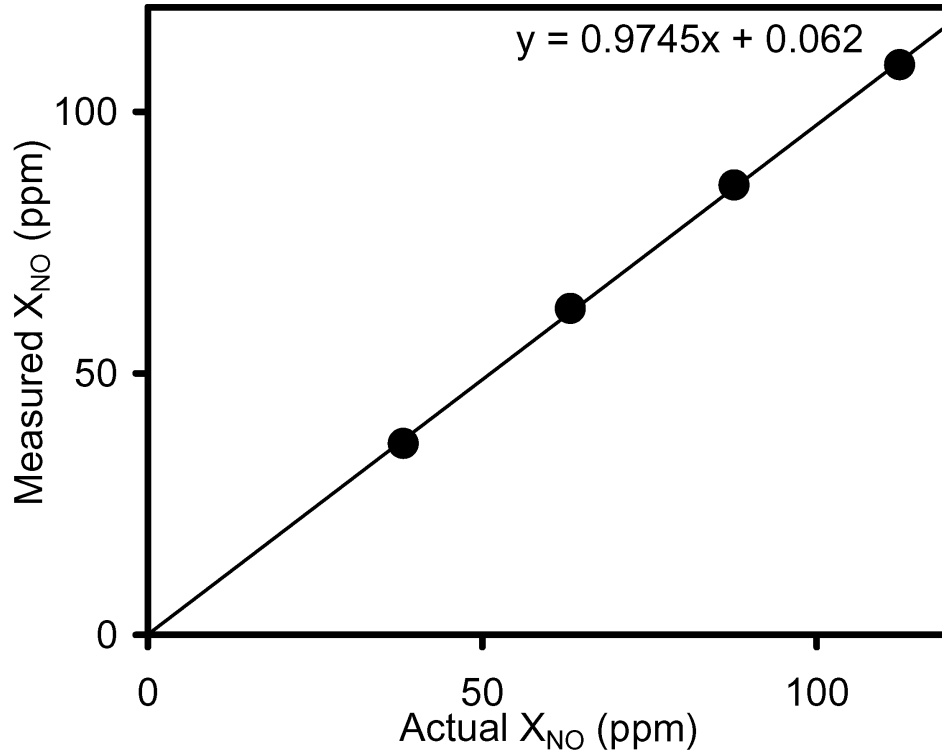


**Figure 5.11.**

Confirmation of NO calibration from flat premixed methane flames where the  $N_2$  is doped with NO. Plotted are the mean values.

### 5.4.3. NO LIF Calibration

Calibration of the NO LIF was different for each case. For the first case studied (methane-air jet), NO was calibrated in the traditional manner. A flat, premixed  $CH_4$ - $O_2$ - $N_2$  flame with a stoichiometry of  $\phi = 0.72$  was used for the NO calibration. Laminar flame calculations show that, for these conditions, doping the  $N_2$  with NO results in negligible changes in NO mass fraction through the flame. For these conditions, the NO is partially converted to  $NO_2$  then back to NO in the reaction zone resulting in no net change. In calibration of the NO LIF, three different conditions are measured. Figure 5.11 below shows the NO calibration results.

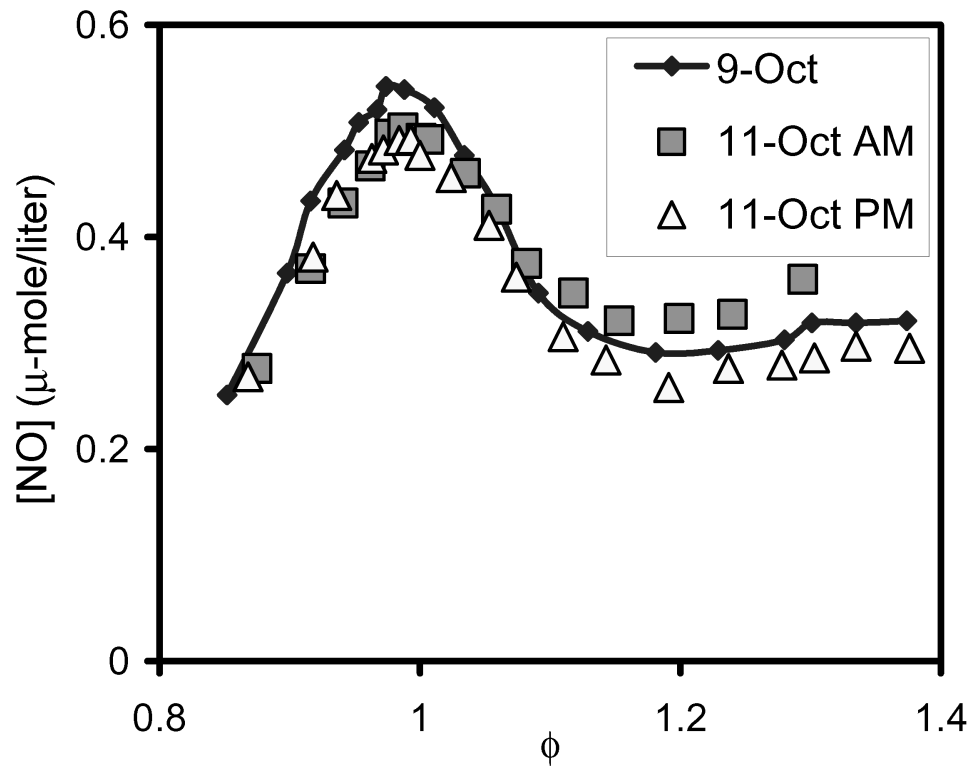


**Figure 5.12.**

NO LIF calibration using Hencken burner flames. Calibrated reference (Oct. 9) and the new calibrations with common calibration factors (Oct. 11 A and B). Plotted is the normal mean data.

Unfortunately, the supply of  $N_2$  doped with NO was exhausted before the hydrogen jet flame experiments. For this experiment, the Hencken calibration flame measurements were used as a rough calibration for these experiments. Figure 5.12 shows the best fit for the NO concentrations from the Hencken flame experiments conducted on October 11, 2000 data (before: AM and after: PM) and October 9. It should be noted that this is only a rough calibration since the levels of NO are at the lower detection limit of the system ( $\approx 1$  ppm). Fortunately, the lower maximum temperature ( $\approx 1500$  K) associated with diluted hydrogen flames will result in lower concentrations of NO and thereby afford the reduced accuracy.

#### 5.4.4. System Uncertainties

The precision and accuracy of the Raman-Rayleigh-LIF system is determined with the use of flat calibration flames (Barlow et al. 2000). The precision of single-shot measurements in a H<sub>2</sub> flame (no fluorescence interferences) is limited by the photoelectron shot noise (Dibble et al. 1987), and it is indicated by the standard deviations (RMS) of the Hencken flame measurement. The standard deviations are: temperature 1%, N<sub>2</sub> 3%, H<sub>2</sub>O 5%, CO<sub>2</sub> 6%, OH 10%, NO 10%, and mixture fraction 6%. Figure 5.13 shows the measurements of a CH<sub>4</sub>/Air Hencken-burner taken prior to the H<sub>2</sub>/N<sub>2</sub> lifted flame experiment. The RMS of the concentration or temperature and the mixture fraction data binds the ellipse that surrounds each point in Figure 5.13.

The accuracy of the experiment is limited by possible systematic errors introduced by the data collection and reduction process. Inaccuracies may exist in the reduction process, specifically when determining the temperature dependent correlation matrix. Calibration data for the correlation matrix exist for low and high temperatures; however, there are some gaps at the intermediate temperatures. The sensitivity of the Raman and LIF responses to temperature are measured using electronic heaters and laminar flame experiments. Gaps exist for the sensitivity of CO<sub>2</sub>, H<sub>2</sub>, CO and OH signals at intermediate temperatures and CH<sub>4</sub> signals at temperatures above 850 K. For these situations, the estimated uncertainties are greater since the correlation factors are either interpolated or extrapolated. The gaps in calibration data used for the correlation matrix (especially for CH<sub>4</sub>) do contribute to the estimated uncertainties for temperature and mixture fraction.

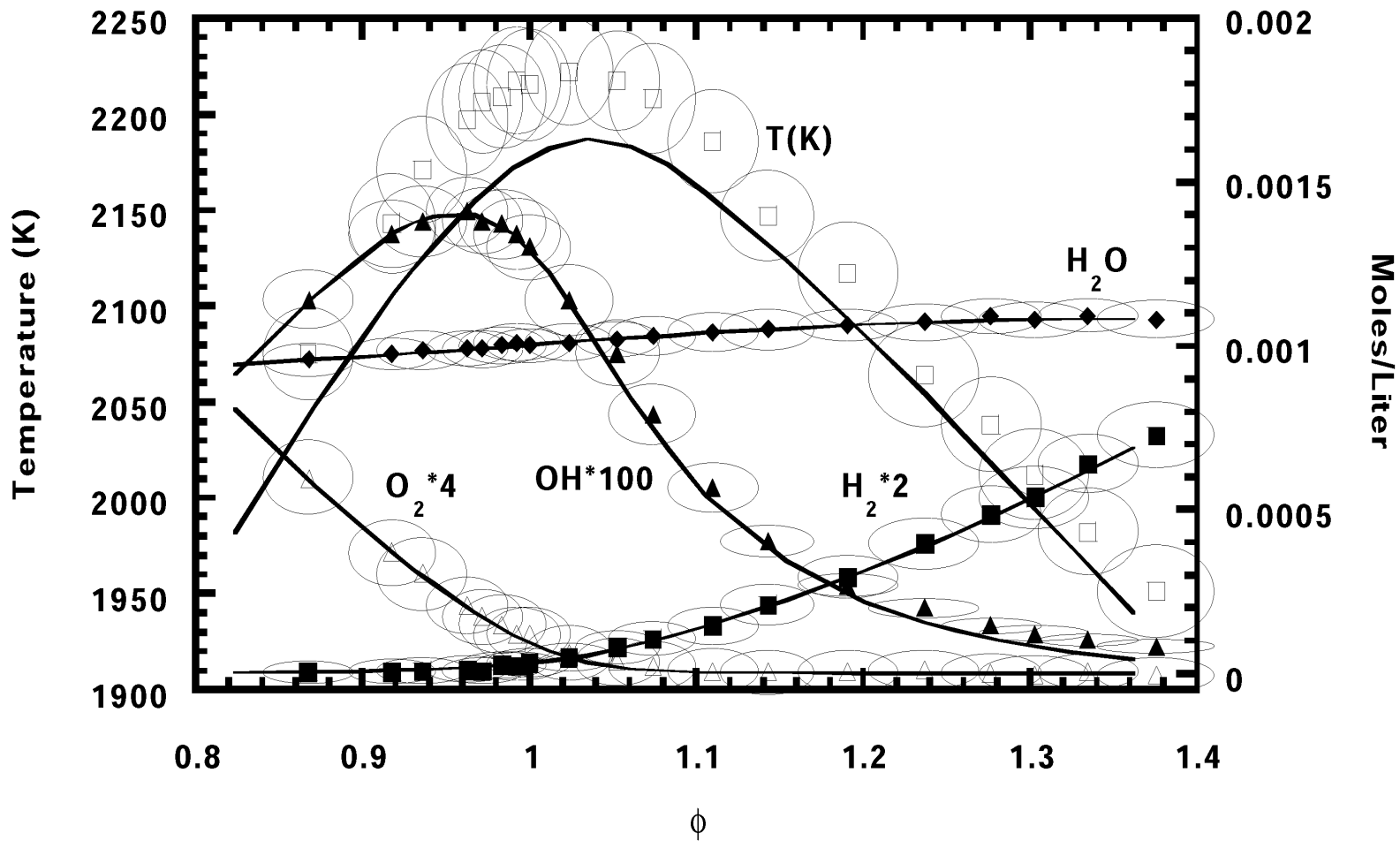


Figure 5.13.

Processed mean values (Normal Mean) of temperature and concentrations in the  $\text{CH}_4$ -Air Hencken-burner flames.

Further systematic uncertainties may arise due to drift in the laser, optical and electronic components. To account for these drifts, the system is calibrated twice daily (before and after each day), as described in the previous sections. Drifts in the optical components, those made of metal and glass, may occur due to thermal loads exerted by radiation heat transfer from the flame, which is a reason why the exit collar is water cooled (see Section 4.3.6).

Uncertainties in Raman signals attributable to interferences from resonant contributions of the laser-induced fluorescence are negligible for the conditions studied. As shown in Figure 5.2, the spectral emission from a lean methane-air flame shows negligible interference. The same is true for the diluted H<sub>2</sub>-N<sub>2</sub> flame. Measurements from the PMTs at 590 nm, 615 nm, and 640 nm consistently show negligible levels of LIF caused interferences throughout the experiment.

Spatial resolution may be an issue since the probe volume has a diameter and length of 750 μm. Research conducted by Brockhinke et al. (1996) show via 1-D laser Raman scattering that temperature gradients in turbulent flames can reach 1100-1350 K/mm. Temperature gradients of this magnitude in the vitiated coflow flames are improbable because (1) the fuel jet flame is immediately surrounded by a high temperature coflow, not cool ambient air, and (2) the vitiated coflow flames are much larger than the flames studied by Brockhinke et al. (1996) and Tacke et al. (1998).

A summary of the estimated uncertainties for the laser Raman-Rayleigh-LIF system is listed in Table 5.2. Detailed documentation of system uncertainties may be found in the literature (Barlow et al. 2000, Nooren 1998 & Nguyen et al. 1996).

**Table 5.2.**

Estimated uncertainties of the laser Raman-Rayleigh-LIF systems (Barlow 2001).

Scalar	Conditions ( $Y$ , $T$ )	Uncertainty	Special conditions	Uncertainty or bias
$T$	2140 K <sup>a</sup>	3%		
$F$	Typical	3%	Rich, $T \approx 1000\text{K}$	-5%
$Y_{N_2}$	0.73, 2140 K <sup>a</sup>	3%		
$Y_{O_2}$	$T > 1000\text{K}$	0.004	Max interference	$\pm 0.006$
$Y_{CH_4}$	Typical	0.005	Rich, $T \approx 1000\text{K}$	-0.008
$Y_{H_2O}$	Typical	4%		
$Y_{CO_2}$	Typical	4%	Max interference	+0.005
$Y_{H_2}$	0.003, 2020 K <sup>b</sup>	10%	Very rich	+10–30%
$Y_{OH}$	0.0016, 2140 K <sup>a</sup>	10%	Peak	-5%
$Y_{CO}$	0.062, 2020 K <sup>b</sup>	10%	Very rich	$\pm 10$ –20%
$Y_{NO}$	lean, 1760 K <sup>c</sup>	15%		

<sup>a</sup> Premixed CH<sub>4</sub>/air,  $\phi = 0.96$ , Hencken burner (uncooled).

<sup>b</sup> Premixed CH<sub>4</sub>/air,  $\phi = 1.27$ , Hencken burner (uncooled).

<sup>c</sup> Premixed CH<sub>4</sub>/O<sub>2</sub>/N<sub>2</sub>,  $\phi = 0.72$ , McKenna burner (cooled).

## Chapter 6

### Simultaneous Multiscalar Point Measurements

Chapter 6 presents results obtained using the systems at the Turbulent Diffusion Flame Laboratory at the Combustion Research Facility of Sandia National Laboratories; these systems were introduced and discussed previously in Chapter 5. Two lifted flames are studied, (1) a jet of hydrogen-nitrogen into a hot coflow and (2) a jet of methane-air into a hot coflow. These two conditions were selected to provide a logical set of data for validation of combustion models. These cases are consistent with pedagogical validation procedures where well-known hydrogen chemical kinetics is first modeled, followed by the increasingly complex hydrocarbon chemical kinetics.

#### 6.1. Lifted Hydrogen Jet Flame

The first experimental conditions studied with the laser Raman-Rayleigh-LIF system consisted of hydrogen chemistry only. This condition is meant to be an first step toward model development of the hydrocarbon chemistry flow. The following sections outline the flame conditions, TDF experimental results, and then some comparisons with the EDC and PDF combustion models.

##### 6.1.1. Hydrogen Flame Conditions

Experiments were conducted on a lifted turbulent  $H_2/N_2$  jet flame into a hot vitiated coflow as shown in Figure 6.1. The combustor consists of a central  $H_2/N_2$  turbulent jet with a coaxial flow of hot combustion products from a lean premixed  $H_2/Air$

flame. For the conditions listed in Table 6.1, the observed lift-off height was  $H/d \cong 10$ , and the total flame length was  $H_F/d = 30$  (nozzle diameter is  $d = 4.57$  mm).

Peak temperatures in the flow were not high enough (1600 K) to facilitate significant levels of NO chemical kinetics. Consequently, the NO concentrations were consistently low ( $Y_{NO} < 3$  ppm) with high levels of noise because the signals were near the detection limit of the NO LIF system (1 ppm). Therefore, the NO results will not be presented.

**Table 6.1.**

H<sub>2</sub>/N<sub>2</sub> experimental conditions.

Central Jet		Coflow	
Q <sub>H2</sub> (slm)	25	Q <sub>H2</sub> (slm)	225
Q <sub>N2</sub> (slm)	75	Q <sub>AIR</sub> (slm)	2,100
T <sub>JET</sub> (K)	305	T <sub>COFLOW</sub> (K)	1,045
V <sub>JET</sub> (m/s)	107	V <sub>COFLOW</sub> (m/s)	3.5
Re <sub>JET</sub>	23,600	Re <sub>COFLOW</sub>	18,600
d <sub>JET</sub> (mm)	4.57	D <sub>COFLOW</sub> (mm)	210
		ϕ	0.25
X <sub>H2</sub>	0.25	X <sub>O2</sub>	0.15
X <sub>N2</sub>	0.74	X <sub>H2O</sub>	0.099
		X <sub>N2</sub>	0.75

Q: volumetric flow rate; X: mole fraction; Re: Reynolds number; d and D: diameter; ϕ: equivalence ratio.

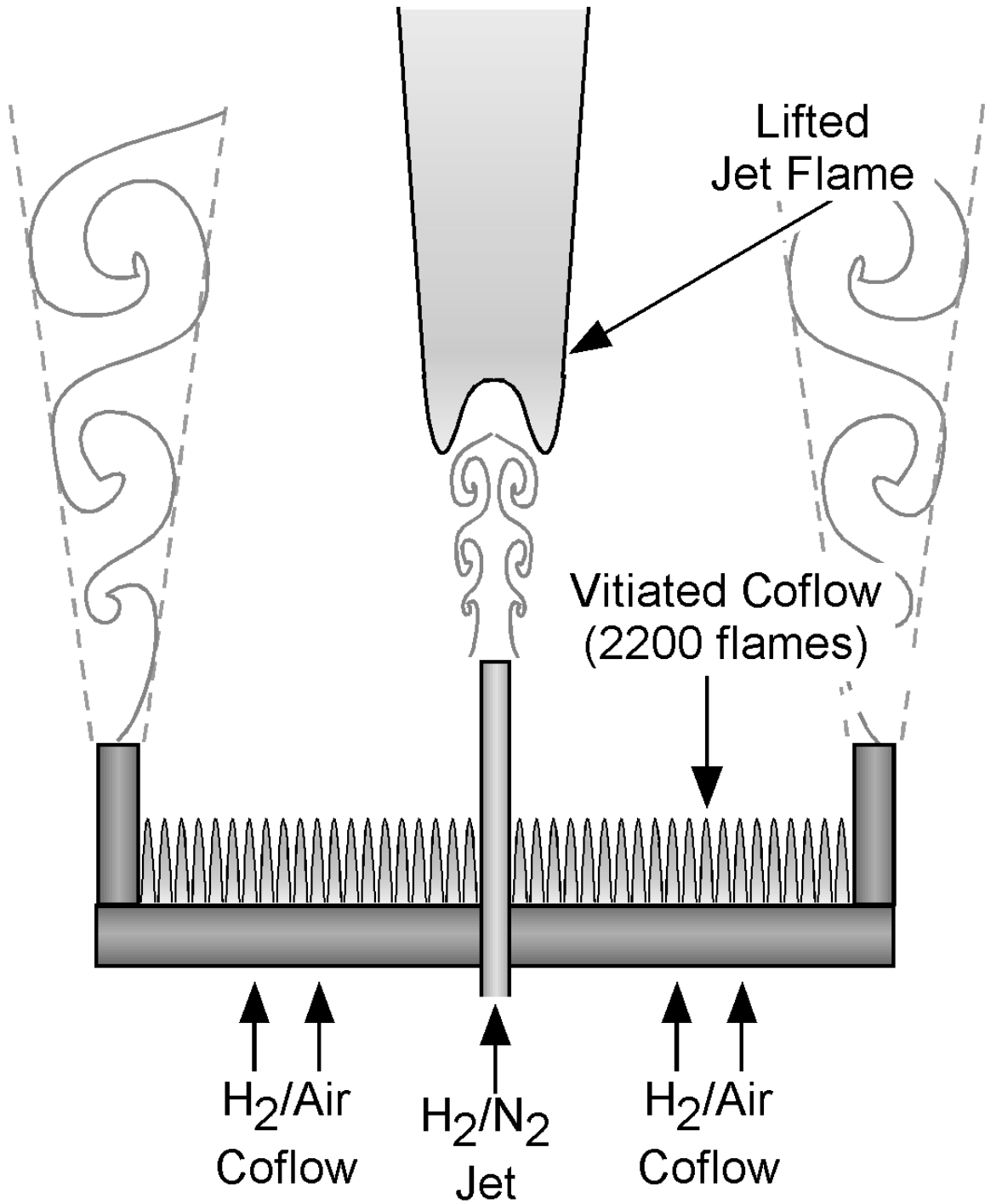


**Figure 6.1.**

Schematic of the lifted H<sub>2</sub>/N<sub>2</sub> jet flame into a coflow of hot products from a lean H<sub>2</sub>/Air flame. The lift-off height of the flame is  $H/d = 10$  ( $d = 4.57$  mm). See Table 1 for additional flame information.

### 6.1.2. Experimental Region

The structure of the lifted turbulent H<sub>2</sub>/N<sub>2</sub> jet flame is investigated by examining the measured temperature and species concentration profiles. Centerline measurements were taken from z/d=1 to 34 downstream of the nozzle exit. Radial profiles were obtained at several axial locations (z/d=1, 8, 9, 10, 11, 14 and 26). The radial domain covered by these profiles was -3 mm to 50 mm, with spacing typically between 1 and 3mm. Figure 6.2 shows the measurement locations for the hydrogen flame. The single-shot data was processed and the Favre averages and RMS fluctuations were generated. The following formulation, modified for the current H<sub>2</sub>/N<sub>2</sub> system, determines the mixture fraction (Bilger et al. 1990).

$$f = \frac{(1/2M_H)(Y_H - Y_{H,2}) - (1/M_O)(Y_O - Y_{O,2})}{(1/2M_H)(Y_{H,1} - Y_{H,2}) - (1/M_O)(Y_{O,1} - Y_{O,2})} \quad (6.1)$$

Where Y is the elemental mass fraction and M is the atomic weight. Subscript 1 denotes the fuel stream and subscript 2 denotes the oxidizer stream. The elemental mass fractions at the boundary conditions are derived from the compositions listed in Table 6.1. The stoichiometric mixture fraction for these boundary conditions is  $f_S = 0.47$ .

### 6.1.3. Well-Defined Boundary Conditions

The radial profiles attest to the success of the experimental design in providing a uniform vitiated coflow. The radial profiles of temperature and oxygen mole fraction at z/d = 1 shown in Figure 6.3 exhibit upside-down “top hat” profiles with uniform, steady (2% RMS) jet and coflow conditions. This 2% RMS is on the order of the photoelectronic shot noise as discussed in the previous sections and shown in Table 5.2.

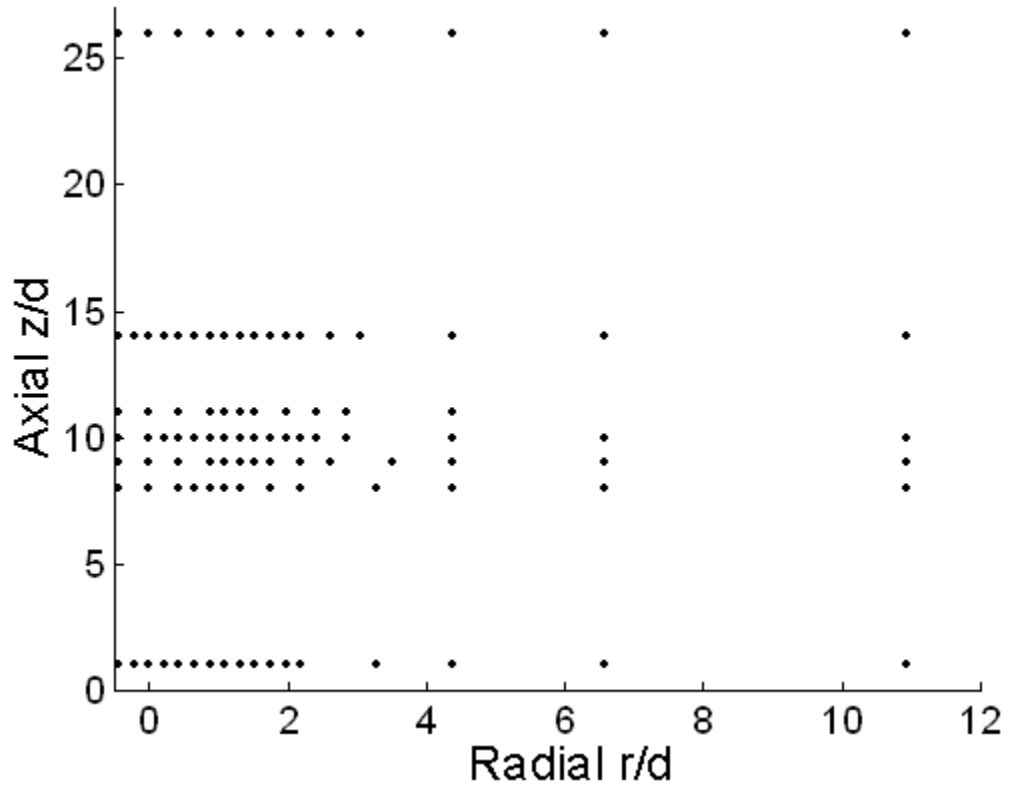


**Figure 6.2.**

Location of measurement points. The horizontal axis is expanded, and the nozzle diameter is  $d = 4.57$  mm.

The uniform coflow condition can be extended in the axial direction for these conditions. Figure 6.4 shows the evolution of the Favre averaged temperature and species concentration profiles with increased distance downstream of the nozzle exit. The results show that for each measurement, the far-field (coflow) measurements do not change with axial distance. Thus, the integrity of the coflow is maintained in the entire test region. These results demonstrate that the flame can be modeled as a two-stream flow consisting of a jet flame issuing into an infinite hot coflow.

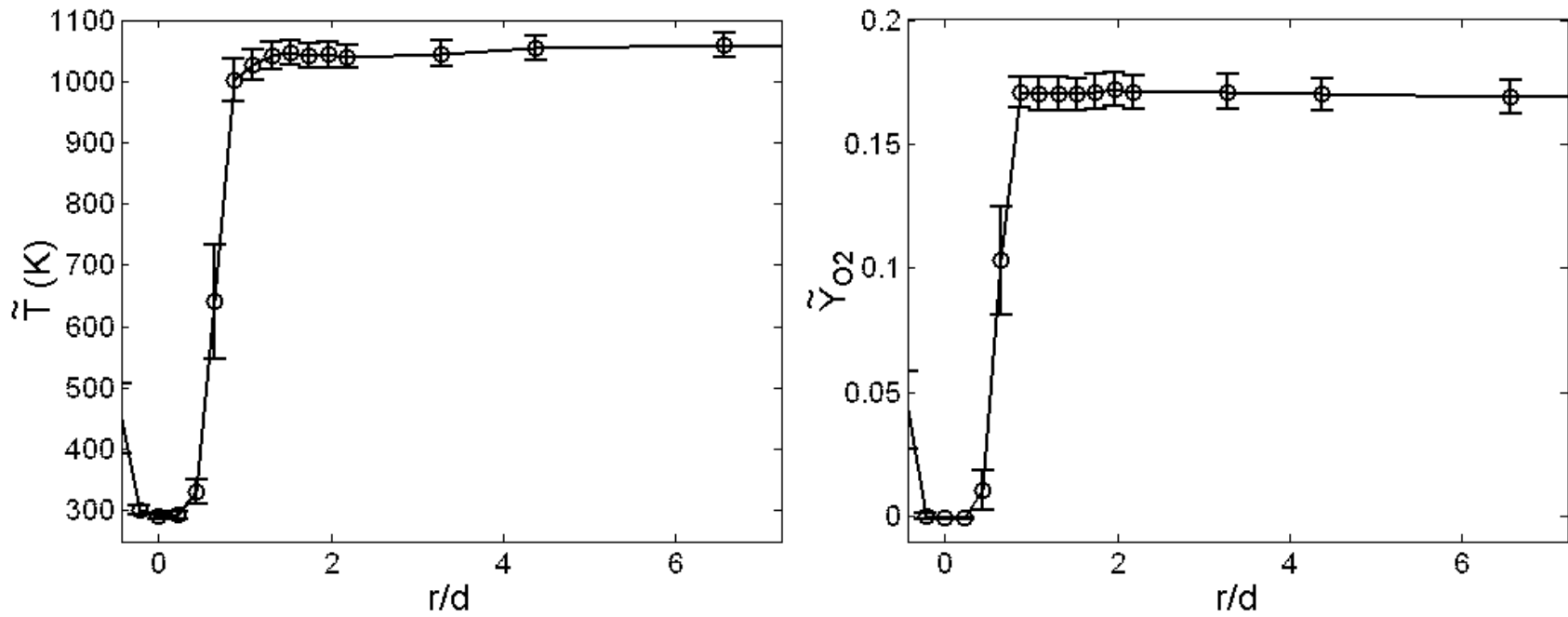


**Figure 6.3.**

Uniform and steady inlet conditions (the jet has yet to ignite). Radial profiles for temperature and oxygen mole fraction at  $z/d = 1$  for the lifted  $H_2/N_2$  jet flame into a vitiated coflow. The plotted symbols denote the Favre average while the error bars denote the associated variance.

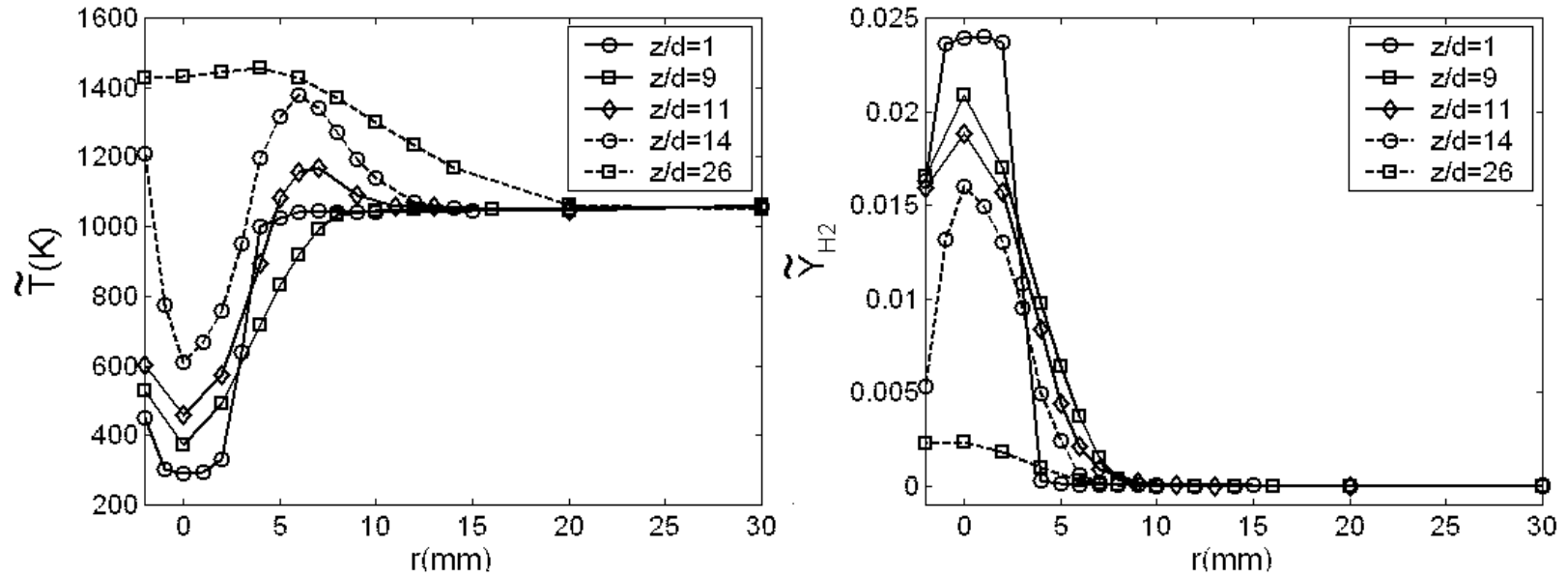


**Figure 6.4A.**

Radial distributions of temperature and hydrogen mass fraction for the  $H_2/N_2$  jet flame into a vitiated coflow. Plots show the evolution of radial profiles for the Favre averaged temperature and hydrogen mass fraction with increased axial distance from the nozzle exit.

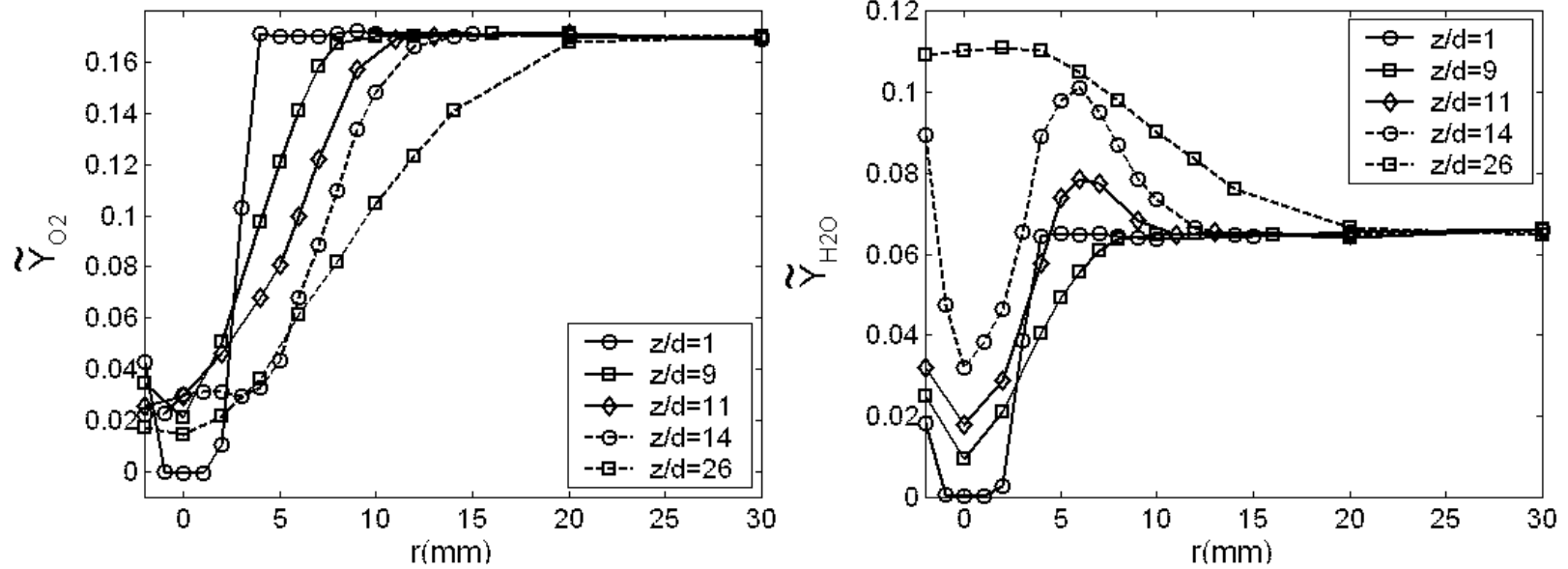


**Figure 6.4B.**

Radial distributions of oxygen and water mass fraction for the  $H_2/N_2$  jet flame into a vitiated coflow. Plots show the evolution of radial profiles for the Favre averaged oxygen and water mass fraction with increased axial distance from the nozzle exit.

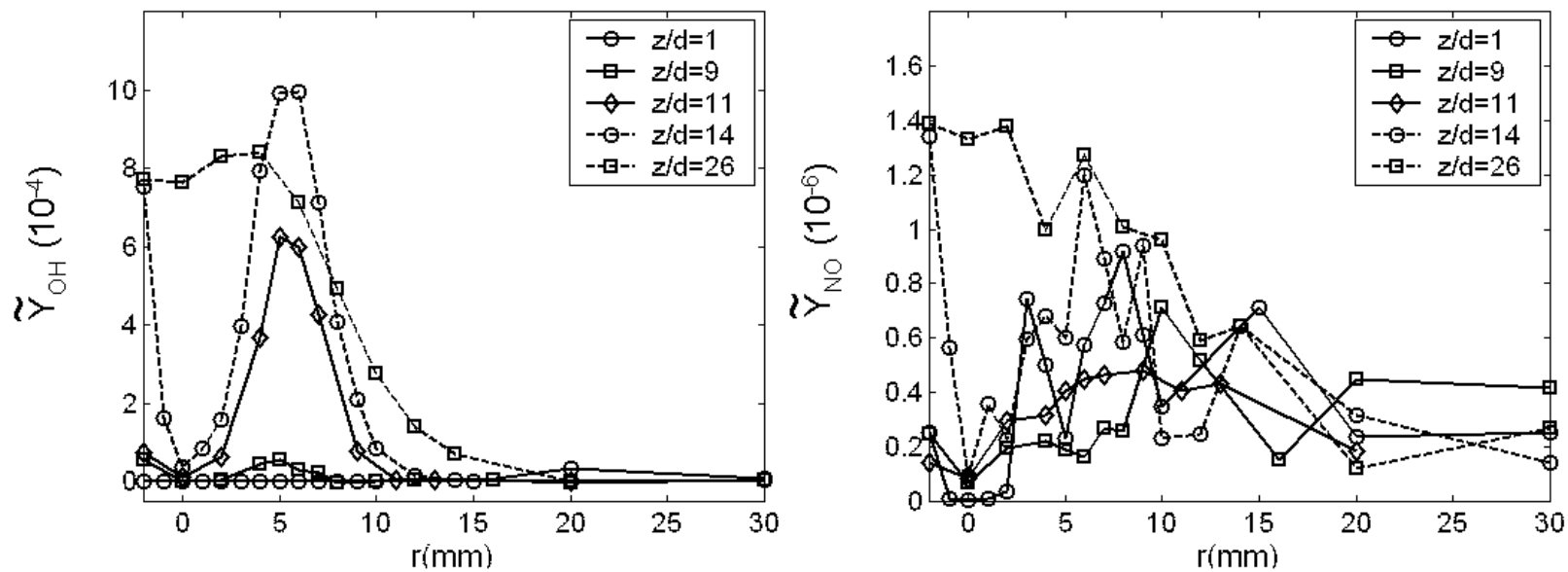


**Figure 6.4C.**

Radial distributions of OH and NO mass fraction for the H<sub>2</sub>/N<sub>2</sub> jet flame into a vitiated coflow. Plots show the evolution of radial profiles for the Favre averaged OH and NO mass fraction with increased axial distance from the nozzle exit.

#### 6.1.4. Flame Structure

The OH mass fraction  $Y_{OH}$  is used as a marker of the flame structure, and the average flame lift-off height. The reaction zone was taken to be the region where the Favre averaged OH mass fraction exceeded 600 ppm. Figure 6.5A shows a contour map generated using an aggregate of the point measurements (white dots) for the experimental conditions. More specifically, Matlab was used to interpolate the surface between adjacent points. The resolution is rather coarse; however, several points were taken in the flame stabilization region to provide adequate resolution for determination of the lift-off height,  $H/d \approx 10$ . Also plotted with the experimental conditions are the numerical model results conducted by Mr. Tore Myhrvold (EDC) and Dr. J.Y. Chen (PDF) that were introduced in Chapter 3.

The numerical models each predict a lifted flame structure, which is a significant result in itself, regardless of the accuracy of the predicted lift-off height. It was not obvious, a priori, that the PDF model would predict a lifted flame, because the present calculation proceeds in a downstream marching solution and includes no explicit mechanism for propagation of a turbulent premixed or partially premixed flame into the convecting flow. However, it is apparent from Figure 6.5B that there is reaction progress for some fraction of the PDF particles well upstream of the flame stabilization location at the  $Y_{OH} = 600$  ppm contour. We associate this result with auto-ignition of mixed fluid, a process that would not occur with a cold air coflow. There were no visually obvious auto-ignition events well below the lift-off height; autoignition may have been revealed with additional multiscale point measurements taken at intermediate axial locations ( $1 < z/d < 8$ ). However, the flame does spontaneously ignite in the laboratory, starting at a far

downstream location (at  $z = 3$  m, or  $z/d = 660$ ), when the coflow is operating and jet flow is turned on. The possibility of downstream auto-ignition leading to flame stabilization in both (1) the experiment, and (2) the PDF model, is worthy of further exploration.

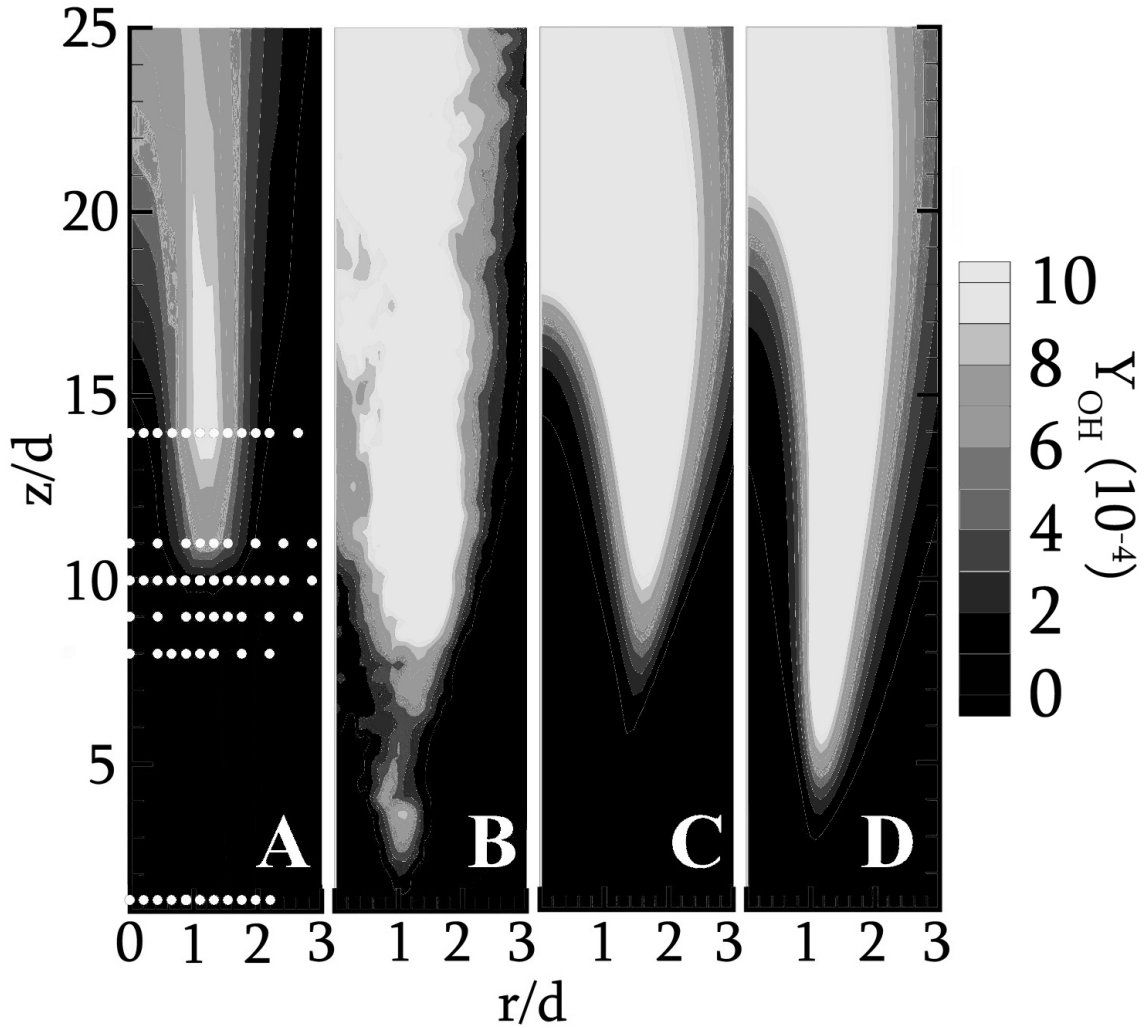


**Figure 6.5.**

Flame structure is represented by the OH mass fraction fields. Presented are experimental results (A), PDF combustion with standard  $k-\epsilon$  turbulence model (B), EDC combustion with  $k-\epsilon$  turbulence model (C) and EDC combustion with LRR Reynolds stress model (D). The white dots in plot (A) denote the locations of the laser based multiscale measurements.

Results from three numerical simulations are shown. Figure 6.5B shows the OH contours from the PDF combustion model and the standard  $k-\varepsilon$  model, which yields a lift-off height of  $H_{PDF}/d=7$ . Using the same  $k-\varepsilon$  model, the EDC model predicts  $H_{EDC}/d=8.5$ , as shown in Figure 6.5C. The standard  $k-\varepsilon$  model is known to overestimate the turbulent diffusivity and, consequently, overpredict the spreading rate of round jets. This may account for the wide flame predictions in these two calculations (Figures 6.5B and 6.5C) relative to the experimental results (Figure 6.5A). The third simulation, using the EDC model and the LRR Reynolds stress model, predicted a shorter lift-off height of  $H_{LRR}/d=5$  (Figure 6.5D). The overall flame shape is narrower than that predicted by the standard  $k-\varepsilon$  model and in better agreement with the measured flame width, even though the lift-off height is under predicted.

#### **6.1.5. Centerline Profiles**

The centerline profiles ( $r = 0$ ) provide some information on the evolution of the flow. Figure 6.6 shows the evolution of the Favre averaged temperature and species concentration profiles along the centerline. Of particular interest is the centerline profile of the Favre average oxygen mass fraction. The centerline ( $r = 0$ ) peak in oxygen seen near  $z/d \approx 14$  illustrates the upstream penetration (increased with lift-off height) and subsequent consumption of oxygen by the flame. By presenting an entrainment rate profile similar to the  $Y_{O_2}$  centerline profile, Han and Mungal (2001) observed a similar correlation between mixing and lift-off height.

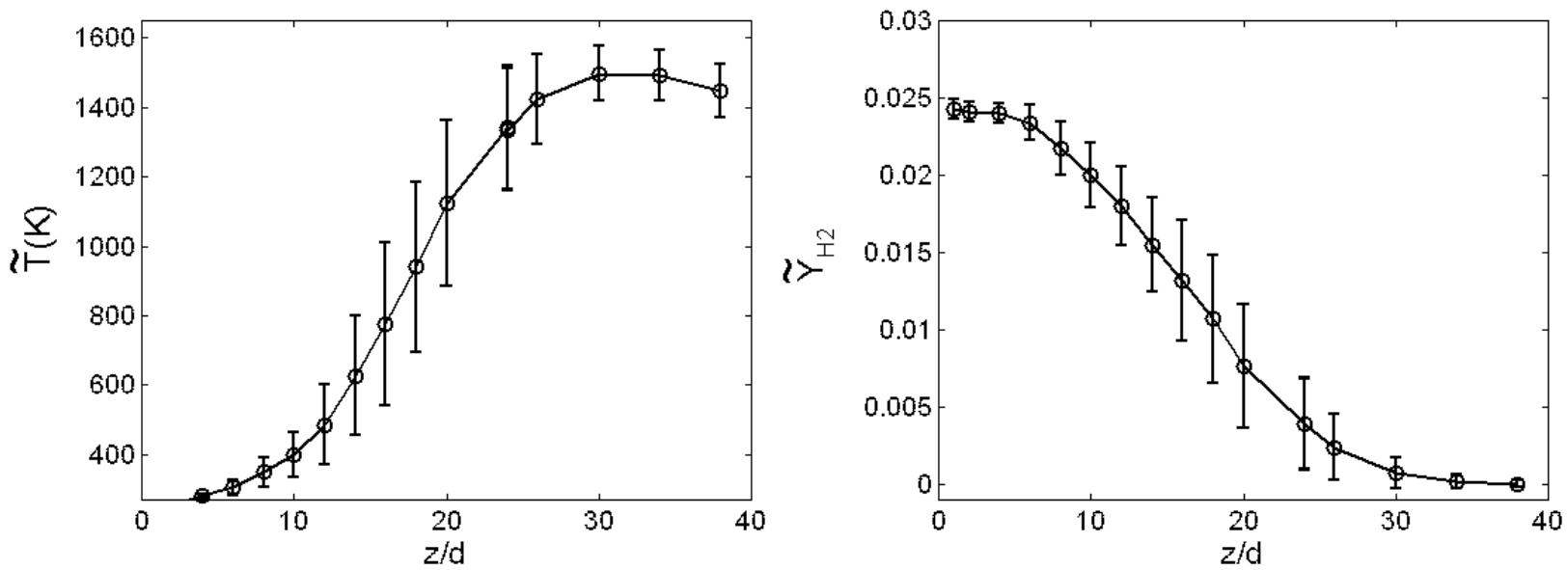


**Figure 6.6.A.**

Centerline profiles of temperature and  $H_2$  mass fraction measurements. Error bars denote the signal RMS.

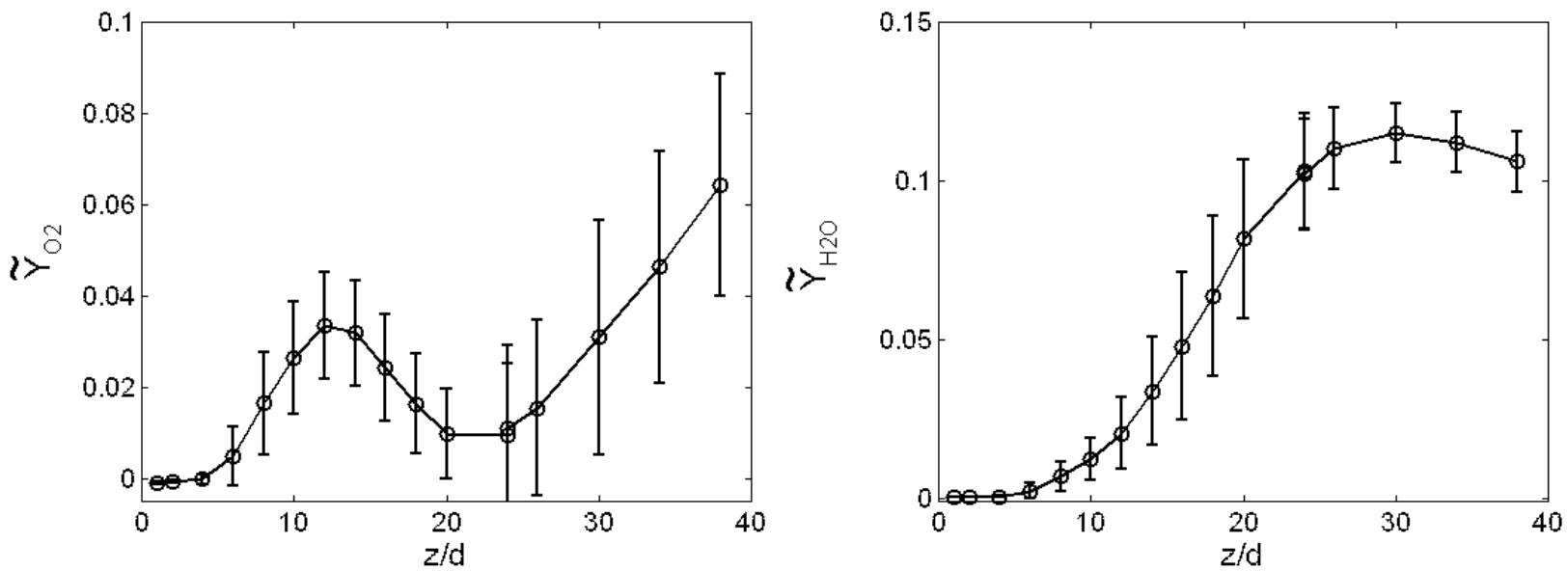


**Figure 6.6.B.**

Centerline profiles of  $O_2$  and  $H_2O$  mass fraction measurements. Error bars denote the signal RMS.

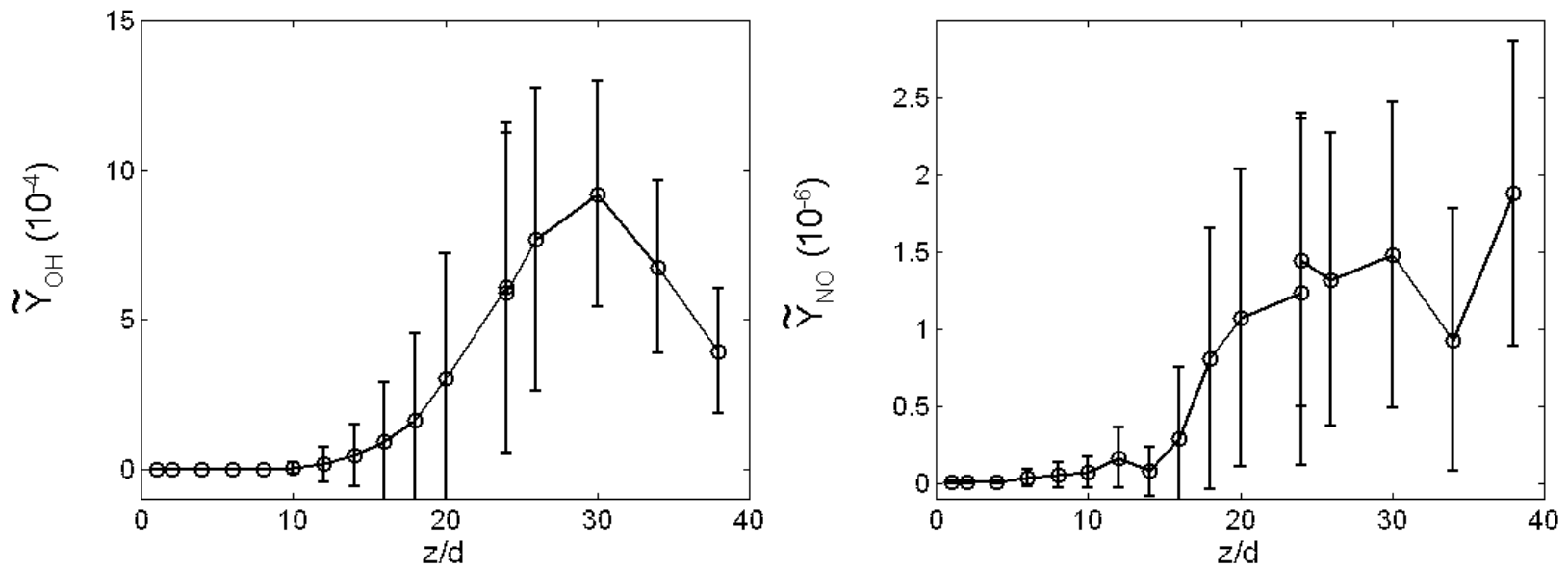


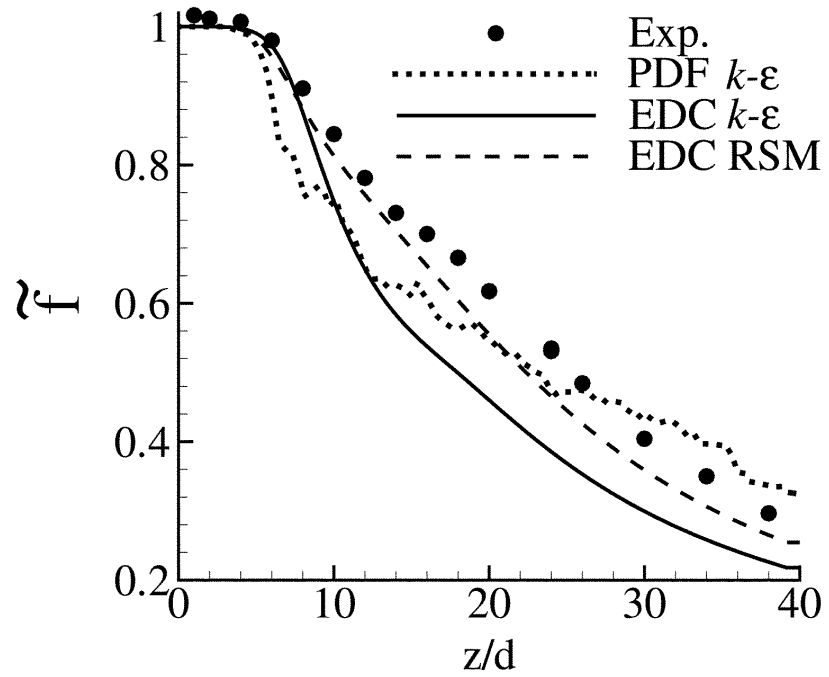
**Figure 6.6.C.**

Centerline profiles of OH and NO mass fraction measurements. Error bars denote the signal RMS.

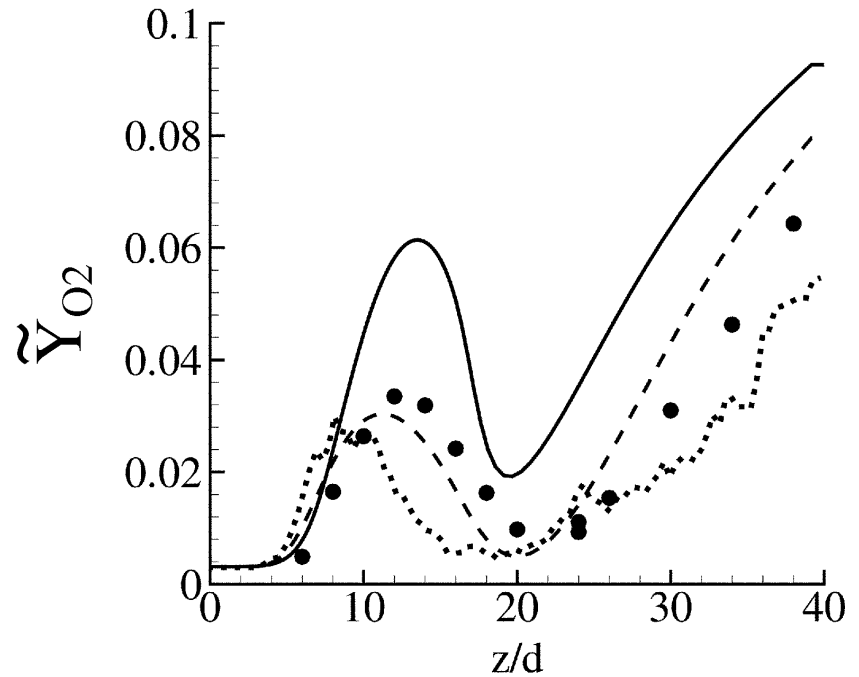
The centerline profiles of oxygen and mixture fraction measurements provide another means to test numerical models. Comparisons of the combustion model results with the experimental results are shown in Figure 6.7. Since the standard  $k-\varepsilon$  model over-predicts turbulent diffusion for round jets, the predicted oxygen penetration is higher than the experimental results, as evident by the early in location ( $z/d = 8$ , PDF) or high in magnitude ( $Y_{O_2} = 0.06$ , EDC) centerline peaks in  $Y_{O_2}$ . The centerline profiles of mixture fraction exhibit more rapid decay because of the over-prediction of mixing. While the lift-off height predicted by the EDC with the Reynolds stress model is low, both predicted centerline profiles agree well with the data. Therefore, while the centerline profiles do exhibit the key molecular mixing and chemical kinetic features of the flame, they should be used in conjunction with other validation metrics.

#### **6.1.6. Combustion Statistics of Probe-Volume Conditions**

Joint statistics of the turbulence-chemistry interaction are obtained by use of scatter plots of the entire data set. Of interest is the stabilization region, as well as the data obtained at the highest axial location. The evolution of the flow conditions through the stabilization region and beyond is shown by the scatter plots in Figure 6.8. Presented is the series of scatter data of temperature and OH mole fraction vs. mixture fraction. For each axial location ( $z/d = 8, 11, 14, 26$ ), approximately 4,000 point measurements from different radial positions were grouped together to form a probability density map. There is a clear progression from a predominantly mixing condition ( $z/d = 8$ ) to vigorous flame burning ( $z/d = 14$ ) that corresponds to the transition from mixing only to mixing combined with ignition and flame stabilization.



(A)



(B)

**Figure 6.7.**

Axial profiles of the mixture fraction and oxygen mass fraction. Presented are Favre averaged experimental results (solid circles), PDF combustion with  $k-\epsilon$  turbulence model (dotted line), EDC combustion with  $k-\epsilon$  turbulence model (solid line), and EDC combustion with LRR Reynolds stress model (dashed line).

Since the flame is not attached to the nozzle, the central fuel jet entrains hot oxidizer from the coflow, evolving into a premixed flow with fluid temperatures corresponding to the mixing line between the jet and coflow boundary conditions in Figure 6.8 ( $z/d = 8$ ). Beyond the potential core of the jet there is progressive dilution of the mixture fraction, such that at the fuel-rich boundary condition for combustion at  $z/d = 14$ , the mixture fraction has decreased from  $f = 1.0$  to values between  $f \sim 0.9$  and  $f \sim 0.6$ . Also plotted in Figure 6.8 ( $z/d = 14$ ) are the results from a series of laminar opposed flow flame calculations (with equal molecular and thermal diffusivities). Corresponding calculations with full transport (i.e. with differential diffusion included) poorly matched the data, suggesting that turbulent stirring is more important than differential molecular diffusion in determining the relative mass fractions of major species in the measured flame. Further discussion on differential diffusion will be included in the following Section 6.1.7. The fuel side boundary condition for the laminar flame calculations was set at  $f = 0.8$ , to represent this measured departure from the initial jet composition.

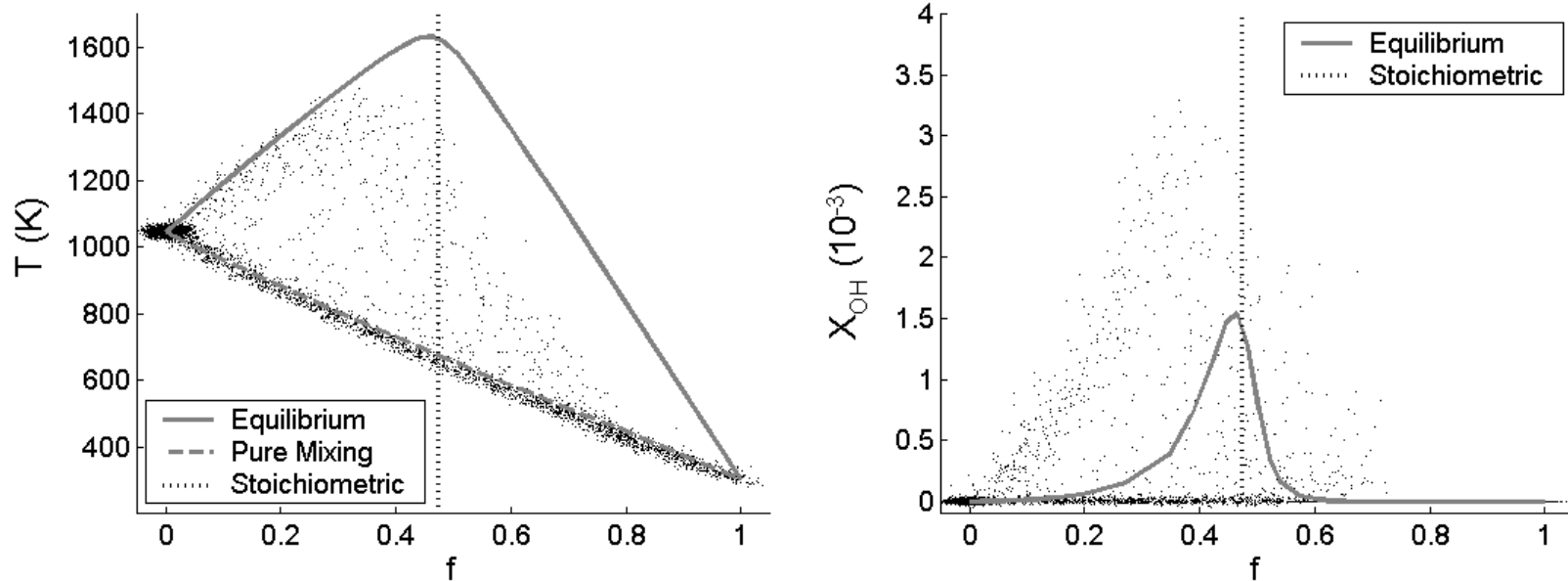


**Figure 6.8A.**

Scatter plots of temperature and OH mole fraction at  $z/d = 8$  ( $d = 4.57$  mm). Also plotted are laminar flamelet calculation results of various strain rates, the equilibrium, unstrained flamelet result and the pure mixing (frozen) condition.

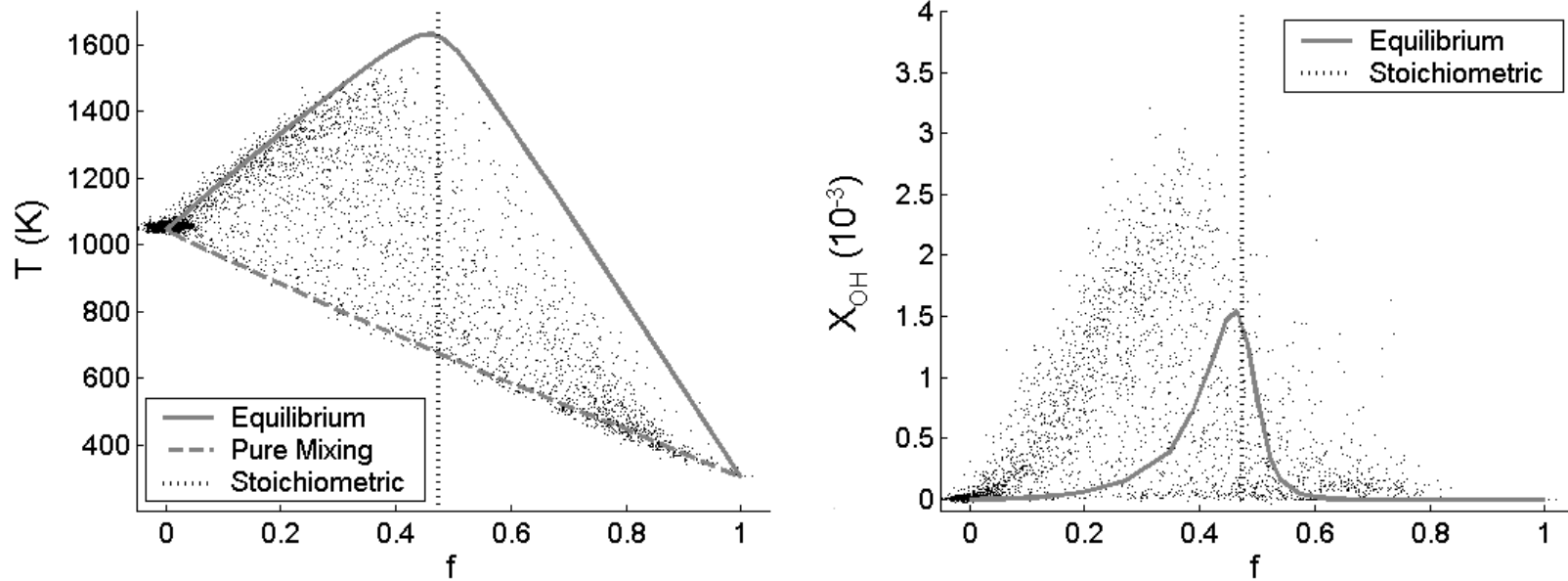


**Figure 6.8B.**

Scatter plots of temperature and OH mole fraction at  $z/d = 11$  ( $d = 4.57$  mm). Also plotted are laminar flamelet calculation results of various strain rates, the equilibrium, unstrained flamelet result and the pure mixing (frozen) condition.

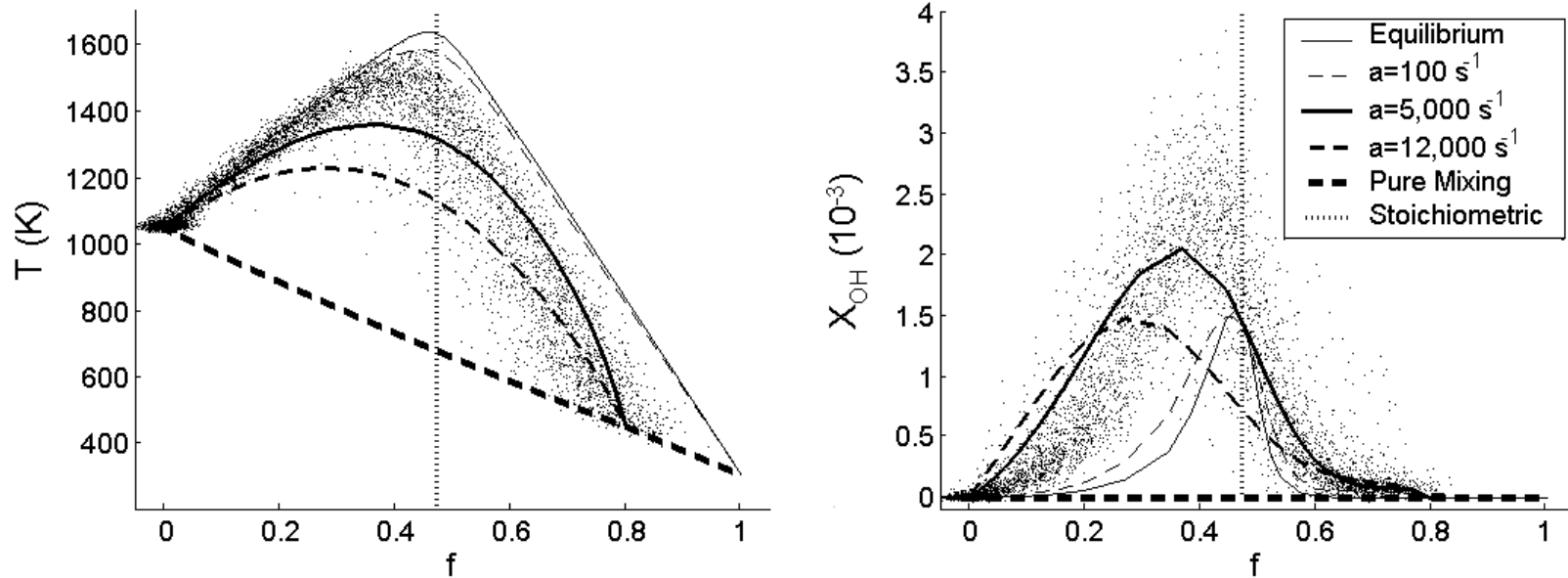


**Figure 6.8C.**

Scatter plots of temperature and OH mole fraction at  $z/d = 14$  ( $d = 4.57$  mm). Also plotted are laminar flamelet calculation results of various strain rates, the equilibrium, unstrained flamelet result and the pure mixing (frozen) condition.

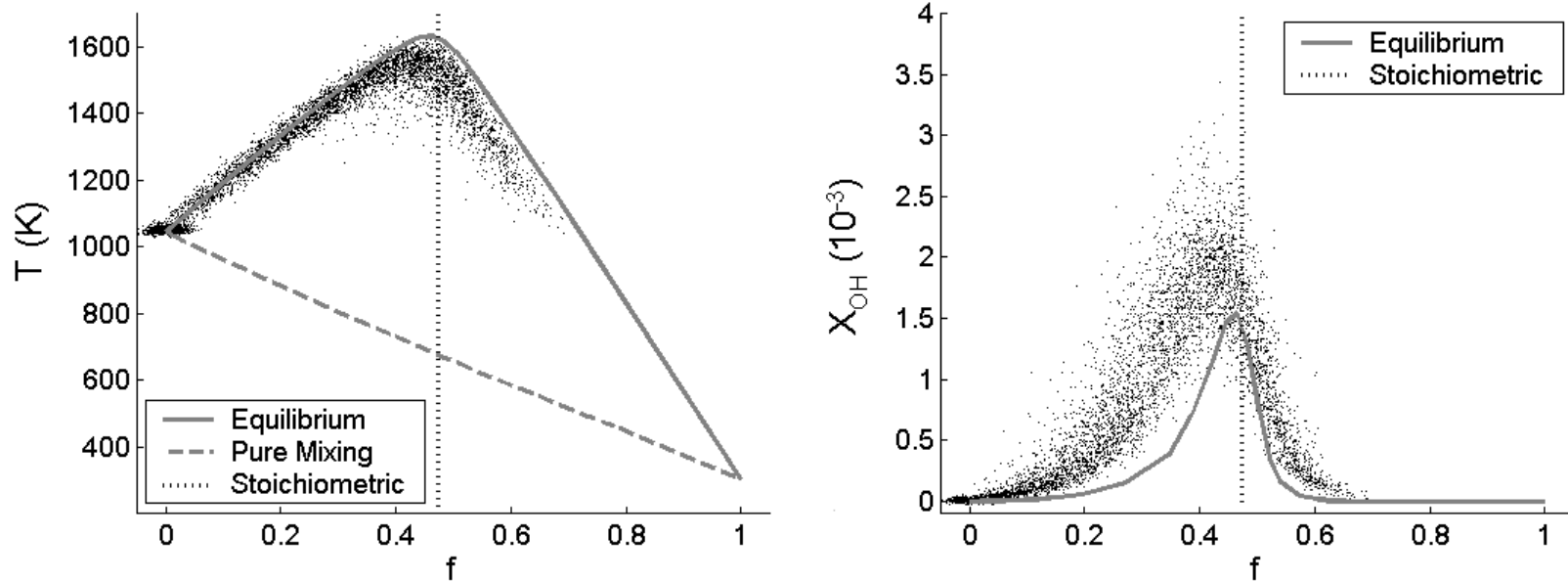


**Figure 6.8D.**

Scatter plots of temperature and OH mole fraction at  $z/d = 26$  ( $d = 4.57$  mm). Also plotted are laminar flamelet calculation results of various strain rates, the equilibrium, unstrained flamelet result and the pure mixing (frozen) condition.

The range of scalar dissipation rates in the turbulent flame above the stabilization region can be estimated by determining the strain rates whose corresponding opposed flow laminar flame solutions match the upper and lower bounds of the laser shot measurements, particularly on the fuel-lean side. In Figure 6.8 ( $z/d = 14$ ), the laser shot data is approximately bounded by solutions with strain rates of  $100\text{s}^{-1}$  and  $5,000\text{s}^{-1}$ . The computed strain rate prior to laminar flame extinction was  $13,000\text{s}^{-1}$ , and a number of data points are below the  $5,000\text{s}^{-1}$  solution. The low strain rate calculations adequately describe the lean side results as expected, since these results correspond to the hot coflow where low strain should prevail and where viscosity is still relatively high. The rich-side experimental results cannot be adequately represented by this limited set of laminar flame calculations because of the broad range of fuel-side boundary conditions produced by mixing upstream of the reaction zone.

Also shown in Figure 6.8 is the depression of the maximum flame temperatures at higher strain rates. The strain rates are higher upstream in the stabilization region. This high strain results in sharper concentration gradients, and correspondingly greater temperature gradients. While reaction rates increase with increased strain, the higher heat dissipation resulting from steeper temperature gradients is enough to depress the maximum temperatures. The relaxation of the strain rates downstream ( $z/d = 26$ ) is identifiable by the increase in maximum temperatures. This suppression in the flame temperatures results in super-equilibrium concentrations of the radical OH. As the temperature increases, the levels of OH approach the equilibrium levels. This is consistent with the results shown by Cheng et al. (1992).

Perhaps the most interesting condition can be seen in Figure 6.8B ( $z/d = 11$ ), where the data are scattered throughout the envelope bounded by the mixing (lower) and fast chemistry (upper) limits on temperature. This axial position ( $z/d = 11$ ) is one diameter above the observed lift-off height. The behavior of the scatter data in Figure 6.8 ( $z/d = 11$ ) is qualitatively different from that reported for lifted  $H_2$  jet flames into cold air (Barlow et al. 1989, Cheng et al. 1992, Brockhinke et al. 1995), where there is clear bimodality between unreacted and reacted samples in the region of flame stabilization. The non-bimodal distribution of instantaneous temperature (Figure 6.8B) suggests a distributed reaction mode of turbulent premixed combustion (Bray 1980, Glassman 1996). This specific mode of turbulent premixed combustion (i.e., the distributed reaction mode) may be an additional stabilization mechanism for lifted flames. Mansour et al. (1999) also reported numerical and experimental results showing near-monomodal distributions at the base of an attached turbulent premixed flame in a large pilot. Further discussion of flame stabilization will follow in Chapter 9.

#### **6.1.7. Negligible Differential Diffusion Effects**

Differences in the molecular mass of hydrogen and nitrogen present differential diffusion in these conditions. As discussed earlier, all scalar measurements, particularly in the scatter plots, are referenced in terms of the Bilger formulation of mixture fraction (Bilger 1990). Although use of this formulation is widely accepted, the possible impact on the measurements by differential diffusion should be examined.

Comparisons on a shot-by-shot basis were made of the mixture fraction formulations based on elemental hydrogen and oxygen. The mixture fraction based on

element J is determined based on the elemental mass fraction Z in the probe volume and boundary conditions.

$$f_J = \frac{Z_J - Z_{J,2}}{Z_{J,1} - Z_{J,2}} \quad (6.2)$$

These mixture fraction formulations are compared in Figure 6.9. In fact, there is atomic hydrogen in both the fuel stream and the oxidizer stream (water vapor) with the undesirable consequence that the difference in elemental hydrogen concentration between the fuel and oxidizer streams is small. As a consequence, there are significant levels of noise in the hydrogen based mixture fraction. With this caveat, overall comparisons of the mixture fractions show no discernable variation that could be attributed to differential diffusion.

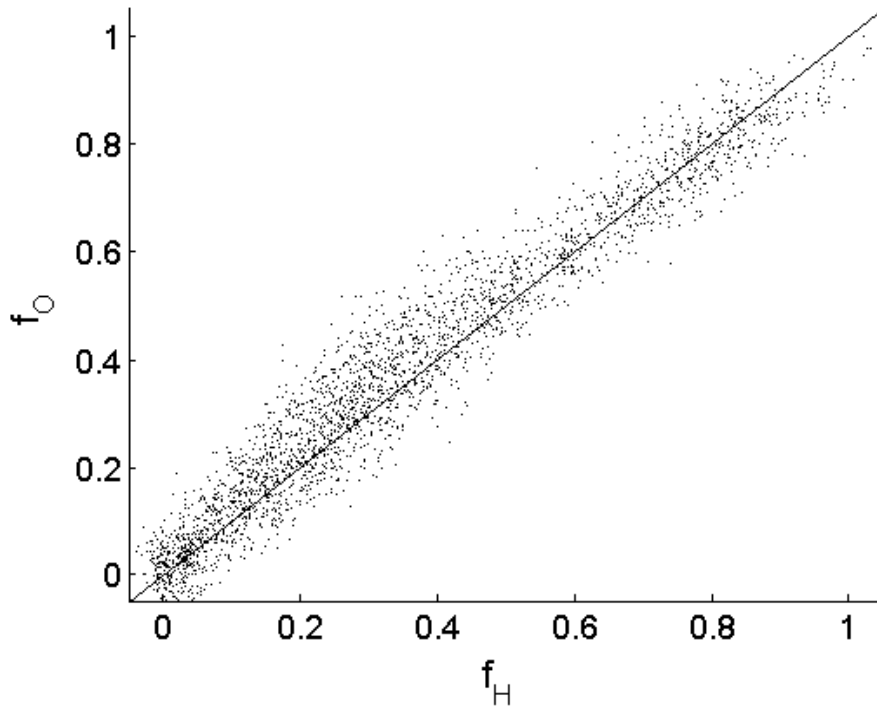


**Figure 6.9.**

Comparison of hydrogen and oxygen based mixture fraction formulations at  $z/d = 11$ .

The lack of observable differential-diffusion effects at these high Reynolds numbers (more accurately, the product of the Reynolds and Schmidt numbers) is consistent with work previously presented by Barlow et al. (2000). In addition to comparisons of the mixture fraction formulations, there is a poor match between the experimental data and the laminar flamelet calculations with full molecular transport. These numerical-experimental comparisons suggest that turbulence is the dominant mixing mode at the resolved length scales (i.e., larger than the probe volume, 750  $\mu\text{m}$ ), and molecular mixing occurs at the unresolved length scales (less than the 750  $\mu\text{m}$ ).

## **6.2. Lifted Methane-Air Jet Flame**

The second experimental flow studied with the laser Raman-Rayleigh-LIF system was a lifted premixed hydrocarbon flame. For combustion modeling, the lifted methane flame is the natural next step from the lifted hydrogen flame discussed in Section 6.1. The following sections outline the flame conditions and TDF experimental results for a lifted  $\text{CH}_4/\text{Air}$  flame into a vitiated coflow.

### **6.2.1. Methane Flame Conditions**

Experiments were conducted on a lifted turbulent  $\text{CH}_4/\text{Air}$  jet flame into a vitiated coflow (Figure 6.10). The combustor consists of a central  $\text{CH}_4/\text{Air}$  turbulent jet with a coaxial flow of hot combustion products from a lean premixed  $\text{H}_2/\text{Air}$  flame. For the conditions listed in Table 6.2, the observed lift-off height was  $H/d \cong 35$ .

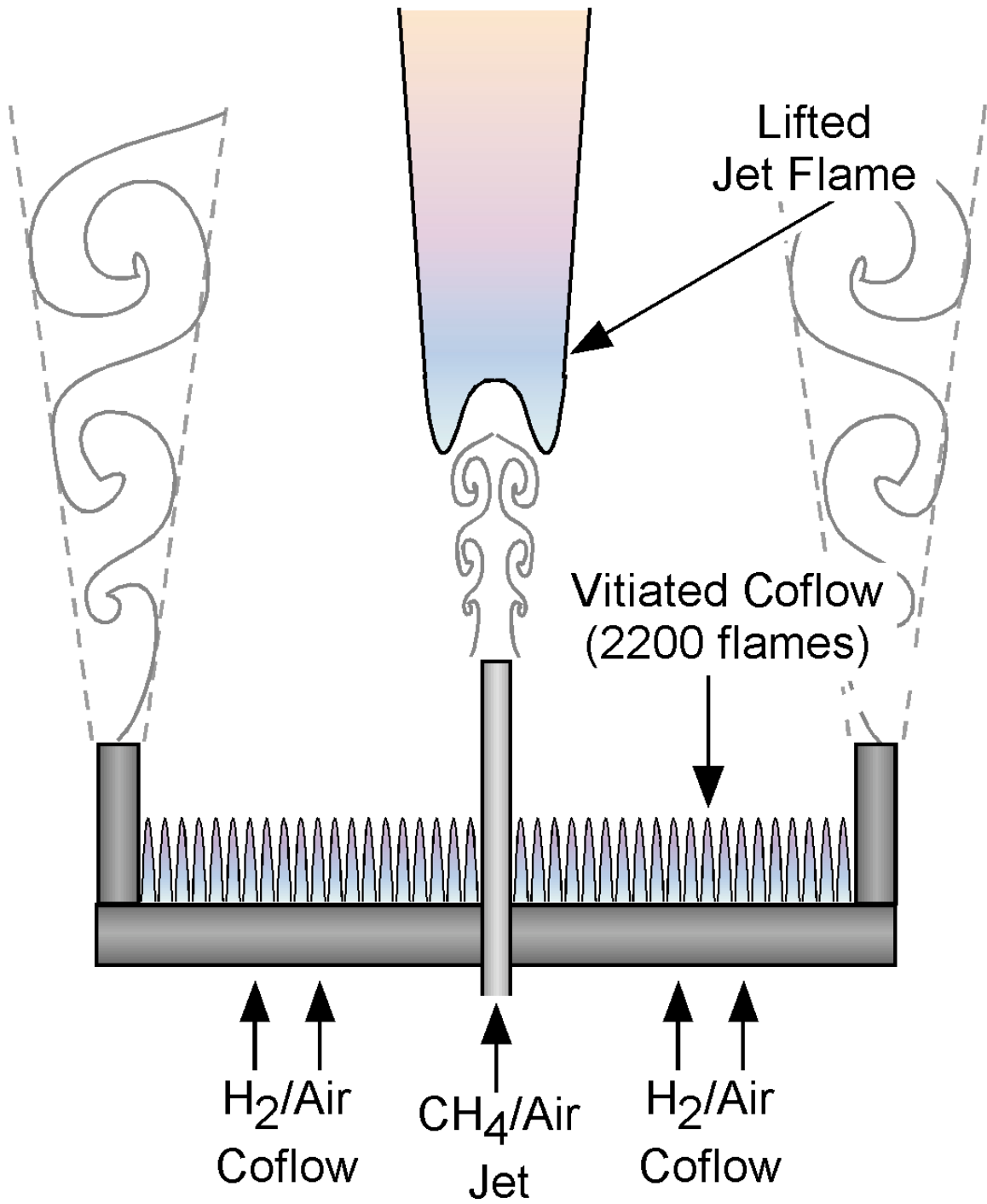


**Figure 6.10.**

Lifted CH<sub>4</sub>/Air jet flame into a coflow of hot products from a lean H<sub>2</sub>/Air flame.

**Table 6.2.**CH<sub>4</sub>/Air experimental conditions.

Central Jet		Coflow	
Q <sub>CH4</sub> (slm)	30	Q <sub>H2</sub> (slm)	360
Q <sub>Air</sub> (slm)	60	Q <sub>AIR</sub> (slm)	2,100
T <sub>JET</sub> (K)	320	T <sub>COFLOW</sub> (K)	1,350
V <sub>JET</sub> (m/s)	100	V <sub>COFLOW</sub> (m/s)	5.4
Re <sub>JET</sub>	28,000	Re <sub>COFLOW</sub>	23,300
d <sub>JET</sub> (mm)	4.57	D <sub>COFLOW</sub> (mm)	210
		φ	0.4
X <sub>CH4</sub>	0.33	X <sub>H2O</sub>	0.15
X <sub>O2</sub>	0.15	X <sub>O2</sub>	0.12
X <sub>N2</sub>	0.52	X <sub>N2</sub>	0.73

Q: volumetric flow rate; X: mole fraction; Re: Reynolds number; d and D: diameter; φ: equivalence ratio.

The methane flame was quite different from the hydrogen flame studied previously (Section 6.1). Fluctuations in lift-off height were considerably greater for the CH<sub>4</sub>/Air flame than for the H<sub>2</sub>/N<sub>2</sub> flame. The increased intermittency is due to the larger length scales of the flame and the slower time scales associated with the chemical kinetics of methane combustion. The intermittencies (or fluctuations) are more easily detected with the naked eye.

The measurements obtained by the NO laser-induced fluorescence systems have poor precision. Signal RMS values were consistently high. For the methane case, the NO results are not presented.

### 6.2.2. Experimental Region

In a manner similar to the hydrogen flame analysis, the structure of the lifted turbulent CH<sub>4</sub>/Air jet flame is investigated by examining the measured temperature and species concentrations profiles. Centerline measurements were taken from z/d=1 to 100

downstream of the nozzle exit. Radial profiles were obtained at several axial locations ( $z/d = 1, 15, 30, 40, 50$  and  $70$ ). The radial domain covered by these profiles was  $-3$  mm to  $50$  mm, with spacing typically between  $2$  and  $3$ mm. Figure 6.11 shows the experimental locations for the methane flame.

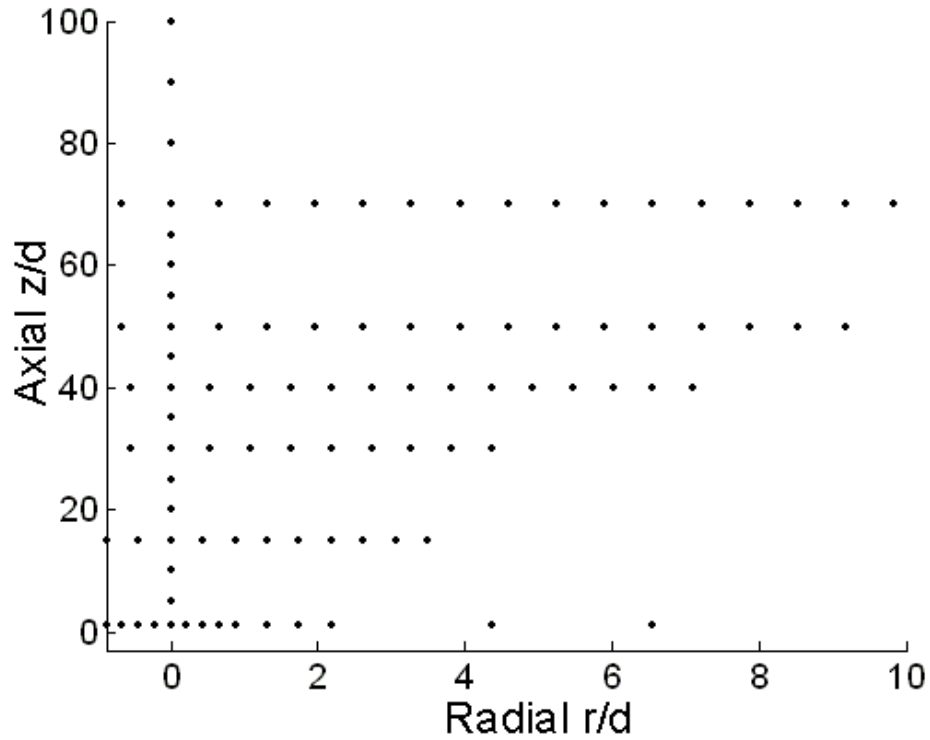


**Figure 6.11.**

Location of measurement points (horizontal axis is expanded).

The single-shot data were processed and the Favre averages and RMS fluctuations were generated. For all comparisons, the Bilger (1990) formulated mixture fraction was used.

$$f = \frac{(2/M_C)(Y_C - Y_{C,2}) + (1/2M_H)(Y_H - Y_{H,2}) - (1/M_O)(Y_O - Y_{O,2})}{(2/M_C)(Y_{C,1} - Y_{C,2}) + (1/2M_H)(Y_{H,1} - Y_{H,2}) - (1/M_O)(Y_{O,1} - Y_{O,2})} \quad (6.3)$$

For the conditions listed in Table 6.2, the stoichiometric mixture fraction was  $f_s = 0.17$ ; this value is lower than the stoichiometric value for the hydrogen flame. The lower

stoichiometric mixture fraction places the flame further out into the coflow, making the conditions less turbulent, hotter, and more sensitive to coflow conditions.

### 6.2.3. Extended Well-Defined Boundary Conditions

The experimental results further support the assumption of a two-stream flow condition provided by the large vitiated coflow. The radial profiles of temperature and oxygen mass fraction at  $z/d = 1$  shown in Figure 6.12 exhibit similar “top hat” profiles as those from the hydrogen flame results. Coflow and jet conditions are also uniform and steady (2% RMS). As discussed earlier, the 2% signal RMS is on the order of the photoelectronic shot noise (Table 5.2).

The hydrogen flame results show uniform coflow conditions up to  $z/d = 26$  (Figure 6.4), results for the current methane flame show that the uniform coflow condition extends even further downstream. Figure 6.13 shows the evolution of the Favre averaged temperatures and species concentration radial profiles with increased downstream distance from the nozzle exit. The hydrogen flame results show a uniform coflow (isolating the jet from the lab air) for an axial distance of  $z/d = 26$  (Figure 6.4). As shown in Figure 6.13, specifically the water, oxygen and temperature plots, the coflow is uniform for a distance up to  $z/d = 50$ , but is contaminated at  $z/d = 70$ .

As can be seen in the radial profiles of Figure 6.13, no reaction is detected in the first 30 diameters from the nozzle. Initially, pure mixing occurs between the hot coflow and cool jet streams. It is not until  $z/d = 40$  that the production of radicals and increase in temperature is observed in the results. These observations are consistent with the observed lift-off height of  $H/d = 35$  ( $d = 4.57$  mm).

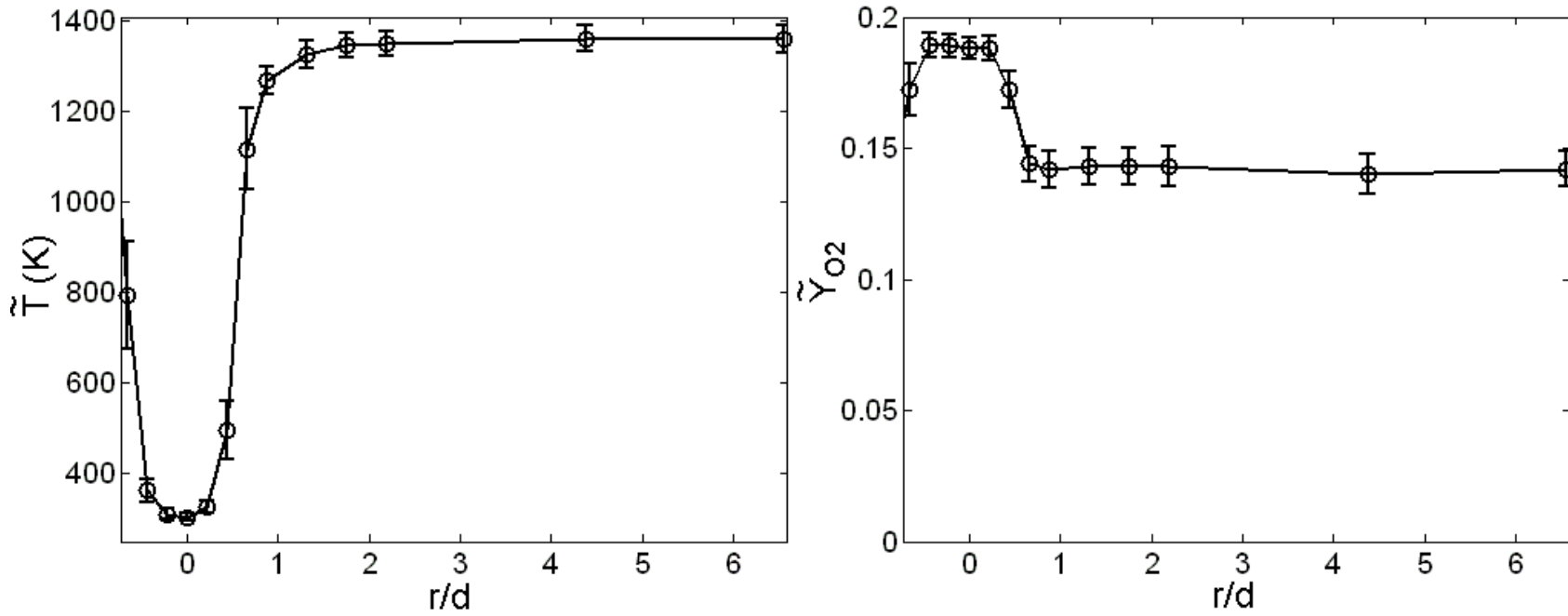


**Figure 6.12.**

Uniform and steady inlet conditions. Radial profiles for temperature and oxygen mass fraction at  $z/d = 1$  for the methane flame. The plotted symbols denote the Favre average while the error bars denote the associated variance.

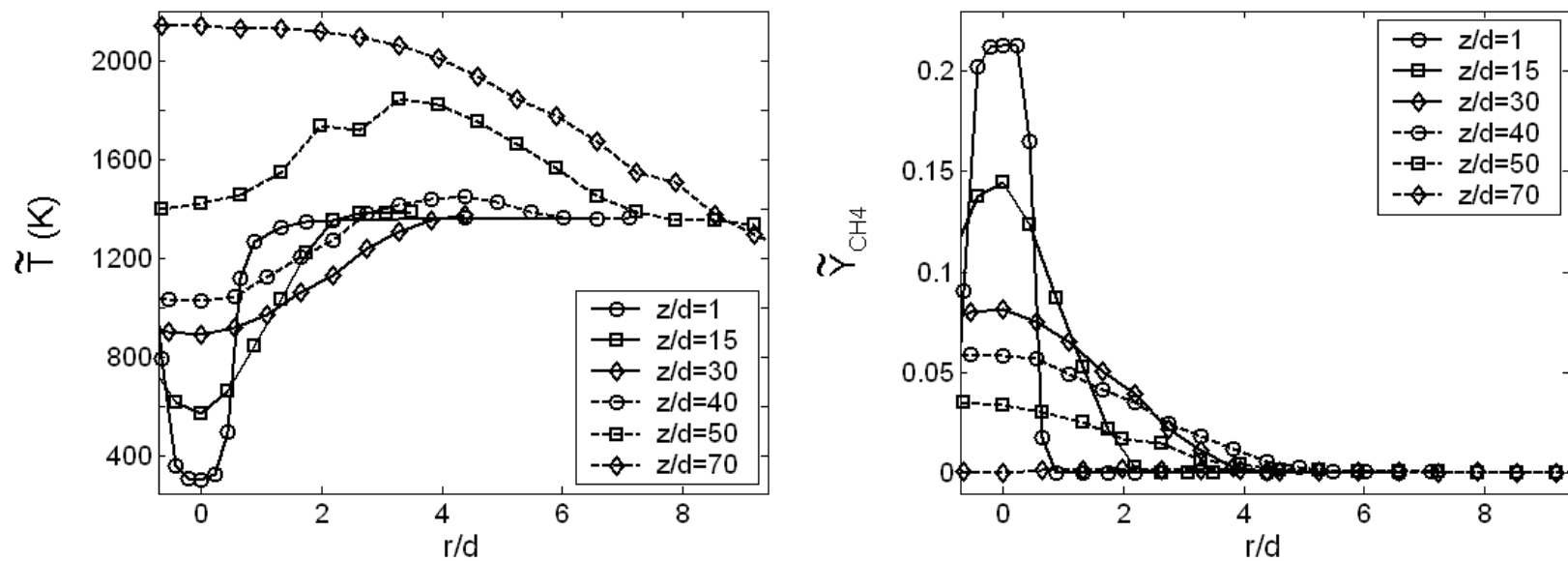


**Figure 6.13A.**

Evolution of radial profiles for the Favre averaged temperature and  $\text{CH}_4$  mass fraction measurements with increased axial distance from the nozzle exit.

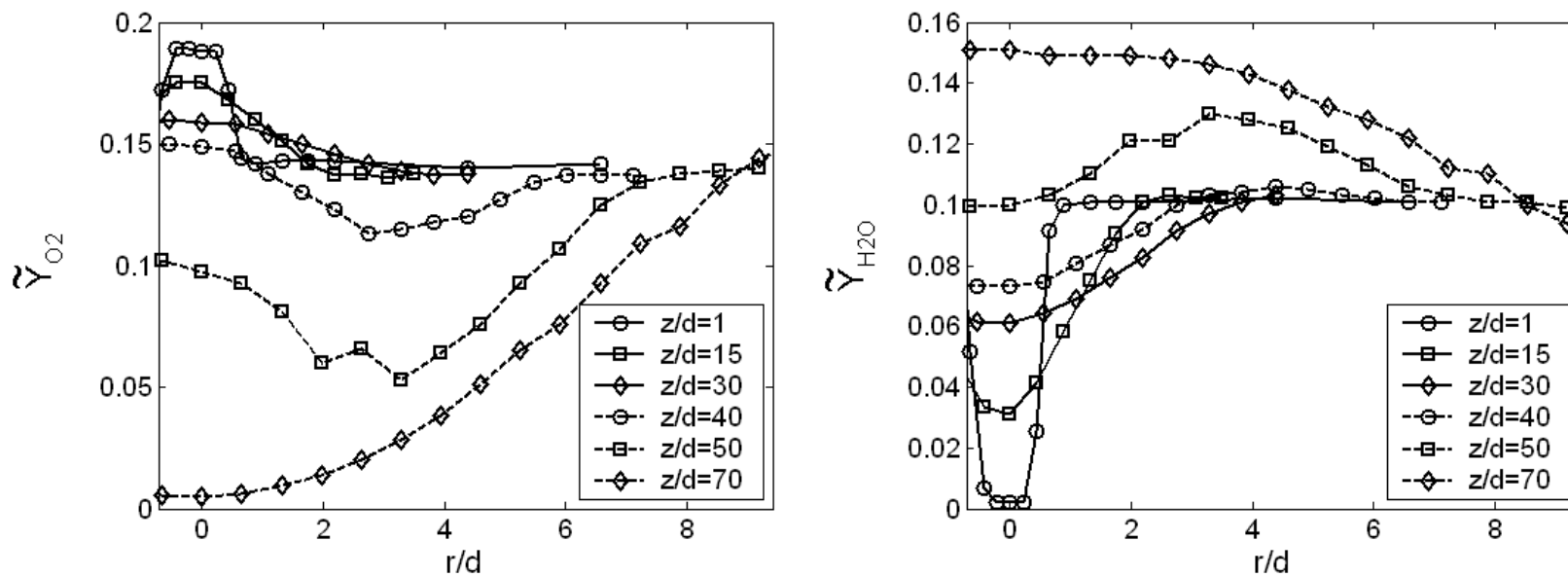


**Figure 6.13B.**

Evolution of radial profiles for the Favre averaged  $O_2$  and  $H_2O$  mass fraction measurements with increased axial distance from the nozzle exit.

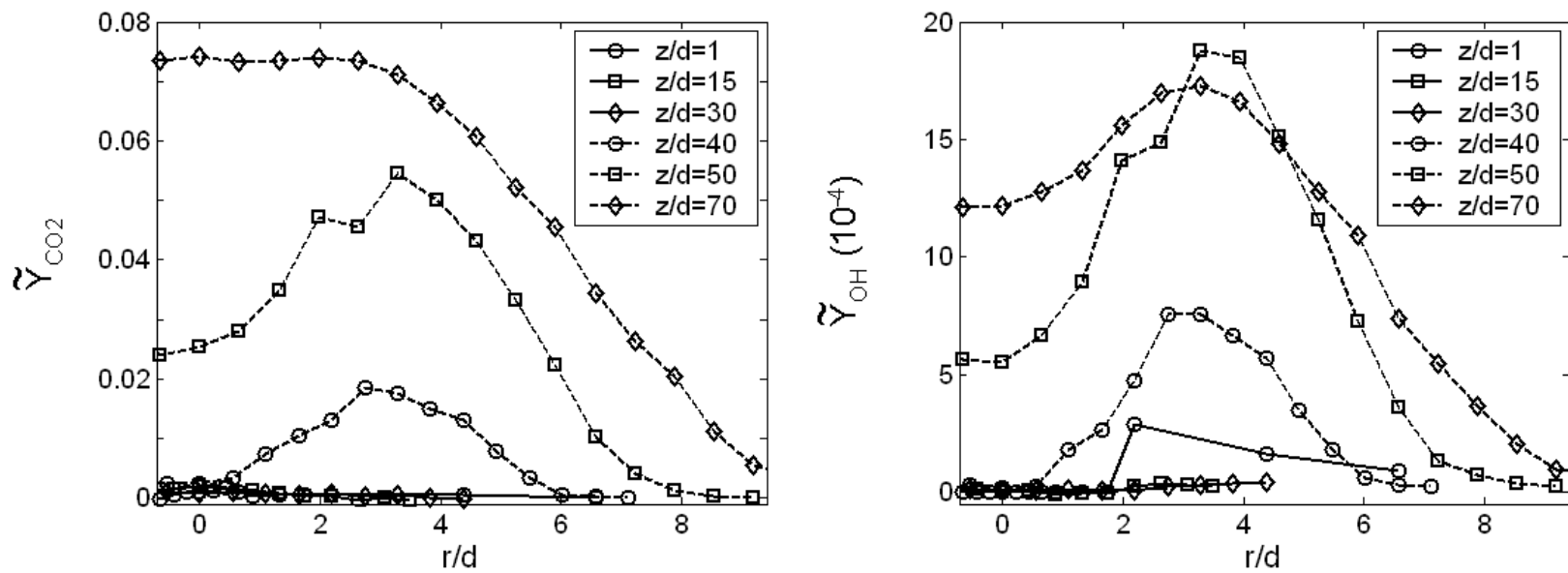


**Figure 6.13C.**

Evolution of radial profiles for the Favre averaged CO<sub>2</sub> and OH mass fraction measurements with increased axial distance from the nozzle exit.

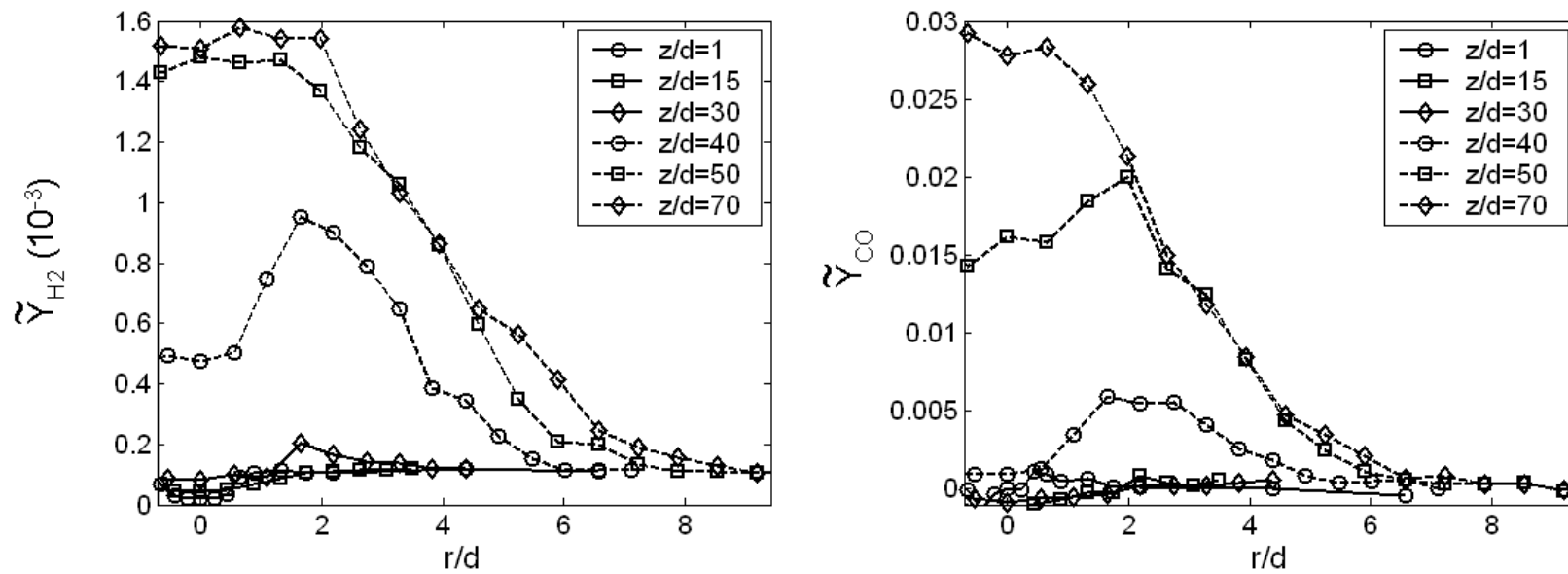


**Figure 6.13D.**

Evolution of radial profiles for the Favre averaged  $H_2$  and CO mass fraction measurements with increased axial distance from the nozzle exit.

#### 6.2.4. Flame Structure

The averaged OH mass fraction field does not accurately represent the flame structure. Figure 6.14 presents the Favre averages and RMS (variance) fields of the OH mass fraction measurements. The contour plot of the OH mass fraction RMS indicates the intermittent nature of this flame, while showing an accurate lift-off height of  $H/d = 35$ .

As stated earlier in Section 6.2.1, the methane flame was observably quite different than the hydrogen flame. The length and time scales associated with the intermittent methane flame were much larger, making the fluctuation noticeable to the naked eye. These fluctuations may be present in the hydrogen case; however, they are undetectable to the naked eye because of the shorter length and time scales associated with rapid chemical kinetics. Further analysis of this phenomenon follows in the discussion on combustion statistics for this flow (Section 6.2.6).

#### 6.2.5. Centerline Profiles

Centerline profiles provide some information on the evolution of the flow that can be used to validate numerical models. Figure 6.15 presents the evolution of Favre averaged temperature and species concentration profiles along the centerline. The centerline profile of the Favre averaged O<sub>2</sub> mass fraction exhibits characteristics similar to the results from the hydrogen flame (Figure 6.6). However, the jet stream initially contains oxygen levels greater than that found in the coflow. The coflow therefore dilutes the oxygen and we see a decline in oxygen concentration prior to combustion. The varying rates of oxygen decline pre and post combustion ( $z/d \approx 40$ ) provide metrics for the mixing and chemical kinetic components of combustion models.

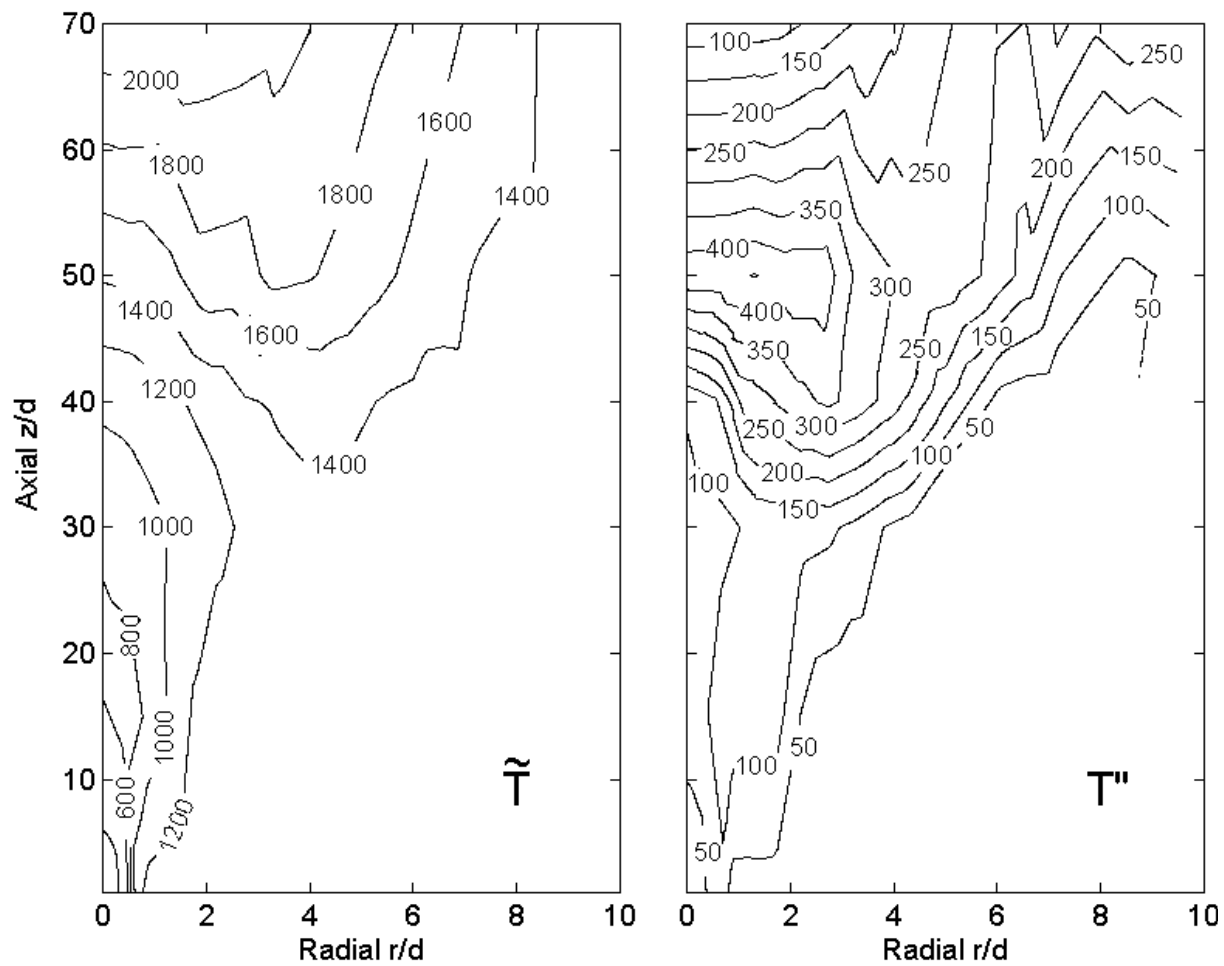


**Figure 6.14.**

Intermittency of the flame is exhibited by the temperature contour plots (Favre average, Favre RMS).

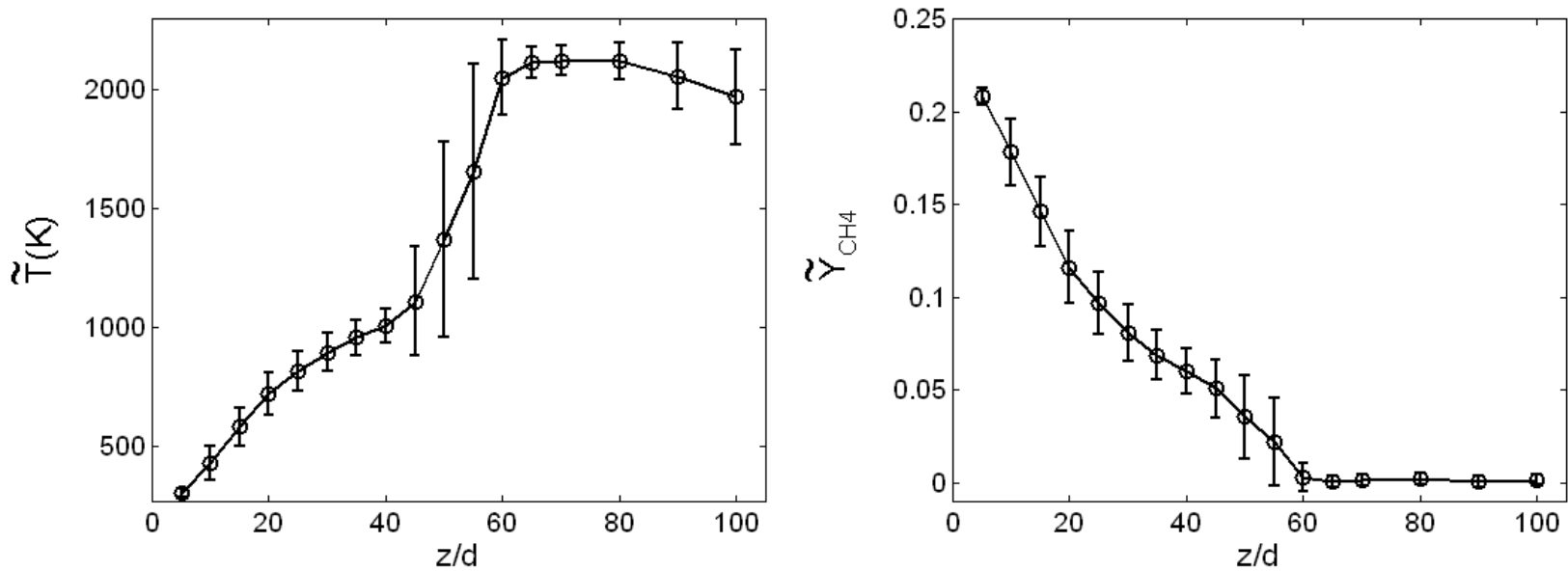


**Figure 6.15A.**

Centerline profiles of the Favre averaged temperature and CH<sub>4</sub> mass fraction measurements. Error bars denote the signal RMS.

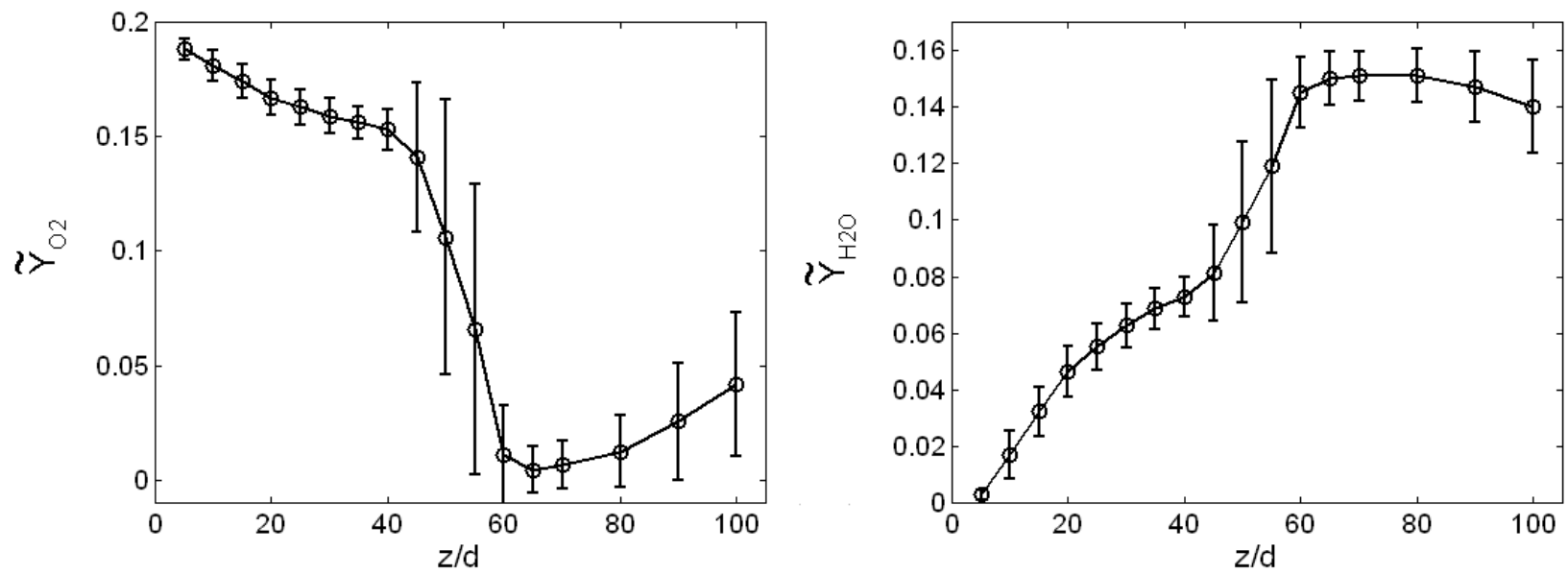


**Figure 6.15B.**

Centerline profiles of the Favre averaged O<sub>2</sub> and H<sub>2</sub>O mass fraction measurements. Error bars denote the signal RMS.

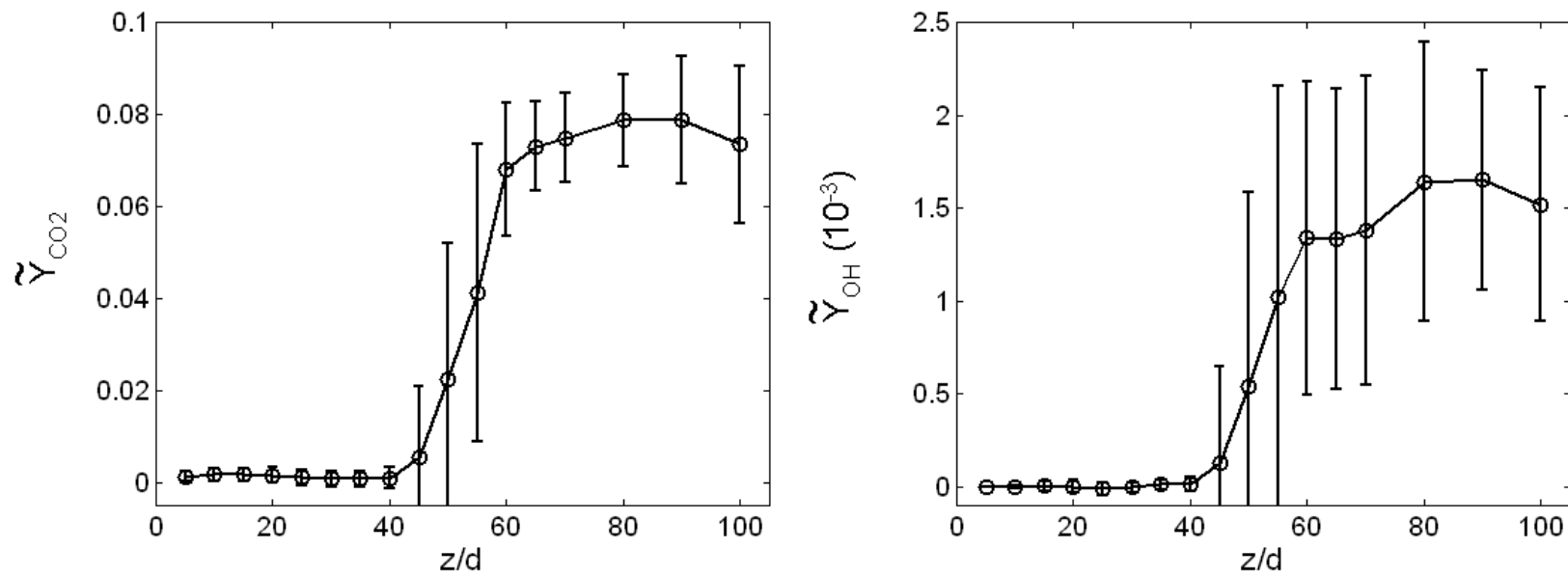


**Figure 6.15C.**

Centerline profiles of the Favre averaged CO<sub>2</sub> and OH mass fraction measurements. Error bars denote the signal RMS.

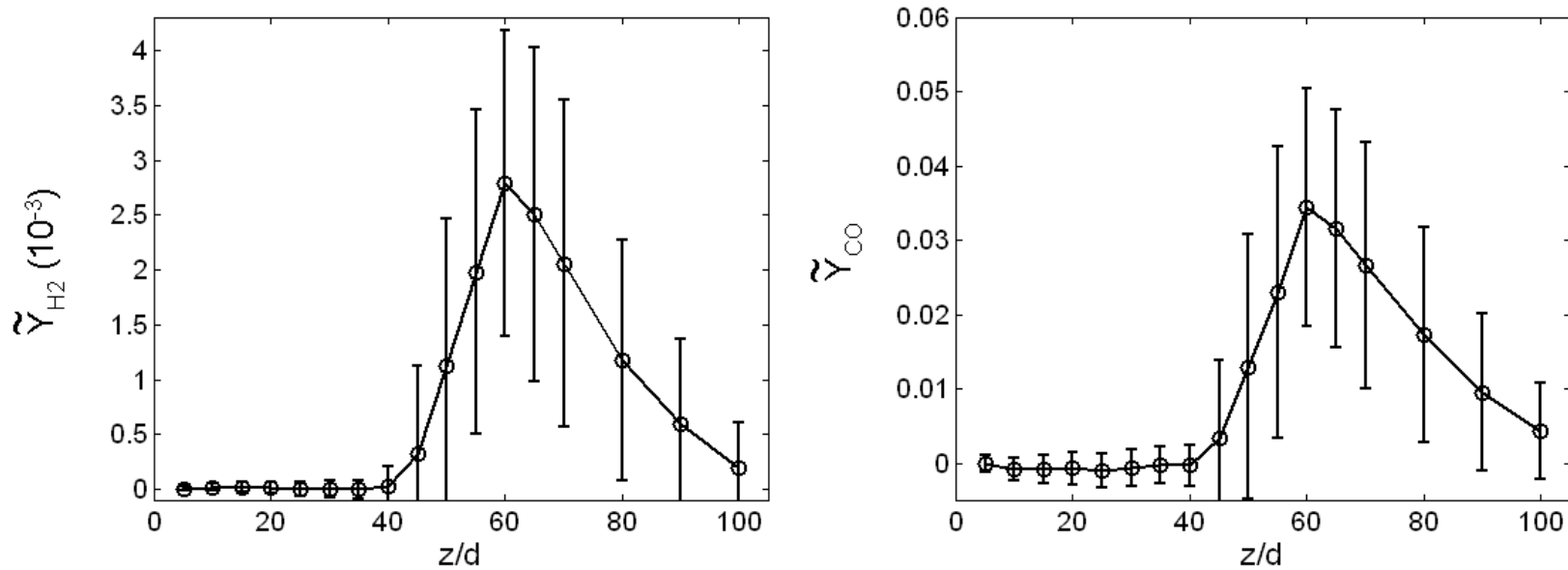


**Figure 6.15D.**

Centerline profiles of the Favre averaged H<sub>2</sub> and CO mass fraction measurements. Error bars denote the signal RMS.

The centerline profile of the Favre averaged mixture fraction can also be used to test combustion models. Mixture fraction decay along the centerline is presented in Figure 6.16. As can be seen, the mixture fraction decay rate changes as a result of flame stabilization in a manner similar to the oxygen results in Figure 6.15. The dilatation (expansion) of the fluid in and around the reaction zone (i.e., flame front) greatly inhibits further mixing of the coflow with nozzle fluid as evidenced by the abrupt change in the mixture fraction decay rate at  $z/d = 14$  (Figure 6.16).

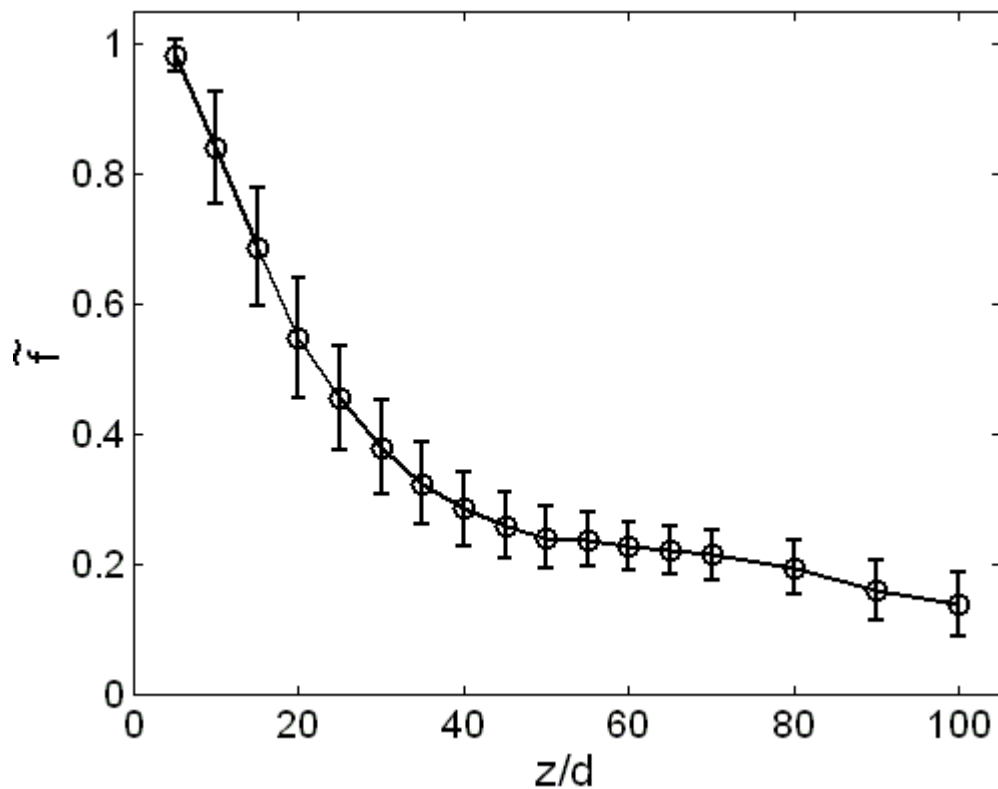


**Figure 6.16.**

Centerline profile of the Favre averaged mixture fraction. Error bars denote the signal RMS.

### 6.2.6. Combustion Statistics of Probe-Volume Conditions

The combustion conditions are analyzed in the same fashion as described for the hydrogen flame. The evolution of the flame through and beyond the flame stabilization point at  $z/d = 35$  is presented in Figure 6.17. A series of plots of instantaneous temperature and OH mole fraction versus mixture fraction are shown. The contour plots in the center column show the distribution of probe volume conditions in temperature-mixture fraction space. As can be seen in the plots, a transition from a mixing to reacting condition is shown; this result is similar to the hydrogen flame result. Also in agreement with the presented hydrogen results is the increase in maximum temperature downstream of the flame base. This result is associated with the higher strain rates at the flame base that quickly dissipate the heat released. Consistent with these results is the “relaxation” of OH super-equilibrium conditions where OH concentrations decrease to equilibrium values at downstream locations.

Results shown in Figure 6.17 do not suggest a distributed reaction zone similar to the hydrogen flame condition. Figure 6.17 presents a broadened bimodal distribution of probe volume conditions consistent with the results reported in the literature (Barlow et al. 1989, Cheng et al. 1992, Brockhinke et al. 1995). Regardless of the higher temperatures and premixing, these results show how methane combustion is not as robust as hydrogen combustion. In particular, this methane flame does not exhibit the same extent of flame broadening associated with intense mixing and energy dissipation. Further analysis of these results is presented in the following chapter on flame stabilization.

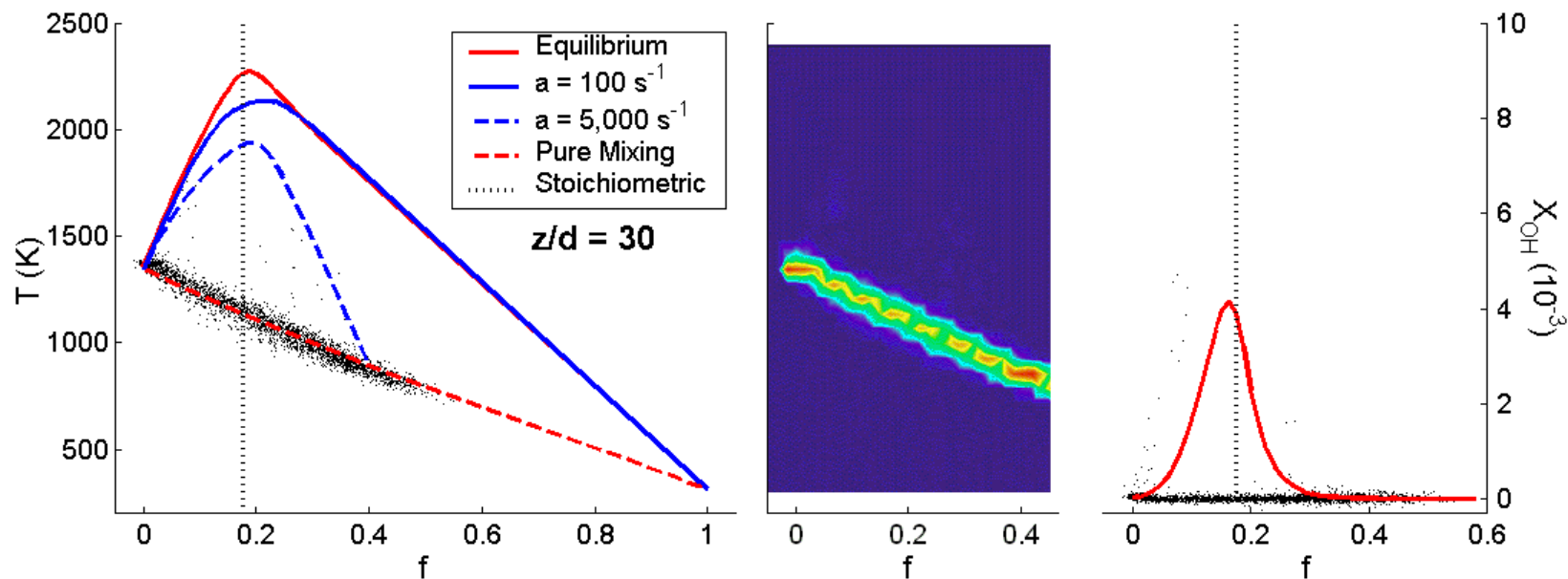


**Figure 6.17A.**

Ensemble of instantaneous temperature and OH mole fraction measurements with respect to mixture fraction at  $z/d = 30$ . The center contour plot shows the distribution of conditions in temperature- mixture fraction space. Also plotted are laminar flamelet calculations: Equilibrium, Strained ( $a = 100 \text{ s}^{-1}$  &  $5,000 \text{ s}^{-1}$ ) and the pure mixing (frozen) condition.

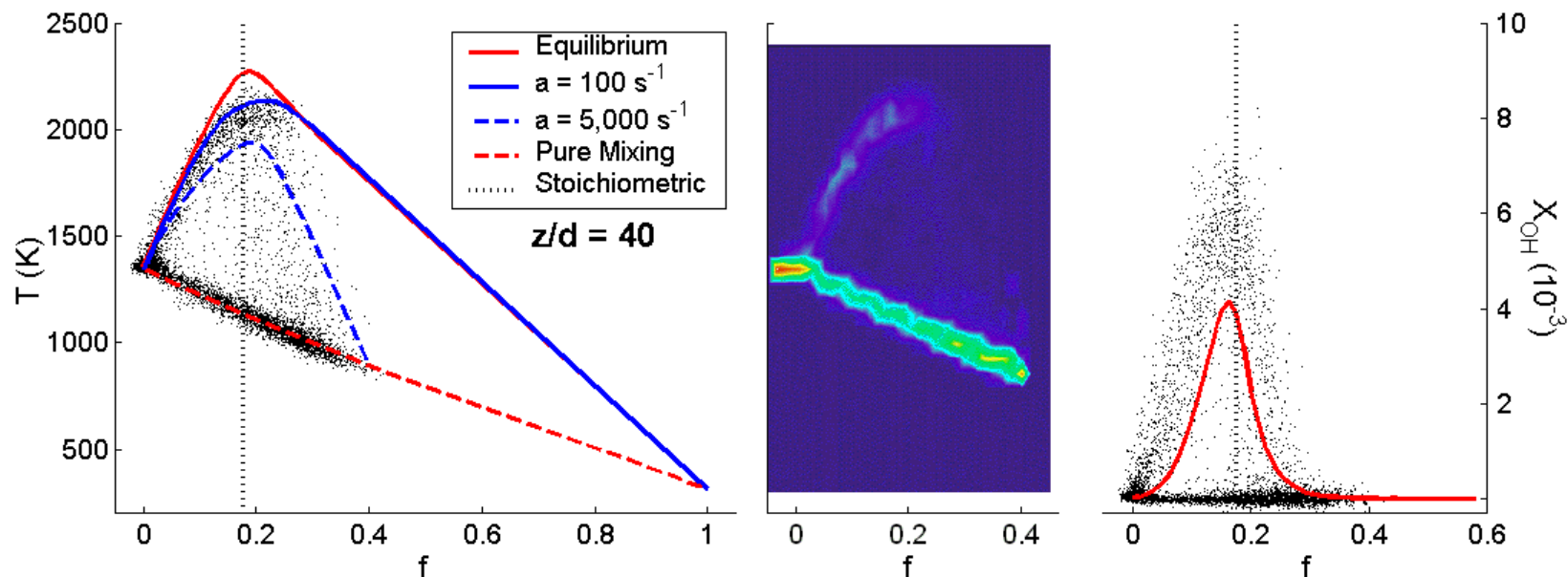


**Figure 6.17B.**

Ensemble of instantaneous temperature and OH mole fraction measurements with respect to mixture fraction at  $z/d = 40$ . The center contour plot shows the distribution of conditions in temperature- mixture fraction space. Also plotted are laminar flamelet calculations: Equilibrium, Strained ( $a = 100 \text{ s}^{-1}$  &  $5,000 \text{ s}^{-1}$ ) and the pure mixing (frozen) condition.

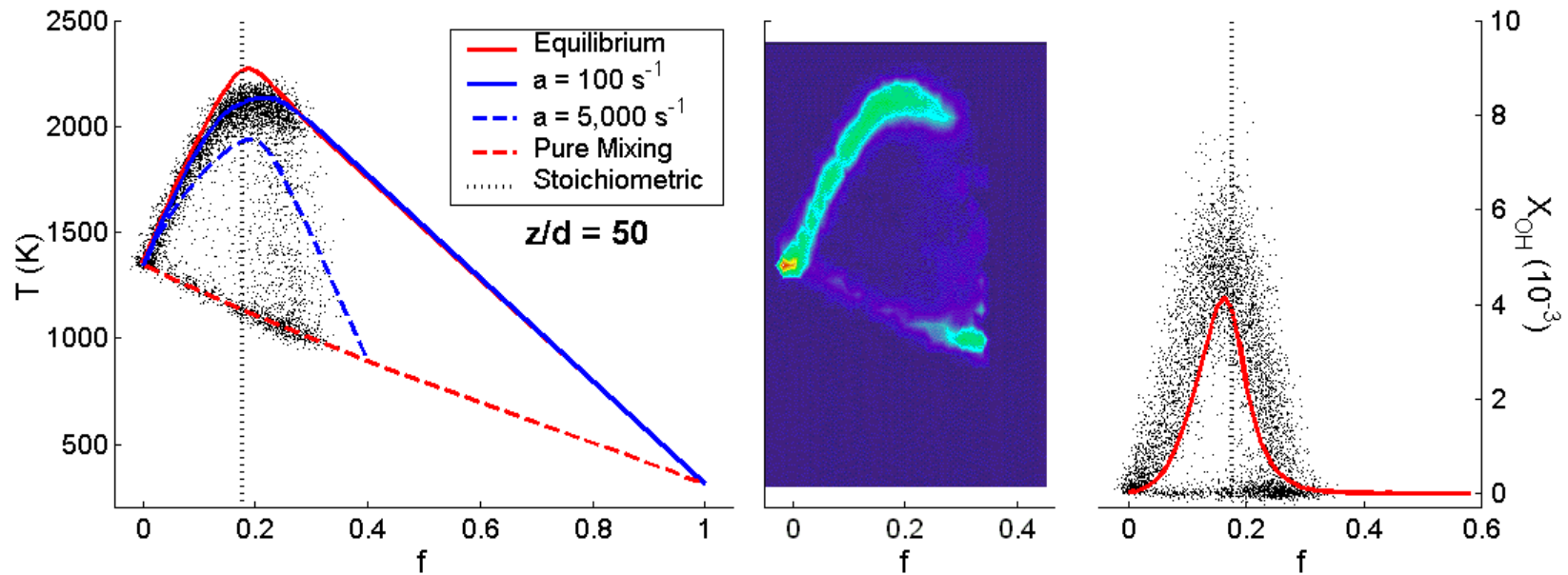


**Figure 6.17C.**

Ensemble of instantaneous temperature and OH mole fraction measurements with respect to mixture fraction at  $z/d = 50$ . The center contour plot shows the distribution of conditions in temperature- mixture fraction space. Also plotted are laminar flamelet calculations: Equilibrium, Strained ( $a = 100 \text{ s}^{-1}$  &  $5,000 \text{ s}^{-1}$ ) and the pure mixing (frozen) condition.

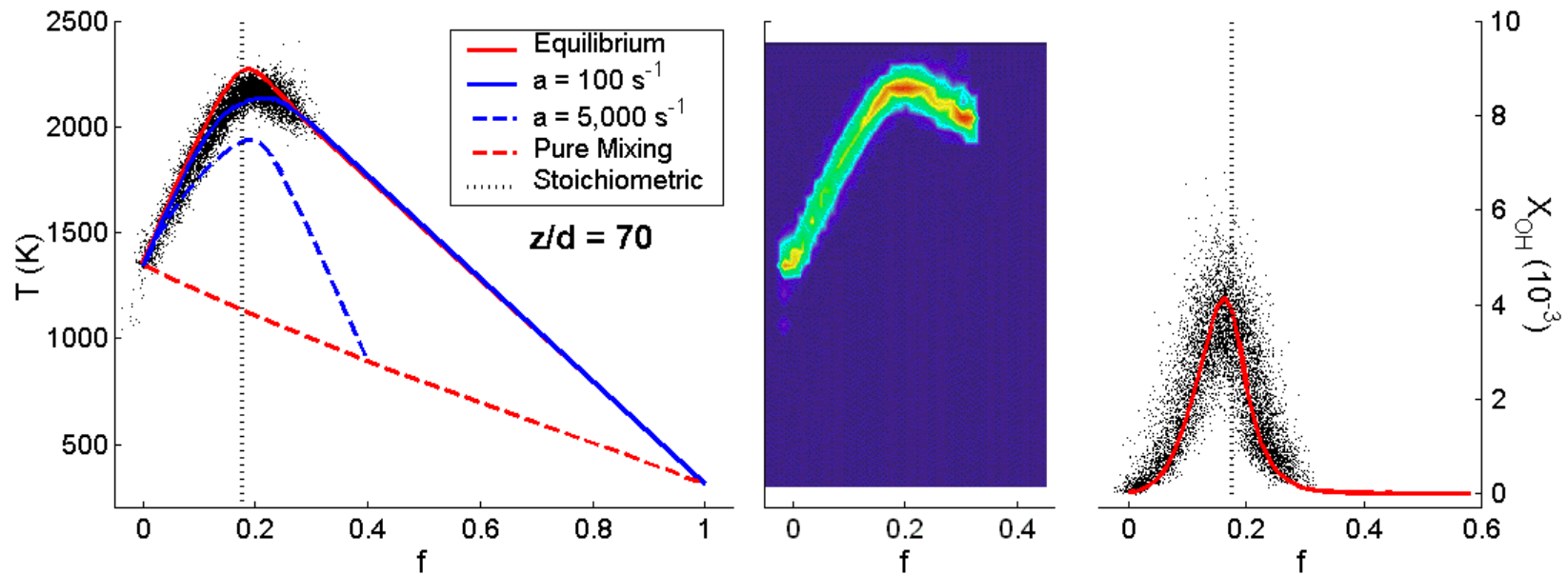


**Figure 6.17D.**

Ensemble of instantaneous temperature and OH mole fraction measurements with respect to mixture fraction at  $z/d = 70$ . The center contour plot shows the distribution of conditions in temperature- mixture fraction space. Also plotted are laminar flamelet calculations: Equilibrium, Strained ( $a = 100 \text{ s}^{-1}$  &  $5,000 \text{ s}^{-1}$ ) and the pure mixing (frozen) condition.

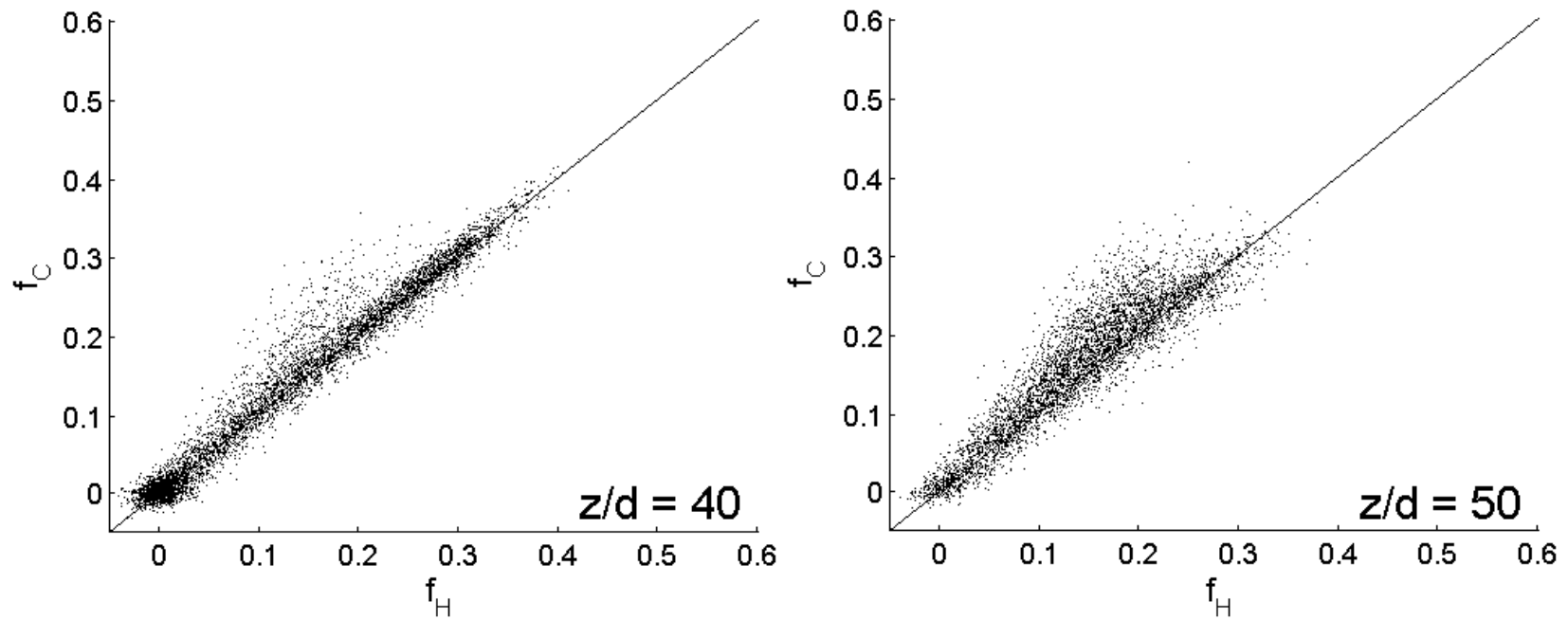


**Figure 6.18.**

Comparison of hydrogen and carbon based mixture fraction formulations ( $z/d = 40$  &  $50$ ).

### 6.2.7. Negligible Differential Diffusion Effects

Although the differential diffusion effects for the hydrogen flame were shown to be negligible, they are analyzed for the current conditions. Figure 6.18 presents the comparisons on a shot-by-shot basis of mixture fraction formulations based on elemental hydrogen and elemental carbon at two axial locations ( $z/d = 40$  &  $50$ ). As was the case for the hydrogen flame, both fuel and oxidizer streams contained elemental hydrogen. The small difference in elemental hydrogen between the two streams also resulted in a considerable amount of noise. The small departure in the correlations at the stoichiometric mixture fraction ( $f_s = 0.17$ ) shows that differential diffusion effects are minimal. As was the case with the hydrogen flame, results from laminar flamelet calculations with full molecular transport poorly matched the methane experimental data. These results further support turbulence dominant mixing.

### 6.3. Chapter Summary

A survey of multiscalar measurements for two conditions of the vitiated coflow lifted jet flame was conducted at the Turbulent Diffusion Flame laboratory at Sandia National Laboratories' Combustion Research Facility. Results confirm that the large momentum driven coflow effectively isolates the jet from the lab air for a distance beyond  $z/d = 50$  but less than  $z/d = 70$ . Radial profiles at  $z/d = 1$  downstream of the nozzle exit show uniform and steady inlet conditions with top-hat profiles of temperature and specie concentrations. The coflow is well mixed, as exhibited by the low RMS of the measurements in the far field. Comparisons of different elemental mixture fraction formulations on a shot-by-shot basis confirm that differential diffusion effects are negligible for this turbulent flow. Numerical results produced at the University of

California at Berkeley adequately predict the lifted flame structure for the hydrogen flame, a nontrivial task. These results attest to the success of the design in providing a two-stream flow.

Statistical data of the probe-volume conditions (i.e., scatter plots) show different conditions for the two flames. Both flames exhibit similar transitions from mixing (frozen) conditions to reactive conditions. The results also show similar downstream flame relaxation associated with decreased strain rates, increased maximum temperatures, and decreased OH concentrations. However, the distributions of probe-volume conditions at the flame stabilization region are quite different. For the hydrogen flame, results indicate a thick reaction zone, in which a uniform distribution of probe-volume conditions exists between frozen and reactive conditions (distributive reaction). In contrast, a bimodal distribution of sample conditions is reported for the methane flame. These interesting findings are dependent on the flame stabilization for each flame. In order to better understand the flame stabilization process, more conditions must be investigated.

## Chapter 7

### Boundary Conditions (Numerical Considerations)

A summary of boundary condition information is presented in Chapter 7. Results from the Sandia TDF measurements are summarized. Information regarding the flow field and thermal interactions are presented; these results are based on analytical, numerical and experimental investigations. The measured temperature field of a nonreacting (pure-mixing) condition is presented for possible use in model validation. Results show that the large vitiated coflow provides a two-stream flow with uniform far-field conditions; therefore, the flame can be modeled as a jet flame in an infinite coflow. The axial distance over which this two-stream condition exists is also analyzed and determined to be most sensitive to coflow temperature. Numerical explorations show that possible undetected radicals in the coflow have a small effect on the combustion processes. More specifically, it is shown that the flame is most sensitive to coflow temperature.

#### 7.1. Inlet Flow Field

The jet flow upstream of the nozzle exit is fully developed and turbulent ( $Re = 20,000-25,000$ ). The velocity distribution is assumed related to the average jet velocity  $U_J$  via the  $1/7^{\text{th}}$  power law (Bird et al. 2002).

$$\frac{U}{U_J} = \frac{5}{4} \left( 1 - \frac{a}{r} \right)^{1/7} \quad (7.1)$$

The hot flow on the outer side of the jet wall is assumed laminar and developing. The velocity boundary layer is related to the thermal boundary layer via the Prandtl number (Incropera and DeWitt 1996).

$$\frac{\delta}{\delta_T} \approx \text{Pr}_C^{1/3} \quad (7.2)$$

Under normal operating conditions, the thermal boundary condition is on the order of 1 diameter (see Equation 7.5 in Section 7.2) and the Prandtl number is approximately 0.7. Therefore, the momentum boundary layer of the outer coflow is approximately 0.9 diameters.

The flow field at the nozzle exit is illustrated by the solid line shown Figure 7.1. The velocity is zero at the jet wall surface and there are boundary layers on each side of the jet wall. The jet velocity is much greater than the coflow velocity. The effect of the velocity deficit ( $V = 0$ ) at the jet wall was studied using the EDC concept (Cabra et al. 2002). Cabra and coworkers showed that the detailed modeling of the wall was unnecessary to duplicate the temperature profile at  $z/d = 1$ . Moreover, the lift-off height was insensitive to the modeling of the velocity deficit at the tube wall. More specifically, both velocity distributions (solid and dashed curves in Figure 7.1) were modeled with the EDC. The simplified dashed line distribution was sufficient for a reasonable prediction of the lifted flame structure ( $V(a/d \leq 0.5) = \text{Equation 7.1}$ ,  $V(a/d > 0.5) = V_C$ ).

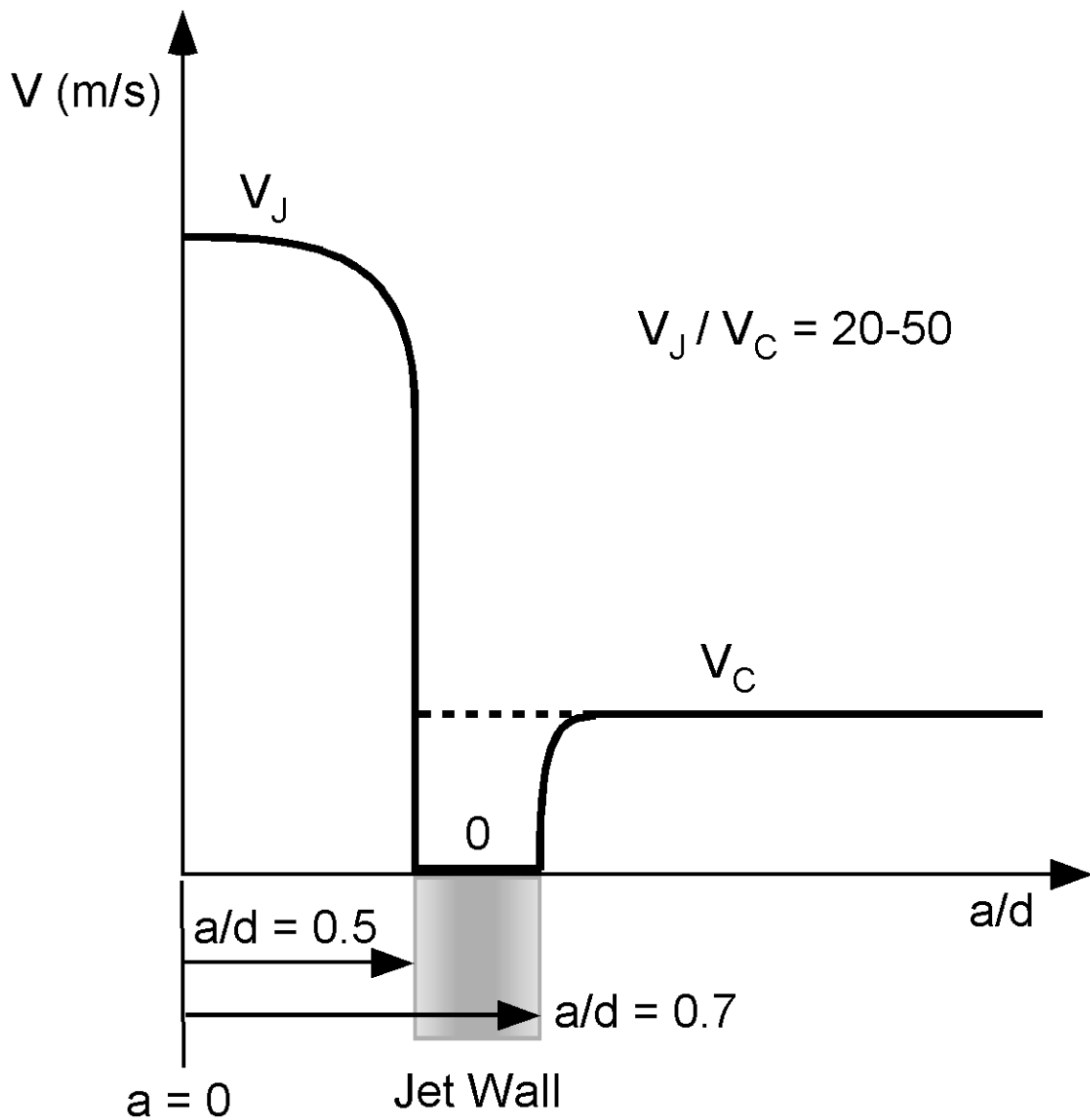


**Figure 7.1.**

Average flow field at the nozzle exit ( $d = 4.57$  mm). Solid line is the actual velocity distribution, and the dashed line is the simplification used for the EDC calculations (Figure 6.5).

## 7.2. Inlet Temperature Field

An analysis of the heat transfer from the hot coflow to the jet fluid within the nozzle (i.e., heat transfer to a fluid inside a pipe) provides a model for the elevated jet temperature due to heating from the coflow. The analysis assumes one directional heat transfer towards the gas flowing inside the pipe that is (1) convected from the coflow to the nozzle wall, (2) conducted through the nozzle wall, and (3) convected to and absorbed by the gas flowing inside of the nozzle.

The heat transfer analysis is simplified with the assumption that the nozzle wall is isothermal. The uniform temperature assumption corresponds to convection dominant heat transfer. Use of the lumped capacitance method is valid when the Biot number is much less than one.

$$\text{Bi} = \frac{hL}{k} \quad (7.3)$$

The convective heat transfer coefficient  $h$  is taken to be the average of the inner and outer convective heat transfer coefficients. The convective heat transfer coefficient at the outer surface of the nozzle wall  $h_R(x)$  is approximated as that of a laminar developing flow over a flat plate (Incropera and DeWitt 1996). At the plate surface  $x = 0$ .

$$h_R(x) = 0.332 \frac{k_C}{x} \left( \frac{U_C x}{\nu_C} \right)^{0.5} \text{Pr}_C^{1/3} \quad (7.4)$$

The corresponding thermal boundary layer  $\delta_T(x)$  is (Incropera and DeWitt 1996):

$$\delta_T(x) = 5 \sqrt{\frac{\nu_C x}{U_C}} = \frac{5x}{\sqrt{\text{Re}_x}} \quad (7.5)$$

For typical operating conditions, the thermal boundary layer for the outer flow is on the order of 1 diameter, which is consistent with the Sandia laser diagnostic results plotted in

Figures 6.3 and 6.12. The inner flow of the nozzle is a fully developed turbulent pipe flow. The convective heat transfer coefficient  $h_r$  is uniform over the length of the pipe (Incropera and DeWitt 1996).

$$h_r = 0.023 \frac{k_J}{d} \left( \frac{U_J d}{\nu_J} \right)^{0.8} Pr_J^{0.4} \quad (7.6)$$

All fluid properties are approximated as those for air at 300 K for the jet fluid within the nozzle (subscript J) and 1,000 K for the coflow (subscript C). The thermal conductivity  $k$  for the stainless steel tube is 14.5 kW/m-K. The jet ID is 4.57 mm and OD is 6.35 mm. For typical conditions ( $U_J = 100$  m/s and  $U_C = 5$  m/s), the estimated Biot number of 0.012 validates the isothermal nozzle wall assumption.

At steady state, the heat transfer from the coflow to the nozzle wall balances the heat transfer from the nozzle wall to the flow of the nozzle.

$$\delta \dot{Q} = h_R(x) [T_C - T_W(x)] dA_R = h_r [T_W(x) - T(x)] dA_r \quad (7.7)$$

The convective heat transfer coefficient  $h$ , temperature  $T$ , and differential surface area  $dA$  have subscripts denoting the radial coordinate ( $R =$  outer nozzle wall surface,  $r =$  inner nozzle wall surface).  $T(x)$  is the average jet stream temperature and  $T_W(x)$  is the wall temperature. The differential surface area over which the heat transfer occurs is simply:

$$\begin{aligned} dA_R &= 2\pi R dx \\ dA_r &= 2\pi r dx \end{aligned} \quad (7.8)$$

The energy transferred as heat is stored by the jet fluid in the nozzle (subscript J):

$$\delta \dot{Q} = \dot{m}_J C_{p,J} \frac{dT}{dx} dx \quad (7.9)$$

The set of three equations (Equations 7.7 and 7.9) for three unknown functions ( $\dot{\delta Q}$ ,  $T_w(x)$ , and  $T(x)$ ) yields a differential equation for the temperature of the jet fluid at the nozzle exit  $T_L = T(L = 70\text{mm})$ . Recasting the function  $T(x)$  to  $\theta(x)$  results in the following differential equation:

$$K_1 \partial x = K_2 \frac{\partial \theta}{\theta} \quad (7.10)$$

where

$$K_1(x, U_J, U_C) = \frac{2\pi R h_R(x)}{1 + \frac{R h_R(x)}{r h_r}} \quad (7.11)$$

$$K_2(U_J) = -\dot{m}_J C_{p,J} \quad (7.12)$$

$$\theta(x, T_C) = T_C - T(x) \quad (7.13)$$

Solving equation 7.9 provides the following expression.

$$\frac{\theta_L}{\theta_O} = \frac{T_C - T_L}{T_C - T_O} = \exp\left(\frac{K_3(U_J, U_C)}{K_2(U_J)}\right) \quad (7.14)$$

The function  $K_3$  is a numeric integral dependent on the jet fluid and coflow velocities.

$$K_3(U_J, U_C) = \int_0^L K_1(x, U_J, U_C) dx \quad (7.15)$$

Equations 7.11 through 7.15 show that the temperature function  $\theta_L/\theta_O$  is dependent on the coflow and jet velocities as shown in Figure 7.2. The jet fluid initial temperature is  $T_O = T(0) = 293 \text{ K}$ .

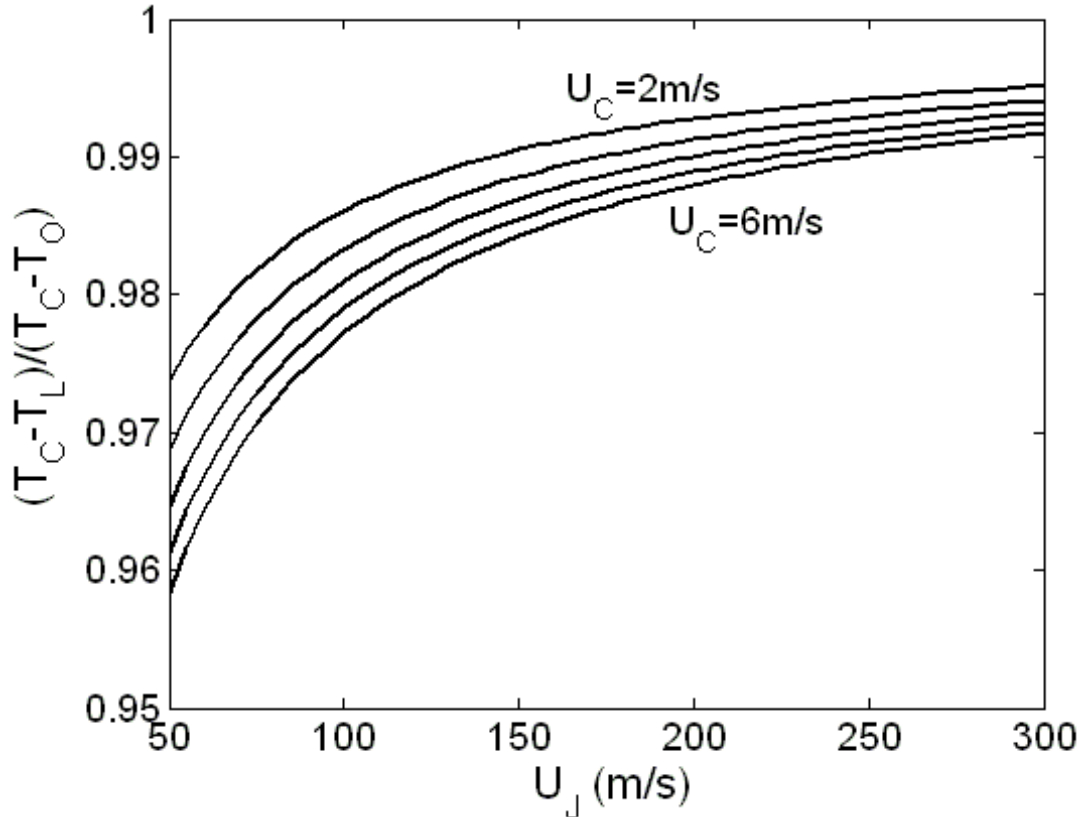


**Figure 7.2.**

Jet exit temperature  $T_L$  dependence on the co-flow temperature  $T_C$  and the co-flow and jet velocities ( $U_C$  and  $U_J$ ). Plotted data is from the numerical solution to Equation 7.14.

The wall temperature at the nozzle exit can be determined once the nozzle exit temperature is known. Solving Equation 7.7 for  $T_w(x)$ :

$$T_w(x=L) = \frac{T_C + K_4 T(x=L)}{1 + K_4} \quad (7.16)$$

where

$$K_4(U_J, U_C) = \frac{r}{R} \frac{h_r}{h_R(x=L)} \quad (7.17)$$

The  $K_4$  ratio is shown in Figure 7.3 for the same ranges of co-flow and jet velocity as in Figure 7.2. As shown in Figure 7.3, the  $K_4$  ratio is on the order of 20 to 60. These values

suggest that the greatest temperature gradient is in the thermal boundary layer between the coflow and the nozzle wall.

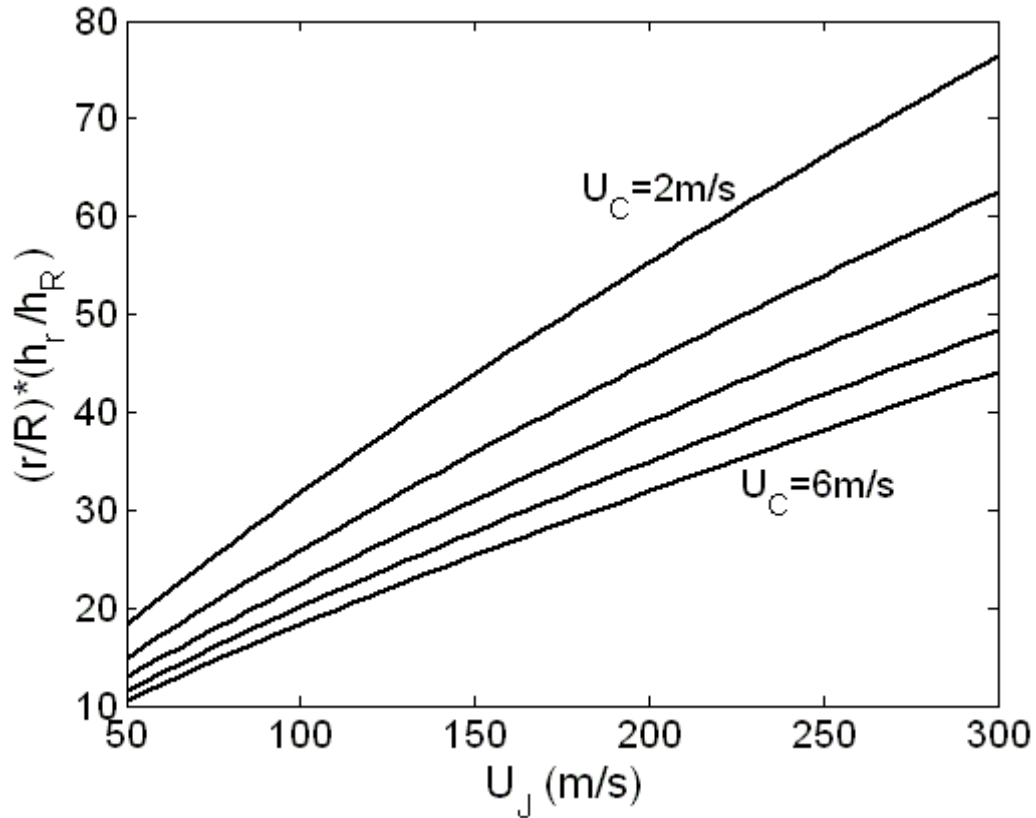


**Figure 7.3.**

The  $K_4$  ratio as a function of the jet fluid and coflow velocities (Equations 7.16 and 7.17).

### 7.3. Mixing (Nonreacting) Jet in Coflow Structure

The measured temperature field of a nonreacting condition is presented to assist in the development of combustion models for the vitiated coflow flame. This nonreacting flow is illustrated in Figure 7.4. A 100% air jet issues into a coflow of products from a  $H_2$ /Air flame with a stoichiometry of  $\phi = 0.31$ . At the nozzle exit, the jet fluid temperature is 310 K and the average velocity is 170 m/s. The coflow temperature is 1,190 K and the approximate coflow velocity is 4.4 m/s.

As previously discussed, the coflow is approximately at the equilibrium composition. Given the stoichiometry ( $\phi = 0.31$ , based on flow rates), the equilibrium conditions are determined with StanJAN; results are listed in Table 7.1.

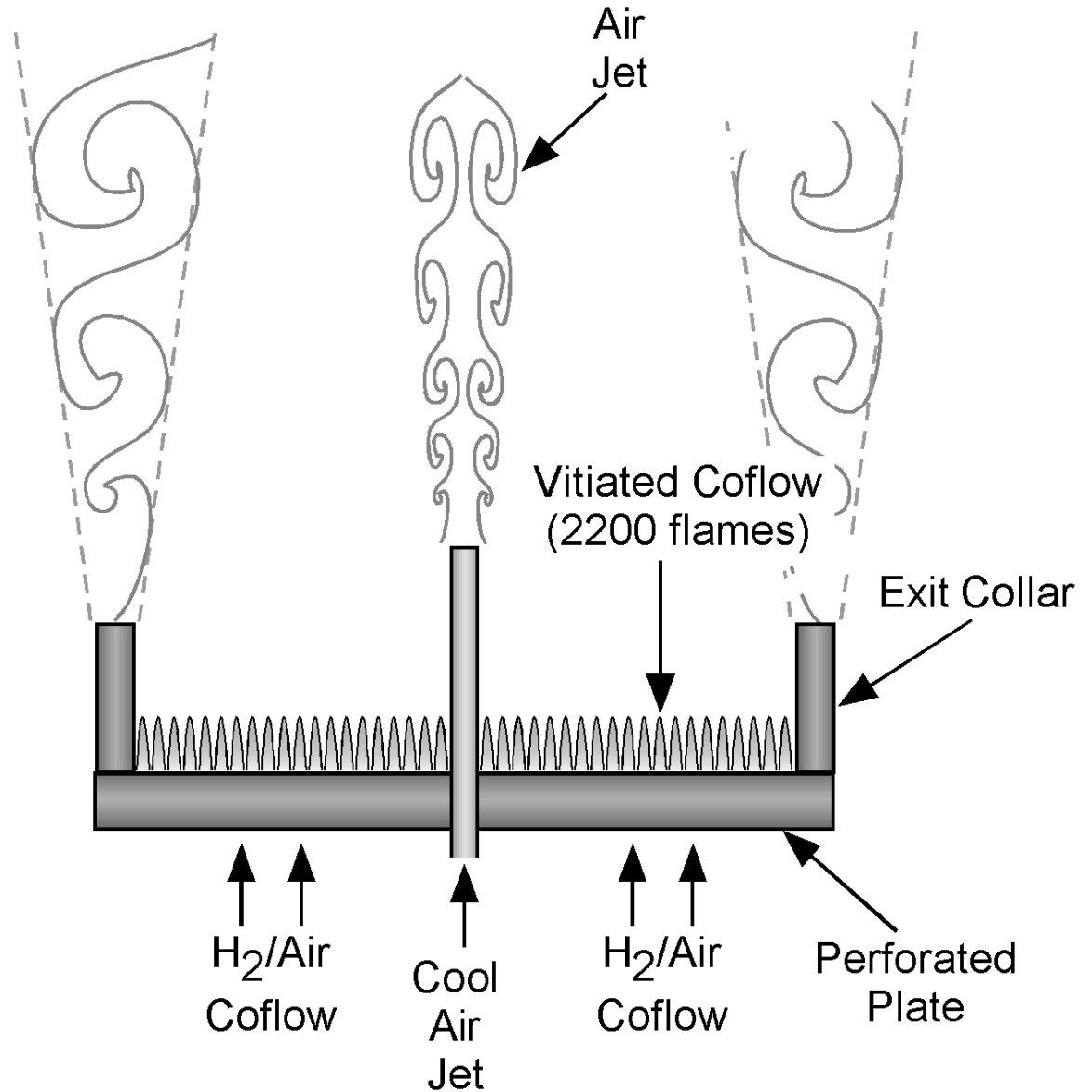


**Figure 7.4.**

Air jet into a vitiated coflow. Burner Geometry: Nozzle ID = 4.57 mm, Nozzle OD = 6.35 mm, Coflow Diameter = 210 mm, Height of Nozzle Exit = 70 mm.

**Table 7.1.**

Equilibrium limit as calculated via StanJAN

Equilibrium Conditions for $\phi = 0.31$ H <sub>2</sub> /Air Flame			
T (K)	1227	X <sub>NO</sub>	204 ppm
X <sub>O<sub>2</sub></sub>	0.135	X <sub>NO<sub>2</sub></sub>	2.37 ppm
X <sub>H<sub>2</sub>O</sub>	0.124	X <sub>O</sub>	1.6x10 <sup>-8</sup>
X <sub>N<sub>2</sub></sub>	0.741	X <sub>H<sub>2</sub></sub>	7.35x10 <sup>-8</sup>
X <sub>OH</sub>	4.2 ppm	X <sub>H</sub>	2.74x10 <sup>-11</sup>

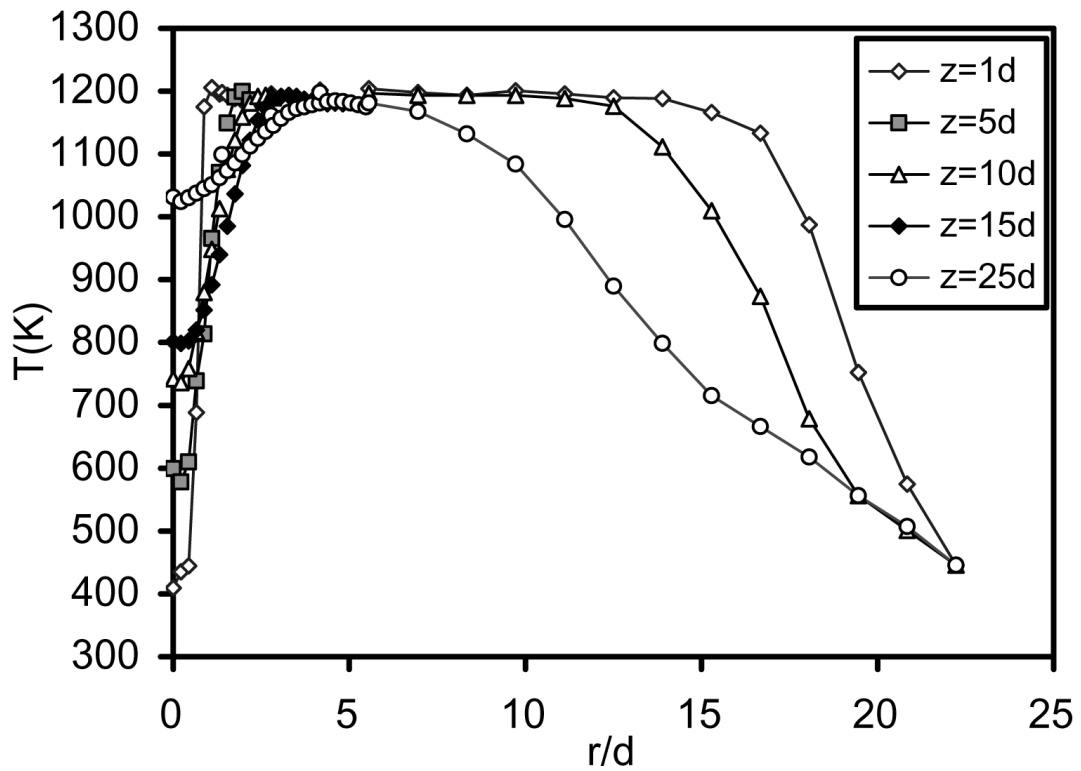


**Figure 7.5.**

Temperature field of a nonreacting air jet in the vitiated coflow ( $\phi = 0.31$ , Figure 7.4).

The temperature field for the nonreacting case was obtained via thermocouple measurements. The temperature radial profiles at 1, 2, 10, 15 and 25 diameters

downstream of the nozzle exit are shown in Figure 7.5. An exposed type K thermocouple with a 1/8" uninsulated sheath was mounted on a two-axis movement stage. The estimated uncertainties are  $\pm 5\%$  ( $\approx 60$  K) for the thermocouple, and  $\pm 2$  mm for the positioning device.

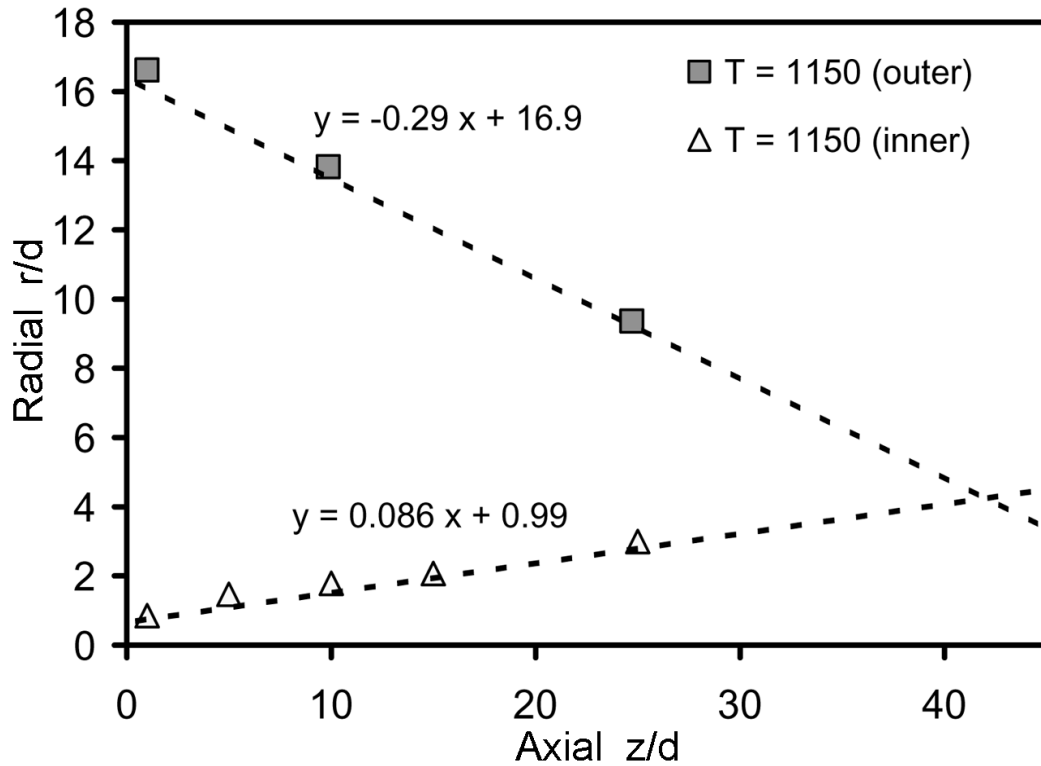


**Figure 7.6.**

Jet spreading rate and coflow rate of degradation for the nonreacting conditions.

The thermocouple used is the same model as the one used to monitor coflow stoichiometry discussed in Section 4.4.3; therefore, the radiative heat losses are the same. The calibration ( $C_{\text{Rad}} = 1.225$ , Equation 4.12) is fairly accurate at the coflow temperatures (1,000-1,400 K). However, the data in Figure 7.5 reveals inaccuracies at lower temperatures where radiative losses are minimal (e.g., jet fluid exit temperature of  $\approx 400$  K). The jet fluid exit temperature is approximately 310 K, as measured by a thin thermocouple in the jet nozzle about 3 diameters upstream of the exit; also, this value is

consistent with the prediction ( $T_L = 306$  K) from the heat transfer model previously discussed in Section 7.2. While this disparity is rather large (100 K), the results do provide useful mixing characteristics for the validation of numerical models.

The spreading rate of the central jet can be used to test numerical models. Figure 7.6 shows the spreading rate of the central jet, and the rate of degradation of the coflow for the nonreacting conditions. Both boundaries are determined as the location of the temperature contour of 1,150 K (about 95% of the coflow temperature). The coflow and jet structure presented in Figure 7.6 show that the jet is isolated from the coflow up to an axial distance of  $z/d \approx 42$ .

#### **7.4. Two-Stream Flow Condition**

It is imperative that the coflow (isolate the jet flame from the laboratory air for a maximum downstream distance, providing a two-stream flow. At lower coflow Froude numbers (i.e., ratio of momentum flux to buoyant forces, Section 4.3.4), an increase in velocity increases the distance over which the two-stream flow is achieved by reducing the buoyancy effects. Once the coflow is momentum driven (i.e., Froude number  $Fr > 1$ ), any further increase in Froude number does not increase the target volume because the coflow degradation rate becomes solely dependent on the ratio of coflow and ambient air densities. An analysis is now presented that shows the extent to which the two-stream condition may be assumed over a range of coflow temperatures.

The instabilities due to velocity gradients between the jet-coflow and coflow-ambient air streams give rise to turbulent shear layers. Figure 7.7 illustrates the coaxial turbulent shear layers between the three streams in the vitiated coflow flame (i.e., jet, coflow, and ambient/quiescent air). As seen in Figure 7.7, the distance over which the

central jet is isolated from the lab air is  $Z_{2S}$  (distance of two-stream condition). In order to determine this distance, both shear layers must be characterized.

It is often the case that the turbulent shear layer grows linearly with distance. For the coflow into the quiescent medium (i.e., ambient air) the spread rate of the shear layer is linear with distance, and independent of the coflow velocity (Abamovich 1963). It is, however, dependent on the density ratio between the two streams. The jet and coflow shear layer, there is a dependence on the velocity ratio of the two flow streams.

Figure 7.8 compares the nonreacting-spreading rate upstream of the flame base for the methane and hydrogen flames presented in Chapter 6, with the nonreacting air jet presented in the Section 7.3. The methane and hydrogen flames in Chapter 6 are henceforth called “VCB@Sandia” flames. The jet boundary width for each condition is defined as the location where the coflow temperature drops 5%. Results show that all three nonreacting conditions exhibit similar spreading rates. The differences between the air jet and the two VCB@Sandia flames are attributable to a 70% higher jet to coflow velocity ratio ( $U_J/U_C$ ) and to a 10% higher jet density. As the theory predicts, the VCB@Sandia flame structures are closely similar because of comparable density and velocity ratios. Interestingly, despite a density ratio ( $\theta = \rho_C/\rho_J$ ) of 0.2, the spread rate for these jets is virtually identical to the empirical spread rate of an isothermal jet in a quiescent medium ( $R = z/11.6$ , Blevins 1992). Note that the coflow is nearly quiescent since the jet velocity (100 to 170 m/s) is much greater than the coflow velocity (3 to 6 m/s).

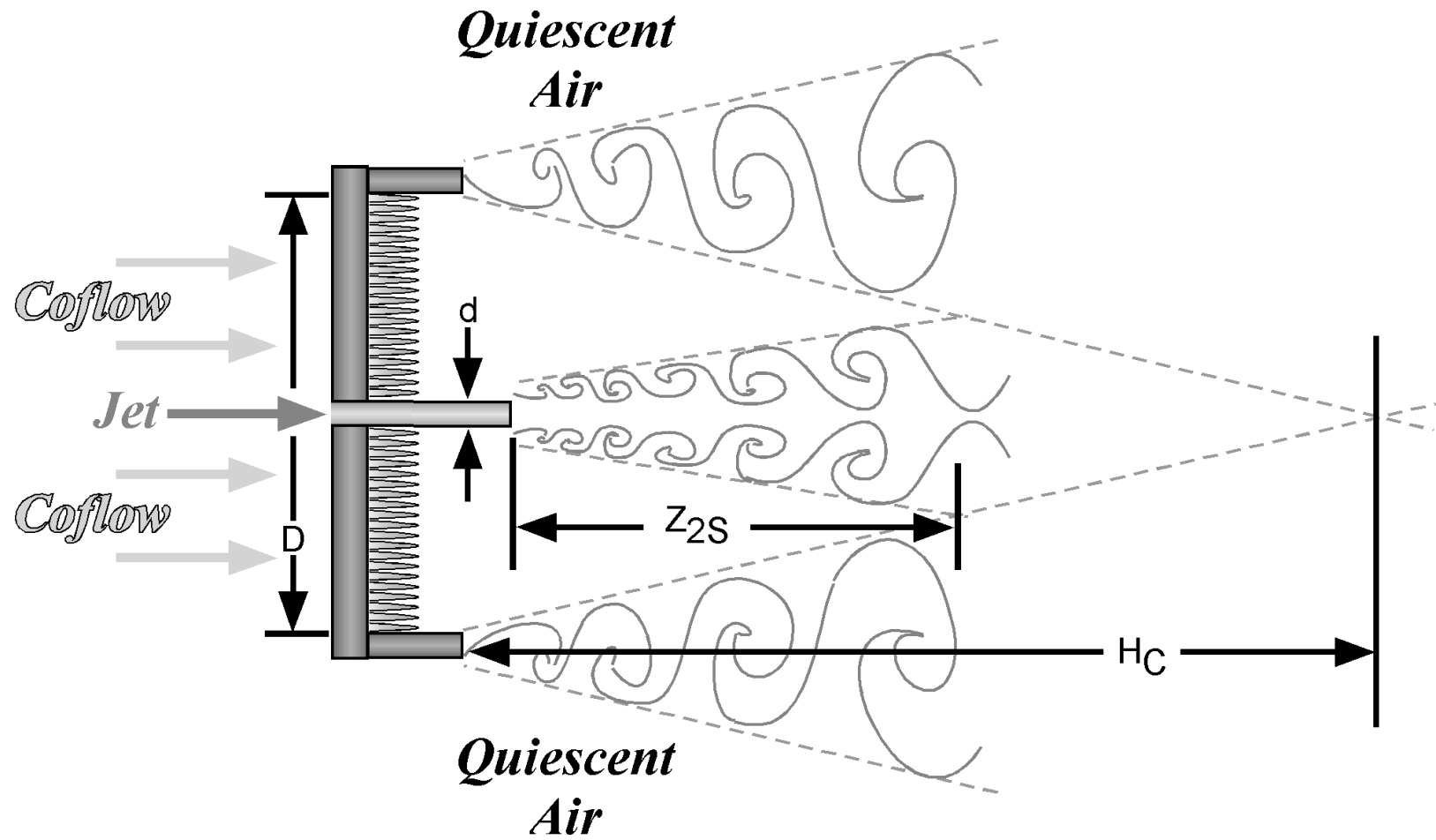
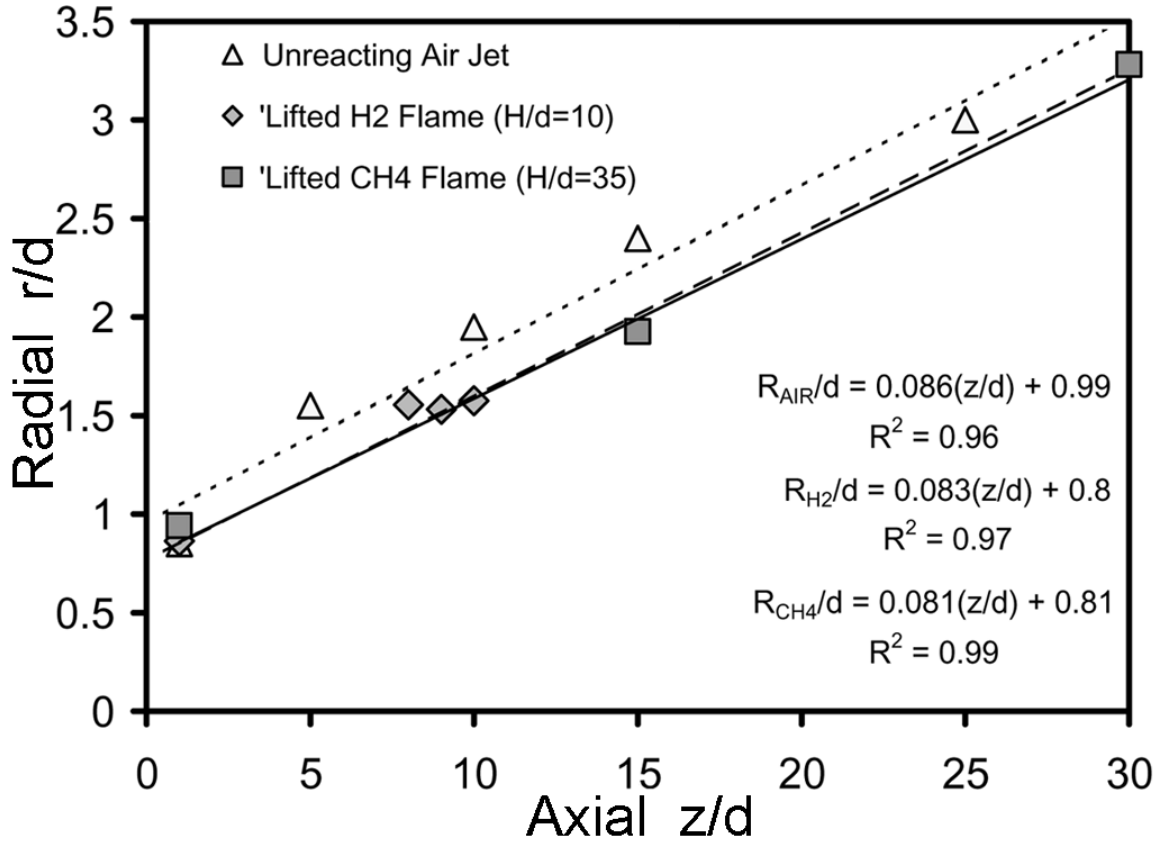


Figure 7.7.

Turbulent shear layers between the three streams of the vitiated coflow flame.



**Figure 7.8.**

Nonreacting jet spreading rate for the VCB@Sandia flames and the nonreacting flow.

In order to determine the height of the two-stream condition  $Z_{2S}$ , the coflow degradation rate is also needed. The degradation rate is determined via the coflow potential core  $H_C$ , as shown in Figure 7.7. The potential core is the height over which the temperature and the velocity fields are uniform and isolated from the ambient laboratory air. Because only two observations have been made (i.e., VCB@Sandia methane flame, and mixing condition), the turbulent model described by Abramovich (1963) was also implemented.

$$\frac{H_C}{D} = \left[ \frac{r_1}{\delta} \left( \frac{\delta}{x} \right)_{\theta=1} \left( \frac{\theta+1}{2} \right) \left( \frac{1-m}{1+\theta m} \right) \right]^{-1} \quad (7.18)$$

Where the inner boundary of the coflow  $r_1/\delta$  is determined by a set of equations dependent on the density ratio between the coflow and the ambient air  $\theta = \rho_A/\rho_C \approx T_C/T_A$  and the velocity ratio  $m = U_A/U_C$ .

$$\frac{r_1}{\delta} = \theta[(A(\theta) - 2B(\theta) + C(\theta)) + m(B(\theta) - A(\theta))] \quad (7.19)$$

$$A(\theta) = \frac{0.316}{1 + 0.28(\theta^{0.75} - 1)} \quad (7.19a)$$

$$B(\theta) = \frac{0.450}{1 + 0.375(\theta^{0.75} - 1)} \quad (7.19b)$$

$$C(\theta) = \frac{\ln \theta}{\theta - 1} \quad (7.19c)$$

The potential core degradation rate for a uniform density jet  $b = (\delta/x)_{\theta=1}$  is reported in the literature to be between 0.22 and 0.3. The best fit for the vitiated coflow data is  $b = 0.24$ .

The potential core height for the VCB@Sandia methane flame and the mixing condition is determined by the radial profiles of the temperature. Since the ambient temperatures are identical at about 15 °C, the relationship between the potential core and the coflow temperature is plotted in Figure 7.9. Plotted alongside these two data points is the model, Equation 7.18. The uniform density potential core degradation rate  $b$  and the velocity ratio  $m$  are adjusted for the best fit.

The exhaust system at Sandia is much stronger than that at the University of California at Berkeley's Combustion Analysis Laboratory at the time the mixing experiment was conducted (June 2000). Therefore, it is reasonable to assume that Berkeley's mixing flow is of a hot coflow in a quiescent environment ( $m \approx 0$ ) and the VCB@Sandia flow is that of a hot coflow in a slow moving environment ( $m \approx 0.1$ ). In

the Fall of 2000, Berkeley's exhaust system was upgraded and a sheath was constructed (similar to the one at Sandia) to isolate the experiment from drafts in the laboratory. The parametric study (presented in Chapter 8) was conducted with the upgraded exhaust system to preserve similarity with the Sandia experiments.

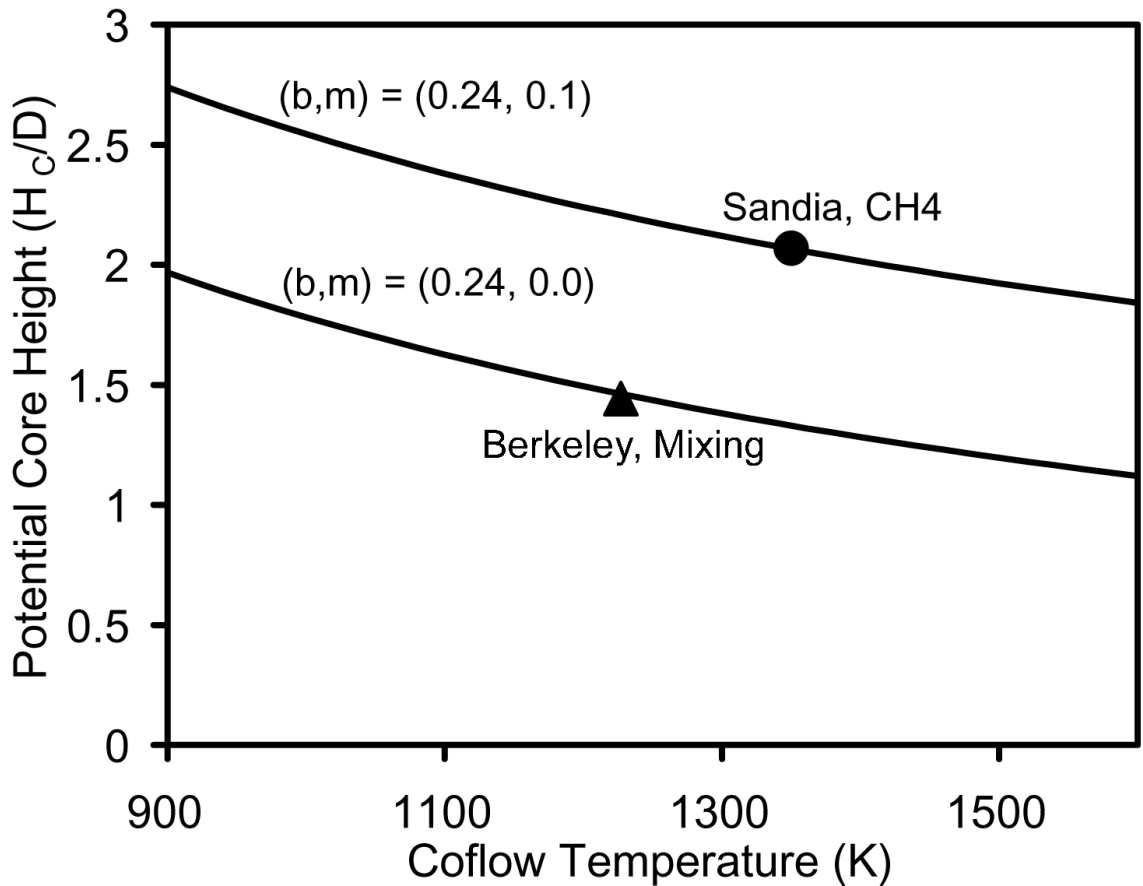


**Figure 7.9.**

The coflow potential core height as a function of the coflow temperature. The solid line is an empirical model (Abramovich 1963, Equation 7.18).

The dependence of the two-stream condition height on the coflow temperature is shown in Figure 7.10. The data points are from the temperature radial profiles of the Sandia methane flame and the Berkeley mixing condition, while the solid curves are from an empirical model based on the coflow potential core height  $H_C$  (Equation 7.18, Figure

7.9) and the jet width spreading rate (Figure 7.10). These limits must be taken into account when analyzing experimental observations made at high axial locations, as will be presented in the next Chapter.

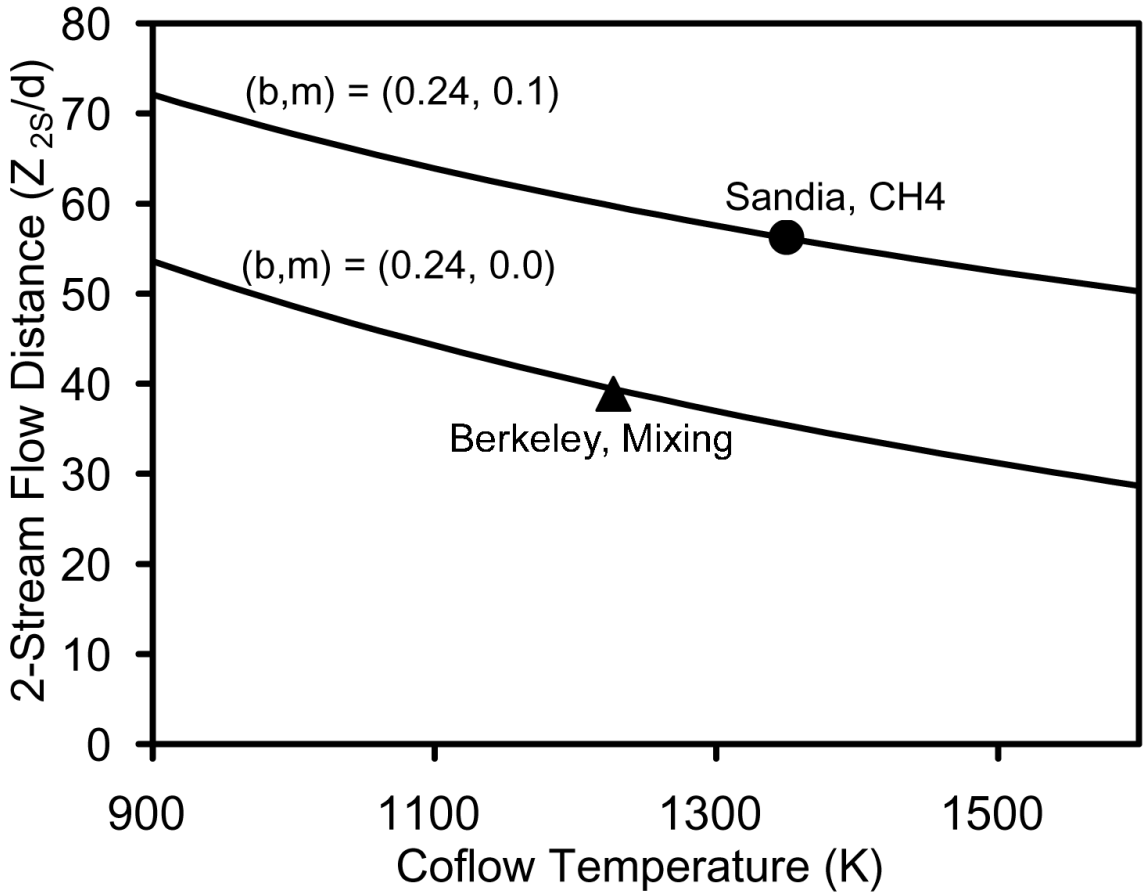


**Figure 7.10.**

The two-stream condition height (Figure 7.7) relationship to the coflow temperature.

### 7.5. Near-Equilibrium Coflow Conditions

The laser diagnostic results presented in Chapter 6 demonstrate that the coflow was nearly at the equilibrium limit. The coflow temperature and composition as measured were closely similar to the equilibrium values calculated via StanJAN. The close comparisons between the expected and measured boundary conditions (initial conditions) are listed in Table 7.2. Besides the jet fluid temperature at the nozzle exit, the

flow measurements were used to determine the “Expected” conditions. Jet fluid temperature was estimated using the heat transfer model developed in Section 7.2. Coflow composition and temperature were calculated with StanJAN. The values listed in the “Actual” columns are the Favre averaged measurements from the Sandia experiments.

**Table 7.2.**

Comparisons between expected and actual boundary conditions.

<b>Methane Flame</b>				
	Expected		Actual (Favre Ave.)	
	Jet	Coflow	Jet	Coflow
<b>T (K)</b>	318	1427	320	1350
<b>XCH<sub>4</sub></b>	0.333	0	0.33	0.0003
<b>XO<sub>2</sub></b>	0.155	0.116	0.15	0.12
<b>XN<sub>2</sub></b>	0.511	0.728	0.52	0.73
<b>XH<sub>2</sub>O</b>	0	0.155	0.0029	0.15
<b>XOH (ppm)</b>	0	44.4	< 1	200
<b>XNO (ppm)</b>	0	655	< 1	< 1
<b>XH<sub>2</sub> (ppm)</b>	0	0.31	100	100
<b>f<sub>st</sub></b>	0.172		0.177	
<b>Hydrogen Flame</b>				
	Expected		Actual (Favre Ave.)	
	Jet	Coflow	Jet	Coflow
<b>T (K)</b>	306	1,080	305	1,045
<b>XO<sub>2</sub></b>	0	0.148	0.0021	0.15
<b>XN<sub>2</sub></b>	0.748	0.749	0.74	0.75
<b>XH<sub>2</sub>O</b>	0	0.103	0.0015	0.099
<b>XOH (ppm)</b>	0	0.46	< 1	< 1
<b>XH<sub>2</sub></b>	0.252	0	0.25	5 x 10 <sup>-4</sup>
<b>f<sub>st</sub></b>	0.478		0.473	

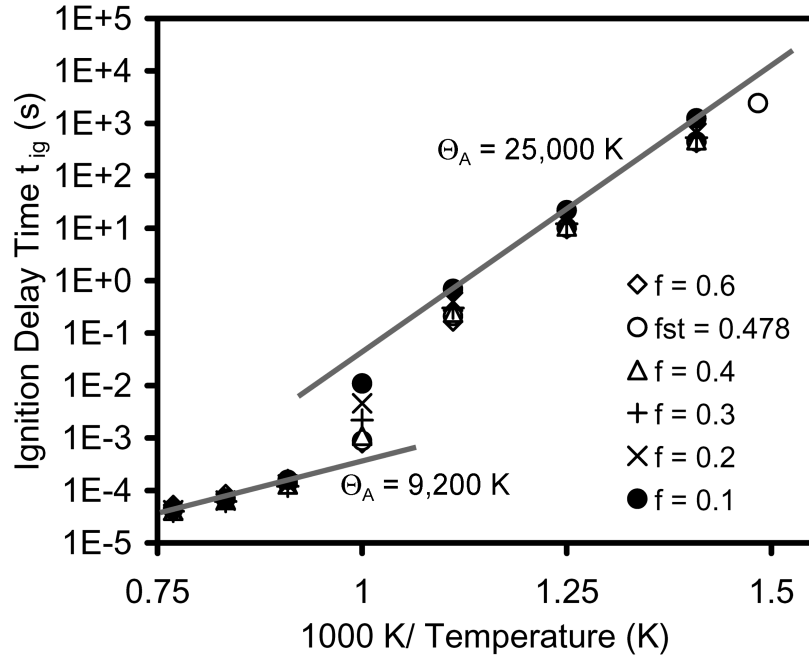
## 7.6. Sensitivity of Reactions to Coflow Radical Species and Temperature

Coflow temperatures and major specie compositions are well known, however, the minor specie concentrations are not. The Sandia laser diagnostic measurements provide temperature, major specie, and some minor specie concentrations in the coflow. Radiative and convective heat losses result in a departure from adiabatic temperature and composition. The laser diagnostic results show that the major specie concentrations are virtually at equilibrium for the two cases studied. Also, oxygen probe measurements show equilibrium concentrations over the entire range of coflow conditions (Figure 4.19). The reduced coflow temperature is also well characterized (Figure 4.20 and Equation 4.15). However, there is limited information regarding the minor specie concentrations in the coflow; these observations are made on the two VCB@Sandia flames.

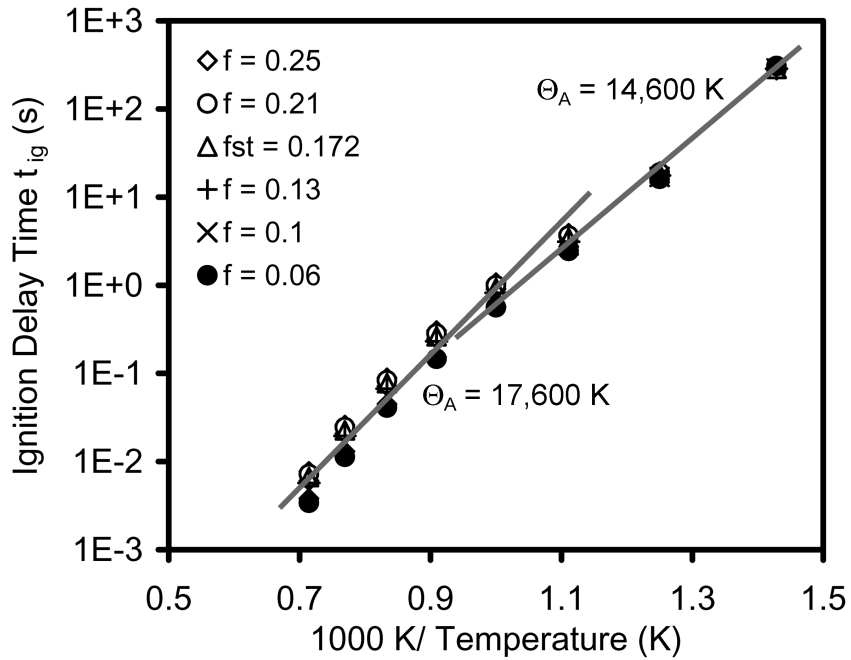
Numerical results show that departure from adiabatic coflow temperature is much more influential on the jet flame than the departure of minor specie concentration. Of course, this is only a confirmation of the well-known Arrhenius model for the chemical reaction rate, where the production rate is exponentially related to the temperature and often linearly related to reactant composition. E.g.,

$$\frac{d[P]}{dt} \propto [R]^a \exp\left(-\frac{E_A}{R_U T}\right) \propto [OH]^b \exp\left(-\frac{\Theta_A}{T}\right) \quad (7.20)$$

An associated time scale for a given reaction is the ignition delay time, where the ignition delay time is inversely proportional to the rate term of Equation 7.20 (Warnatz et al. 2000).



(A) Hydrogen flame conditions, PFR numerical model



(B) Methane flame conditions, PFR numerical model

**Figure 7.11.**

Ignition delay time versus initial mixture temperature for the VCB@Sandia flames as calculated with the Plug Flow Reactor (PFR) numerical model.

Ignition delay times calculated by the Plug Flow Reactor (PFR) option of the Well-Mixed Reactor model (WMR, Section 3.2) are much more sensitive to the initial temperature than the initial OH mole fraction. Given the initial jet and coflow compositions for the two VCB@Sandia flames, the mixture fraction and temperature were varied independently. Figure 7.11 shows the high sensitivity of the ignition delay time to the inverse temperature ( $1000/T$ ). The curves exhibit the exponential relationship between the ignition delay time and the mixture temperature. Interestingly, there are transitions in the chemical kinetics for both conditions at temperatures around 1,000 K ( $1000/T = 1$ ). The activation temperature (Equation 7.20,  $\Theta_A = E_A/R$ ) switches from 25,000 K to 9,200 K as the temperature increases beyond 1,000 K (i.e., from right to left on Figure 7.11A and B,  $1000/T > 1$  to  $1000/T < 1$ ) for hydrogen conditions and from 14,600 K to 17,600 K for the methane conditions. The transitions illustrate the vast difference between laboratory flames into ambient air and flames into hot environments such as the vitiated coflow burner and actual combustors. The implications of this transition and the vitiated coflow environment will be discussed with respect to stabilization in Sections 9.1 and 9.2.

On the other hand, the numerical results show that the combustion processes are weakly sensitive to the OH concentration. Figure 7.12 shows the effect OH concentration has on the ignition delay time as modeled by PFR. As can be seen in Figure 7.12, it takes at least a one order of magnitude departure from equilibrium of the OH concentration to significantly effect the ignition delay time. The measured coflow OH concentration for both VCB@Sandia flames are less than 1 order of magnitude greater than the equilibrium condition (Methane:  $X_{OH,Act} = 200$  ppm,  $X_{OH,Eq} = 40$  ppm;

Hydrogen:  $X_{OH,Act} < 1$  ppm,  $X_{OH,Eq} = \frac{1}{2}$  ppm). The results plotted in Figure 7.12 therefore suggest that the possible departure from equilibrium of the OH concentration in the coflow has a negligible impact on the combustion processes in the vitiated coflow environment.

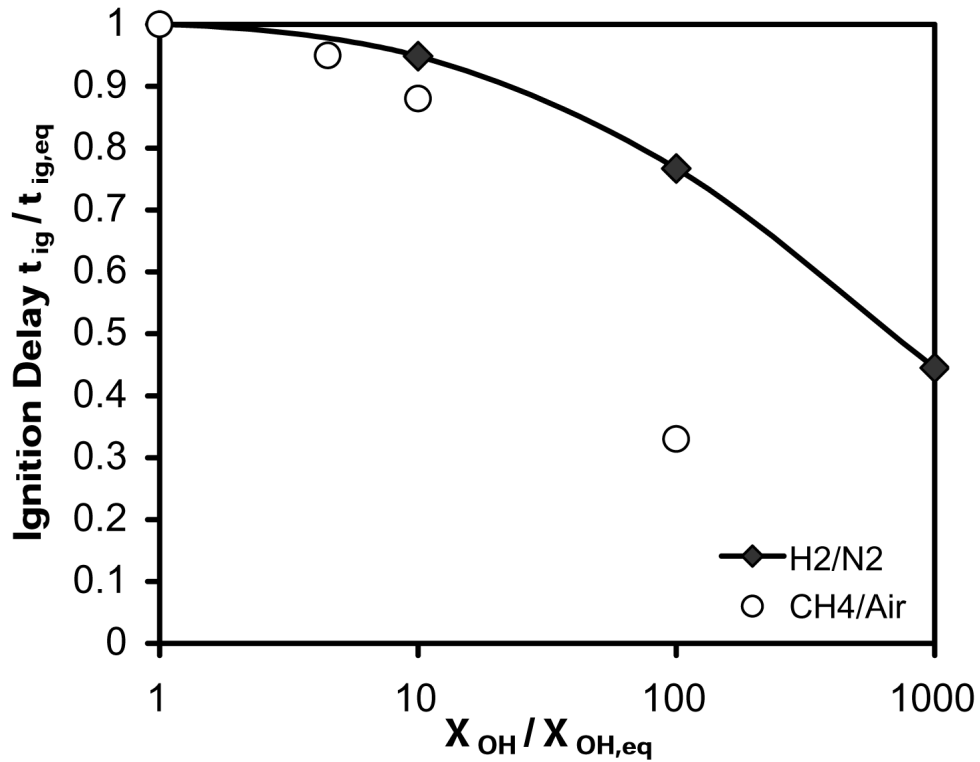


**Figure 7.12.**

Ignition delay time versus departure from equilibrium of OH mole fraction for the VCB@Sandia flames. The OH LIF detection limit is 1 ppm, or  $X_{OH,Det}/X_{OH,eq} = 2$  for H<sub>2</sub>/N<sub>2</sub>, and  $X_{OH,Det}/X_{OH,eq} = 0.02$  for CH<sub>4</sub>/Air.

## Chapter 8

### Parametric Study of CH<sub>4</sub>/Air Lifted Jet Flames

A study of the flame structure sensitivity to flow conditions was conducted to complement the comprehensive experimental results for the two specific conditions reported in Chapters 6 and 7. The sensitivity of flame lift-off height and blow-off to flow composition, temperature and velocity is reported in Chapter 8. These results round off the body of data that can be used in the development and validation of combustion models. The sequence of experimental results are as follows: (1) temperature measurements for a nonreacting condition, (2) comprehensive multiscale measurements for a hydrogen flame, (3) comprehensive multiscale measurements for a methane flame, and (4) parametric study of methane flame structure. This sequence of increased complexity is consistent with the typical approach for validation of analytical and numerical models.

**Table 8.1.**

Base Case Conditions for CH<sub>4</sub>/Air Flame.

Central Jet		Coflow	
T <sub>JET</sub> (K)	320	T <sub>COFLOW</sub> (K)	1,350
V <sub>JET</sub> (m/s)	100	V <sub>COFLOW</sub> (m/s)	5.4
Re <sub>JET</sub>	28,000	Re <sub>COFLOW</sub>	23,300
d <sub>JET</sub> (mm)	4.57	D <sub>COFLOW</sub> (mm)	210
		φ	0.4
X <sub>CH4</sub>	0.33	X <sub>H2O</sub>	0.15
X <sub>O2</sub>	0.15	X <sub>O2</sub>	0.12
X <sub>N2</sub>	0.52	X <sub>N2</sub>	0.73

The parametric study represents a set of excursions from the methane flame condition studied at the TDF laboratory. The base case condition was presented in Chapter 6 (Table 6.2) and is summarized in Table 8.1. The coflow velocity and jet velocity may be varied independently of each other and independently of the jet and coflow compositions. The jet temperature is dependent on the coflow temperature and jet and coflow velocities (Section 7.3). Adjusting the coflow stoichiometry controls the coflow temperature; accordingly, the coflow temperature and composition are dependent.

### **8.1. Lift-Off Height**

The lift-off height of the methane flame was measured using a novel digital imaging experimental setup. A Sony Mavica digital camera (MVC-FD85), with a 1.3 Megapixel resolution was implemented for this purpose. The camera was mounted on a stand, and calibrated with a target before and after each set of experiments. The lift-off height is determined as the lowest point where luminosity from the flame is detected. Figure 8.1 illustrates how the lift-off height is determined.

### **8.2. Lift-Off Height Sensitivity to Jet and Coflow Velocities**

The sensitivity of the lift-off height to jet and coflow velocities is presented in Figure 8.2. The linear relationship between the lift-off height and the jet velocity is in agreement with previously reported results (Kalghatgi 1984). The coflow velocity affects the lift-off height by creating an offset in the jet velocity correlation. The shaded area in Figure 8.2 represents the base case condition as presented in Chapter 6. The solid black line is the engineering correlation presented by Kalghatgi (1984).

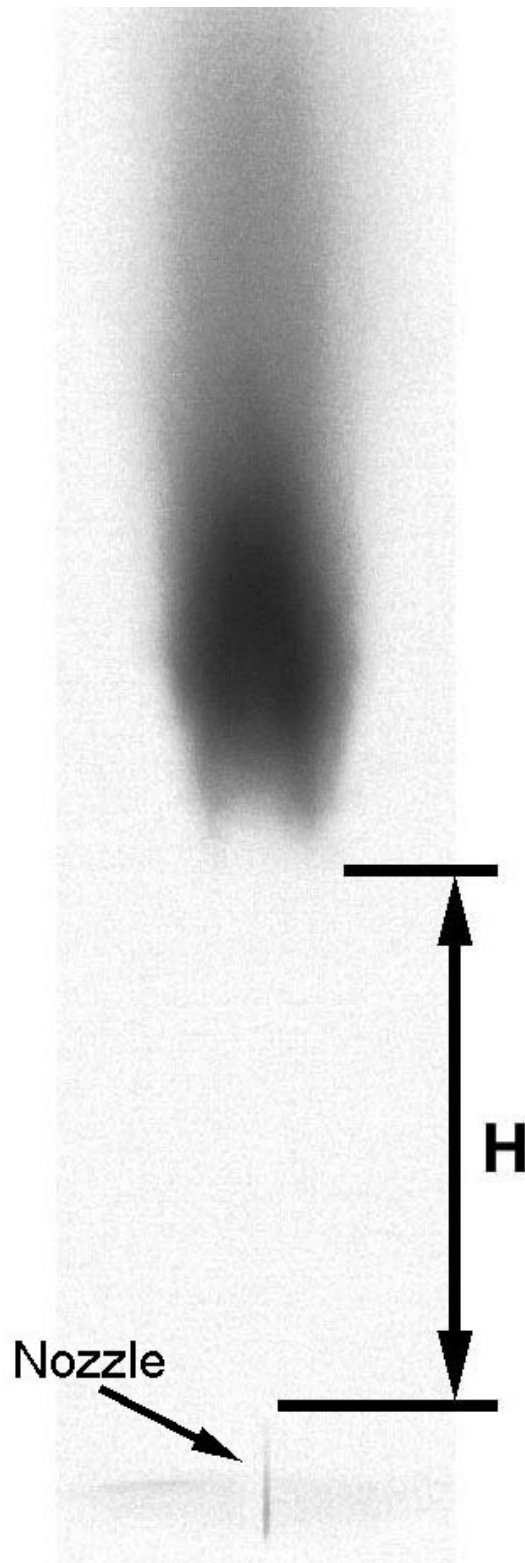


**Figure 8.1.**

Image of the lifted jet flame. The image is a negative of the acquired digital picture.

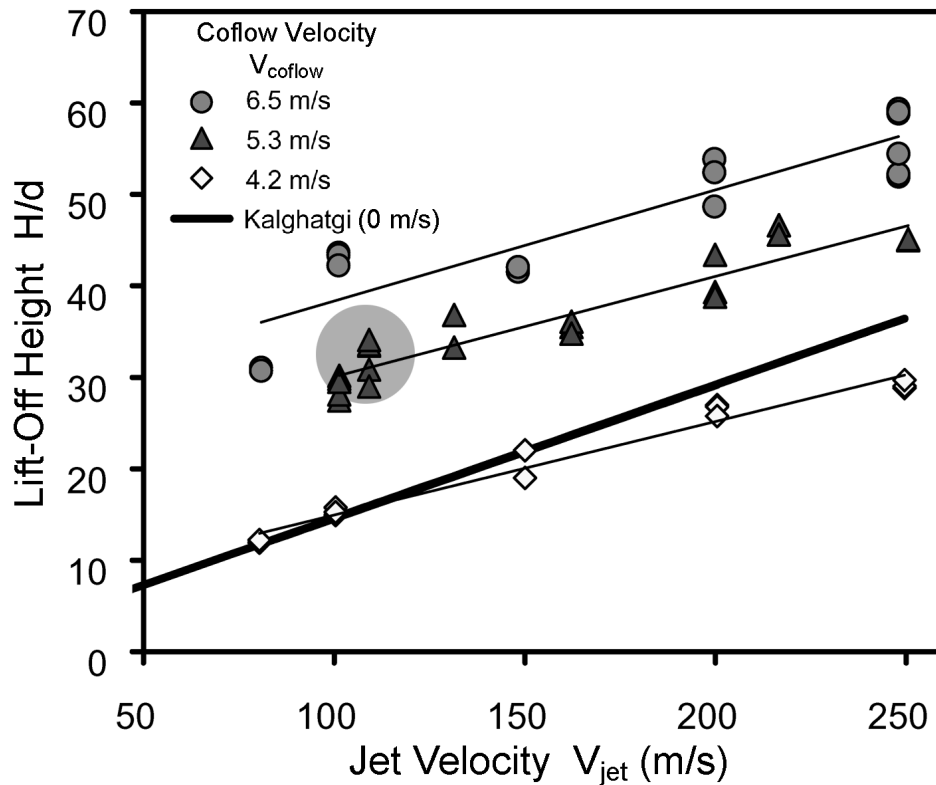


**Figure 8.2.**

Sensitivity of methane/air flame lift-off height to coflow and jet velocities. The shaded circle represents the base case condition. Thin lines are trend lines for the experimental data.

Kalghatgi initially proposed a correlation for the lift-off height based upon scaling arguments (1984). This correlation is dependent on the laminar flame speed, coflow density, as well as jet velocity, viscosity and density. Assuming both coflow and jet gases are ideal, manipulation of the correlation results in the following expression:

$$H_K = 50 \left( \frac{v_{jet} U_{jet}}{S_{L,max}^2} \right) \left( \frac{T_{coflow} M_{jet}}{T_{jet} M_{coflow}} \right)^{1.5} \quad (8.1)$$

Lift-off height data for a vast array of flow conditions and fuels was used to develop this correlation. For the hydrogen flame presented in Chapter 6 ( $H/d = 10$ ), this engineering correlation reasonably predicts the lift-off height ( $H_K/d = 11.4$ ). However, there is a discrepancy between the correlation and the methane flame data presented in Figure 8.2; this is due in part to the conspicuous omission of coflow velocity in Equation 8.1. Regardless of coflow velocity, there is a common sensitivity of the lift-off height to the jet velocity (i.e., thin parallel trend lines in Figure 8.2). As can be seen in Figure 8.3, there is also a linear relationship between the coflow velocity and the lift-off height.

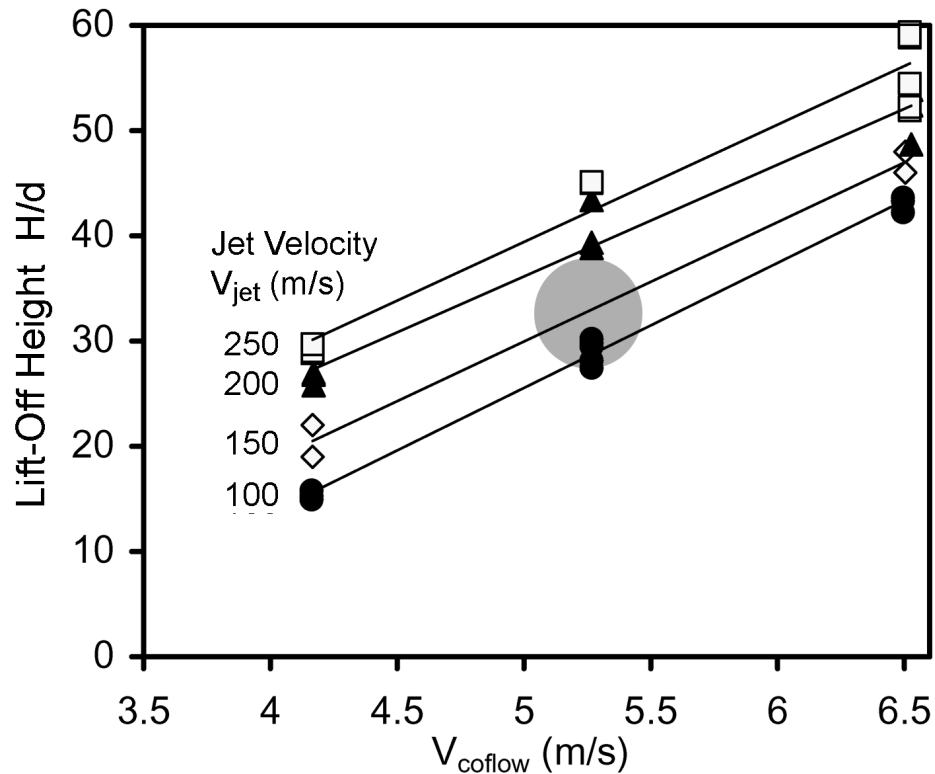


**Figure 8.3.**

Sensitivity of methane/air flame lift-off height to coflow and jet velocities. The shaded circle represents the base case condition. Thin lines are trend lines for the experimental data.

The lift-off height data indicates a stronger sensitivity to coflow velocity than to jet velocity. Dahm and Dibble (1988) reported a similar coflow velocity sensitivity for jet flames into a cool, quiescent air environment. Their experimental results can be loosely compared to numerical results from the EDC combustion model; this EDC model was implemented on the hydrogen flame condition (Cabra et al. 2002). The EDC results showed that a 20% increase in jet velocity resulted in a 25% increase in lift-off height; this is in agreement with the presented data (Figure 8.2). The model predicted only a 50% increase in the lift-off height from a 300% increase in coflow velocity; the experimental results presented (Figure 8.3) indicate a much higher sensitivity to coflow velocity. These comparisons to the EDC model are only loose because of the differences in chemical kinetic detail as well as the difference in length scales of the flame structure.

### **8.3. Lift-Off Height Sensitivity to Coflow Temperature**

The sensitivity of the lift-off height to the coflow temperature was observed. While maintaining constant jet and coflow velocities (base case conditions), the coflow temperature was reduced. Reduction of the coflow stoichiometry also reduces the coflow temperature, resulting in higher oxygen content and lower water vapor content in the coflow (Section 4.3.3). Also, the nozzle exit temperature of the jet fluid decreases with reduced coflow temperature (Section 7.3). As expected, the lift-off height is highly sensitive to coflow temperature, as shown in Figure 8.4. The Kalghatgi correlation is less sensitive to coflow temperature; this is possibly due to oversimplification of the chemistry by the Kalghatgi model.

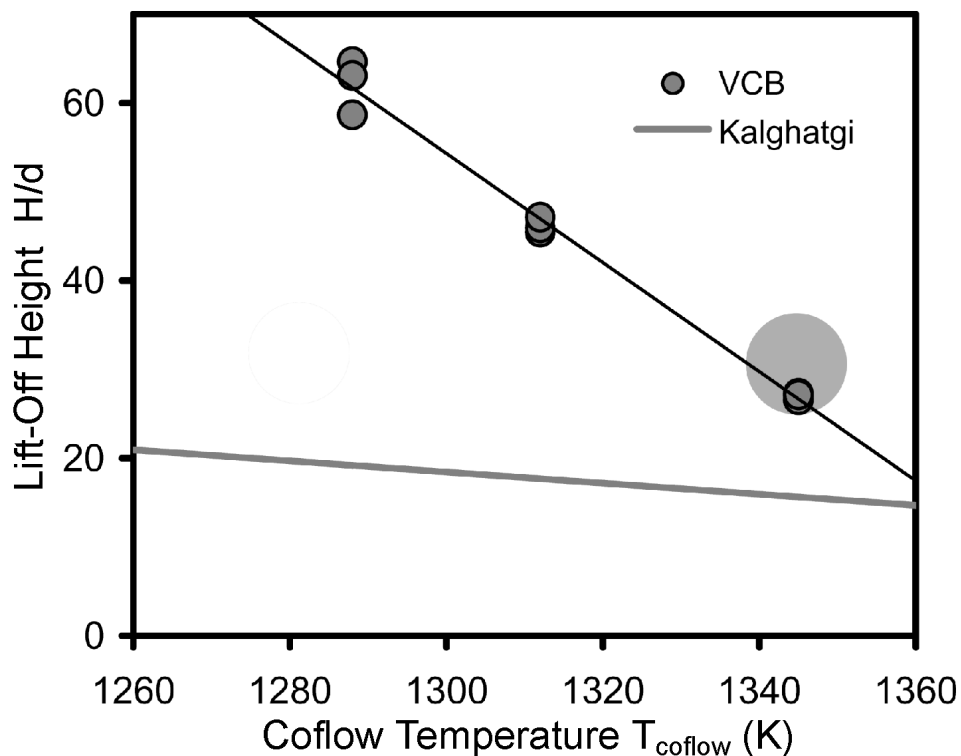


**Figure 8.4.**

Sensitivity of methane/air flame lift-off height to coflow temperature. The shaded circle represents the base case condition. Thin line is a trend line for the experimental data.

#### **8.4. Flame Blow-Off Due to Reduced Coflow Temperature**

During the temperature sensitivity experiments (Figure 8.4), jet flame was observed to blow off at coflow temperatures below 1260 K, regardless of adjustment in velocity. In experiments where the jet and coflow velocities were initially set, the coflow temperature is reduced to below 1260 K. The results are shown below in Figure 8.5. As initially thought, the flame would blow-off at coflow temperatures of 1260 K regardless of jet or coflow velocity.

This blow-off phenomenon was studied using the SSPSR numerical code (described in Section 3.2). The SSPSR model examines the chemical kinetics at extinction due to shorter and shorter reactor residence times. The inlet composition is

that of the stoichiometric mixture for the base case conditions (Table 8.1). The inlet PSR temperature is adjusted dependent on the coflow temperature, jet temperature, and stoichiometric mixture fraction. For a range of coflow temperatures, the extinction time scale was determined and the results are plotted in Figure 8.6. As can be seen, the extinction time scale rapidly increases with decreased coflow temperatures below 1260 K. Therefore, a possible explanation for the trend shown in Figure 8.5 is that the time scale required for sustained reaction would be too long for coflow temperatures below 1260 K.

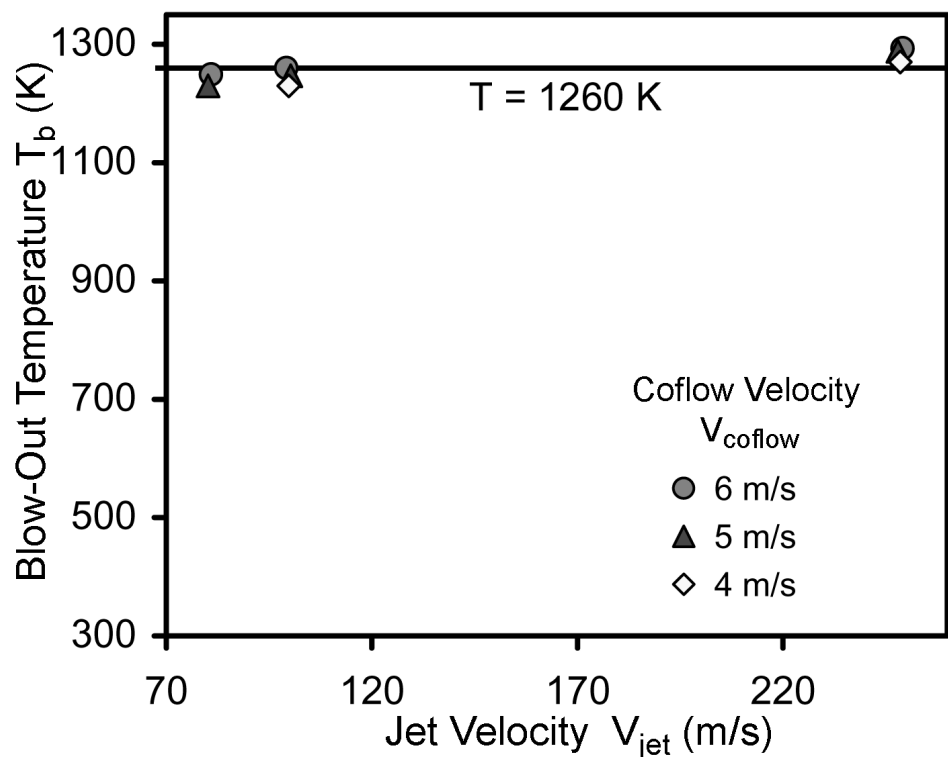


**Figure 8.5.**

Temperature of coflow at flame blow-off is independent of jet and coflow velocities.

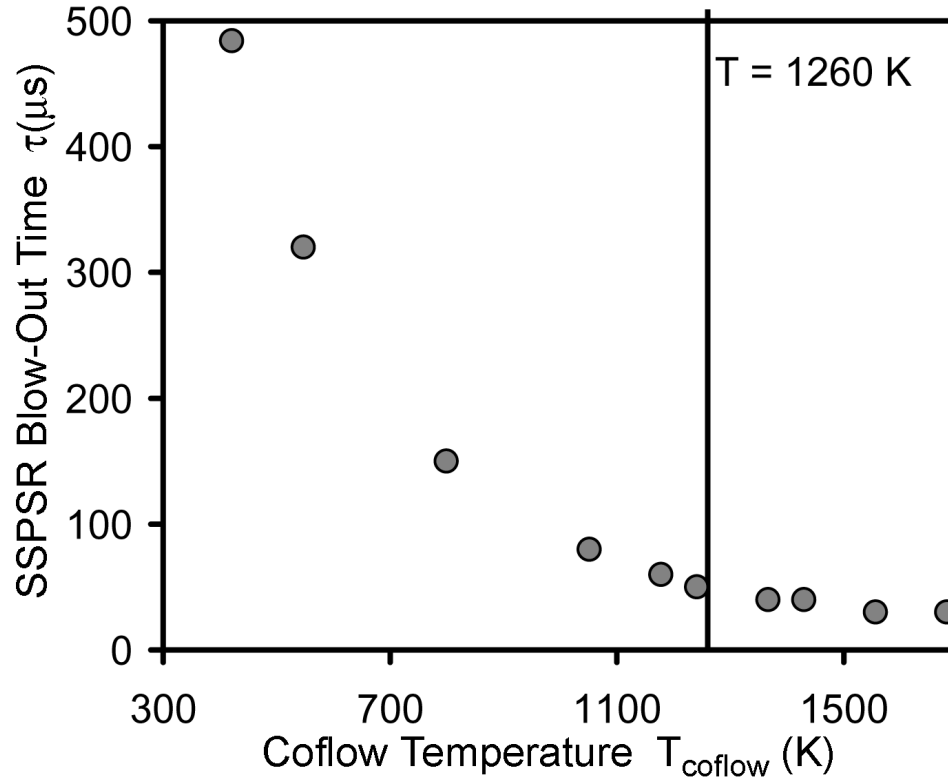


**Figure 8.6.**

The extinction time scale increases dramatically with decreased coflow temperature.

The common blow-off temperature for the diverse set of flow conditions shown in Figure 8.5 suggest that blow-off of lifted flames into a vitiated coflow is the result of dilution of the jet and coflow with ambient air. Since the jet-coflow and coflow-ambient shear layers' growth rates are dependent on temperature only, the geometry of the flow (i.e., the spatial parameters shown in Figure 7.7) is the same at all blow-off conditions. It has been shown (Figure 8.4) that as the coflow temperature is decreased towards 1260 K, the lift-off height increases beyond the two-stream condition height ( $Z_{2s}/d = 60$ , Figure 7.12), meaning that the jet and coflow mixture have been diluted by cool ambient air. It may be this ambient air entrainment that dramatically retards the chemical kinetics (Figure 8.6), causing blow-off. It is possible that, in the case of an infinitely large

vitiated coflow (i.e., no ambient air), blow-off of an already lifted flame would not occur. The presented findings provide a basis for discussion of possible flame stabilization mechanisms of jet flames into a vitiated coflow.

## Chapter 9

### Stabilization of Lifted Jet Flames

The hot environment provided by the vitiated coflow enables the stabilization of highly turbulent, lifted jet flames that would otherwise blow off if the jet were into a cool ambient environment. The previously presented flame stabilization theories (Section 2.2) are evaluated in Chapter 9 with the relevant results. The vitiated coflow raises the potential for autoignition of mixed fluid, and allows for speculation on variations or additional mechanisms that may contribute to stabilization of the present family of flames. The following discussion is a summary and analysis of results leading to the conclusion that stabilization of lifted flames is a result of interplay between 3 components: (1) flame propagation, (2) localized extinction and (3) autoignition events.

#### 9.1. Hydrogen Flame Observations

Experimental, numerical, and analytical model results provide information regarding the stabilization mechanism of the lifted hydrogen jet flame. The EDC combustion models (Section 3.5) and Kalghatgi's model (1984, Section 8.2) support the flame propagation theory. The Kalghatgi model, which is based on velocity scales, reasonably predicted the lift-off height of the hydrogen flame studied at Sandia ( $H/d \approx 10$ ,  $H_K/d = 11.4$ ); this suggests a balance of flame speed and gas velocity at the flame base. The EDC combustion model, which also reasonably predicted the lift-off height using different turbulence models (Figures 6.5C-D), calculated gas velocities on the order of 3 times the laminar flame speed of the stoichiometric mixture. The maximum laminar

premixed flame speed was calculated to be 3 m/s. A factor of 3 increase in velocity for a propagating turbulent premixed flames is plausible (Ruetsch et al. 1995, text by Glassman 1996).

The PDF model also reasonably predicted the flame structure of the hydrogen flame (Figure 6.5b). The major difference between the EDC and PDF combustion models is that the PDF model is a forward-marching (downstream) solution; as a result, the model does not explicitly allow for flame propagation upstream towards the nozzle. In the absence of upstream flame propagation, flame stabilization in the model is limited to autoignition of hot mixtures (i.e., fuel and vitiated air).

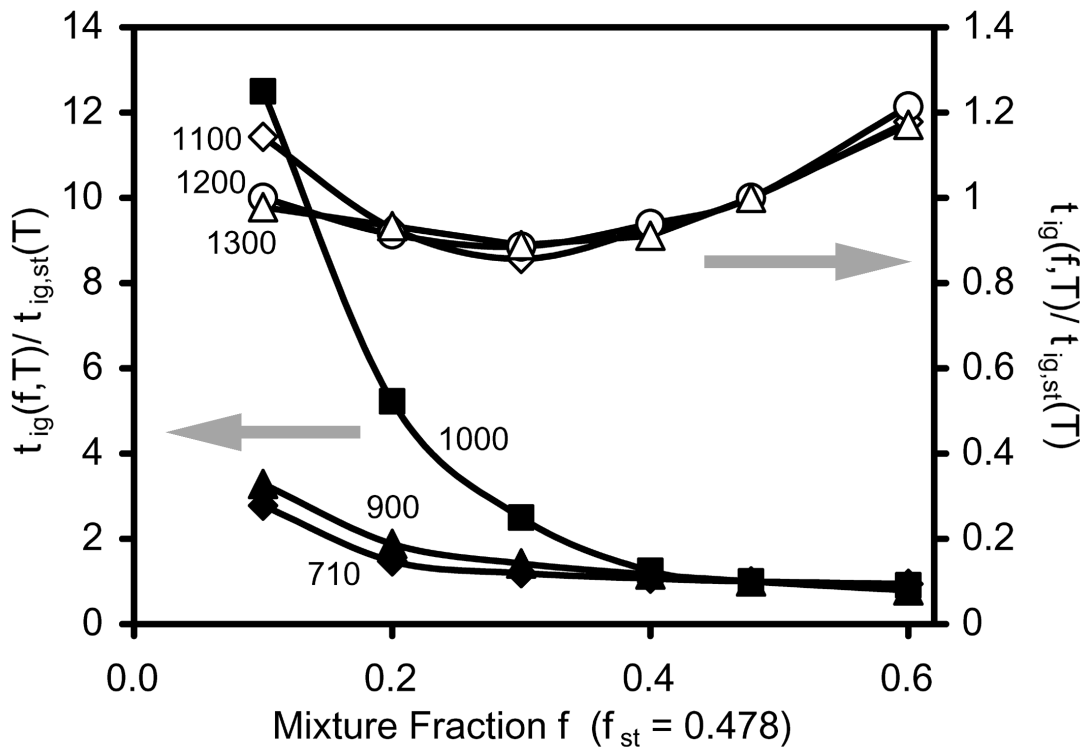


**Figure 9.1.**

Effect of stoichiometry on the ignition delay time for the hydrogen jet flame into vitiated coflow in the PFR model. The ignition delay time is far more sensitive to temperature (Figure 7.11A).

Autoignition in the hot and lean regions of the flow may play a role in the stabilization of the lifted hydrogen flame (i.e., high temperature, low mixture fraction regions of flow, Figures 6.1 and 6.8). Ignition delay times dramatically decrease with increased temperature, as shown in Figure 7.11A. The same Plug Flow Reactor (PFR) calculations for the hydrogen conditions are plotted with respect to stoichiometry in Figure 9.1. The plotted ignition delay time is normalized by the ignition delay time for the stoichiometric mixture at the given temperature ( $t_{ig}/t_{ig,st}$ ). Figure 9.B shows a shift in the chemical kinetics of autoignition from 900 to 1100 K, where there is a reduced sensitivity to stoichiometry. Although the ignition delay time increases with decreased stoichiometry, as shown in Figure 9.1, these effects are much smaller than the decreases due to increased temperature of the leaner mixtures in the flow.

Quantitatively, the PDF and EDC model results can determine the premixed turbulent combustion mode for the hydrogen flame conditions. The one-dimensional laminar premixed flame model (Section 3.3) predicts an unstrained flame speed of  $S_L = 3$  m/s & flame thickness of  $\delta_L = 2.5$  mm for stoichiometric mixtures. The integral length scale for the flow is determined via the relationship reported by Stårner and Bilger (1980) based on the axial velocity radial profile at the lift-off height ( $z/d = 10$ ).

$$\frac{\lambda_0}{R_U} = 0.7 \quad (9.1)$$

The EDC and PDF combustion model results show a velocity half radius  $R_U \approx 7$  mm, yielding an integral length scale  $\lambda_0$  on the order of 5 mm. The Kolmogorov length scale  $\lambda_K$  is (Pope 2000):

$$\lambda_K = \left( \frac{\nu^3}{\epsilon} \right)^{0.25} = \left( \frac{\nu^3}{(U_{RMS}^3/\lambda_0)} \right)^{0.25} \quad (9.2)$$

For the given integral length scale, a range of Kolmogorov length scales can be determined. At the flame base, the kinematic viscosity varies from  $\nu = 1 \times 10^{-4} \text{ m}^2/\text{s}$  for fluid at 1,000K to  $3.5 \times 10^{-4} \text{ m}^2/\text{s}$  for fluid at 2,000K (based off temperature measurements). The turbulent intensity varies from  $U_{RMS}$  2-10 m/s (via PDF and EDC model results). Given these values, the Kolmogorov length scale range is 50-400  $\mu\text{m}$ . Therefore, there is a substantial number of turbulent eddies on the order of, and smaller than, the flame thickness, indicating a distributed reaction zone (Bray 1980). The shaded area in Figure 9.2 is the region associated with the distributed reaction mode for the present conditions, where the flame thickness is within the inertial range ( $\lambda_K < \delta_L < \lambda_0$ ). As illustrated in Figure 9.2, the distributed reaction (broadened reaction zone) mode also is associated to intense turbulence ( $u'/S_L > 1$ ) and Damköhler numbers on the order of unity,  $O(1)$ .

A consequence of distributed turbulent premixed combustion is that reactants and products are more uniformly dispersed throughout the region. Experimentally, this condition yields instantaneous temperature measurements that are not bimodal, but well distributed. The Sandia experimental results show this sort of condition. The uniform distribution of instantaneous temperature measurements for the hydrogen flame (Figure 9.3) indicates a distributed reaction mode of turbulent premixed combustion at the flame base. Interestingly, Mansour et al. (1999) also reported numerical and experimental results with similar uniform temperature distributions at the base of an attached turbulent premixed flame with a large pilot (Section 2.1).

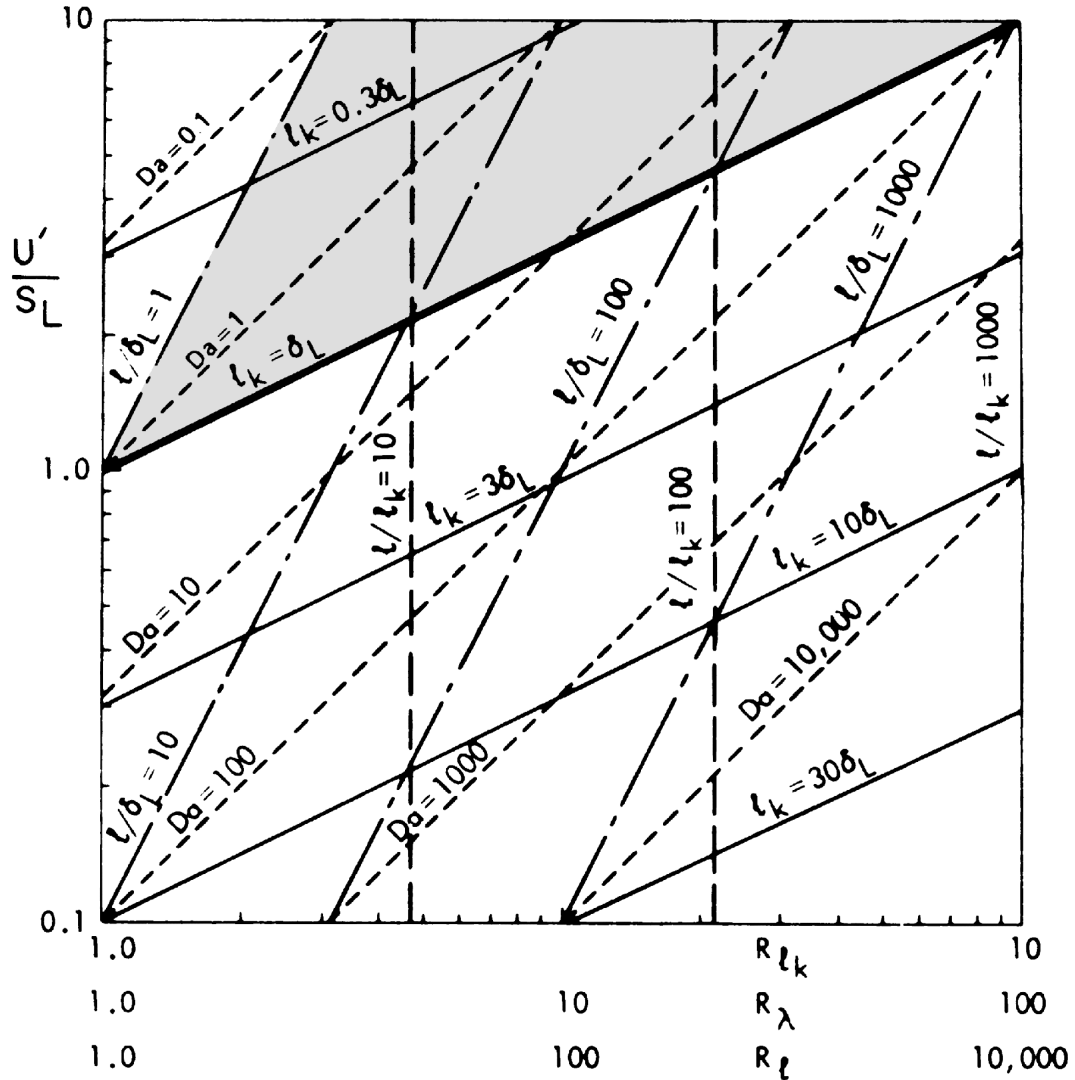


**Figure 9.2.**

Characteristic parametric relationships for turbulent premixed combustion (Bray 1980).

The shaded region denotes the hydrogen conditions.

Direct numerical simulation (DNS) calculations of a lifted hydrogen flame in still air by Mizobuchi et al. (2000) show that the leading edge of the lifted flame as a triple flame. The DNS results also show a laminar lean premixed flame branch and a rich premixed branch in the intensely turbulent region closer to the jet centerline (Figure 2.4). The turbulent rich premixed branch burns in the distributed reaction mode. The

stoichiometric mixture fraction for Mizobuchi and coworkers' flow is  $f_{st} \approx 0.03$ ; therefore, the lean premixed flame branch is laminar as it propagates through a low velocity, low turbulence region. Conversely, the hydrogen flame studied at Sandia is different since the stoichiometric mixture fraction is  $f_{st} \approx 0.47$ . If there were a triple flame structure at the flame base, both branches would be in the intensely turbulent region closer to the jet centerline. This phenomenon would explain the distributed nature of the temperature measurements shown in Figure 9.3.

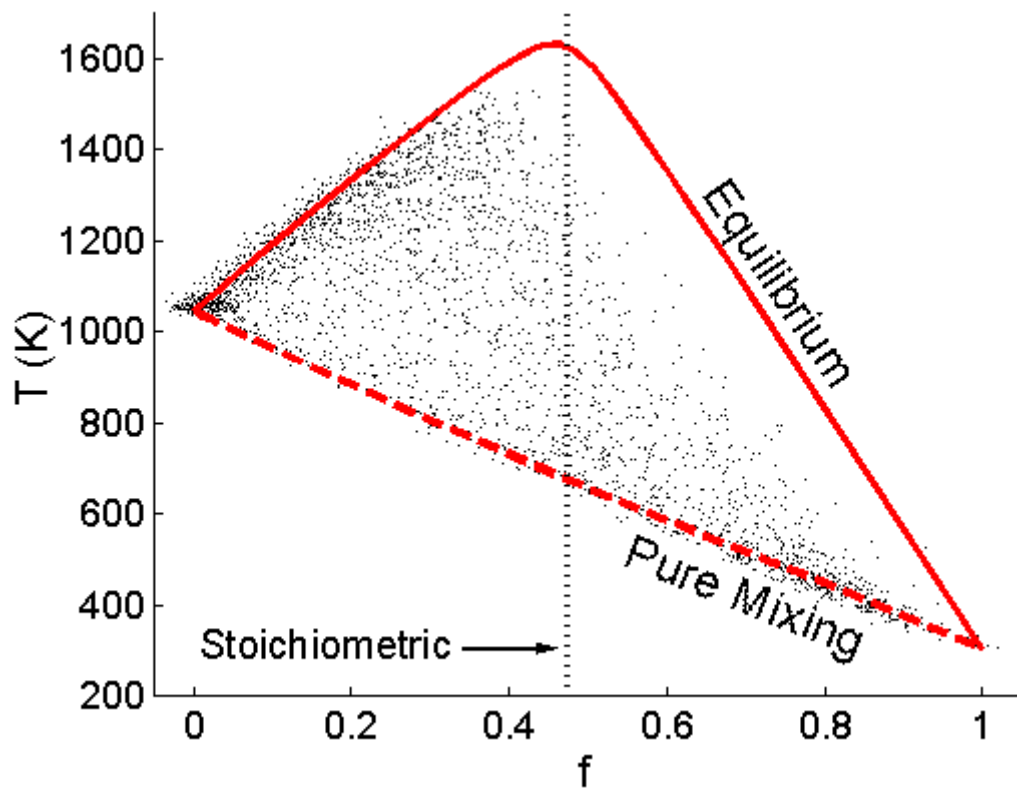


**Figure 9.3.**

Temperature distribution in the hydrogen flame stabilization region ( $z/d = 11$ ).

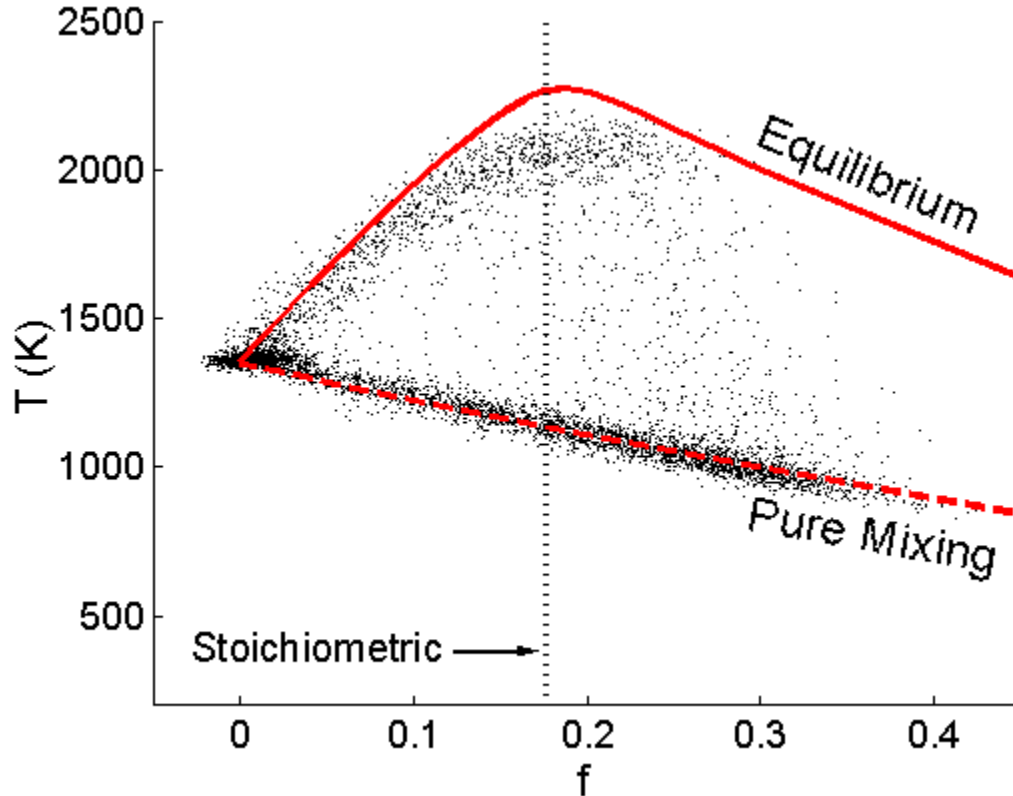


**Figure 9.4.**

Temperature distribution just above the methane flame stabilization region ( $z/d = 40$ ).

## 9.2. Methane Flame Observations

The parametric study and multiscale point measurement results for methane conditions are discussed with respect to flame stabilization. The instantaneous point measurements (Figure 9.4) just above the flame stabilization region show a broadened bimodal distribution of probe volume temperature measurements. The broadened bimodal distribution suggests interplay between combustion modes (i.e., distributed reaction and wrinkled flamelet). The leading edge of the flame is situated in the leaner, less turbulent region because of the lower stoichiometric mixture fraction ( $f_{st} \approx 0.17$ ); this results in a shift in turbulent length scales. The turbulent eddy spectrum is similar to the hydrogen conditions ( $\lambda_K < \delta_L < \lambda_0$ ), but the laminar flame thickness is closer in size to the

Kolmogorov length scale. The lower percentage of eddies smaller than the flame thickness reduces the distributed reaction mode contribution, a possible explanation of the “fuzzy” bimodal distribution exhibited by the measurements in Figure 9.4.

The lift-off height ( $H/d \approx 35$ ) is higher for the methane flame than the hydrogen flame. Because of the higher lift-off, the jet entrains more hot, viscous coflow; consequently, the entrained hot coflow dissipates more jet turbulence, resulting in a less turbulent flow at the flame base. The methane flame lift-off height illustrates how methane combustion is not as robust as hydrogen combustion; more specifically, the methane flame into a vitiated coflow (Figure 9.4) does not exhibit as much high turbulence induced flame broadening as the hydrogen flame (Figure 9.3).

The parametric study in Chapter 8 presents evidence in support of a theory that flame stabilization is achieved by autoignition. As shown in Section 8.4, the methane jet flame into a vitiated coflow blows off at a given coflow temperature, regardless of flow conditions. The growth rate of the coflow-ambient air shear layer is the same (Section 7.4) for a given coflow temperature. The lift-off height at these lower temperatures is beyond the two-stream flow condition, which means that the flame base is in a region downstream where jet-coflow mixture is mixed or diluted with cool ambient air. Blow off of the methane flame occurs at a common coflow temperature and is most likely a result of cool laboratory air entrainment. Since blow-off occurs in downstream flow conditions of low strain, it is unlikely that cool air entrainment results in extinction of the flame. It is more probable that dilution of cool ambient air prevents autoignition.

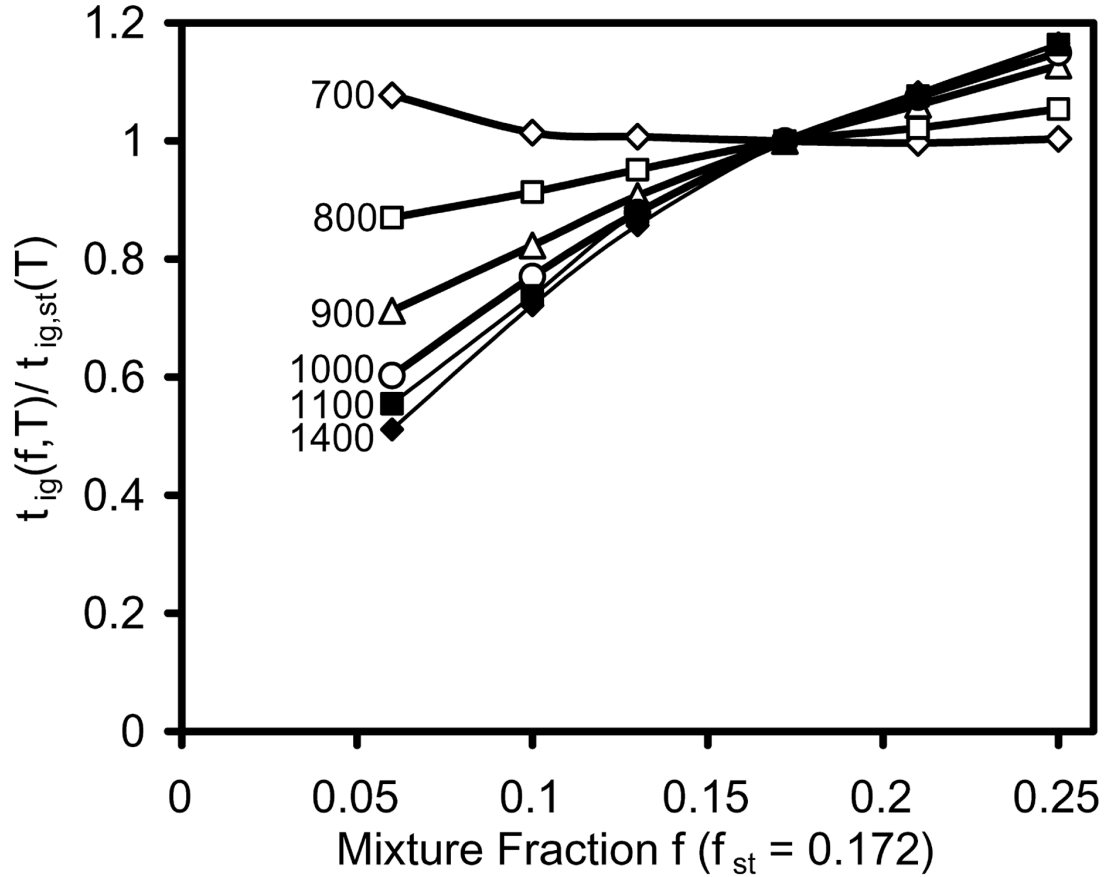


**Figure 9.5.**

Effect of stoichiometry on the ignition delay time for the methane conditions in the PFR model. The absolute temperature relationships are far more influential (Figure 7.11B).

Ignition delay time calculations obtained calculated by the Plug Flow Reactor (PFR) model found that autoignition is most likely to occur in the lean, hot regions of the flow (i.e., high temperature, low mixture fraction). As shown in Figure 7.11B, the autoignition delay time decreases dramatically with increased temperatures. At these higher temperatures, the autoignition delay time also decreases with decreased stoichiometry, as shown in Figure 9.5. Given that the coflow is hot, autoignition is most likely to occur in the lean (low mixture fraction), hot (high temperature) regions of the flow. Lean mixtures in the flow are hot and viscous; therefore, the preferential ignition

characteristics and low turbulence (strain) in these regions are conducive to the onset of autoignition events.

### **9.3. Autoignition and the Stabilization of Lifted Flames**

Through analysis of the experimental and numerical observations, it is concluded that autoignition events may also play a role in the stabilization of lifted flames in a hot, vitiated environment. The first set of clues pointing towards this additional stabilization mechanism is the startup sequence of the experiment:

1. Initiate the coflow air and the jet diluents (either air or nitrogen).
2. Inject fuel into the coflow air stream and light the coflow mixture with a torch.
3. Once the coflow is stabilized, introduce fuel to the jet flow.
4. An autoignition event occurs far downstream ( $Z \approx 3$  m,  $Z/d = 660$ ).
5. This first autoignition event is followed by a sequence of loud autoignition events, each successively closer to the nozzle exit.
6. These autoignition events stop as the lifted flame is stabilized ( $H/d = 10-70$ ).

While there is no question that autoignition initiates the flame, the final stabilization mechanism is not so easily resolved. Autoignition delay time calculations, from the PFR model, show that the lean (low mixture fraction), hot (high temperature) regions of the flow are conducive to these autoignition events.

The parametric study and the PDF combustion model results point to autoignition as the stabilization mechanism of the lifted flame. The PDF model reasonably predicts the flame structure, and the only mechanism for flame stabilization in this downstream

marching solution is autoignition. The parametric blow-off study revealed that the methane flame blows off at a common coflow temperature regardless of coflow and jet velocities; this is reasoned to be the result of cool laboratory air entrainment preventing autoignition.

The instantaneous multiscalar measurements show that combustion in the stabilization region is distributed in nature. The uniformly distributed instantaneous temperature measurements for the hydrogen flame (Figure 9.3) and the broadened bimodal distribution for the methane flame (Figure 9.4) are consistent with the distributed reaction mode of turbulent premixed combustion. It is also possible that this distribution of temperature is solely due to ignition, as illustrated in Figure 9.6. The illustration is based on transient flamelet model results of an ignition event (Paczko et al. 1999).

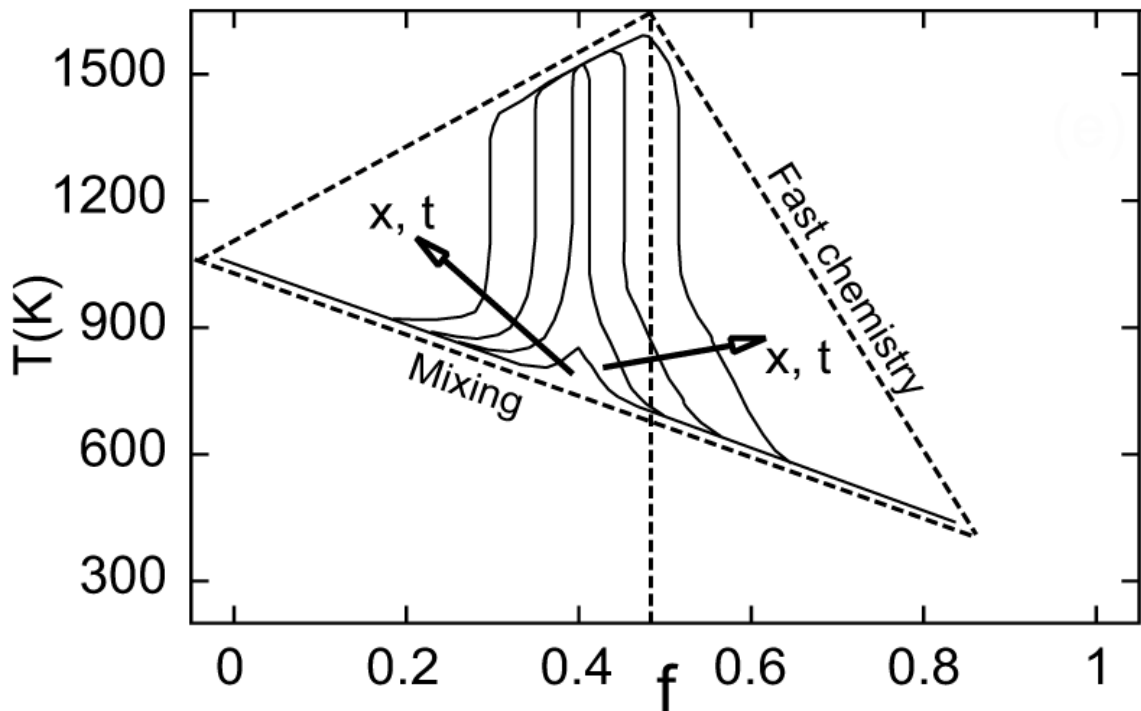


**Figure 9.6.**

Illustration of the transient flamelet response to an autoignition event.

Typically, a distributed reaction (Bray 1980), “broken” reaction (Peters 2000), or “torn” reaction (Warnatz et al. 1999), is a thin flame front that has been broadened into a flame zone by intense turbulence. The flame broadening is a result of intense mixing associated with turbulence at scales on the order and smaller than the flame thickness ( $\lambda_K < \delta_L < \lambda_0$ ). As shown in Figure 9.7, the flame is broadened and there is localized extinction due to increased heat dissipation to the cooler regions of the flow (cool reactants).

I propose an additional view of the distributed reaction mode for turbulent premixed combustion, where the flame zone is broadened due to autoignition events. The range of turbulence is the same ( $\lambda_K < \delta_L < \lambda_0$ ), but now the reactants are hot, as a result of the environment (i.e., the vitiated gases). The heated reactants require less or even no energy from the reaction zone to autoignite. Therefore, in a hot environment, intense turbulence at the smallest scales facilitates the reaction because of these autoignition events, as shown in Figure 9.8. It is very probable that this mode of combustion explains the distributions measured at Sandia (Figures 9.3-4) given the preferential ignition characteristic of lean, hot mixtures in the vitiated coflow flame.

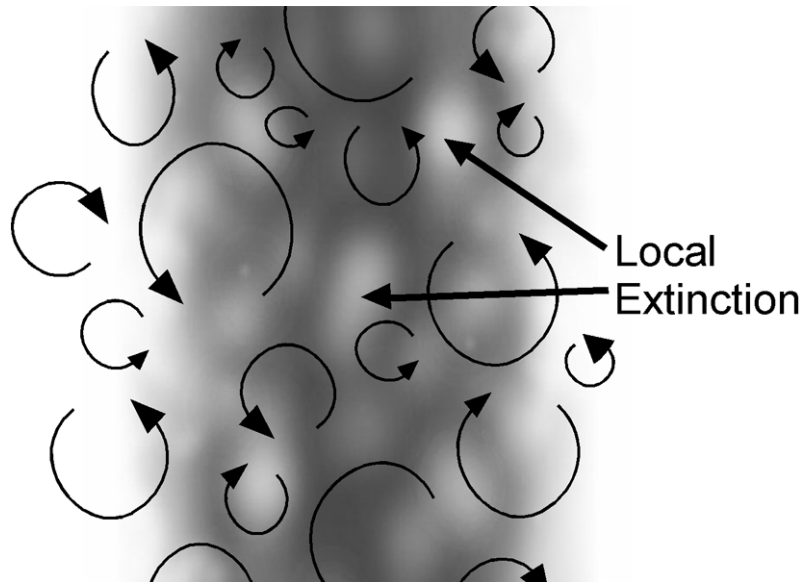


**Figure 9.7.**

Traditional view of distributed reaction mode for premixed turbulent combustion.

Shaded area is the reaction zone; white regions denote areas of localized extinction.

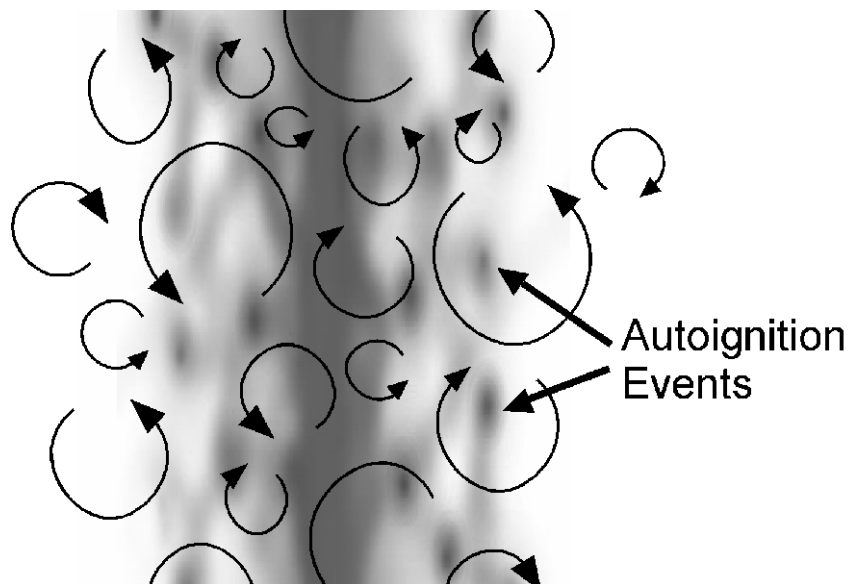


**Figure 9.8.**

Expanded view of distributed reaction mode for premixed turbulent combustion. The

shaded area is the reaction zone; the dark spots indicate autoignition events.

It is possible that auto-ignition of mixed fluid is only important for the transient startup of the laboratory flame and that, once ignited, a propagating premixed flame advances upstream to a lift-off height for which convective times from the nozzle are shorter than ignition delay times for any fluid sample along the mixing line. This balancing of flame speed and gas velocities would be consistent with the EDC calculations in which the gas velocities at the flame base are within the accepted values of turbulent premixed flame speeds.

It is likely that autoignition events augment or anchor the propagating flame; such a mixing-ignition-propagation mechanism is consistent with the measured distributions of instantaneous temperature (Figures 9.3 and 9.4). Additionally, these distributions most likely consist of both localized extinction and autoignition events. There is a shift in the role of the environment that depends on environment temperature. At lower temperatures, the environment acts as a heat sink and extinguishes the flame. Conversely, autoignition events become more prevalent in elevated temperature environments, such as in the vitiated coflow burner and practical combustors.

# Chapter 10

## Conclusions

The vitiated coflow burner is presented and studied in the preceding chapters. The burner was built to study combustion processes in hot, vitiated air environments similar to practical combustors, but with simplified flow conditions. Analytical, numerical, and experimental tools aid in the analysis of a family of flames that provides a database for model validation. An analysis of the results increases our understanding of flame stabilization processes in lifted flames, which may be extended to combustion processes in advanced combustion systems.

### 10.1. Vitiated Coflow Flame Data Set

The vitiated coflow burner provides a simplified flow condition for studying recirculation combustion in the absence of detailed recirculation fluid mechanics. The geometry (Figure 1.4) consists of a central jet into a coaxial flow of hot products from a lean premixed flame (i.e., vitiated coflow). The studied set of flow conditions are of increasing complexity and can be successively used to validate combustion models while in development. They are:

1. Temperature measurements in nonreacting flow: Air jet into a vitiated coflow (Section 7.5).
2. Multiscalar point measurements in all hydrogen flow: Lifted  $H_2/N_2$  flame into a vitiated coflow (Section 6.1).

3. Multiscalar point measurements in methane flow: Lifted CH<sub>4</sub>/Air flame into a vitiated coflow (Section 6.2).
4. Parametric study of methane flows: Lift-off height and blow-off limit sensitivities to coflow temperature, coflow velocity and jet velocity for CH<sub>4</sub>/Air flame into a vitiated coflow (Chapter 8).

The mixing models can first be tested using the nonreacting flow measurements. The transition from an all hydrogen flow target to a methane target can be applied to the evaluation of combustion models with reduced chemistry. The parametric study results are a possible measure for combustion model robustness.

The experimental results attest to the success of the vitiated coflow burner design. The main design objective of the vitiated coflow burner was to isolate the central jet from the cool laboratory air for a maximum downstream distance. In this test volume, results show that the coflow is uniform and steady, validating the assumption that the flame can be modeled as a 2-stream flow. Results also show that coflow conditions are nearly at equilibrium.

Analytical and numerical analyses provide complementary boundary condition information (Chapter 7) to augment the database of measurements obtained for the flame set. Information regarding the thermal and viscous boundary layers is provided for numerical modeling consideration. The jet-coflow and coflow-ambient shear layers are characterized to determine the operating range in which the two-stream condition is valid (typically for  $z/d < 50-70$ ). Analysis confirms that the combustion processes in the vitiated coflow flame are most sensitive to the elevated coflow temperature, not the small, undetectable variations in radical composition.

The parametric study results provide information regarding methane flame lift-off height sensitivity to flow conditions. The well-known linear relationship between the lift-off height and jet velocity is confirmed. Subsequently, linear lift-off height sensitivities to coflow velocity and temperature are also found. The blow-off study reveals that the methane flame blows off at a common coflow temperature (1260 K) regardless of coflow or jet velocity. Because the lift-off height at this coflow temperature is beyond the two-stream condition height, it is suggested that blow-off of the flame is due to the prevention of autoignition caused by entrained cool air.

## **10.2. Stabilization by Committee (Autoignition-Propagation-Extinction)**

Analysis of the results leads to the conclusion that lifted flames are stabilized by a combination of flame propagation, autoignition, and localized extinction processes. Results confirm recent numerical findings that show turbulent combustion in the distributed reaction mode at the flame stabilization region. The instantaneous multiscalar measurements show a uniform distribution of probe volume conditions between the fast chemistry and pure mixing conditions for the hydrogen flame; this indicates distributed reaction combustion at the flame base. A broadened bimodal distribution for the methane flame suggests a combination of distributed reaction and wrinkled flamelet combustion.

The hot coflow enables speculation concerning an additional mode of stabilization related to the distributed reaction conditions. The contribution of autoignition events becomes more plausible in mixtures at elevated temperatures (i.e., mixtures of fuel and vitiated air). Typically, intense turbulence results in quick energy dissipation to the cool reactants and subsequent localized extinction. A hot environment yields the reverse effect, in which intense turbulent mixing leads to ignition of reactants at elevated

temperatures. It is proposed that these autoignition events augment premixed flame propagation and effectively broaden the reaction zone, explaining the measured instantaneous temperature distributions (Figures 9.3 and 9.4). This expanded view of distributed reaction combustion is responsible, in varying degrees, for flame stabilization. In hot environments such as the vitiated coflow burner, internal combustion engines, and other advanced combustors, the contribution of these small autoignition events becomes greater precisely because of reaction sensitivity to temperature.

### **10.3. Future of Vitiated Coflow Flame**

The many attractive experimental and numerical features of the vitiated coflow flame will hopefully result in further interest and investigation by the combustion science community. Numerically, the data set provides a set of targets for the evaluation and refinement of models.

Experimentally, there are many possibilities for further research. The most obvious starting point is to characterize the flow-field with a diagnostic like LDV or PIV. Other areas of possible interest include visualization of the scalar field and possibly determining scalar dissipation rates. Less complex parametric studies can also be conducted to isolate different combustion sub-processes. These include:

1. Global emission index measurements (e.g.,  $\text{NO}_x$ , CO,  $\text{CO}_2$ ).
2. Radiative loss measurements.
3. Mixing studies upstream of flame base with line-of-sight fuel content measurements.
4. Additional lift-off height sensitivity experiments (i.e., to coflow temperature).

A study of the sensitivity of flame location in the flow field may also be conducted by varying the stoichiometric mixture fraction.

Of greatest interest are the investigative possibilities closely related to combustion processes in industrial applications. For example, fuel-lean coflow mixtures with reduced oxygen content enable the investigation of flameless oxidation (FLOX, Wüning and Wüning 1997), a combustion mode used in industrial combustors. In addition, oxidation by air jets in combustion chambers can be studied with an air jet in a fuel-rich coflow.

In conclusion, there are many interesting combustion phenomena that can be studied with the vitiated coflow burner. The hot environment provided by the vitiated coflow burner is similar to that of real-world combustors and has been shown to produce combustion phenomena nonexistent in traditional laboratory jet flames in cool-air. The vitiated coflow burner may bridge the gap between the body of combustion fundamentals and ubiquitous engineering knowledge.

## References

- Abramovich, G.N., *The Theory of Turbulent Jets*, The MIT Press, Cambridge, 1963.
- Barlow, R.S., & Carter, C.D., “Raman/Rayleigh/LIF Measurements of Nitric Oxide Formation in Turbulent Hydrogen Jet Flames,” *Combustion and Flame* **97**: 261-280 (1994).
- Barlow, R.S., & Frank, J.H., “Effects of Turbulence on Species Mass Fractions in Methane/Air Jet Flames,” *Proceedings from the 27<sup>th</sup> International Symposium on Combustion*, The Combustion Institute, Pittsburgh, 1087-1095 (1998).
- Barlow, R.S., & Miles, P.C., “A Shutter-Based Line-Imaging System for Single-Shot Raman Scattering Measurements of Gradients in Mixture Fraction,” *Proceedings from the 28<sup>th</sup> International Symposium on Combustion*, The Combustion Institute, Pittsburgh (2000).
- Barlow, R.S., Dibble, R.W., & Fourquette, D.C., “Departure From Chemical Equilibrium in a Lifted Hydrogen Flame,” *AIAA/ASME/SAE/ASEE 25<sup>th</sup> Joint Propulsion Conference*, AIAA, Monterey #AIAA-89-2523 (1989).
- Barlow, R.S., Dibble, R.W., & Lucht, R.P. “Simultaneous Measurement of Raman Scattering and Laser-Induced OH Fluorescence in Nonpremixed Turbulent Jet Flames,” *Optics Letters*, Vol. 14, No. 5: 263-265 (1989)
- Barlow, R.S., Dibble, R.W., Chen, J.-Y., & Lucht, “Effect of Damköhler Number on Superequilibrium OH Concentration in Turbulent Nonpremixed Jet Flames,” *Combustion and Flame* **82**: 235-251 (1990).

- Barlow, R.S., ed., *International Workshop on Measurement and Computation of Turbulent Nonpremixed Flames (TNF)*, Sandia National Laboratories, [www.ca.sandia.gov/TNF](http://www.ca.sandia.gov/TNF) (2003).
- Barlow, R.S., Fiechtner, G.J., Carter, C.D., & Chen, J.-Y., “Experiments on the Scalar Structure of Turbulent CO/H<sub>2</sub>/N<sub>2</sub> Jet Flames,” *Combustion and Flame* **120**: 549-569 (2000).
- Barlow, R.S., Karpetis, A.N., Frank, J.H., & Chen, J.-Y., “Scalar Profiles and NO Formation in Laminar Opposed-Flow Partially Premixed Methane/Air Flames,” *Combustion and Flame* **127**: 2102-2118 (2001).
- Barlow, R.S., Private communication, Combustion Research Facility, Sandia National Laboratories, Livermore (2003).
- Berl, W.G., & Wilson, W.E., “Formation of BN in Diborane Hydrazine Flames,” *Nature*, **191**: 380 (1961).
- Bilger, R. W., Stårner, S.H., & Kee, R. J., “On Reduced Mechanisms for Methane-Air Combustion in Nonpremixed Flames,” *Combustion and Flame* **80**: 135-149 (1990).
- Bird, R.B., Stewart, W.E., & Lightfoot, E.N., *Transport Phenomena 2<sup>nd</sup> Edition*, John Wiley & Sons, New York, 2002.
- Borman G.L., & Ragland, K.W., *Combustion Engineering*, McGraw-Hill, Boston, 1998.
- Bowman, C.T., Hanson R. K., Davidson, D. F., Gardiner Jr., W. C., Lissianski V., Smith, G. P., Golden, D. M., Goldenberg, M., Frenklach, M., Gri-Mech 2.11, [http://www/me.berkeley.edu/gri\\_mech/](http://www/me.berkeley.edu/gri_mech/) (1999).

- Bray, K.N.C., in *Turbulent Reacting Flows* (Editors: P.A. Libby & F.A. Williams), p. 115. Springer-Verlag, Berlin (1980)
- Broadwell, J.E., & Lutz, A.E., "A Turbulent Jet Chemical Reaction Model: NO<sub>x</sub> Production in Jet Flames," *Combustion and Flame* **114**: 319-335 (1998).
- Broadwell, J.E., Dahm, W.J.A., & Mungal, M.G., "Blowout of Turbulent Diffusion Flames," *Proceedings from the 20<sup>th</sup> International Symposium on Combustion*, The Combustion Institute, Pittsburgh, 303-310 (1984).
- Brockhinke, A., Andresen, P., & Höinghaus, K., "Quantitative One-Dimensional Single-Pulse Multi-Species Concentration and Temperature Measurement in the Lift-Off Region of a Turbulent H<sub>2</sub>/Air Diffusion Flame," *Applied Physics B* **61**: 533-545 (1995).
- Brockhinke, A., Andresen, P., & Kohse-Höinghaus, K., "Contribution to the Analysis of Temporal and Spatial Structures Near the Lift-Off Region of a Turbulent Hydrogen Diffusion Flame," *Proceedings from the 26<sup>th</sup> International Symposium on Combustion*, The Combustion Institute, Pittsburgh, 875-881 (1996).
- Brockhinke, A., Haufe, S., & Kohse-Höinghaus, K., "Structural Properties of Lifted Hydrogen Jet Flames Measured by Laser Spectroscopic Techniques," *Combustion and Flame* **121**: 367-377 (2000).
- Cabra, R.C., Myhrvold, T.M., Chen, J.Y., Dibble, R.W., Karpetsis, A.N., & Barlow, R.S., "Lifted H<sub>2</sub>/N<sub>2</sub> Jet Flame," *Proceedings from the 29<sup>th</sup> International Symposium on Combustion*, The Combustion Institute, Pittsburgh, in print (2002).
- Carter, C.D., & Barlow, R.S. "Simultaneous Measurement of NO, OH and the Major Species in Turbulent Flames," *Optics Letters*, Vol. 19, No. 4: 299-301 (1994).

- Chao, Y.C., Wu, C.Y., Yuan, T., & Cheng, T.S., "Stabilization Process of a Lifted Flame Tuned by Acoustic Excitation," *Combustion Science and Technology*, **174**: 87-110 (2002).
- Chen, J.-Y. & Kollmann W., "PDF Modeling of Chemical Nonequilibrium Effects in Turbulent Nonpremixed Hydrocarbon Flames," *Proceedings from the 22<sup>nd</sup> International Symposium on Combustion*, The Combustion Institute, Pittsburgh, 645-653 (1988).
- Chen, Y.C. & Mansour, M.S., "Simultaneous Planar Imaging of LIPF of OH Radical and Rayleigh Thermometry in Turbulent Premixed Flames Near Extinction," *Proceedings from the 1<sup>st</sup> Asia-Pacific Conference on Combustion*, The Combustion Institute, Pittsburgh, 18-21 (1997).
- Chen, Y.C. & Mansour, M.S., "Simultaneous Rayleigh Scattering and Laser-Induced CH Fluorescence for Reaction Zone Imaging in High-Speed Premixed Hydrocarbon Flames," *Applied Physics B*, **64**: 599-605 (1997).
- Chen, Y.C., & Bilger, R.W., "Stabilization Mechanisms of Lifted Laminar Flames in Axisymmetric Jet Flows," *Combustion and Flame* **123**: 23-45 (2000).
- Chen, Y.C., Peters, N., Schneemann, G.A., Wruck, N., Renz, U., & Mansour, M.S., "The Detailed Flame Structure of Highly Stretched Turbulent Premixed Methane-Air Flames," *Combustion and Flame*, **107**: 223-244 (1996).
- Cheng, T.S., Wehrmeyer, J.A., & Pitz, R.W., "Simultaneous Temperature & Multispecies Measurement in a Lifted Hydrogen Diffusion Flame," *Combustion and Flame* **91**: 323-345 (1992)

- Dahm, W.J.A., & Dibble, R.W., "Coflowing Turbulent Jet Diffusion Flame Blowout," *Proceedings from the 22<sup>nd</sup> International Symposium on Combustion*, The Combustion Institute, Pittsburgh, 801-808 (1988).
- Dally, B.B., Karpetis, A.N., & Barlow, R.S., "Structure of Turbulent Nonpremixed Jet Flames in a Diluted Hot Coflow," *Proceedings from the 29<sup>th</sup> International Symposium on Combustion*, The Combustion Institute, Pittsburgh, in print (2002).
- Dally, B.B., Masri, A.R., Barlow, R.S., and Fiechtner, G.J., "Instantaneous and Mean Compositional Structure of Bluff-Body Stabilized Nonpremixed Flames," *Combustion and Flame* **114**: 119-148 (1998).
- Dally, B.B., Masri, A.R., Barlow, R.S., Fiechtner, G.J., & Fletcher, D.F., "Measurements of NO in Turbulent Nonpremixed Flames Stabilized on a Bluff Body," *Proceedings from the 26<sup>th</sup> International Symposium on Combustion*, The Combustion Institute, Pittsburgh, 2191-2197 (1996).
- Delichatsios, M.A., "Transition from Momentum to Buoyancy-Controlled Turbulent Jet Diffusion Flames and Flame Height Relationships," *Combustion and Flame* **92**: 349-364 (1993).
- Deutschmann, O., Maier, L., Riedel, U., Stroemann, A. H., & Dibble, R.W., "Hydrogen Assisted Catalytic Combustion of Methane on Platinum," *Catalysis Today* **59**: 141-150 (2000).
- Dibble, R.W., Masri, A.R., & Bilger, R.W., "The Spontaneous Raman Scattering Technique Applied to Nonpremixed Flames of Methane," *Combustion and Flame* **67**: 189-206 (1987).

- Eckbreth, A.C., *Laser Diagnostics for Combustion Temperature and Species*, 2<sup>nd</sup> Edition, Gordon & Breach, Amsterdam, 1996.
- Elliot and Denues, U.S. Bureau of Standards, *Journal of Research*, **17**: 7-43 (1936).
- Ertesvåg, I. S., Magnussen, B. F., “The Eddy Dissipation Turbulence Energy Cascade Model,” *Combustion Science and Technology* **159**: 213-235 (2000).
- Ertesvåg, I. S., *Turbulent Flow & Combustion (in Norwegian)*, Tapir Academic Publisher, Trondheim, 2000.
- Flowers, D., & Dibble, R.W., Private communication, Lawrence Livermore National Laboratories, Livermore (2001).
- Fristrom, R.M., *Flame Structure and Processes*, Oxford University Press, New York, 1995.
- Fujimori, T., Hamano, Y., & Sato, J., “Radiative Heat Loss and NO<sub>x</sub> Emission of Turbulent Jet Flames in Preheated Air Up To 1,230 K.” *Proceedings from the 28<sup>th</sup> International Symposium on Combustion*, The Combustion Institute, Pittsburgh, 455-461 (2000).
- Girard, J.W., Dibble, R.W., Arellano, L.O. & Smith, K.O., ‘Use of an Extractive Laser Probe for Time-Resolved Mixture Fraction Measurements in a 9 ATM Gas Turbine Fuel Injector.’ *International Gas Turbine & Aeroengine Congress & Exhibition*, ASME Paper 20001-GT-372 (2001).
- Glassman, I., *Combustion*, 3<sup>rd</sup> Edition, Academic Press, San Diego (1996).
- Gran, I. R., Magnussen B. F., “A Numerical Study of a Bluff-Body Stabilized Flame. Part 2: Influence of Combustion Modeling and Finite-Rate Chemistry,” *Combustion Science and Technology* **119**: 191-217 (1996).

- Han, D.H. & Mungal, M.G., "Direct Measurement of Entrainment in Reacting/Nonreacting Turbulent Jets," *Combust and Flame* **124**: 370-386 (2001).
- Han, D.H., & Mungal, M.G., "Stabilization in Turbulent Lifted Deflected-Jet Flames," *Proceedings from the 29<sup>th</sup> International Symposium on Combustion (to appear)*, The Combustion Institute, Pittsburgh (2002).
- Hasselbrink, E.F., & Mungal, M.G., "Characteristics of the Velocity Field Near the Instantaneous Base of Lifted Non-Premixed Turbulent Jet Flames," *Proceedings from the 27<sup>th</sup> International Symposium on Combustion*, The Combustion Institute, Pittsburgh, 867-873 (1998).
- Incropera, F.P., & DeWitt, D.P., *Introduction to Heat Transfer 3<sup>rd</sup> Edition*, John Wiley & Sons, New York, 1996.
- Ishizuka, S., & Tsuji, H., "An Experimental Study of Effect of Inert Gases on Extinction of Laminar Diffusion Flames," *Proceedings from the 18<sup>th</sup> International Symposium on Combustion*, The Combustion Institute, 695-703 (1981).
- Jones, W. P., & Musonge, P., "Closure of the Reynolds Stress and Scalar Flux Equations," *Physics of Fluids* Vol. 31, No. 12, 3589-3604 (1988).
- Jones, W. P., *Turbulent Reacting Flows*, Academic Press Ltd., 1994 p.171-189.
- Kalghatgi, G.T., "Lift-Off Heights and Visible Lengths of Vertical Turbulent Jet Diffusion Flames in Still Air," *Combustion Science and Technology* **41**: 17-29 (1984).
- Kalt, P.A.M., Al-Abdeli, Y.M., Masri, A.R., and Barlow, R.S., "Turbulent Swirling Nonpremixed Flames of Methane: Flowfield and Compositional Structure," *Proceedings from the 29<sup>th</sup> International Symposium on Combustion*, The Combustion Institute, Pittsburgh, in print (2002).

- Kean, A., Schlegel, A., & Dibble, R.W., "Experimental and Numerical Investigation of NO<sub>x</sub> Emissions From a Propane Fueled Hybrid Catalytic Combustor," *Western States Section*, The Combustion Institute, Paper WSS/CI 98S-57 (1998).
- Kee, R. J., Grcar, J. F., Smooke, M. D., & Miller, J. A., "A FORTRAN Program for Modeling Steady Laminar One-Dimensional Premixed Flames," *Sandia Report*, SAND 85-8240 (1985).
- Kee, R. J., Rupley, F. M., & Miller, J. A., "Chemkin-II: A FORTRAN Chemical Kinetics Package for the Analysis of Gas-Phase Chemical Kinetics," *Sandia Report*, SAND 89-8009 (1989).
- Kohse-Höinghaus, K., & Jeffries, J.B., ed., *Applied Combustion Diagnostics*, Taylor and Francis, New York, 2002.
- Launder, B. E., Reece, G. J., & Rodi, W., "Progress in the Development of Reynolds-Stress Turbulence Closure Models," *Journal of Fluid Mechanics* Vol. 68, No. 3, 537-566 (1975).
- Lee, J.G., Kim, K., Santavicca, D.A., "Measurement of Equivalence Ratio Fluctuation and Its Effect on Heat Release During Unstable Combustion," *Proceedings from the 28<sup>th</sup> International Symposium on Combustion*, The Combustion Institute, Pittsburgh, 415-421 (2000).
- Lutz, A. E., Kee, R. J., Grcar, J. F., & Rupley, F. M., "OPPDIF: A Fortran Program For Computing Opposed-Flow Diffusion Flames," *Sandia Report*, SAND 96-8243 (1996).

- Lyons, K.M., & Watson, K.A., "Visualizing Diffusion Flame Formation in the Wake of Partially Premixed Combustion," *Journal of Energy Resources Technology*, ASME, **123**: 221-227 (2001).
- Malvern/INSITEC Technical Specifications: EPCS, Malvern/INSITEC (1998)
- Mansour, M.S., Chen, Y.C., & Peters, N., "Highly Strained Turbulent Rich Methane Flames Stabilized by Hot Combustion Products," *Combustion and Flame* **116**: 136-155 (1999).
- Masri, A.R., Dibble, R.W. & Barlow, R.S., "The structure of turbulent nonpremixed flames revealed by Raman-Rayleigh-LIF measurements," *Progress in Energy and Combustion Science* **22**:307-362 (1996).
- Melaen, M.C., Ph.D. Dissertation, University in Trondheim, Trondheim, 1990.
- Miake-Lye, R.C., & Hammer, J.A., "Lifted Turbulent Jet Flames: A Stability Criterion Based on the Jet Large-Scale Structure," *Proceedings from the 22<sup>nd</sup> International Symposium on Combustion*, The Combustion Institute, Pittsburgh, 817-824 (1988).
- Miller, J.A., Private communication, Combustion Research Facility, Sandia National Laboratories, Livermore (2000).
- Mizobuchi, Y., Tachibana, S., Shinjo, J, Ogawa, S., & Takeno, T., "A Numerical Analysis on Structure of Turbulent Hydrogen Jet Lifted Flame," *Proceedings from the 29<sup>th</sup> International Symposium on Combustion*, The Combustion Institute, Pittsburgh, in print (2002).

- Mongia, R., "Optical Probe for Measuring the Extent of Air and Fuel Mixing in Lean Premixed Combustors and the Effect of Air and Fuel Mixing on Combustor Performance," Ph.D. Dissertation, University of California, Berkeley, 1998.
- Mongia, R., Dibble, R.W., Lovett, J., "Measurements of Air-Fuel Ratio Fluctuations Caused by Combustor Driven Oscillations." ASME Paper No. 98-GT-304 (1998).
- Montgomery, C.J., Kaplan, C.R., & Oran, E.S., "The Effect of Coflow Velocity on a Lifted Methane-Air Jet Diffusion Flame," *Proceedings from the 27<sup>th</sup> International Symposium on Combustion*, The Combustion Institute, Pittsburgh, 1175-1182 (1998).
- Nguyen, Q.V., Dibble, R.W., Carter, C.D., Fiechtner, G.J., & Barlow, R.S., "Raman-LIF Measurements of Temperature, Major Species, OH, and NO in a Methane-Air Flame," *Combustion & Flame* **105**: 499-510 (1996)
- Nooren P.A., Versluis, M., van der Meer, T.H., Barlow, R.S., & Frank, J.H. "Raman-Rayleigh-LIF Measurements of Temperature & Species Concentrations in the Delft Piloted Turbulent Jet Diffusion Flame," *Applied Physics B*, **71**: 95-111 (2000)
- Nooren, P., Ph.D. Dissertation "Stochastic Modeling of Turbulent Natural-Gas Flames," Technical University of Delft, Delft, 1998.
- Paczko, G., Barths, H., Miikuli, I., & Peters, N., Demo-RIF user Guide, Version 1.0, <http://www.flamelets.com/RiFUG.pdf> (1999).
- Peters, N., *Turbulent Combustion*, Cambridge University Press, Cambridge, 2000.

- Pitts, W.M., "Assessment of Theories for the Behavior and Blowout of Lifted Turbulent Jet Diffusion Flames," *Proceedings from the 22<sup>nd</sup> International Symposium on Combustion*, The Combustion Institute, Pittsburgh, 809-816 (1988).
- Pope, S.B., "Computations of Turbulent Combustion: Progress and Challenges," Invited Plenary Lecture, *Proceedings from the 23<sup>rd</sup> International Symposium on Combustion*, The Combustion Institute, Pittsburgh, 591-612 (1990).
- Pope, S.B., *Turbulent Flows*, Cambridge University Press, Cambridge, 2000.
- Ruetsch, G.R., Vervisch, L., & Liñán A., "Effects of Heat Release on Triple Flames," *Physics of Fluids*, **7**: 1447-1454 (1995).
- Schefer, R.W., Namazian, M., & Kelly, J., "Stabilization of Lifted Turbulent-Jet Flames," *Combustion and Flame* **99**:75-86 (1994).
- Schefer, R.W., Namazian, M., Filtopoulos, E.E.J., & Kelly, J., "Temporal Evolution of Turbulence/Chemistry Interactions in Lifted, Turbulent-Jet Flames," *Proceedings from the 25<sup>th</sup> International Symposium on Combustion*, The Combustion Institute, Pittsburgh, 1223-1231 (1994).
- Scholefield, D.A., & Garside, J.E., "The Structure and Stability of Diffusion Flames," *Proceedings from the 3<sup>rd</sup> Symposium on Combustion*, The Combustion Institute, Pittsburgh, 102-110 (1949).
- Sieder, E.N., & Tate, G.E., "Heat Transfer and Pressure Drop of Liquids in Tubes." *Industrial and Engineering Chemistry*, Vol. 28, No. 12: 1429-1435 (1936).
- Smith, N.S.A., Bilger, R.W., Carter, C.D., Barlow R.S., & Chen, J.-Y., "A Comparison of CMC and PDF Modelling Predictions with Experimental Nitric Oxide

- LIF/Raman Measurements in a Turbulent H<sub>2</sub> Jet Flame,” *Combustion Science and Technology* **105**: 357-375 (1995).
- Stårner, S.H., & Bilger, R.W., “LDA Measurement in a Turbulent Diffusion Flame with Axial Pressure Gradient,” *Combustion Science and Technology* **21**: 259-276 (1980).
- Tacke, M.M., Geyer, D., Hassel, E.P., & Janicka, J., “A Detailed Investigation of the Stabilization Point of Lifted Turbulent Diffusion Flames,” *Proceedings from the 27<sup>th</sup> International Symposium on Combustion*, The Combustion Institute, Pittsburgh, 1157-1165 (1998).
- Tang, Q., & Pope, S.B., "Effects of Pilot Temperature and Radiation Heat Transfer on PDF model Calculations of Piloted Turbulent Jet Flames," *Joint U.S. Sections*, The Combustion Institute (2001).
- Upatnieks, A, Driscoll, J.F., & Ceccio, S.L., “Assessment of the Theory of Jet Flame Stabilization: Using Time-Resolved PIV Measurements of Flame Base Propagation Velocities,” *Proceedings from the 29<sup>th</sup> International Symposium on Combustion (to appear)*, The Combustion Institute, Pittsburgh (2002).
- Vanquickenborne, L, & van Tiggelen, A., “The Stabilization Mechanism of Lifted Diffusion Flames,” *Combustion and Flame* **10**: 59-69 (1966).
- Warnatz, J., Maas, U., & Dibble, R.W., *Combustion: Physical & Chemical Fundamentals, Modeling & Simulation, Experiments, Pollutant Formation, 3<sup>rd</sup> Edition*, Springer-Verlag, Berlin, 2001.
- Watson, K.A., Lyons, K.M., Carter, C.D., & Donbar, J.M., “Simultaneous Two-Shot CH-PLIF and Particle Image Velocimetry Measurements in Lifted CH<sub>4</sub>-Air Diffusion

- Flames,” *Proceedings from the 29<sup>th</sup> International Symposium on Combustion*, The Combustion Institute, Pittsburgh, in print (2002).
- Watson, K.A., Lyons, K.M., Donbar, J.M., & Carter, C.D., “Observations on the Leading Edge in Lifted Flame Stabilization,” (brief communication), *Combustion and Flame* **119**: 199-202 (1999).
- Watson, K.A., Lyons, K.M., Donbar, J.M., & Carter, C.D., “Simultaneous Rayleigh Imaging at CH-PLIF Measurements in a Lifted Jet Diffusion Flame,” *Combustion and Flame* **123**: 252-265 (2000).
- Whitaker, S., “Forced Convection Heat Transfer Correlations for Flow in Pipes, Past Flat Plates, Single Cylinders, Single Spheres, and for Flow in Packed Beds and Tube Bundles,” *American Institute of Chemical Engineering Journal*, Vol. 18, No. 2: 361-371 (1972).
- Wohl K., Kapp, N.M., & Gazley, C., “The Stability of Open Flames,” *Proceedings from the 3<sup>rd</sup> Symposium on Combustion*, The Combustion Institute, Pittsburgh, 3-21 (1949).
- Wolfrum, J., “Lasers in Combustion: From Basic Theory to Real Devices,” *Proceedings from the 27<sup>th</sup> International Symposium on Combustion*, The Combustion Institute, Pittsburgh, 1-41 (1998).
- Wünning J. A., and Wünning, J. G., “Flameless Oxidation to Reduce Thermal NO-Formation,” *Progress in Energy and Combustion Science* **23**:81-94 (1997).

# **Appendix A**

## **Engineering Drawings & Parts List**

**A.1. Perforated Plate**

**A.2. Adaptor Plate**

**A.3. Adaptor Ring**

**A.4. Nozzle Adaptor**

**A.5. Portable Safety System**

**A.6. Cabinet Safety System**

**A.7. Parts List**

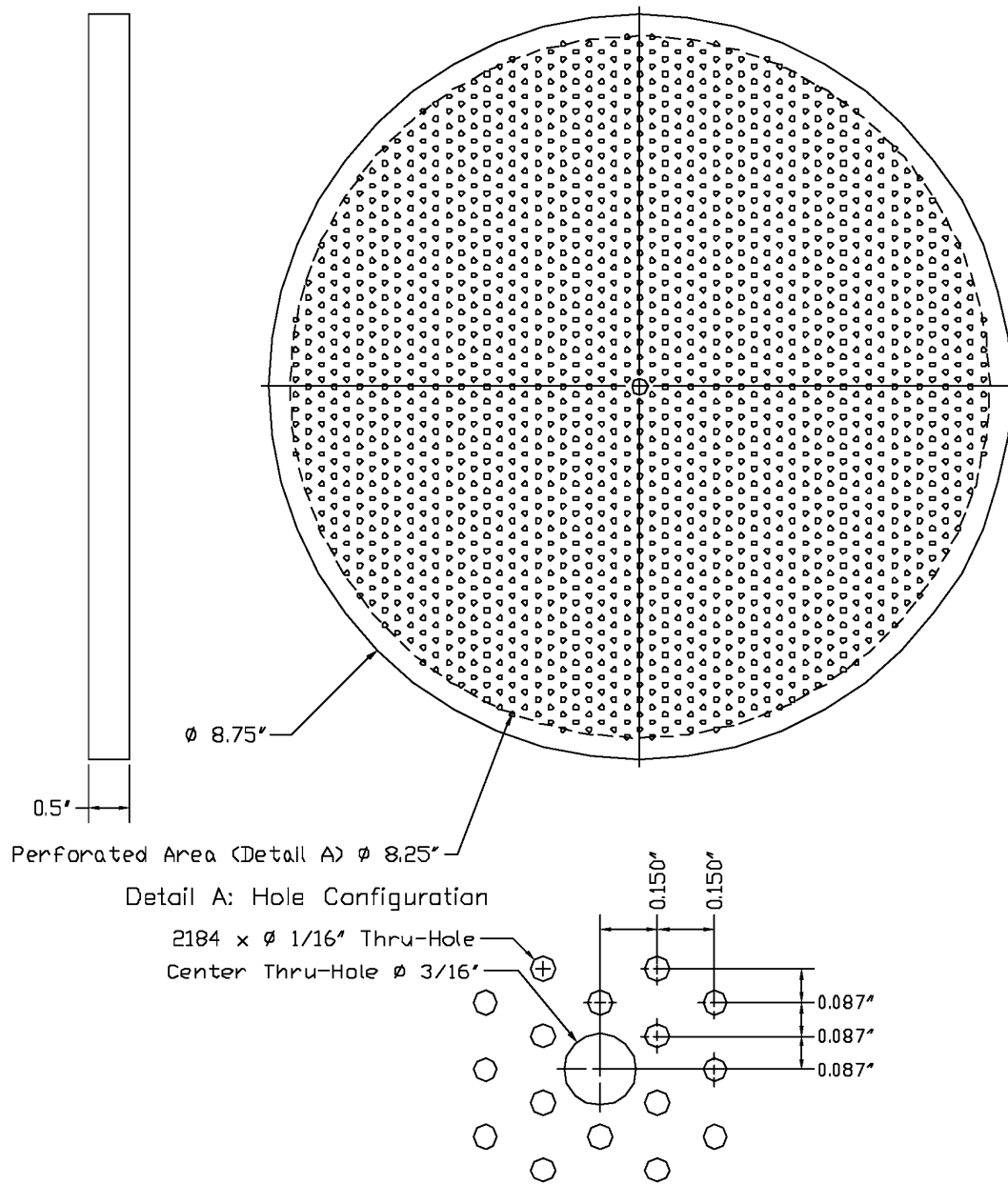


**Figure A.1.**  
Perforated Plate

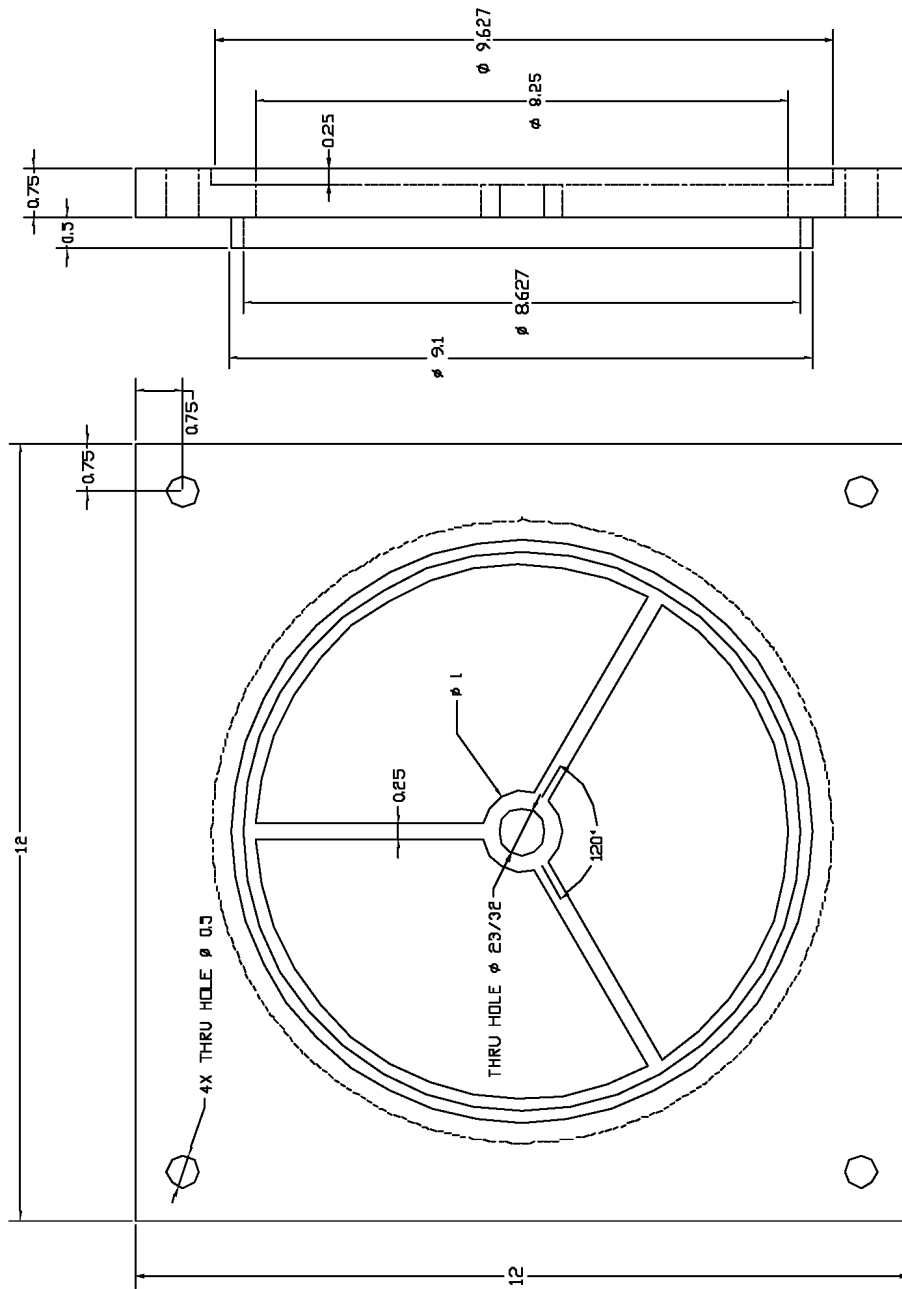
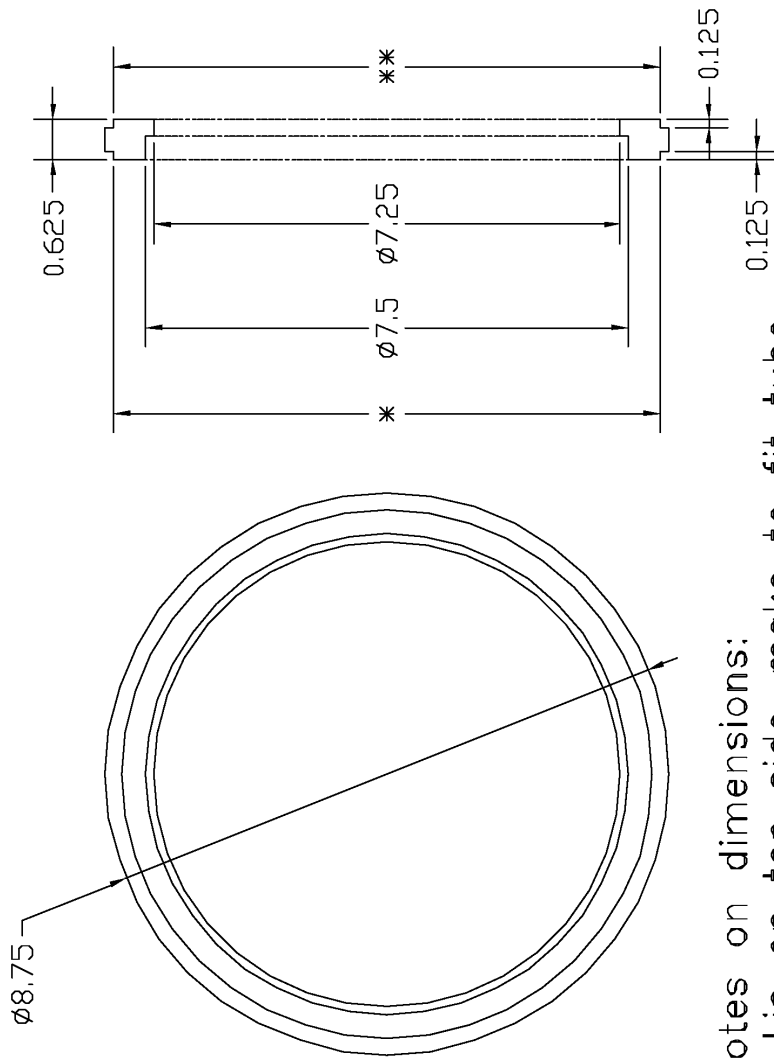


**Figure A.2.**  
Adaptor Plate



Notes on dimensions:  
 \* Lip on top side—make to fit tube with fittings  
 \*\* Lip on bottom side—make to fit SS roll-up

**Figure A.3.**  
 Adaptor Ring

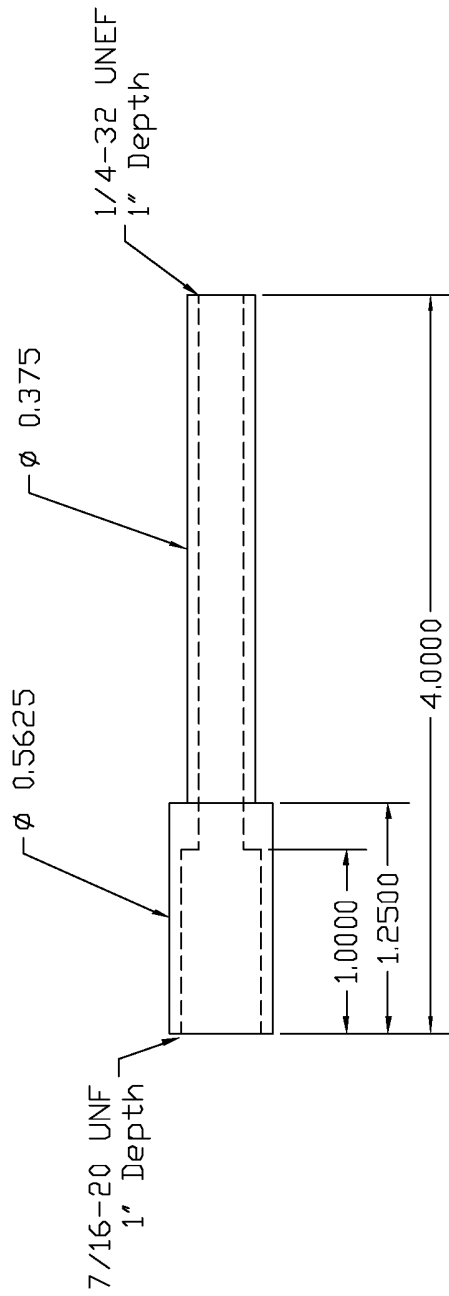


**Figure A.4.**  
 Nozzle Adaptor

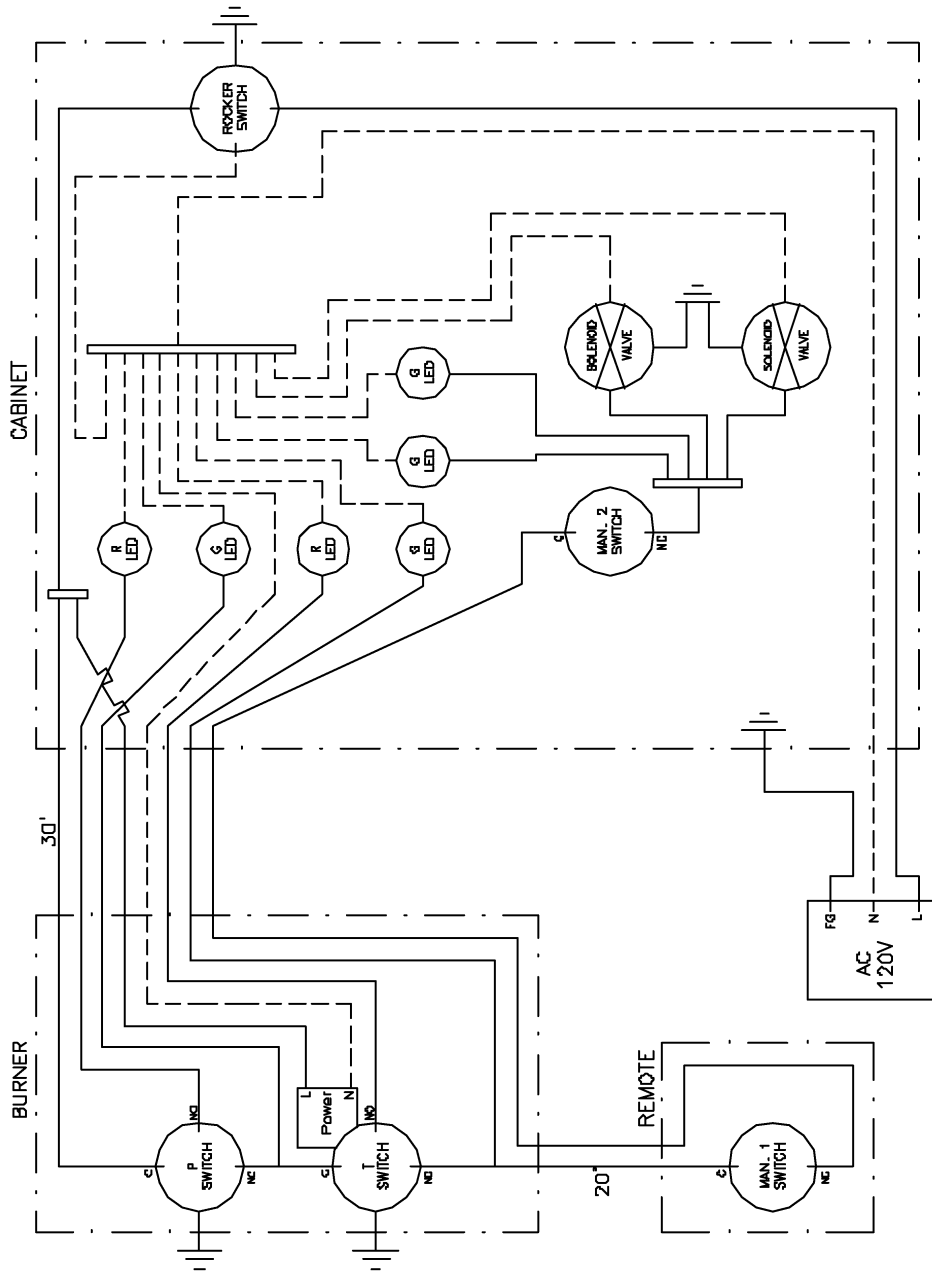


**Figure A.5.**

Cabinet Safety System

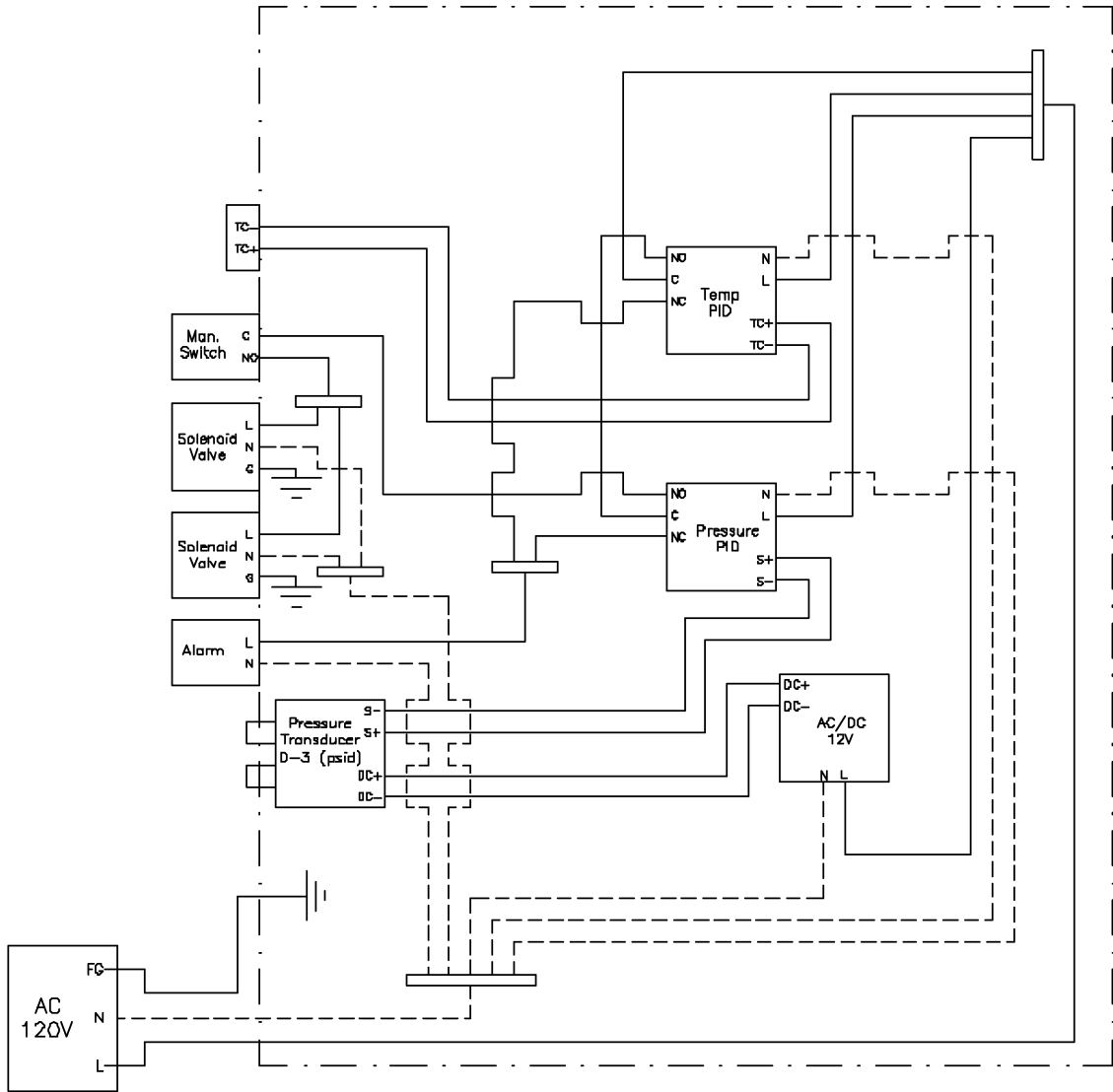


**Figure A.6.**

Portable Safety System

**Table A.7.**  
Parts List

Part	Qty.	Material	Dimensions	Cost (\$)
<b>Air Supply</b>				
Variable Speed Controller	1		Allen-Bradley 160 SSC (Series B)	1000
1.5hp Blower	1			500
Car Air Filter	1			25
Flexi-hose	1	PP	4"OD x 12'L	50
<b>Flashback Chamber Assy.</b>				
Adaptor Chamber	1	PVC	4"OD - 8"OD	100
Adaptor Plate	1	Al	-	500
Section 1	1	SS	8.25OD x 0.25"W x 5"L	400
Adaptor Ring	1	Al	-	300
Flame Arrestor	1	Ceramic	7.5"OD x 2.5"L	100
Section 2	1	SS	8.65"OD x 0.15"W x 9"L	500
Pressure Port	2	SS	0.25"	30
Thermocouple Port	2	SS	0.125"	20
<b>Safety System</b>				
Temperature Switch/PID	1		Set at 35 C	300
Pressure Transducer/PID	1		Set at 1/2" & 10" H <sub>2</sub> O	300
Thermocouple K	1			10
Housing	1	Al	8" x 8" x 6"	20
<b>Flame-Holder Assy.</b>				
Perforated Plate	1	Brass	-	1100
Exit Collar	1	SS	8.65"OD x 0.25"W x 1.25"L	250
Cooling Coils	1	Cu	0.25"OD x 18'L	20
Thermocouple K	2			20
<b>Jet/Spray</b>				
Tube (gas)	1	SS	0.25"OD x 25"L	10
Delavan Nozzle (67700-5)	1	SS	0.7FN x 45 Angle	150
Nozzle Adaptor	1	SS	-	200
<b>Other</b>				
RTV, Duct Tape				30

5935

# Appendix B

## Conditional Mean Data Plots

Figure B.1.

Hydrogen Flame Conditions, Conditional Favre Average and Variance

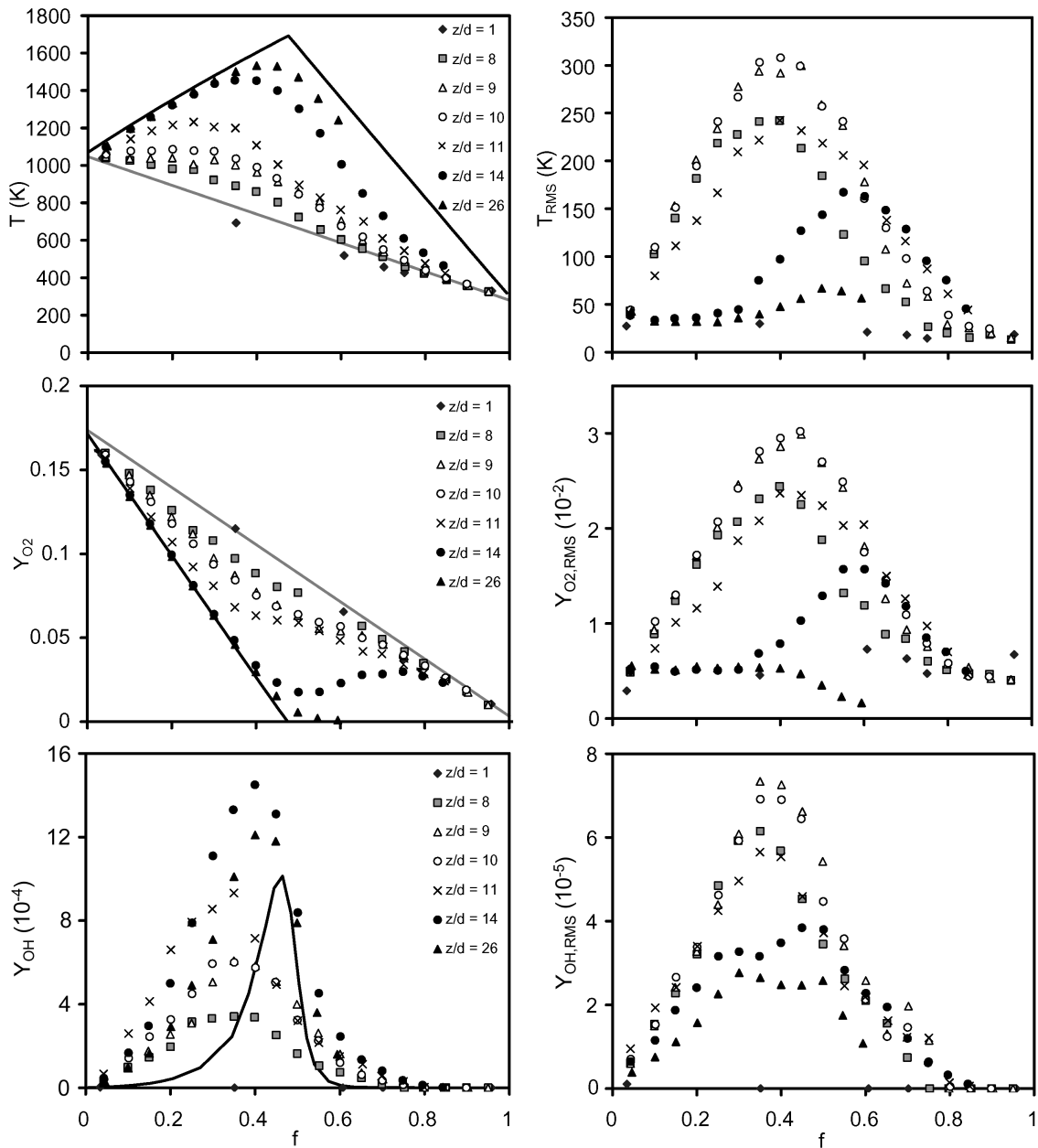
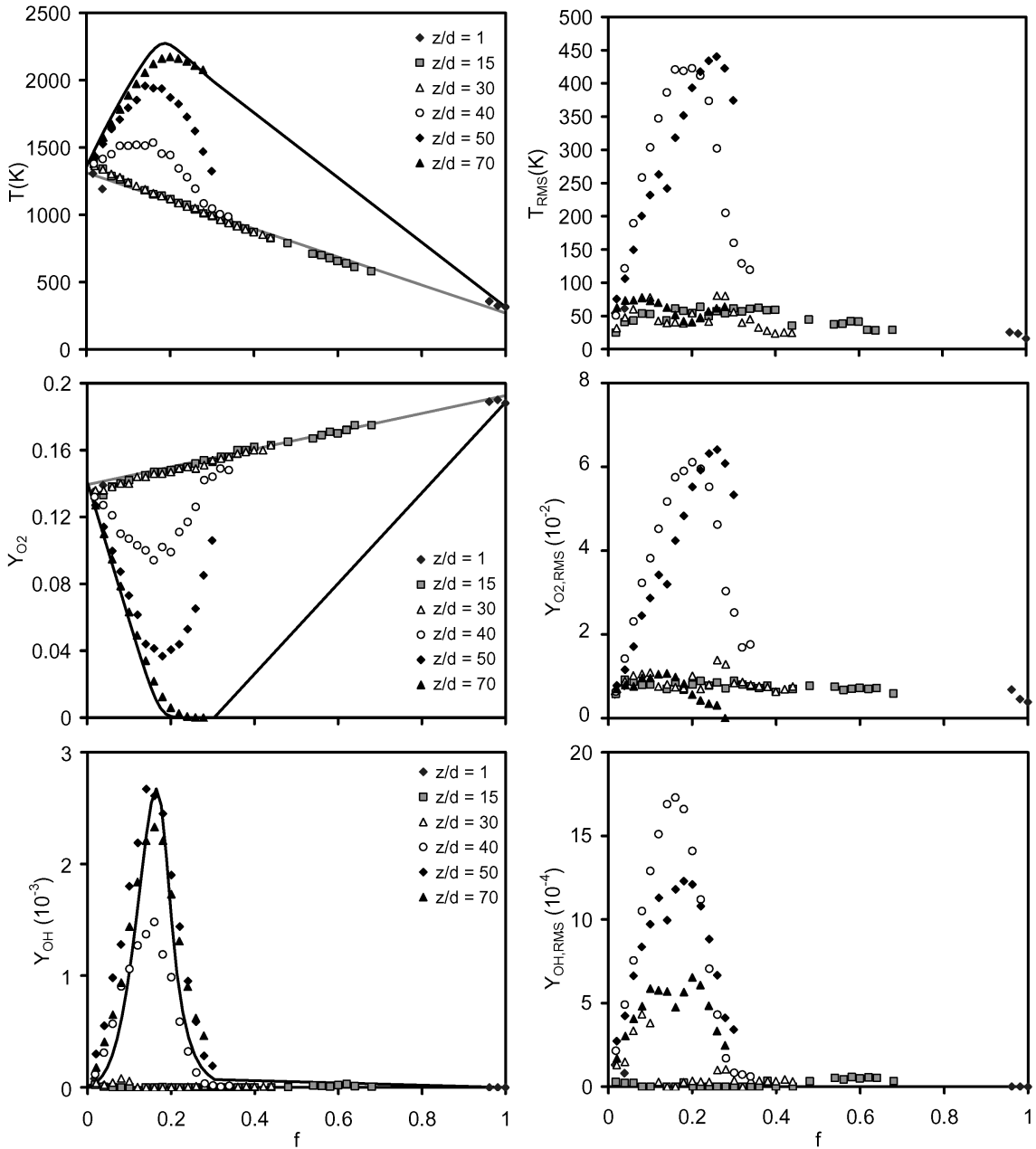


Figure B.2.

Methane Flame Conditions, Conditional Favre Average and Variance



## Appendix C

# Characterization of Liquid Fuel Evaporation of a Lifted Methanol Spray Flame in a Vitiated Coflow

### Abstract

An experimental investigation of lifted spray flames in a coflow of hot, vitiated gases is presented. The vitiated coflow burner is a spray flame that issues into a coaxial flow of hot combustion products from a lean, premixed H<sub>2</sub>/Air flame. The spray flame in a vitiated coflow emulates the combustion that occurs in many advanced combustors without the detailed fluid mechanics. Two commercially available laser diagnostic systems are used to characterize the spray flame and to demonstrate the vitiated coflow burner's amenability to optical investigation. The *Ensemble Particle Concentration and Size (EPCS)* system is used to measure the path-averaged droplet size distribution and liquid volume fraction at several axial locations while an extractive probe instrument named the *Real-time Fuel-air Analyzer (RFA)* is used to measure the air to fuel ratio downstream of the spray nozzle with high temporal and spatial resolution. The effect of coflow conditions (stoichiometry) and dilution of the fuel with water was studied with the *EPCS* optical system. As expected, results show that water retards the evaporation and combustion of fuels. Measurements obtained by the *RFA* extractive probe show that while the *Delavan* manufactured nozzle does distribute the fuel over the manufacturer specified spray angle, it unfortunately does not distribute the fuel uniformly, providing conditions that may result in the production of unwanted NO<sub>x</sub>. Despite some limitations

due to the inherent nature of the experimental techniques, the two diagnostics can be readily applied to spray flames in the vitiated coflow environment.

### **C.1. Introduction**

In today's advanced combustors, spray combustion is typically employed where liquid fuel is injected into a hot and/or pressurized environment of air and combustion products. Staged combustors of gas turbine engines and direct injection diesel engines are examples of spray combustion in vitiated gases. The research presented here investigates spray combustion without the detailed recirculation fluid mechanics typically embedded in advanced combustor flow. Two commercially available optical diagnostic tools are applied to determine the amenability of the vitiated coflow burner to experimental spray flame research.

A vitiated coflow burner is a spray flame that issues into a coaxial flow of hot combustion products from a lean premixed flame (vitiating coflow) as shown in Figure C.1. This configuration is such that the vitiated coflow isolates the spray flame from the lab air for a maximum downstream distance. The simplified flow provides a unique opportunity to investigate chemical kinetics of spray combustion in a hot, vitiated environment without the detailed fluid mechanics typical of advanced combustors. The vitiated coflow burner provides both well-defined boundary conditions and optical access, thus facilitating both computational explorations and optical diagnostics.

A laser-suction probe instrument, dubbed the *Real-time Fuel-air Analyzer (RFA)* characterizes the spatial and temporal variations of the fuel-air ratio with high resolution (Girard et al. 2001). The *RFA* is applied to determine the effectiveness of an industrial spray nozzle to uniformly distribute fuel in the coflow. A commercial ensemble light

diffraction (ELD) optical tool named the *Ensemble Particle Concentration and Size (EPCS)* system characterizes the spray evolution between the nozzle exit and the flame base. The *EPCS* system obtains path-averaged measurements of the spray droplet size distribution and the liquid volume fraction (*Malvern/INSITEC* 1998). Such information can determine the nozzle's fuel atomization effectiveness and the fuel evaporation rate of sprays in the hot vitiated environment.

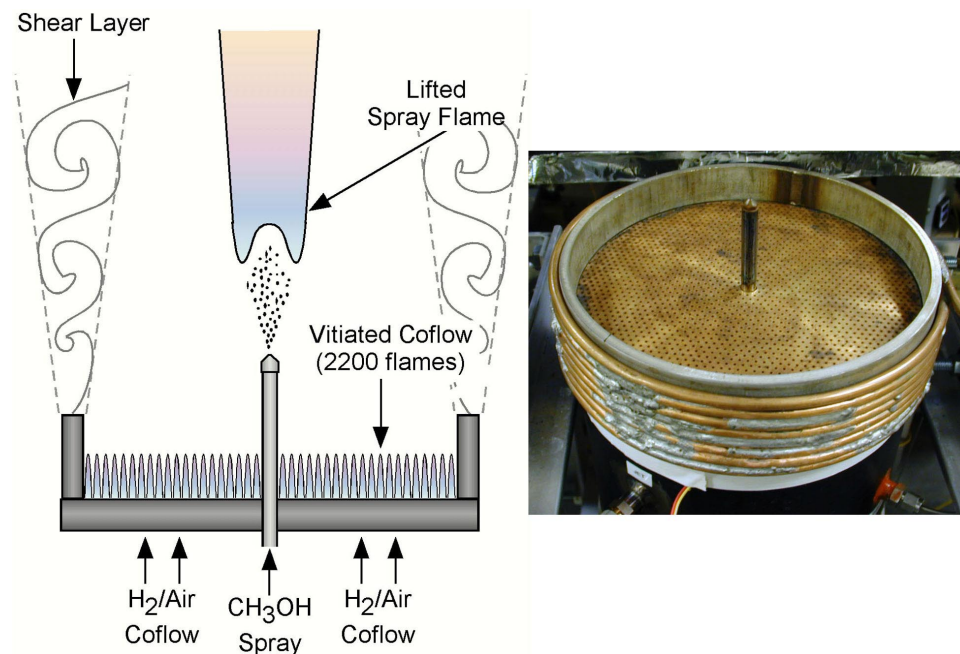


**Figure C.1.**

Vitiated coflow burner with axisymmetric spray

The research presented here is part of a larger experimental and numerical research effort concerning turbulent gaseous jet flames in the vitiated coflow. In the early stages of this research, it became apparent that a number of collaborative opportunities were possible in the area of liquid spray combustion. Consequently, the vitiated coflow burner was applied to liquid sprays to demonstrate the design's amenability to experimental spray flame research. The open configuration of the vitiated

coflow burner provides optical access, the *EPCS* laser diagnostic system is therefore used to characterize the spray evolution from the nozzle exit to the flame base. However, the hot coflow environment can be hostile to intrusive diagnostics; therefore the *RFA* extractive probe was employed to determine the feasibility of probe measurements. Also studied is the effect of coflow conditions (stoichiometry) and fuel composition (dilution with water).

## C.2. Experimental Setup

Experiments were conducted on a lifted  $\text{CH}_3\text{OH}$  spray flame in a vitiated coflow. As shown in Figure C.1, the combustor consists of a central  $\text{CH}_3\text{OH}$  spray with the vitiated coflow presented in Chapter 4. The spray exit is positioned at a location high enough (10cm) above the perforated plate so that a uniform flow field with isotropic turbulence can be assumed. The coflow provides an environment that isolates the spray flame from the cool lab air.

### *Fuel Spray System*

For this study a *Delavan* industrial nozzle produces the methanol spray flame. The *Delavan* fuel nozzle has a manufacturer specified spray angle and fuel number. The fuel number determines the mass flow rate given the back-pressure on the nozzle.

$$\text{FN} = \frac{\dot{m}(\text{lb/hr})}{\sqrt{P(\text{psi})}} \quad (\text{C.1})$$

The mass flow rate is determined via a modification of Equation (C.1).

$$\dot{m}(\text{kg/s}) = \text{FN} \sqrt{P(\text{psi})} \left( 1.26 \times 10^{-4} \frac{\text{kg/s}}{\text{lb/hr}} \right) \quad (\text{C.2})$$

The addition of water to methanol in the fuel spray was also researched. Evaporation and the subsequent combustion of fuels are retarded with the dilution of

water. Table C.1 lists a number of physical properties of methanol and liquid water at 1atm. As can be seen in Table C.1, the addition of water to methanol increases density, dynamic viscosity, heat of vaporization and boiling temperature; resulting in a delay of the onset of combustion, and lower flame temperatures.

*Ensemble Light Diffraction (ELD) Optical System*

The *Malvern/INSITEC EPCS* (Ensemble Particle Concentration and Size) system is designed to provide real-time particle size distribution measurements from mixtures of aerosols or powder. The *EPCS* uses the ensemble light diffraction (ELD) technique to measure the particle size distribution. This system applies the Fraunhofer theory that relates the angle at which the beam is scattered by a particle to the size of that particle; larger particles scatter laser light at smaller angles.

**Table C.1.**

Physical Properties of Methanol and Water at 1atm

	Methanol	Water
Heat of Vaporization $\Delta H_{\text{vap}}$ (kJ/kg)	1100	2257
Dynamic Viscosity $\mu$ (Ns/m <sup>2</sup> )	$4.6 \times 10^{-4}$	$1.12 \times 10^{-3}$
Boiling Temperature $T_b$ (°C)	64.5	100
Density $\rho$ (kg/m <sup>3</sup> )	787	1000

A schematic and an image of the *EPCS* system are shown in Figure C.2. The system consists of a laser diode, lens and two detectors. A diode generates a 5 mW, red (670 nm) laser beam. The scattering detector has log-scaled annular detectors at various radii and a small center hole through which the incident beam passes. The incident beam is focused at a sharp point at the center of the second detector, giving a measure of the

transmission through the spray. A computer running the *RTSizer* (Real Time particle Sizer) by *Malvern/INSITEC* executes the data reduction.

Based on the geometry of the system, the scattering detector provides the capability to measure the light intensity at several scattering angles. The lens also focuses all scattered light of a specific angle to a specific ring on the detector; independently of the location of the particle. The particle size distribution  $V(d_j)$  is then calculated

$$S(\theta_i) = \sum_j C_{i,j} V(d_j) \quad (C.3)$$

using the scattering signal  $S(\theta_i)$  and transform function  $C_{i,j}$ . The transform function is determined by particle and system optical properties.

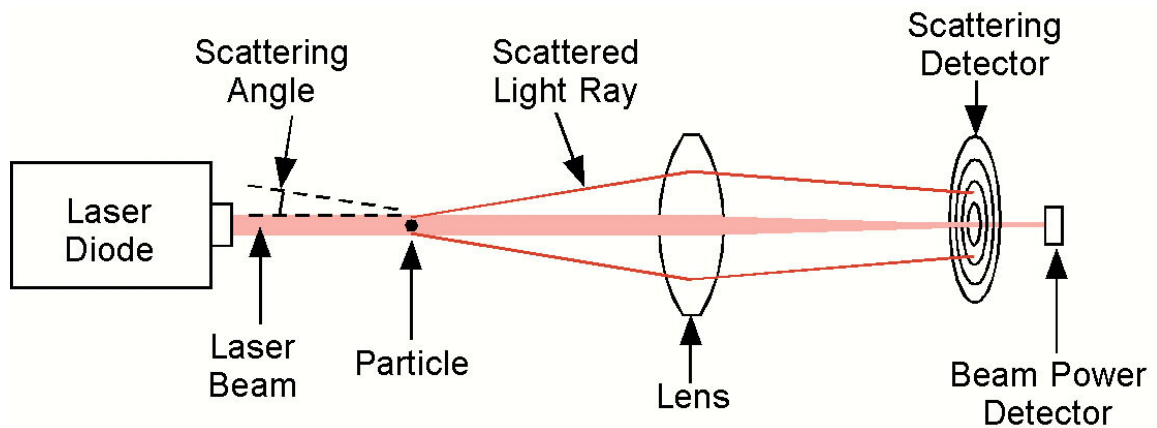
The beam power detector measures the transmission through the spray. The Beer-Lambert Law relates this transmission to the volume concentration  $C_V$  of the droplets.

$$T = e^{-\left(1.5 C_V L Q / D_{32}\right)} \quad (C.4)$$

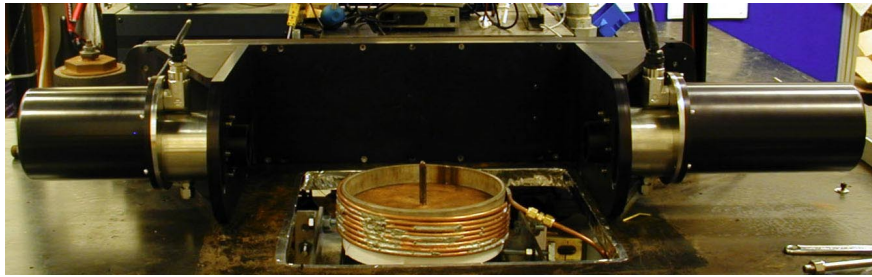
The transmission  $T$  is measured and the optical path length  $L$  is approximated via the vertical position and the nozzle manufacturer specified spray angle. The light scattering efficiency  $Q$  ( $\approx 2$ ) depends on the instrument geometry. The Sauter mean diameter  $D_{32}$  of the particle size distribution  $V(d_j)$  is proportional to the ratio of the ensemble droplet volume to the ensemble droplet surface area.

$$D_{32} = \frac{\sum_j V(d_j) d_j^3 \Delta d}{\sum_j V(d_j) d_j^2 \Delta d} \quad (C.5)$$

The Sauter mean diameter is a good metric of the average droplet size in the spray since it is not biased to larger diameter droplets that scatter more light.



(a) ELD Schematic



(b) Photo of *Malvern/INSITEC EPCS* System

**Figure C.2.**

Schematic and image of the Ensemble Light Diffraction (ELD) optical system.

Flame radiation incident on the detectors will cause error in measurements. Since the ring detector areas are log scaled (smaller areas closer to the center), the outer rings detected more of the flame radiation. The outer rings detect scattered light from small particles; therefore the presence of a flame results in a false bias to smaller droplets when determining the droplet size distribution. For the experiments where the laser beam intersects the flame, the data is corrected by omitting the outer detector ring measurements from the calculations. This practice is sound since the flame radiation affects the measurements for very small droplets ( $d < 5 \mu\text{m}$ ) whose populations are insignificant in these experiments.

The *EPCS* system was applied to the spray flame to determine path-averaged spray statistics at several axial locations. Droplet size distribution, Sauter mean diameter and liquid volume concentration measurements are made at each position. The effect of the addition of water to methanol is also studied. The sensitivity of spray flame lift-off to varying coflow conditions and water dilutions is also investigated; where the lift-off height is measured via digital imaging. The coflow conditions for the *EPCS* experiments are summarized in Table C.2.

**Table C.2.**

Coflow and Spray Experimental Conditions for *EPCS* and *RFA* experiments

	<i>EPCS</i>	<i>EPCS</i> / H <sub>2</sub> O	<i>RFA</i>
Liquid Spray Fuel	CH <sub>3</sub> OH	CH <sub>3</sub> OH/H <sub>2</sub> O	CH <sub>3</sub> OH
Coflow Equivalence Ratio ( $\phi$ )	0.3	0.3,0.35	0.2
Coflow Temperature (K)	1200	1200,1280	790
Coflow Oxygen X <sub>O<sub>2</sub></sub> (%)	16	16,14.5	18
Nozzle Pressure (kPa/psi)	241/35	310/45	276/40
Spray Flow-rate (g/s)	0.5	0.8	0.9
Nozzle Fuel Number (FN)	0.7	0.7	1.1
Nozzle Spray Angle	45°	45°	115°
Delavan Nozzle Part No.	67700-5	67700-5	27710-4

*Real-Time Fuel-Air Analyzer (RFA) Suction Optical Probe System*

The mixedness of the fuel in the spray flame was measured by the *Real-time Fuel-air Analyzer (RFA)* extractive laser probe developed at U.C. Berkeley (Mongia et al. 1998, Mongia 1998, Girard et al. 2001) and manufactured by *Panamint Technologies*. The *RFA* instrument applies a high-speed sampling laser absorption technique to temporally and spatially measure the air to hydrocarbon fuel ratio. The hydrocarbon vapor in the sample gas absorbs the laser beam as it passes through an absorption cell. A

schematic of the *RFA* system is shown in Figure C.3. This instrument consists of a small diameter probe, absorption cell, infrared laser, high sensitivity IR light detector, and vacuum pump. The sample gas is extracted from the flow with the probe, flows through the absorption cell and is ventilated by the pump. The pressure and temperature are measured just downstream of the absorption cell. In the sampling probe, the inner diameter is 1mm and the flow is sonic. Since the flow in the probe is sonic, the pressure in the cell is stable and independent of the pressure at the sampling point. The absorption cell is a cylinder with sapphire windows on both ends. The cell is 12.7 mm long and has an inner diameter of 4.75 mm, yielding a volume of 0.225 cm<sup>3</sup>. The combination of sonic flow, a small absorption cell volume and a small sampling probe diameter translates to a short residence time of the sample in the system; resulting in a high sampling rate. The maximum resolvable frequency of fluctuation in the fuel-air ratio due to the short residence time is approximately 625 Hz (Girard et al., 2001). Spatial resolution is obtained by simply repositioning the probe in the flow. An infrared He-Ne laser beam ( $\lambda_{\text{He-Ne}}=3.39\mu\text{m}$ ) passes through the sample gas in the absorption cell. The laser intensity is measured by the IR detector (attached to the opposite end of the absorption cell).

The fuel-air ratio is determined using the measured transmission of the laser beam and the Lambert-Beer equation (Mongia et al., 1998, Lee et al., 2000). Beer's law determines the path-averaged methanol mole fraction ( $X_{\text{CH}_3\text{OH}}$ ) with the ratio of the detected and the unattenuated laser radiation intensities ( $I/I_0$ ).

$$X_{\text{CH}_3\text{OH}} = -\frac{\ln(I/I_0)}{\alpha P_{\text{abs}} l_{\text{bp}}} \quad (\text{C.6})$$

Where  $\alpha$  is the absorption coefficient,  $l_{\text{bp}}$  is the laser beam path length and  $P_{\text{abs}}$  is the absolute pressure.

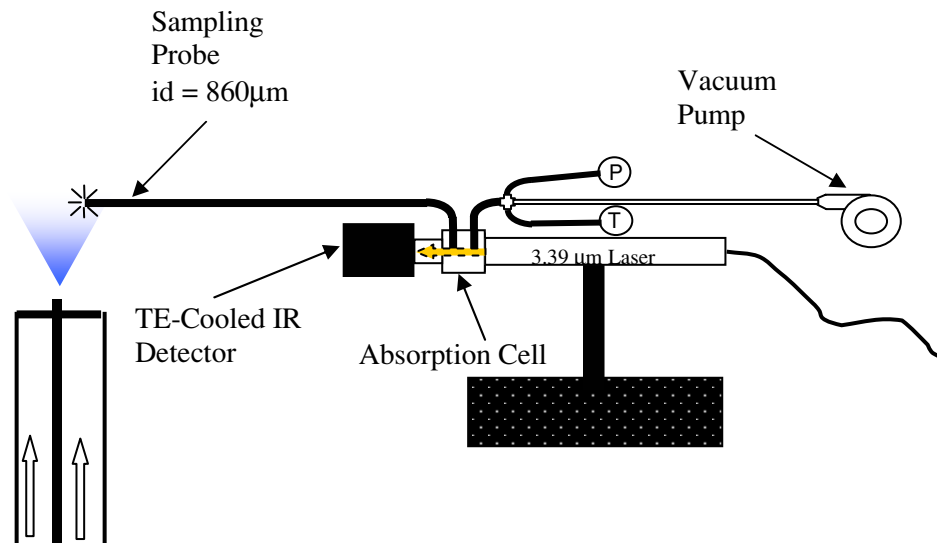


**Figure C.3.**

Schematic of the Real-time Fuel-air Analyzer (RFA) instrument

There are two issues that must be taken into account with the implementation of this extractive probe device; these are condensation and over-heating of the probe. It was originally thought that a droplet extracted from the flow would evaporate due to the large pressure drop in the absorption cell and completely absorb the laser beam. Unfortunately, at points where the laser absorption was 100%, a liquid film would form on the absorption cell windows, requiring the instrument to be disassembled and cleaned. The operating temperature and pressure of the absorption cell were set to prevent condensation. Also, if the coflow was too hot, the stainless steel probe would over-heat and reach a temperature that would initiate premature combustion of the spray flame, causing instabilities of the flow, probe location and measurements. This intrusiveness of the probe limited the investigations to non-reacting sprays; therefore the *RFA* instrument was used to study the evaporation of non-reacting sprays in a vitiated coflow.

The spatial and temporal resolution of the *RFA* instrument was used to determine the effectiveness of the nozzle to distribute fuel uniformly in the vitiated coflow. Measurements were taken along the spray axis and at radial locations in the vicinity of the spray cone edges. The non-reacting spray conditions of the *RFA* experiments are summarized in Table C.2.

#### *Vitiated Coflow and Fuel Spray Experimental Conditions.*

A summary of the experimental conditions for each set of experiments has been given in Table C.2. The conditions for each of the experiments are different because of the limitations of the *RFA* experimentation as outlined in the previous section. Therefore, for the *EPCS* experiments, a lifted spray flame was stabilized and the evaporation of the droplets between the nozzle exit and the flame base was characterized by the *EPCS* system. For the *RFA* experiments, the associated limitations (condensation, premature combustion) resulted in the characterization of a non-reacting spray in a hot coflow. Also studied is the effect of coflow conditions (stoichiometry) and fuel composition (dilution with water).

### **C.3. Results And Discussion**

#### *Spray Droplet Size Distribution*

At each axial location, the *EPCS* system measures the path-averaged droplet size distribution of the spray. For each lifted spray flame experiment (Table C.2), measurements were made at several axial locations between the nozzle exit and the lift-off height ( $H = 125$  mm). Per the methodology previously discussed, the *RTSizer* software produces a distribution similar to the one shown in Figure C.4. As can be seen, a histogram is produced based on the signals from the annular ring detectors.

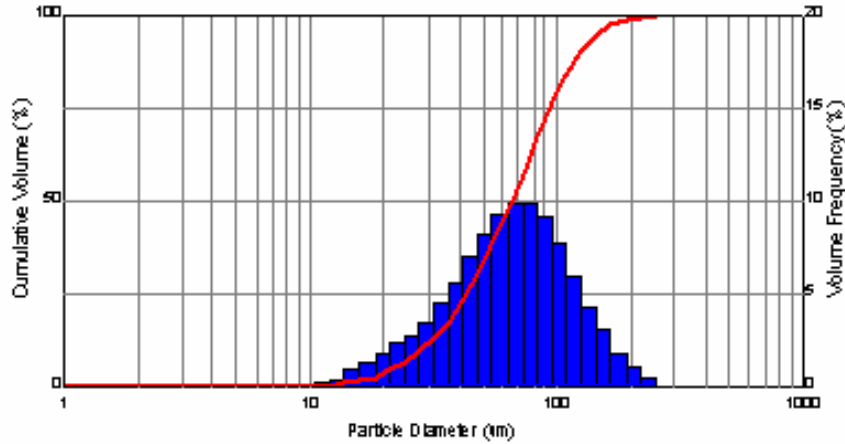


**Figure C.4.**

Droplet size distribution results from *RTSizer* software (*Malvern/INSITEC*). The curve is the cumulative volume per diameter.

The Sauter mean diameter is also determined by *RTSizer* at each axial location. The evolution of the spray between the nozzle exit and the flame base is characterized by measuring the Sauter mean diameter at several axial locations; this axial profile is shown below in Figure C.5. As can be seen, as smaller droplets initially evaporate, the mean diameter slightly increases until complete evaporation and combustion occurs when the droplet size quickly decreases.

Another spray metric is the volume concentration of liquid droplets. The axial profile of the liquid volume concentration is also shown in Figure C.5. For these calculations, the Delevan specified spray angle ( $45^\circ$ ) was incorporated to determine the path length  $L$  used in Equation (C.2) to determine the volume concentration. As can be seen in Figure C.5, this change in concentration is not significantly different from its change due strictly to droplet divergence. The divergence of the spray cone scales with the square of the axial distance from the nozzle exit  $z$ ; therefore without evaporation the liquid volume fraction of the spray decreases as  $\sim 1/z^2$ . The effect of droplet evaporation

or non-uniform spray distribution is exhibited in the axial profile with a steeper curve ( $\sim 1/z^{2.33}$ ) than pure divergence.

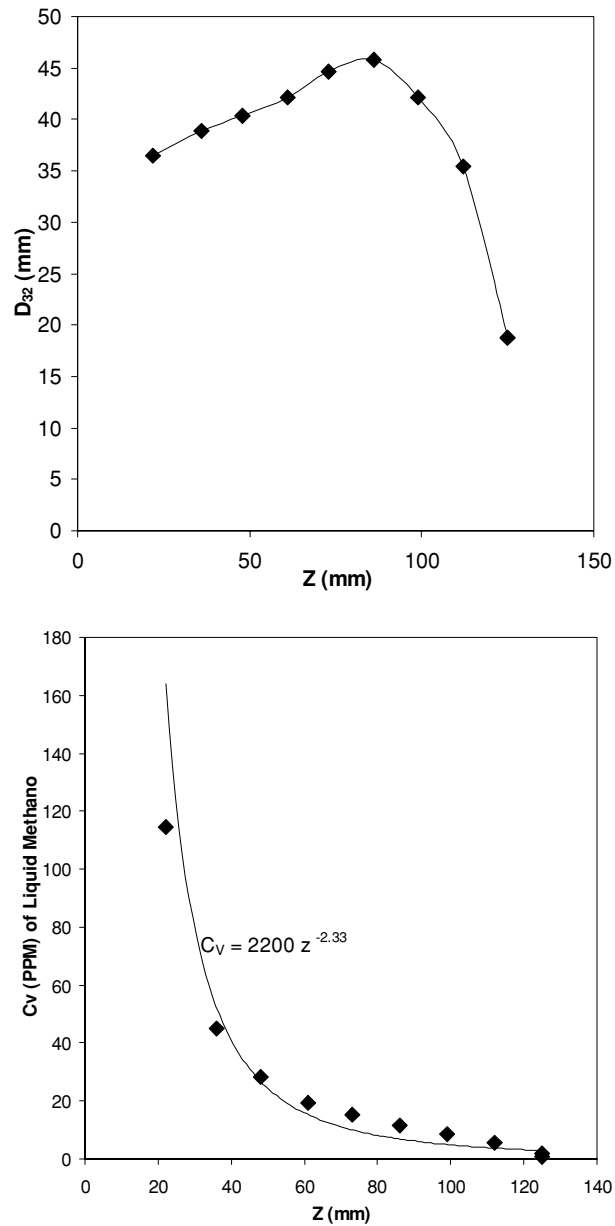


**Figure C.5.**

Evolution of the methanol spray Sauter mean diameter ( $D_{32}$ , left) and spray volume concentration ( $C_V$ , right) with axial distance from the nozzle exit.

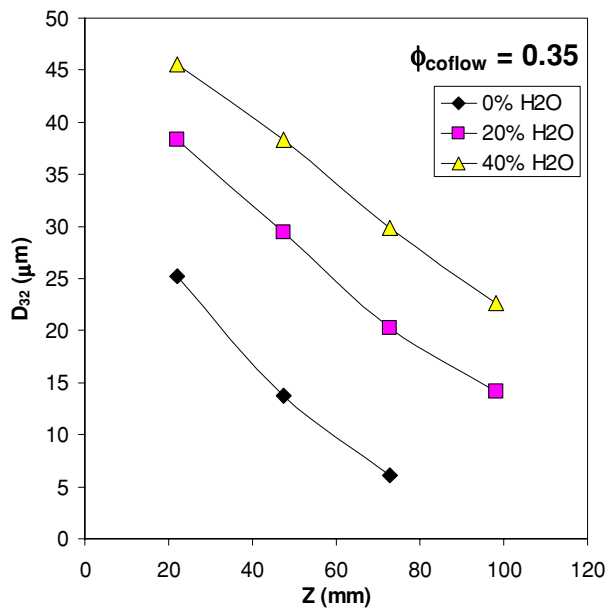
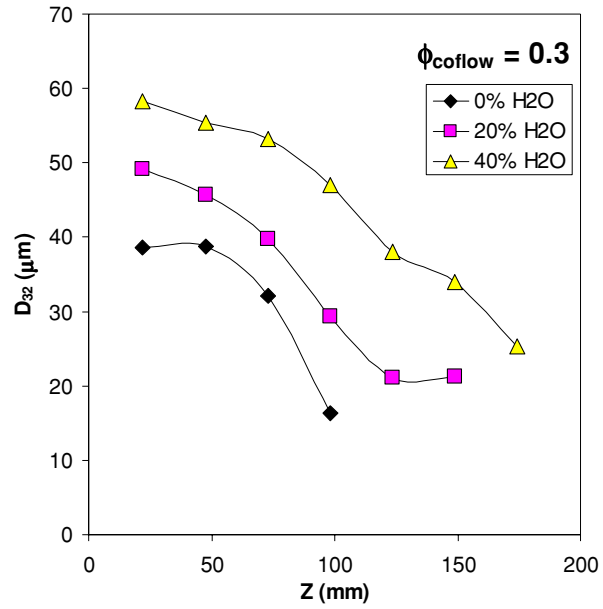


**Figure C.6.**

Axial profiles of Sauter mean diameter for varying water concentration and coflow conditions.

### *Spray Flame of Methanol in an Aqueous Solution*

Increased water concentration retards combustion of the fuel spray mixture. The effect of the addition of water was studied by varying the mass concentration of water from 0 to 40% and the effect of the coflow on the spray is also investigated by varying coflow stoichiometries ( $\phi = 0.3$  &  $0.35$ , Table C.2). Shown in Figure C.6 is the evolution of the spray Sauter mean diameter between the nozzle and the flame base for the different fuel mixtures and coflow conditions. Since the viscosity of water is greater than that of methanol, increased water concentration results in increased mixture viscosity. For mixtures with increased water concentration, initial droplet sizes are larger (increased viscosity) and the duration of the spray is longer (increased heat and temperature of vaporization); these water effects can be seen in Figure C.6. The differences in evaporation rate between mixtures are not evident since the profiles in Figure C.6 decrease at approximately the same rate.

The sensitivity of the lift-off height to coflow stoichiometry and spray composition has been studied and the results can be presented in Figure C.7. As expected, the addition of water and/or reduced coflow stoichiometry results in an increase of the spray flame lift-off height. As discussed earlier, this is a result of larger initial droplet sizes and larger heat of vaporization due to the addition of water. No results were obtained for the addition of water at the hotter coflow condition ( $\phi = 0.4$ ) because of nozzle failure.

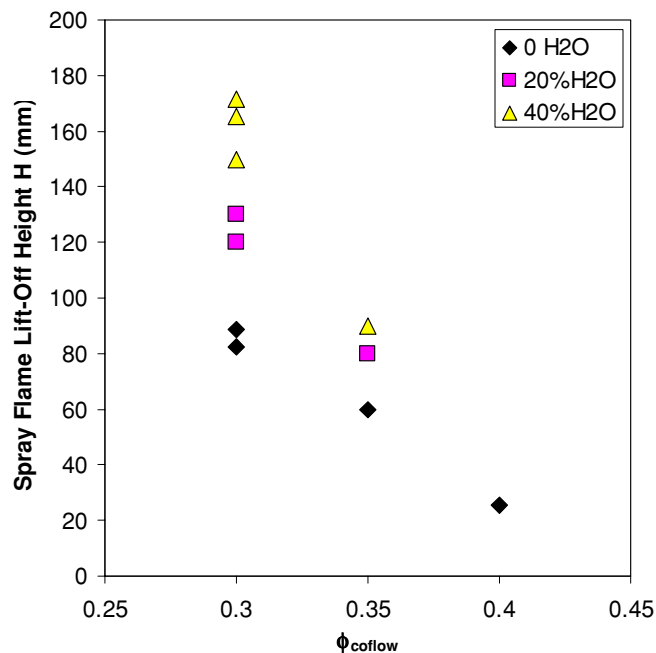


**Figure C.7.**

Lift-off height of methanol-water spray flames with varying water concentrations and coflow conditions.

*Gaseous Fuel to Air Ratio*

The schematic of the spray setup with the measured methanol concentrations displayed at the selected positions is shown in Figure C.8. As expected, the highest concentrations of methanol were found along the axis in the spray cone.

Measurements along the axis were taken and the results are shown in Figure C.9. As expected, the center-point concentration decreases with distance from the nozzle. However, the rate at which the concentration decreases is less ( $\sim 1/z^{0.4}$ ) than that of a uniformly divergent spray ( $\sim 1/z^2$ ). At a downstream distance of 150 mm, the concentration was below the detection limits of the instrument ( $X_{\text{CH}_3\text{OH}} < 0.01$ ).

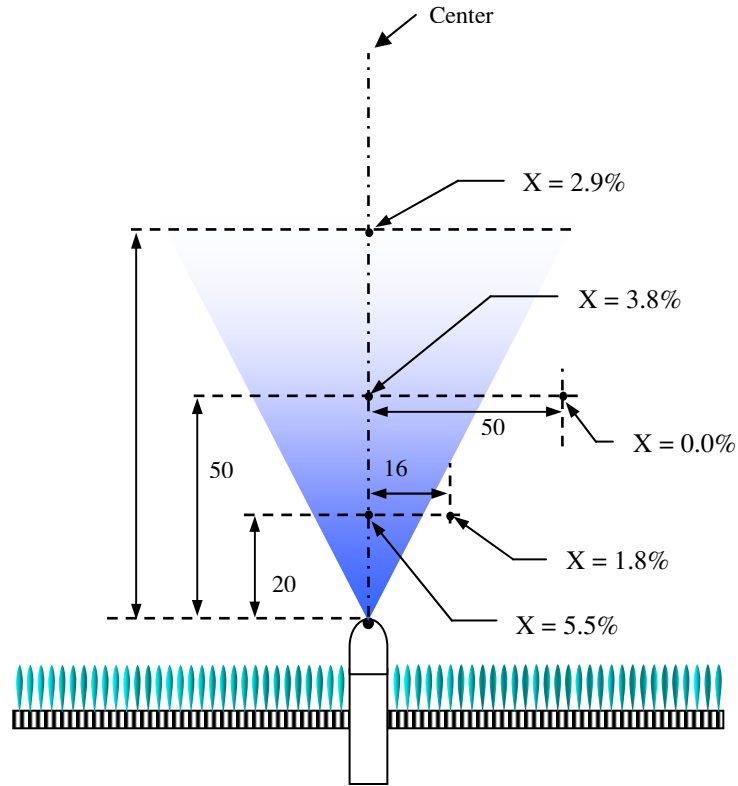


**Figure C.8.**

Schematic of spray experiment showing concentrations of methanol at selected locations.

Unlike the path-averaged measurements of the *EPCS* system, the *RFA* system provides the spatial resolution to investigate radial diffusion of the methanol from the centerline. A radial profile of the methanol concentration at an axial height of 20 mm above the spray nozzle is shown in Figure C.10. Since centerline fuel concentration decreases slowly, this means the spray does not uniformly distribute the fuel radially, resulting in steep radial gradients. The manufacturer specified spray angle ( $110^\circ$ ) should result in a cone radius of 28.6 mm at this axial location; and is verified by the fuel concentration reaching zero at approximately 25 mm in Figure C.10. Note the low signal RMS measured at the centerline and high signal RMS at the edge of the spray cone. The

non-uniformity and high RMS values make possible the production of NO<sub>x</sub> at these local hot spots.

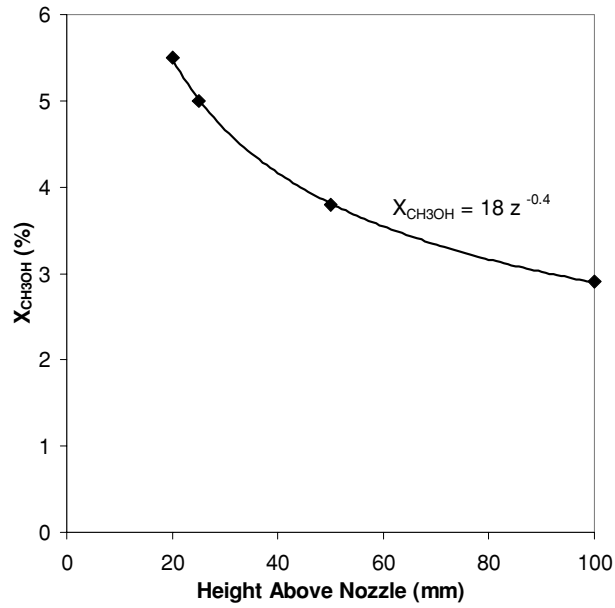


**Figure C.9.**

Centerline concentration of methanol vs. axial distance.

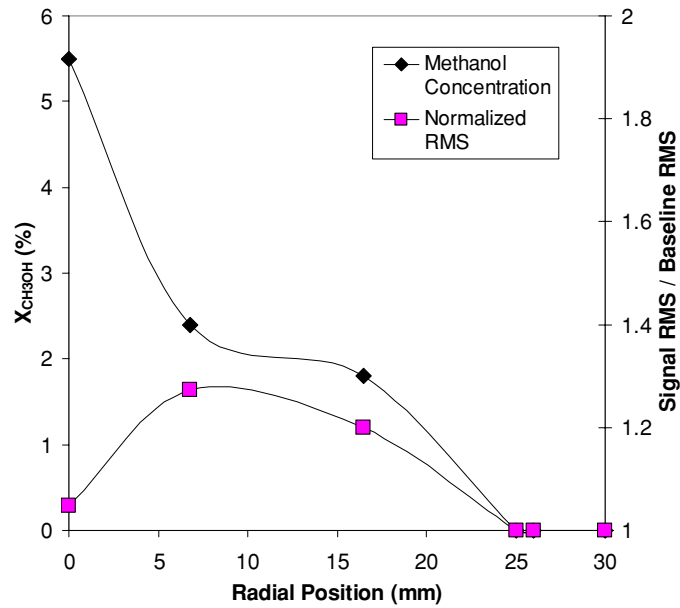


**Figure C.10.**

Radial profile of methanol concentration and concentration RMS at z = 20 mm.

#### C.4. Conclusions

Two commercially available diagnostics were used to characterize a spray flame in the vitiated coflow environment. The evolution of the spray droplet size distribution and liquid volume fraction were determined by the *EPCS* optical diagnostic while the spatial and temporal fluctuations of the fuel concentration was determined by the *RFA* extractive probe instrument. Despite certain limitations of each technique, it was shown that the spray in a vitiated coflow can be characterized. The effect of coflow conditions (stoichiometry) and spray conditions (water dilution) was studied with the *EPCS* system showing, as expected, that water retards the evaporation and combustion of fuels. The *RFA* probe measurements show that while the Delavan nozzle does distribute the fuel over the manufacturer specified spray angle, it unfortunately does not distribute the fuel uniformly, providing conditions that may result in the production of unwanted  $\text{NO}_x$ .

<b>REPORT DOCUMENTATION PAGE</b>			<i>Form Approved</i> <i>OMB No. 0704-0188</i>	
Public reporting burden for this collection of information is estimated to average 1 hour per response, including the time for reviewing instructions, searching existing data sources, gathering and maintaining the data needed, and completing and reviewing the collection of information. Send comments regarding this burden estimate or any other aspect of this collection of information, including suggestions for reducing this burden, to Washington Headquarters Services, Directorate for Information Operations and Reports, 1215 Jefferson Davis Highway, Suite 1204, Arlington, VA 22202-4302, and to the Office of Management and Budget, Paperwork Reduction Project (0704-0188), Washington, DC 20503.				
<b>1. AGENCY USE ONLY (Leave blank)</b>		<b>2. REPORT DATE</b> March 2004	<b>3. REPORT TYPE AND DATES COVERED</b> Final Contractor Report	
<b>4. TITLE AND SUBTITLE</b>  Turbulent Jet Flames Into a Vitiated Coflow			<b>5. FUNDING NUMBERS</b>  WBS-22-708-90-01 NAG3-2103	
<b>6. AUTHOR(S)</b>  Ricardo Cabra				
<b>7. PERFORMING ORGANIZATION NAME(S) AND ADDRESS(ES)</b>  University of California, Berkeley Berkeley, California 94720			<b>8. PERFORMING ORGANIZATION REPORT NUMBER</b>  E-14301	
<b>9. SPONSORING/MONITORING AGENCY NAME(S) AND ADDRESS(ES)</b>  National Aeronautics and Space Administration Washington, DC 20546-0001			<b>10. SPONSORING/MONITORING AGENCY REPORT NUMBER</b>  NASA CR-2004-212887	
<b>11. SUPPLEMENTARY NOTES</b>  This report was submitted as a dissertation in partial fulfillment of the requirements for the degree Doctor of Philosophy to the University of California, Berkeley, Berkeley, California, Spring 2003. Project Manager, James D. Holdeman, Turbomachinery and Propulsion Systems Division, NASA Glenn Research Center, organization code 5830, 216-433-5846.				
<b>12a. DISTRIBUTION/AVAILABILITY STATEMENT</b>  Unclassified - Unlimited Subject Category: 07  Available electronically at <a href="http://gltrs.grc.nasa.gov">http://gltrs.grc.nasa.gov</a> This publication is available from the NASA Center for AeroSpace Information, 301-621-0390.			<b>12b. DISTRIBUTION CODE</b>	
<b>13. ABSTRACT (Maximum 200 words)</b>  A vitiated coflow flame is examined, which is an experimental condition that decouples the combustion processes of flows found in practical combustors from the associated recirculating fluid mechanics. The configuration consists of a fuel jet into a coaxial flow of hot combustion products from a lean premixed flame. The coflow isolates the jet flame from the cool ambient, providing a hot environment similar to the operating conditions of advanced combustors; this important high temperature element is lacking in the traditional laboratory experiments of jet flames into cool (room) air. Analysis of the results suggests that flame stabilization occurs through a combination of flame propagation, autoignition, and localized extinction processes. An expanded view of distributed reaction combustion is proposed based on analysis of the distributions of probe volume conditions at the stabilization region of the lifted hydrogen and methane flames. Turbulent eddies the size of the flame thickness mix fuel and hot coflow across the flame front, thereby enhancing the reaction zone with autoignition of reactants at elevated temperatures; this is the reverse effect of turbulent flames in ambient air, where intense turbulence in cool mixtures result in localized extinction. Each of the three processes (i.e., flame propagation, autoignition and localized extinction) contributes to flame stabilization in varying degrees, depending on flow conditions.				
<b>14. SUBJECT TERMS</b> Combustion chamber; Gas turbines; Flames; Burners; Raman spectroscopy; Laser induced fluorescence; Numerical analysis; Fuel; Sprays; Liquid fuels; Methyl alcohol			<b>15. NUMBER OF PAGES</b> 260	
			<b>16. PRICE CODE</b>	
<b>17. SECURITY CLASSIFICATION OF REPORT</b> Unclassified	<b>18. SECURITY CLASSIFICATION OF THIS PAGE</b> Unclassified	<b>19. SECURITY CLASSIFICATION OF ABSTRACT</b> Unclassified	<b>20. LIMITATION OF ABSTRACT</b>	